Faults as episodic conduits for hydrocarbons, CO$_2$ and groundwater in sandstones

Megan Elizabeth Heather-Cooley
B.Sc. (Hons) University of Plymouth

Thesis submitted for Degree of Doctor of Philosophy

Department of Civil and Environmental Engineering
Faculty of Engineering
University of Strathclyde

August 2017

Declaration

This thesis is the result of the author's original research. It has been composed by the author, and has not been previously submitted for examination which has led to the award of a degree. The research was supervised by Professor Rebecca Lunn and Professor Zoe Shipton. Any published or unpublished work by other authors has been given full acknowledgment in the text.

The copyright of this thesis belongs to the author under the terms of the United Kingdom Copyrights Acts as qualified by the University of Strathclyde Regulation 3.50. Due acknowledgement must always be made of the use of any material contained in, or derived from, this thesis.

Megan Heather-Cooley

Date – August 2017

Dedication

For those who I lost along the way.

In loving memory of:

Nanny Heather

Nanny Nurse

Aunty Janet

Aunty Ethel

To, Aunty Nette

Abstract

Constraining the dynamic feedback between deforming porous media and fluid is crucial for understanding hydrocarbon reservoirs, CO_2 storage sites and other evolving porous media. In particular, predicting complex fault architecture at depth, currently relies on deterministic algorithms, that do not take account of these dynamic coupling. For instance, creation of permeability due to fracturing may permit fluid flow to enter a fault zone, resulting in cementation (strengthening) or alteration (weakening) of the fault and host rocks. The resulting changes in rock strength may enhance or retard further fracturing and may even result in a switch of deformation mechanism.

Temporal and spatial evolution of fluid flow through faulted porous rocks has been studied in a field site in SE Utah, USA. The field area presents a well-exposed fault system that contains evidence for flow of multiple phases of groundwater with varying chemistries and flow of hydrocarbons. By detailed field mapping and microstructural observations of the fault rocks and of the evidence for fluid flow (e.g. bleaching and hydrocarbon staining) the fluid flow history and evolving flow properties of the rocks has been unravelled.

The 6km long fault presents an erosional scarp of up to 20m high at its centre. This scarp is dissected with canyons that permit cross-sectional views of the fault and associated alteration which has been mapped. The field area contains two general classes of lithology. In porous sandstones, deformation is accommodated by deformation bands and fractures. In tight limestones and siltstones deformation is accommodated by fracturing and the formation of clay-rich fault rocks. Evidence for multiple fluid flow events can be observed. Hydrocarbon staining is confined to the coarsest grained layers in the sandstones, and to fractures in all lithologies. Bleaching surrounds fractures in the fault damage zone and along bedding in the fault zone.

This thesis presents evidence for a reduction in porosity due to increased burial and cementation to be the biggest influence on deformation mechanisms for fault growth and evolution. Evidence of the evolving structural and hydrogeological properties of the fault zone are explored. This thesis discusses how such data can be used to improve the predictive capability of fault zone properties at depth where the faults have accommodated post-faulting fluid flow.

Table of Contents

List of Figures

List of Tables

List of Equations

Acknowledgements

To my parents - Mum and Dad, thank you for always encouraging me and for always supporting whatever decision I've made (even moving to Scotland!) To you both, I will always be so grateful for your love and support.

Finally, to my husband, Tom. You have been my rock, and I have probably taught you a thing or two about rocks! I am so thankful for your continued support and for always believing in me. Thank you.

xx

Chapter 1

Rationale

1.1 Rationale

Faults can be barriers (Antonellini and Aydin, 1994), conduits (Fairley et al., 2003) and partial barrier-conduits (Caine et al., 1996; Evans et al., 1997; Fairley and Hinds, 2004; Bense and Person, 2006) to fluid flow depending on the degree of deformation, the alteration present, the flow direction and the properties of the fluid flow. Faults are inherently heterogeneous (Stewart and Hancock, 1991; Shipton and Evans, 2002; Fay and Humphreys, 2005) and fault properties can vary both spatially and temporally (Caine et al., 1996; Evans, 1997; Johansen et al., 2005).

Constraining the relationship between deforming porous media and fluid flow is crucial for understanding hydrocarbon reservoirs (Knipe, 1997; Knipe et al., 1998; Aydin, 2000), CO_2 storage sites (Pruess, 2008; Dockrill and Shipton, 2010; Rutqvist, 2012) and radioactive waste disposal sites (Winograd, 1981; Wang et al., 2006). The relationship between deforming porous media and fluid flow is dynamic; fault architecture is constantly evolving due to stress changes and the influence of fluid flow on fault rock properties and their deformation mechanisms. For the successful placement of wells and waste/gas storage sites, it is crucial to understand how fault architecture influences fluid flow migration. Without the effective placement of these sites, fluid may leak or become trapped, for example; radioactive waste leakage, inefficient storage of CO_2 and low production rates of hydrocarbons.

It is currently difficult to predict the influence of faulting on fluid flow for a number of reasons. Firstly, even if the host rock lithology is similar between two fault zones, this does not mean that the fault rock will evolve to have the same properties. Burial depth, heterogeneous mixing of sediments in the host rock and fault zone, compaction and varying fluid chemistry from interacting fluids can affect how the rock behaves at depth. These factors will vary between individual faults, making it difficult to predict how fault architecture influences fluid flow migration as a result.

Predicting the hydraulic behaviour of faults at depth currently relies on deterministic algorithms (Lindsay et al., 1993; Fulljames et al., 1997; Yielding et al., 1997; Jones and Hillis, 2003). These contain a variety of assumptions and fail to take into account the heterogeneity of faults at depth (Kremer, 2014). For example, the shale gouge ratio method assumes homogeneous mixing and does not take into account the amount of host rock

integrated into the fault zone. Crucially, these algorithms also fail to incorporate the effect of structural diagenesis on the fault zone through alteration, weakening and cementation of the host rock (Laubach et al., 2010).

Creation of permeability due to fracturing may permit fluid flow to enter a fault zone, resulting in cementation (strengthening) or dissolution (weakening) of the fault and host rocks. The resulting changes in rock strength may enhance or restrict further fracturing and may even result in a switch of deformation mechanism. A switch in deformation mechanism will affect how a fault evolves both spatially and temporally. For example, a decrease in porosity as a result of cementation may lead to the formation of joints or shear fractures. Conversely, an increase in porosity as a result of dissolution can result in the formation of deformation bands.

Limitations in the resolution of seismic data often results in faults being represented as singular planes, since their thickness cannot be resolved. However, studying faults in closer detail shows that faults are often segmented into multiple strands with complex geometries, as well as varying in thickness along strike (Dawers and Anders, 1995; Johansen et al., 2005; Shipton et al., 2006). Whilst large scale through-going sub-surface faults are typically interpreted by using seismic data, and small scale sub-surface faults are identified by using well and bore-hole data, faults which are composed of multiple fault strands are frequently not well recognised on seismic data or well and borehole data (McLeod and Underhill, 2000; Walsh et al., 2002; Lohr et al., 2008).

Segmented faults have the potential to leak or act as barriers to fluid flow. Fault strands may impede or connect flow on a local scale. For example, segmented faults may form breached relays or fault lenses which can channel fluid flow into, or along, the fault zone.

Field data allows for the characterisation of fault architecture on a more local scale. For example understanding how different lithologies juxtaposed against each other produce certain fault rocks and permeabilities and how deformation styles influence the fault zone architecture and fault permeability (Marrett and Allmendinger, 1992; Rice, 1992; Fisher and Knipe, 2001; Trudgill and Cartwright, 1994; Cartwright et al., 1995; Cowie and Shipton, 1998; Shipton and Cowie, 2001; 2003; Johansen et al., 2005). However, there are few field studies of large offset faults with significant along strike exposure; most have displacements of less than 30m (Cartwright et al., 1995; Shipton et al., 2006) and, where

displacement is higher, lack good along strike exposure. Good along strike exposure is particularly important because it gives an insight into the variety of deformation styles within a single fault zone which may have affected the fault mechanics and permeability and which are not seismically resolvable. For example, whether a fault is composed of one through-going fault or comprises multiple fault strands cannot be recognised on a seismic scale but may have a huge influence on its hydraulic properties. Similarly, heterogeneity in fault zone thickness, burial depth, lithology variations and compaction are all important influencing factors for whether a fault will act as a barrier, conduit or baffle.

This thesis aims to improve the understanding of how fault heterogeneity can influence fluid flow. This study looks at a well exposed segmented normal fault, the Crow's Nest Fault in Utah, with a large offset and multiple along-strike exposures. Canyons dissecting the fault allow for a series of cross-sectional exposures through the fault that are rare in faults of this size. The thesis presents evidence of the evolving structural and geochemical history of the fault zone and the final chapter discusses how such data can be used to improve the predictive capability of fault zone properties at depth. Crow's Nest Fault adds to a global database of fault-based field-studies that seek to illuminate fault hydraulic behaviour through understanding the coupling between historic fluid flow and fault architectural development. By having a better understanding of how fluid flow affects fault rock mechanics, better predictions of fault properties at depth can be made.

1.2 Thesis outline

Chapter 2 is a literature review of the key areas of this thesis, fault zone architecture and the role and influence of fluid flow migration and fluid flow properties of faulted, porous sandstones.

Chapter 3 reviews the geological history, tectonic history and host rock lithology of this field area from published work and of the studied fault.

Chapter 4 presents the results of the field observations of the Crow's Nest Fault which encompasses detailed mapping and microanalysis of the fault. In particular, this chapter evaluates the relative timing and mechanisms of the observed deformation structures.

Chapter 5 presents evidence into how fluid flow has shaped the way Crow's Nest Fault has developed. In particular, this chapter focuses on how fluids have affected the formation of deformation structures in the fault zone.

Chapter 6 discusses the limitations of previous models of fault evolution and develops an evolutionary model for the Crow's Nest Fault. The model is then compared to faults elsewhere in Utah and the rest of the world.

Chapter 7 concludes the findings of the thesis and reflects on the study overall. This chapter compiles ideas for future work and further research that could be developed from this study.

Chapter 2

Literature Review

2.1 Introduction

Studying the relationship between fault rocks, fault architecture and fluid flow in the field is important because it bridges gaps between micro-scale (laboratory analysis of fault rock properties), macro-scale (field-scale fault architecture) and mega-scale (whole-fault) observations (Downey, 1984; Schlomer and Krooss, 1997). However, fault architecture is rarely exposed for significant distances along strike, hence, the extrapolation to mega-scale fault properties is frequently not possible.

This chapter reviews the most recent literature on fault zone architecture on a wide range of scales including, how fault development influences fluid flow and how fluid flow influences deformation mechanisms in fault zones. Section 2.2 defines the terminology used to describe fault zone architecture and fault zone development that will be used in subsequent chapters. The influence on fluid flow of fault development and individual fault zone components is discussed in sub-section 2.3. The chapter is summarised in 2.4.

2.2 Fault zone architecture

2.2.1 Fault terminology

A series of terms and definitions will be used in this thesis to describe the different components of a fault. Faults can be described in two main frameworks; by describing the geometries of 'fault rock' (Childs et al., 2009) or by distinguishing separate high and low strain components of a fault (Caine et al. 1996).

'Fault rock' refers to any deformed rock which is associated with a fault and can include (but is not limited to) fault gouge, breccia and cataclastic rocks (Childs et al., 2009). This definition of fault rock denotes the type of characteristics expected of the rock but does not outline the relative position of the fault rock with respect to the location on the fault.

The fault zone model as defined by Caine et al., (1996) distinguishes fault components with regards to strain and the position of each fault component with respect to the location on the fault (figure 2.1).
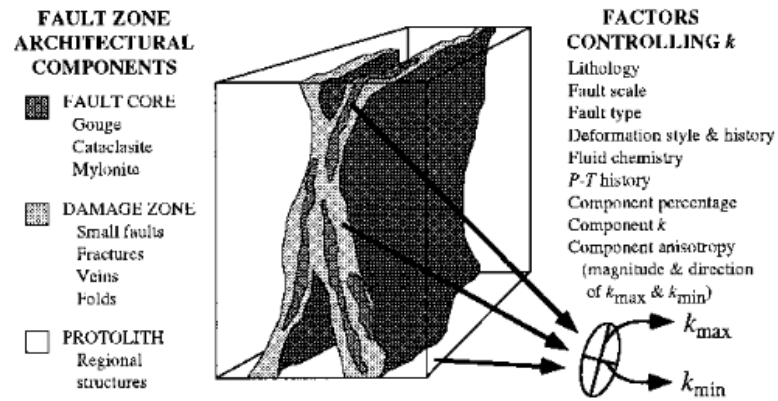
Figure 2.1 – An idealised fault zone model which identifies a fault core and damage zone surrounded by a relatively undeformed protolith (Caine et al., 1996).

Caine et al. (1996) states that a fault zone is composed of a protolith, fault core and damage zone. The 'protolith' or host rock, refers to the rock which is being faulted and which has not been mechanically or chemically altered by the presence of the fault. The 'fault core' is the zone in which most of the displacement has been accommodated. The surrounding 'damage zone' hosts subsidiary structures such as fractures and refers to the zone in which fault-related deformation is accommodated in the protolith (Chester and Logan, 1986; Caine et al., 1996).

Factors that influence the characteristics of the fault core and damage zone include the lithology which is being faulted, the type and style of faulting, deformation history, the degree of displacement and the fluid chemistry (Caine et al., 1996).

A limitation to the fault zone model by Caine et al., (1996) is the problem of defining what exact deformation elements are defined as the fault core and as the damage zone and how does this vary from each fault system. Some fault zones may include the same deformation elements in the damage zone and the fault core but in different concentrations. For example, at the Big Hole Fault in Utah (Shipton and Cowie, 2001), deformation bands and slip surfaces are seen in both the damage zone and the fault core. The fault core consists of a zone of concentrated deformation bands but with one or more through going slip surfaces, however the damage zone consists of deformation bands that are less concentrated and slip surfaces that are less connected.

8

The definition of the above terms are based mainly around the idea of increasing strain as a result of faulting. The Caine et al. (1996) model does not take into account fault geometry on a large scale. For example, a fault over 20km long may be defined by linked segments. This is important as large-scale fault geometry may have a significant influence on local fault architecture.

Faults with multiple fault strands often exhibit complex fault zone geometries (figure 2.2b). For example, the Carboneras Fault in south-east Spain has multiple fault strands of phyllosilicate rich fault gouge present within the fault zone (Faulkner et al., 2003). It is thought that as the Carboneras Fault developed, strain hardening in the fault gouge distributed deformation across the fault zone, widening the fault zone and forming multiple strands of fault gouge. With increasing strands of fault gouge, the fault zone model differs from the fault zone model of Caine et al., (1996) in that the number of fault cores increases with areas of damage zone in between them also increasing in number.
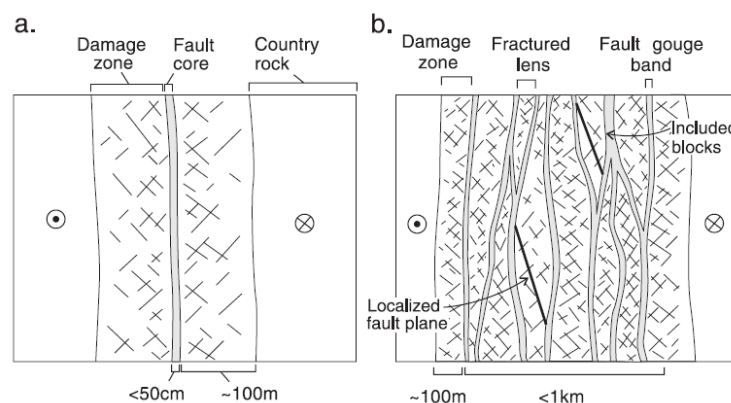
Figure 2.2 - (a) Conceptual model of a typical fault zone using the fault zone model of Caine et al., (1996) which contains a fault core, damage zone and country (host) rock. (b) A conceptual model which presents a fault zone with multiple strands of fault gouge amid a damage zone. Where there are two or more strands of fault gouge, they can surround a lens. Figure by Faulkner et al., (2003).

Despite the limitations associated with the fault zone model of Caine et al., (1996), the definitions used to describe the fault zone structure are useful and can be adapted to suit most larger-scale field geometries. Hence, they have been employed within this thesis to classify fault architecture within the designated field area.

2.2.2 Fault displacement

The distance a point on the fault surface has moved along a fault can be described as true displacement/slip. In an idealised elliptical fault, the maximum displacement is at the centre of the fault. The displacement of the fault then decreases to zero away from the centre toward the ends/tips of the fault (figure 2.3a). However, many faults are composed of linked fault strands which either soft link or hard link together, and hence, may have different displacement profiles (Walsh and Watterson, 1991, Childs et al., 2009). Throw is the vertical component of displacement on the fault and is referred to throughout this thesis.
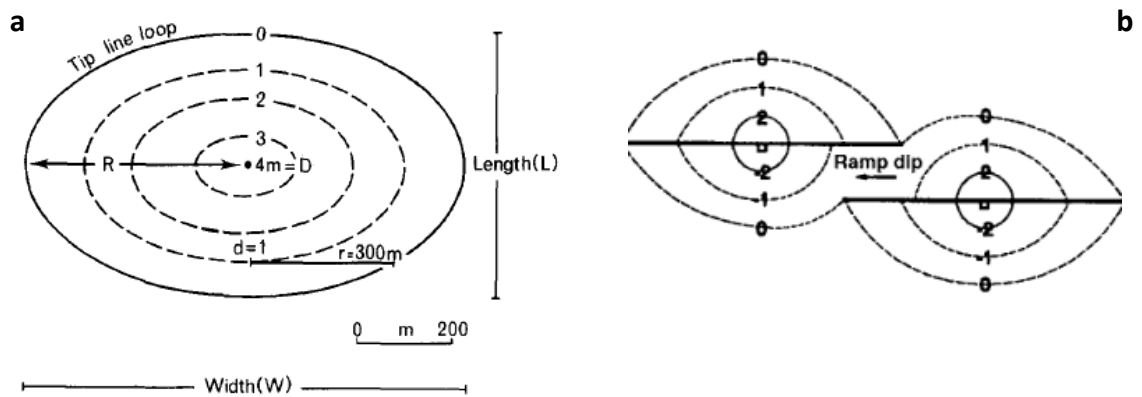
Figure 2.3 – (a) An idealised elliptical fault (Walsh and Watterson, 1991) identifies maximum displacement to be at the centre of a fault and displacement then decreases to zero at the fault tip line. (b) Displacement on a linked fault – the fault strands begin to interact and the displacement is transferred between the faults. (Peacock and Sanderson, 1994).

When two fault strands begin to interact and link together, the displacement is transferred between the faults (figure 2.3b) via formation of what is termed the relay ramp. The rocks in the relay ramp are deformed to accommodate the transfer of displacement and may be rotated (Peacock and Sanderson, 1994).

Seismic data has a limited resolution, with a minimum resolution between 10m and 30m of vertical offset (Maerten et al., 2006); anything below this is classified as sub-seismic. On a seismic scale throw is usually observable, as opposed to fault displacement, because the vertical offset of the lithological boundaries, which act as seismic reflectors, can be defined, but not the slip vector (figure 2.4). To calculate true displacement, the dip of the fault plane needs to be identified as well as the horizontal component of the slip vector.
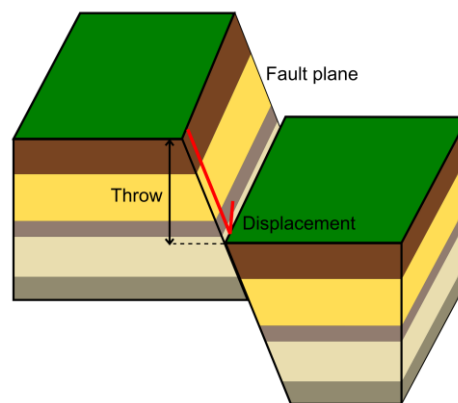
Figure 2.4 – Block diagram showing the difference between displacement and throw and where they are measured with respect to the fault plane (Kremer, 2014).

Because faults grow in a similar way to a crack growing within a material, there is a relationship between the maximum displacement (d) and the length (L) of a fault (Watterson, 1986; Walsh and Watterson, 1988; Marrett and Allmendinger, 1991; Cowie and Scholz, 1992; Dawers et al., 1993; Cartwright et al., 1995; Clark and Cox, 1996; Schultz and Fossen, 2002; Childs et al., 2009). Not all faults have a constant or linear displacement-length relationships and there are many other factors which can inhibit or enhance the growth of a fault with increasing displacement. Cowie and Scholz, (1992) argue that the d/L relationship is dependent on material properties. For example, grain size distribution, burial depth, thermal history, frictional properties of the fault surfaces, deformation history and linkage history (Cartwright and Mansfield, 1998) are all factors which result in heterogeneity that may alter the change in displacement with respect to fault length.

2.2.3 Fault linkage

The style of fault initiation influences the growth of fault zones which ultimately forms a control on fault properties (Knipe, 1997; Hesthammer and Fossen, 2000; Crider and Peacock, 2004). Faults can grow by the propagation of one strand (radial tip propagation), by two or more strands linking together (segment linkage) or by spitting of a single fault strand (tip bifurcation).

Radial tip propagation is the process by which a fault grows by migrating out from the point of initiation (maximum displacement) along a plane (figure 2.5a). Radial tip propagation

assumes that the material properties of the rock that the fault is propagating through are constant during deformation (Cartwright et al., 1995). In reality this is very unlikely due to the heterogeneous nature of rocks at depth. As a result very few fault profiles are symmetrical.

Many faults consist of multiple fault strands or segments. Fault strands can be soft linked, where they are linked through their stress fields alone, or hard linked where they are physically linked together (Walsh and Watterson, 1991). Where faults are soft linked, a zone of high strain occurs between two fault strands, referred to as a relay ramp (Childs et al., 2009). Relay ramps are characterised by rotated bedding (Peacock and Sanderson, 1994). Where faults are hard linked, the displacement is then transferred between the two fault strands (figure 2.3b) that connect the footwall and the hanging wall of a fault together, surrounding the relay ramp. Relay ramps can occur over a wide range of scales (Stewart & Hancock 1991; Peacock & Sanderson 1994; Huggins et al., 1995).

If two or more fault strands are hard linked and a body of rock has been encompassed between the fault strands, this is defined as a 'fault lens' (Childs et al., 1996). The term lens refers to a body of relatively intact host rock trapped within a fault and it can form either by segment linkage or tip bifurcation (Woodcock and Fischer, 1986; Kuiper et al., 2011; Ponce et al., 2013). Fault lenses can occur over a wide range of scales from a few metres to several kilometres (Foxford et al., 1996; Faulkner and Rutter, 2001; Childs et al., 2009).

During segment linkage, the rock bodies between the two kinematically related fault strands are under intense strain (Walsh and Watterson, 1991; Childs et al., 1996; Childs et al., 2009). Eventually as displacement begins to increase at the relay ramp during segment linkage, the relay ramp will fail and result in a 'breached relay ramp'; i.e. hard linkage (Peacock and Sanderson, 1994; Trudgill and Cartwright, 1994; Childs et al., 1996; Ferrill et al., 1999; Childs et al., 2009).
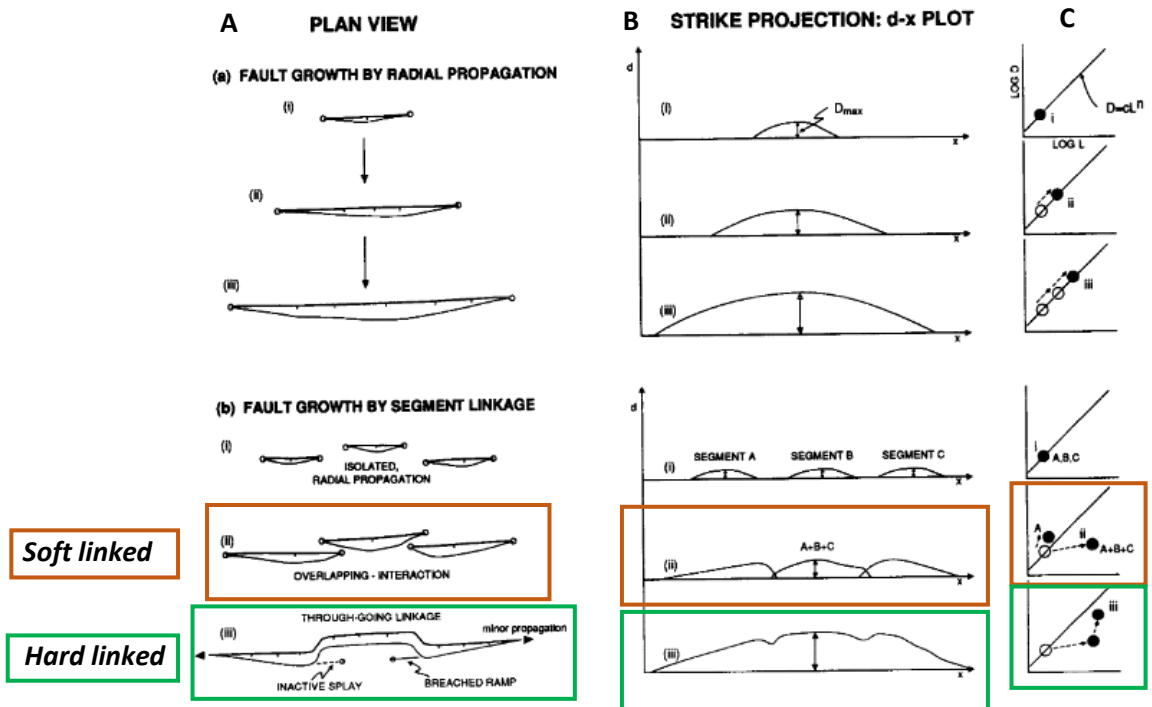
Figure 2.5 – A comparison of fault growth models for radial propagation and segment linkage. Both models are compared on (A) plan view, (B) displacement (d) against distance (x) and for (C) displacement (d) against length (L). Large fault systems usually result from the linkage of smaller faults (Dawers and Anders, 1995). Segment linkage occurs when an isolated fault strand comes into contact with another fault strand. When the two strands interact through their stress fields, they become soft linked. Fault strands then become physically linked, known as hard linked (Gupta and Scholz, 2000). As linkage continues, displacement accumulates near the centre of the fault plane. The strands no longer appear as individuals and the profile approaches that of a single fault. Displacement minima may be preserved at the relays. The fault profile of a soft linked fault is indicated in orange and the fault profile of a hard linked fault is indicated by green.

The breached relay ramp remains as a site of irregularity between the two fault strands even after linkage (Gupta and Scholz, 2000) (figure 2.6). The breached relay ramp is then incorporated into the through-going fault and becomes a fault lens (defined earlier in this section) which is either fault bounded or entrained along the fault surface (Childs et al., 2009).
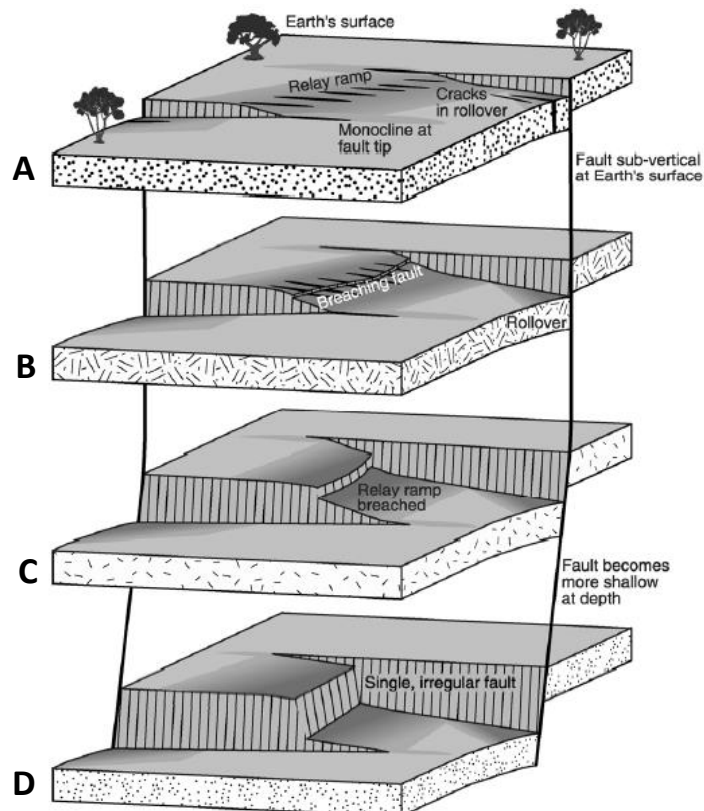
Figure 2.6 - A series of diagrams detailing the different stages of breached relays ramps. A – Relay ramp which is un-breached. B – Breaching starts to occur but the relay ramp is still intact. C – Relay ramp is fully breached. D – Breached relay ramp has fully isolated into a single, irregular fault. (Crider and Peacock, 2004).

Both intact and breached relays can influence the sealing capacities and/or flow properties of faults in hydrocarbon reservoirs (Childs et al., 2003; Moriya et al., 2005). Relay ramps are important foci for hydrocarbon migration (Peacock and Sanderson, 1994) because they may contain a high density of fractures.

Most faults grow by using more than one mode of formation. For example, the Strathspey-Brent-Stratfjord fault in the North Sea grew by a combination of radial tip propagation and segment linkage (MacLeod et al., 2002). Reconstruction of the fault suggests that the now through going fault initially consisted of five isolated fault strands. Multiple fault strands are thought to have grown by radial tip propagation and then linked through their stress fields. After becoming soft linked they began behaving like a single fault with the position of maximum displacement moving away from the centre of the single strands. After some time, the strands linked together and became hard linked through segment linkage.

Other faults grow through the process of tip bifurcation (Childs et al., 1996). Tip bifurcation occurs when a fault tip comes into contact with an asperity. This interaction leads the fault to split into two or more strands and may result in a fault lens forming (figure 2.7c) or a fault tip dying out (figure 2.7d). The bifurcation and re-linkage of strands forms a lens shape fault zone. Asperities develop from a number of geological and lithological occurrences, for example, where there are contrasting lithological horizons (Rawling and Goodwin, 2006).
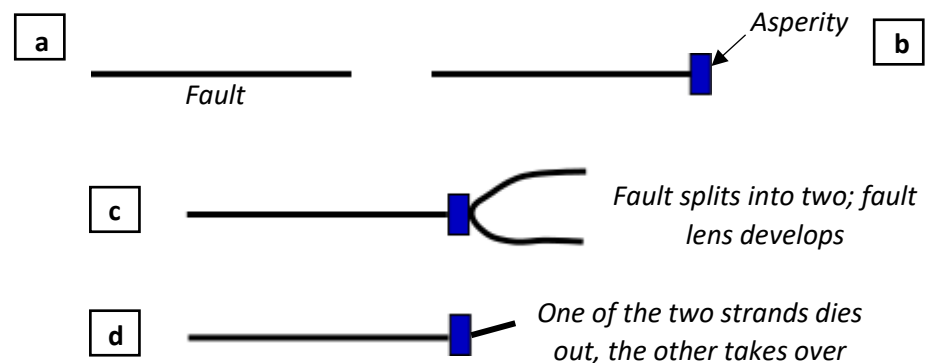
Figure 2.7 – Schematic diagram showing the process of tip bifurcation. When a fault (a) comes into contact with asperity (b), the interaction may lead the fault to split into two or more strands and this could result in a fault lens forming (c) or where one of the two bifurcated strands dies out, leading the other one to take over (d).

2.2.4 Fault thickness

Fault rock thickness (measured perpendicular to the fault plane) is usually heterogeneous along strike and this is dependent on the internal geometry and architecture of the linking fault strands. The model of Childs et al., (2009), which suggests a correlation between fault rock thickness and displacement, also indicates that fault zone thickness and architecture will be influenced by the geometry of any linked fault strands. Other authors also support this observation (Hull, 1988; Marrett and Allmendinger, 1991). Childs et al., (2009) suggest that apart from the damage zone, the thickness of a fault is influenced by the scale of fault linkage, and that the varying degrees of thickness along a fault relate to the different stages in segment linkage and displacement.

Faults accumulate overall displacement by a series of slip events. (Fossen and Hesthammer, 2000; Shipton and Cowie 2003; Shipton et al., 2006). The slip events increase stress surrounding the fault and this causes deformation features, such as deformation bands, to form in response. As stress increases, zones of deformation elements such as deformation

bands increase in numbers and a slip surface is able to develop and repeat the process. As a result, the fault increases in thickness due to incremental increases in displacement.

2.3 Key concepts of faults, fluids and their interaction

The following sections address important controls on fluid migration within fault zones. This section aims to review the influence of faulting on fluid flow and the structural and physical factors that affect the behaviour of fluid flow migration along, and across, faults. Observations of faults at depth are difficult and as a result, many of the studies reviewed in this section are comprised of both field observations and modelling from a range of industry applications and academic research.

Firstly, the key concepts of fluid flow will be addressed in section 2.3. This will include (but not be limited to) the study of fluid flow properties such as single and multi-phase fluid flow and the structural and lithological controls on fluid flow migration within fault zones. This section analyses the current industry standards used to quantitatively estimate fault rock composition and what factors these algorithms rely on.

Section 2.4 will address how fault development influences fluid flow and will look at the effect that different fault components have on fluid flow. This section will include the mechanisms for fault rock juxtaposition and the importance of this for different industries.

2.3.1 Single-phase flow

Porosity and permeability are key controls on how a fluid can migrate through a rock. Fluids are able to move through porous media due to the interconnection of pores between grains or through fractures. The ease with which fluids can do this (permeability) is not however, a direct function of how porous a rock is. This is because not all pore spaces are interconnected, some may be isolated. An example of this is where rocks have been formed during gas emission, such as pumice, in which porosity can be very high, >80% void space, but the permeability of the rock may be low as each gas bubble during rock formation was isolated and, therefore, the connectivity of the pores is poor. In sedimentary rocks, grains which are well rounded have the potential to lower porosity as they can pack closely together whereas more angular grains may result in higher porosities (Meinzer, 1923). In porous rocks, permeability is quantified by Darcy's Law (Darcy, 1856);

$$q = -\frac{\rho g k \Delta h}{\mu \Delta x}$$

Equation 1.1 – Darcy's Law defines the relationship between flow rate and viscosity of a fluid with respect to a drop in pressure of a distance. q corresponds to the Darcy flow rate (m/s), k is the permeability m/s^2), ρ is the fluid density (Kg/m^3), μ is the fluid viscosity (Kg/(m.s)) and Δh is the change in hydraulic head (m) over a small distance Δx (m).

Darcy's Law states that the flow rate q of a liquid flowing through porous media is dependent on the hydraulic head gradient, $\Delta h / \Delta x$ and the permeability, k. Hence, for a fluid to flow, there needs to be a hydraulic gradient.

During brittle deformation, increased fracturing and faulting can result in the interconnection of pore spaces which can lead to increased permeability within the host rock. Other factors which influence interconnectivity of pore spaces in single-phase flow include pore throat size, cementation and grain crushing.

2.3.2 Multi-phase flow

When fluid flow passes through a fault zone it may be in the form of single-phase flow, for example water in a water saturated rock. However, flow could include liquid water and water vapour, or two liquids such as oil-water or methane-water and this is termed multi-phase flow.

If only one phase of fluid is present then fluid flow through the porous medium can be determined by calculating the permeability of the medium and the viscosity of the fluid. However, in multi-phase flow, the relatively permeability of the medium also needs to be known. Relative permeability can be defined as the ratio of permeability of a fluid at a given saturation ratio to the total permeability of the porous medium (Fetter, 1993).

Understanding multi-phase flow is especially important for industries involved in oil and gas, CO_2 storage and radioactive waste disposal. For example, hydrocarbons can be present in three distinct phases; oil, water and gas. For hydrocarbons to move into a water saturated rock, the water has to be displaced to make room for the hydrocarbons. For this to occur, the capillary entry pressure must be exceeded, which is governed by the pore throat diameter and the nature of the fluids. For hydrocarbons to enter a fault rock, the pressure of the hydrocarbon column must exceed the capillary entry pressure for that rock,

if not, the fault may be a seal to hydrocarbons, thus, forming a barrier to hydrocarbon flow (Fisher et al., 2001).

When a fault seal becomes breached, fluid flow is controlled by the relative permeability so it is therefore important to understand relative permeability in porous media where multi-phase flow is present.

2.3.3 Lithological controls on fluid flow

Host rock lithology can play a vital role in deformation mechanisms, the resulting fault architecture and its connectivity for fluid flow. The original lithology plays an important role in determining whether a fault behaves as a barrier, conduit or baffle to fluid flow.

For example, lithological layering can control fault dip. Studying how fault dip is affected by stratigraphy is important because mechanical stratigraphy can strongly influence whether a fault will enhance or inhibit fluid flow. Ferrill and Morris, (2003) suggest that the process of fault refraction can cause changes in the fault dip because of the changes in mechanical strength of the different host rock layers. Stronger more competent layers may cause fault dilation, result in a steeper fault and enhance fluid flow. Whereas weaker, less competent layers may result in an increase of shear failure, result in shallower dips and inhibit fluid flow (figure 2.8).

Other controls on fault flow properties include layer thickness, host rock cementation and shale smearing (which is outlined in more detail in section 2.3.4). Studies of fracture distribution at the Moab Fault, Utah by Berg and Skar, (2005) suggest that fault dip is controlled by both layer thickness and cementation of the host rock. At the Moab Fault, hanging wall fractures dipped less steeply than footwall fractures and this was a function of the host rock layers being thinner and less cemented in the hanging wall than the footwall.

There are two widely recognised types of fault sealing; juxtaposition seals and fault seals. Fault seals occur when the fault zone itself is impermeable. Juxtaposition seals occur when there is juxtaposition of low permeability units against high permeability units across a fault (Knipe, 1997; Pei et al., 2015). If a permeable rock unit is thicker than the fault throw it will self-juxtapose and form migration pathways for fluid flow (Pei et al., 2015).
Offset faulted horizons are mapped in a seismic data set to build a 3D geological model of the faults that can be used to map juxtapositions (Allan, 1989; Knipe, 1997; Yielding et al.,

1997). However, using seismic data to determine juxtaposition is limited to faults which have single planes (van der Zee and Urai, 2005) since in faults with multiple parallel fault strands it is not possible to resolve the location of horizons between the planes. This creates errors in the determination of juxtaposition seals, because most faults have multiple slip surfaces with displacement distributed over more than one fault plane. In addition, segmented faults have the potential to leak or act as barriers to flow on a more local scale.
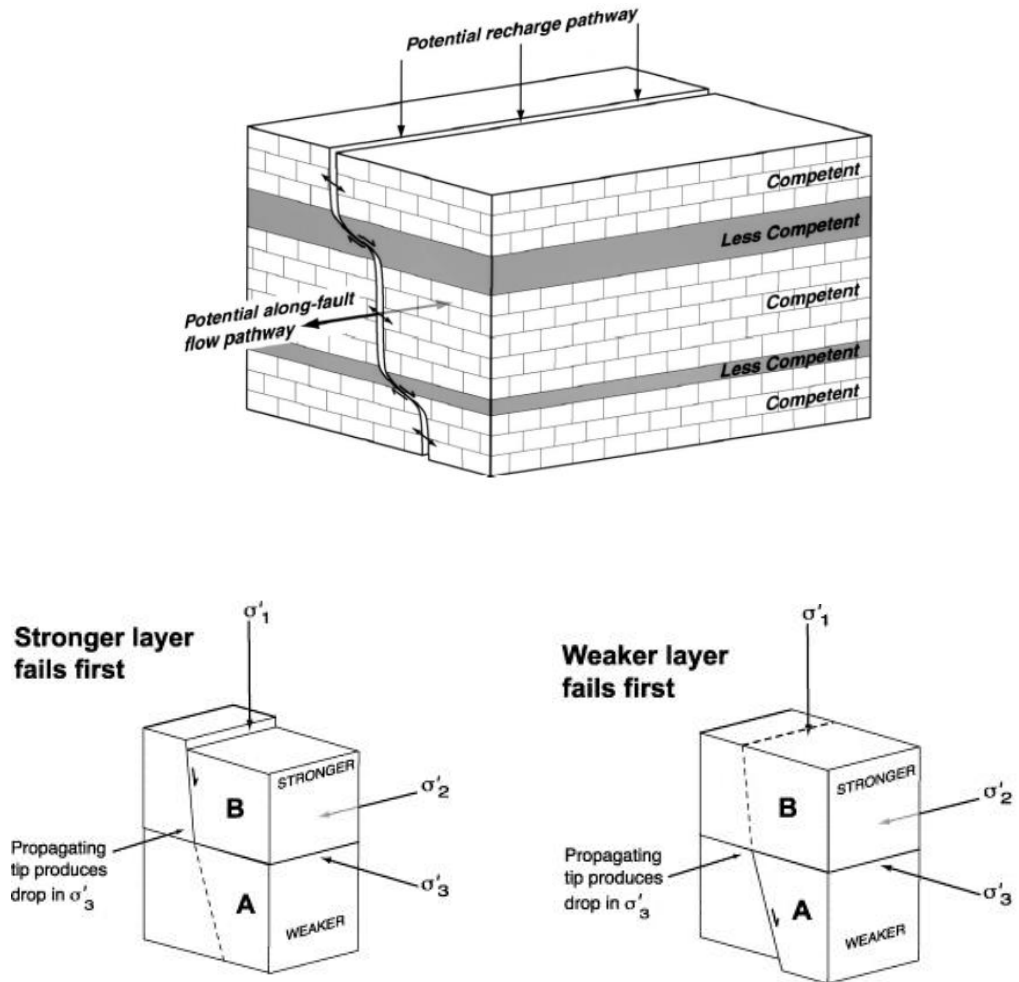
Figure 2.8 – The way host rock lithology is layered affects the dip of a fault and as a result can affect fluid migration. For instance, in a series of alternating stronger and weaker layers of rock, there is a potential for along fault flow pathways to develop due to refraction (Ferrill and Morris, 2003).

Juxtaposition of different lithological units results in the formation of fault rock. In order to estimate the characteristics of varying fault rocks and evaluate fault seal potential, Allan diagrams can be constructed. Allan diagrams are maps which superimpose the hanging wall

and footwall of a fault onto a modelled fault surface (Cerveny et al., 2004). Allan maps make it possible to assess possible fluid flow pathways, leakage points and the sealing potential of faults by juxtaposition.

Allan diagrams require a large amount of data to increase the accuracy of estimations and this is not always available. More simplified diagrams are often used in industry such as juxtaposition and triangle diagrams (Knipe, 1997). These models evaluate the juxtaposition of different lithologies with increasing throw and identify prospective barriers, conduits and baffles to fluid flow.

When there are two or more high permeability reservoir rocks juxtaposed on either side of a fault, the classical assumption is that leakage across the fault can occur. However, the presence of the fault rocks can result in a barrier or 'fault seal'. Such barriers are generally referred to as a membrane seal. Membranes seals are an accumulation of low permeability structures within the fault which inhibit the migration of fluid flow through the presence of small pore throats, and hence high capillary entry pressure (Watts, 1987).

Faults can also act as leakage pathways from reservoirs via along-fault flow. For example, where hydrocarbons are trapped by a top seal, a breach may occur if a fault cross-cuts the seal. This is called a seal bypass system (Cartwright et al., 2007). Seal bypass systems can be defined as a set of seismically resolvable geological features (which may be faults or may be other structures such as igneous intrusions) which promote fluid migration across the seal (Cartwright et al., 2007).

Based on whether faults define or delimit a trap with a sealing component, they can be divided into trap-defining or supratrap faults (Cartwright et al., 2007). Trap-defining faults define a trap with a lateral seal component. The vertical permeability of the fault plane for trap defining faults is dependent on the fault's motion history and local hydrodynamic boundary conditions. Supratrap faults delimit a trap and may include, for example, synthetic and antithetic faults above rollover anticlines. The behaviour of supratrap faults is partly dependent on the reservoir conditions, but is also a function of the fault rocks and the fault architecture, both of which are dependent on the sedimentary structure and the flow history.

Fluids may rise to the surface through faults acting as migration pathways. However, at shallow depths, once the overburden is encountered, faults are no longer permeable up-dip. Therefore, an increased buoyancy and decreased lithostatic pressure are needed to travel through the overburden to the ground surface (Schlomer and Krooss, 1997). Field studies in the Gulf of Mexico have shown a preference for seep structures, associated with faults to occur in the hanging wall (Abrams, 1996; Schlomer and Krooss, 1997; Pilcher and Argent, 2007). This preference has occurred as, once fluid reaches the overburden, it will then take the shortest, most permeable path to the ground surface.

The way in which a rock deforms can have a huge influence on fault permeability. For example, grain crushing and mineralisation can impede flow, whereas fracturing and dissolution can enhance flow. The relationship between fault architecture and fluid flow is dynamic; fault architecture can evolve due to the influences of both fluid flow and stress changes, and fluid flow that leads to dissolution or mineralisation, has the potential to alter subsequent deformation styles which feeds back to fault architecture.

2.3.4 Algorithms for quantitatively estimating fault rock composition

In order to quantitatively predict fault rock composition at depth, three main algorithms are used within industry; Shale Gouge Ratio (Yielding et al., 1997; Fristad et al., 1997; Freeman et al., 1998), Clay Smear Potential (Yielding et al., 1997; Fulljames et al., 1997; Egholm et al., 2008) and Shale Smear Potential (Lindsay et al., 1993; Doughty, 2003).

Shale gouge ratio (SGR) is an algorithm for estimating the clay content of a faulted lithology based on the content of shale within a faulted host rock. This is achieved by calculating the overall amount of shale present in the host rock, displaced past a specific point along the fault. The Shale Gouge Ratio (SGR) assumes that the fault rock is a blended mixture of all the rocks that have been displaced past a specific point along the fault. It estimates the percentage of shale within the fault zone by assuming shale is present in the same percentage as in the host rocks that have been displaced past that point. Hence, to calculate SGR, Yielding et al., (1997) devised the following equation:

$$SGR = \frac{\Sigma(\text{Shale bed thickness})}{\text{Fault throw}} \times 100\%$$

Equation 1.2 – The Shale Gouge Ratio (SGR) - (Yielding et al., 1997).

Studies by Yielding et al., (1997) indicate that faults with an SGR of below 20% do not seal or form a continuous shale smear. However, van der Zee and Urai, (2005) studied faults in Miri, Sarawak, Malaysia and their results showed that some faults with a SGR of below 20% did form a continuous shale smear.

There could be a number of reasons for these discrepancies. Firstly, continuous shale smear is not always visible in 3D and so will never appear when seismically imaging faults. Studies of faults in Miri, Sarawak, Malaysia by van der Zee and Urai, (2005) were able to confirm continuous shale smear through detailed maps of the main structural elements in vertical outcrop faces in the field.

Secondly, SGR essentially assumes a fully blended rock, however, field observations demonstrate that fault rock can be highly heterogeneous (Stewart and Hancock, 1991; Yielding et al., 1997; Shipton et al., 2002). SGR does not distinguish between a single thick clay rich bed that forms 20% of the passing lithologies from multiple thin beds that give the same SGR %, yet, the fault rocks are likely to be different. SGR only assesses the juxtaposition of sand and shale rich lithologies and omits other lithologies which may have the potential to enhance or impede flow such as carbonates. Furthermore, fluids moving along faults may have resulted in subsequent dissolution or cementation of fault rocks and these processes are not taken into account.

Yielding et al., (1997) stated that SGR % gets more accurate the higher the fault throw. However, there is no currently available data in the public domain on the success or accuracy of using the SGR. Vrolijk et al., (2005) reported that local structures in a fault can vary the percentage of shale in the fault zone and that the calculation does not incorporate local variability in the overall estimation. To increase the accuracy of fault seal prediction, local heterogeneity should be taken into account in addition to the SGR value.

Clay smear potential is another estimation tool. Clay smear is defined as all processes that somehow transform clay in the wall rock into clay in the fault (van der Zee and Urai, 2005).

Definitions vary between publications and as a result, the definition of which processes result in clay smear is often unclear (van der Zee et al., 2003). Generally, it is agreed that the three main processes which initiate clay smear are clay abrasion (Lindsay et al., 1993), shear as a result of releasing fault links (Koledoye et al., 2000) and lateral clay injection (van der Zee et al., 2003).

Clay smear potential (CSP) is an estimate of how likely clay smearing is in areas of sand/sand juxtaposition along faults (Bouvier et al., 1989; Yielding et al., 1997). CSP calculates the amount of clay smeared from individual shale source beds at a specific point along a fault.

CSP is estimated by using the following equation:

$$ \text{CSP} = \sum \frac{(\text{Shale bed thickness})^2}{\text{Distance from source bed}} $$

Equation 1.3 - The Clay Smear Potential (CSP) - (Yielding et al., 1997).

Yielding et al., (1997) stated that CSP increases and decreases systematically in three fundamental ways. Firstly, as the number of shale source beds increases, CSP will increase. Secondly, with increasing source beds being displaced past a particular point along a fault, CSP will increase. Finally, CSP will decrease with increasing throw along a fault.

Clay smearing promotes fault sealing (Caine et al., 1996). The clay content of fault gouge is a critical factor which controls the mechanical properties of a fault zone. For industries specialising in groundwater flow and hydrocarbon reservoirs, this is crucial for estimating fluid connectivity in the subsurface (Egholm et al., 2008). It is widely accepted that thick, weak source beds produce the thickest smears and subsequently the best seals (Clausen and Gabrielsen, 2002; Egholm et al., 2008).

CSP is different to SGR in that CSP estimates clay to be dependent on the thickness and proximity of the source rock layers, whereas SGR predicts the amount of clay in the fault gouge to be proportional to the amount of clay in the wall rock units (van der Zee et al., 2003). However, results from van der Zee et al., (2003) demonstrate that when lateral clay injection occurs along a fault, the proportion of clay in the fault gouge can be higher than in the wall rock. This suggests that the CSP estimation needs to take into account not only the

mechanics of the fault zone, but also the geometry of the fault zone and the mechanics of injection.

When calculating CSP and other methods (SGR and SSF), there is an assumption that the fault gouge is the product of a reworked portion of the wall rock (Holland et al., 2006) and that there has been no mixing or diagenesis of sediment. Due to the complex nature of faulting, mechanical properties of the wall and fault rocks are highly heterogeneous; CSP fails to integrate this into the calculations (Schmatz et al., 2010). The mechanical properties for the development of clay smear remain poorly understood (Egholm et al., 2008).

Shale smear factor (SSF) estimates the likelihood of a continuous shale smear (Lindsay et al., 1993) and is defined at a specific point on a fault, for a particular shale bed, as the ratio between fault throw locally and the thickness of a shale bed (Manzocchi et al., 2008).

The method calculates the thickness of shale units along a fault and compares this to the critical throw (Davatzes and Aydin, 2005) where shale is no longer present along the fault zone (Lindsay et al., 1993; Gibson, 1994; Aydin and Eyal, 2002). The calculation gives an estimation of how thick the shale being dragged down into the fault zone is during faulting. The variation in SSF along a fault surface makes it difficult to designate individual faults as seals or non-seals (Yielding et al., 1997).

SSF is estimated by using the following equation:

$$SSF = \frac{\text{Fault throw}}{\text{Shale layer thickness}}$$

Equation 1.4 – Shale Smear Factor (SSF) - (Yielding et al., 1997).

Calculating SSF is dependent on the thickness and offset of individual shale beds (Davatzes and Aydin, 2005). Smears are only found associated with the thickest shale beds and due to the heterogeneous nature of and-shale sequences, it is not possible to map every shale bed or determine the thickness and offset. Davatzes and Aydin, (2005) suggest only considering the bulk properties of shale sequences to determine SSF on a larger scale. Moreover, SSF assumes the fault zone to be homogenous and finer details and heterogeneity are ignored as a result.

Where shale smear is discontinuous, the calculation of SSF does not correspond to SGR because SGR uses all beds in the throw window for estimation (Davatzes and Aydin, 2005). Discrepancies in estimating the SSF mean that fault sealing capacity cannot be solely estimated on the basis of SSF alone, but factors such as heterogeneity of the fault zone and changes in thickness should be taken into account before a reasonable judgement can be made by industries.

Faerseth (2006) presents data from a number of large seismically active faults in offshore Norway that show evidence for continuous (tens of metres) shale smear along faults. Their research leads to the following relationship between SSF and the likelihood of a continuous shale smear:

(1) SSF≤4, a continuous smear is expected.

(2) 4 ≤ SSF ≤6, a decreased confidence with respect to a continuous smear.

(3) SSF > 6, a continuous smear is unlikely for large faults.

2.3.5 The effect of fault zone components on fluid flow

To predict whether a fault will act as a barrier, conduit or baffle, it is important to look at the distribution, frequency and position of the different fault components within a fault zone (Caine et al., 1996; Manzocchi et al., 1999). For example, it is common for fault zones to be heterogeneous and have multiple fault cores (figure 2.9b).
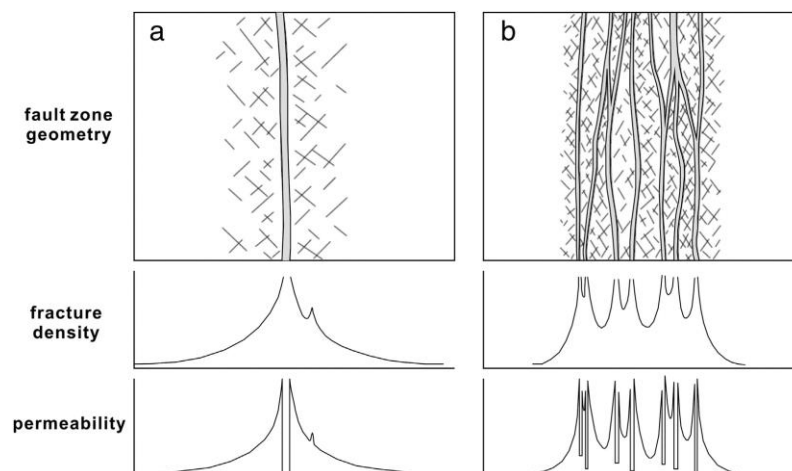
Figure 2.9 – (a) Fault zone model showing a low permeability fault core surrounded by a high permeability damage zone (Caine et al., 1996). (b) Fault zone model showing multiple low permeability fault cores surrounded by high permeability damage zone (Faulkner et al., 2003; 2010) Figure taken from Pei et al., (2015).

Figure 2.9a is the fault zone model of Caine et al., (1996) showing a fault core as a barrier to fluid flow and a damage zone as a conduit to fluid flow. This model suggests that permeability increases towards the fault core due to fracturing in the damage zone, but is low permeability in the fault core. In contrast, figure 2.9b is an example of a fault zone with many fault cores (Faulkner et al., 2003; 2010) which suggests greater heterogeneity within the fault zone associated with multiple fault core strands.

The permeability of open fractures and slip surfaces found in the fault core are influenced by local stress fields. (Faulkner at al., 2010). Creation of permeability due to fracturing may permit fluid flow to enter a fault zone, resulting in mineralisation (strengthening) or alteration (weakening) of the fault and host rocks. The resulting changes in rock strength may enhance or impede further fracturing and may even result in a switch of deformation mechanism. How open fractures and slip surfaces within a fault zone are connected, determines whether the fault will act as a conduit to flow within surrounding lithological units that have a lower permeability. Where fractures are present at relay ramps, permeability may be enhanced depending on factors such as orientation and connectivity. In high porosity sandstones, local deformation may be accommodated through the formation of deformation bands, as opposed to fractures. Deformation bands are narrow bands (~<2mm) of intense cataclasis which are surrounded by relatively undeformed host rock. Deformation bands are a result of rock failure through either dilation, shear or compaction (Aydin et al., 1978; Fossen and Hesthammer, 1997; Fossen et al., 2007).

Due to the porosity reduction within deformation bands, they generally result in a decrease of permeability within a rock unit (Aydin et al., 1978; Antonellini and Aydin, 1994; Fossen and Hesthammer, 1997; Shipton and Cowie, 2001; Fossen et al., 2007; Torabi and Fossen, 2009). For example, the fault core of Big Hole Fault, Utah consists of tightly packed deformation bands which results in a reduction of permeability at the fault zone (Shipton et al., 2002). Studies by Fossen et al., (2007) indicate that deformation bands have permeabilities which range between 0.9–1.3 mD.

In some sites, however, deformation bands have been defined as conduits for fluid flow. For example, Fossen et al., (2007) presented two extreme examples from rocks with almost identical mineralogy. Figure 2.10a represents a deformation band which has a higher porosity and permeability than the surrounding host rock, whereas figure 2.10b represents

a deformation band with a lower porosity and permeability than the surrounding host rock. The reason for this dramatic difference between the effective permeabilities of these deformation bands is due to the mechanism by which they form. Figure 2.10a is a disaggregation band which forms via dilation and increases permeability, whereas figure 2.10b is a cataclastic band and is formed by intense grain rolling and crushing which results in decreased permeability. The type of deformation mechanism which forms a deformation band or any fault component is important to consider when predicting its effect on fluid flow.
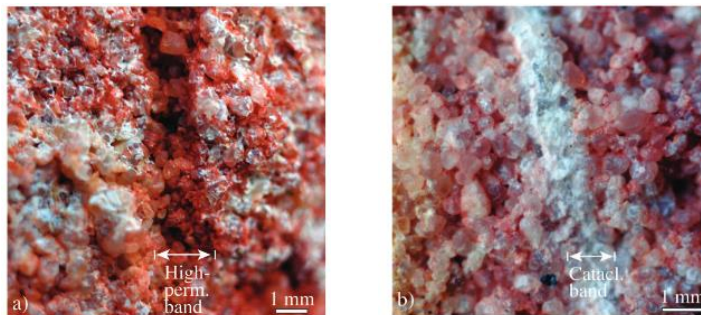
Figure 2.10 – (a) High permeability disaggregation deformation band and (b) low permeability cataclastic deformation band (Fossen et al., 2007).

The fluid flow properties of a fault zone change over time. For instance, during deformation, a fault core may take the role of a conduit, but when mineralisation of pore spaces occurs, it may take on the role of a barrier (Caine and Minor 2009). A fault core may also take on the role of a barrier locally when not actively deforming, this then restricts fluid flow between fault zones, and reduces permeability in the process (Antonellini and Aydin, 1994; Caine et al., 1996; Evans et al., 1997; Caine and Forster, 1999), e.g. deformation opens up permeability for short periods of time.

2.4 Summary

Faults can be described in two main frameworks; as a 'fault rock' which describes fault geometry (Childs et al., 2009), or through a fault zone model by Caine et al., (1996) in which high and low strain components are distinguished.

Many faults are composed of multiple fault strands which can be linked through their stress fields (soft linked) or physically linked (hard linked) and this can result in different displacement profiles (Walsh and Watterson, 1991; Childs et al., 2009).

Faults can grow through a number of different processes; by the propagation of a single fault strand (radial tip propagation), by the linkage of multiple fault strands (segment linkage) or through a single fault strand splitting into multiple fault strands (tip bifurcation). Most faults grow through a combination of these processes.

Faults are not singular planes, they have a thickness. The thickness of a fault is usually heterogeneous along strike and thickness is determined by the internal fault geometry and fault architecture.

Faults can behave as barriers, conduits and baffles to fluid flow. Host rock lithology is a key control for how a fault will behave because lithology influences deformation mechanisms. How a rock deforms will control the fault architecture and the resulting connectivity for fluid flow. For example, host rock lithology, layer thickness, cementation and shale smear control fault dip.

A fault can seal in two ways, through juxtaposition seals and fault seals. Understanding the mechanisms for how a fault can seal is important for fluid flow connectivity as fluids can migrate to the surface through faults and equally, faults can act as barriers or partial barriers to flow. Understanding the behaviour of a fault in fluid flow connectivity is important for industries such as oil and gas, CO_2 storage and radioactive waste disposal.

In order to quantitatively predict fault rock composition at depth, three main algorithms are used within industry; Shale Gouge Ratio (Yielding et al., 1997; Fristad et al., 1997; Freeman et al., 1998), Clay Smear Potential (Yielding et al., 1997; Fulljames et al., 1997; Egholm et al., 2008) and Shale Smear Potential (Lindsay et al., 1993; Doughty, 2003). However, current deterministic algorithms assume homogeneous mixing and no diagenesis.

Key controls on fault zone permeability include the distribution, frequency and position of fault zone components with respect to the fault zone. It is important to understand the percentage of fault zone components within a fault zone to try and predict whether a fault will act as a barrier, conduit or baffle to fluid flow (Caine et al., 1996; Manzocchi et al., 1999).

Chapter 3

Geological History and Host Rock Lithology

3.1 Introduction

Crow's Nest Fault was chosen as the study area for this thesis based on excellent exposure along strike. Exposures occur in multiple eroded valleys across the fault. In this chapter, the tectonic history and host rock lithology of the field area are described to constrain the conditions of fault formation. Microanalysis of lithologies within the field area are described in sections 3.5 to 3.8.

3.2 Tectonic History

3.2.1 The Colorado Plateau and San Rafael Swell

The Colorado Plateau is an area spanning over 140,000 square miles (figure 3.1). A relatively un-deformed region with elevations of up to 14,000 feet, the Colorado Plateau is surrounded by the deformed Rocky Mountains and Basin and Range Province (Foos, 1999). To the north, the Uinta Mountains bound the Plateau and to the south, the Mogollon Rim separates the Plateau from the Basin and Range Province (Foos, 1999).
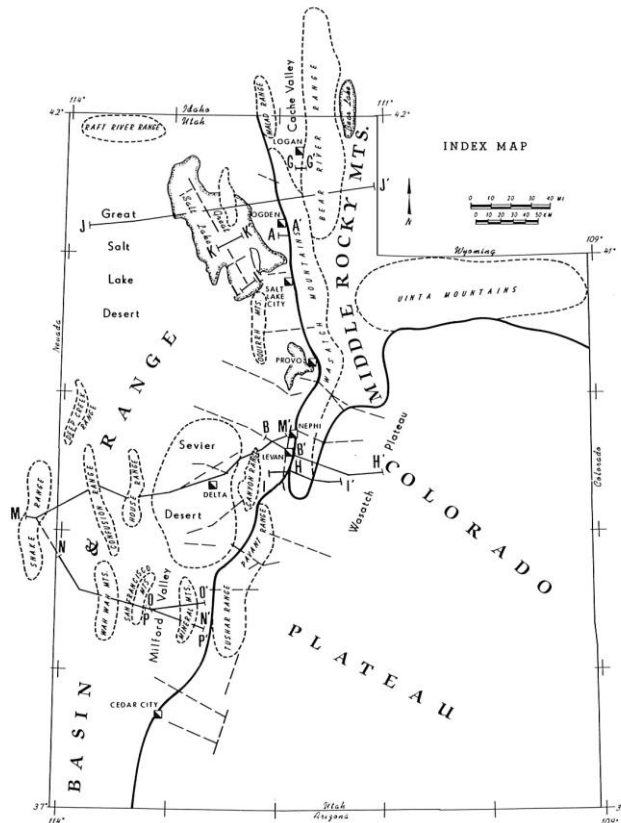
Figure 3.1 – Index map of the Colorado Plateau which is surrounded by the deformed Rocky Mountains and Basin and Range Province. To the north, the Uinta Mountains bound the plateau (Smith and Bruhn, 1984).

The Crow's Nest Fault is situated within the Colorado Plateau and is located on the northern edge of the Paradox Basin (figure 3.2). The Paradox Basin is defined by the maximum extent of salt deposition which occurred during the Mid-Pennsylvanian.
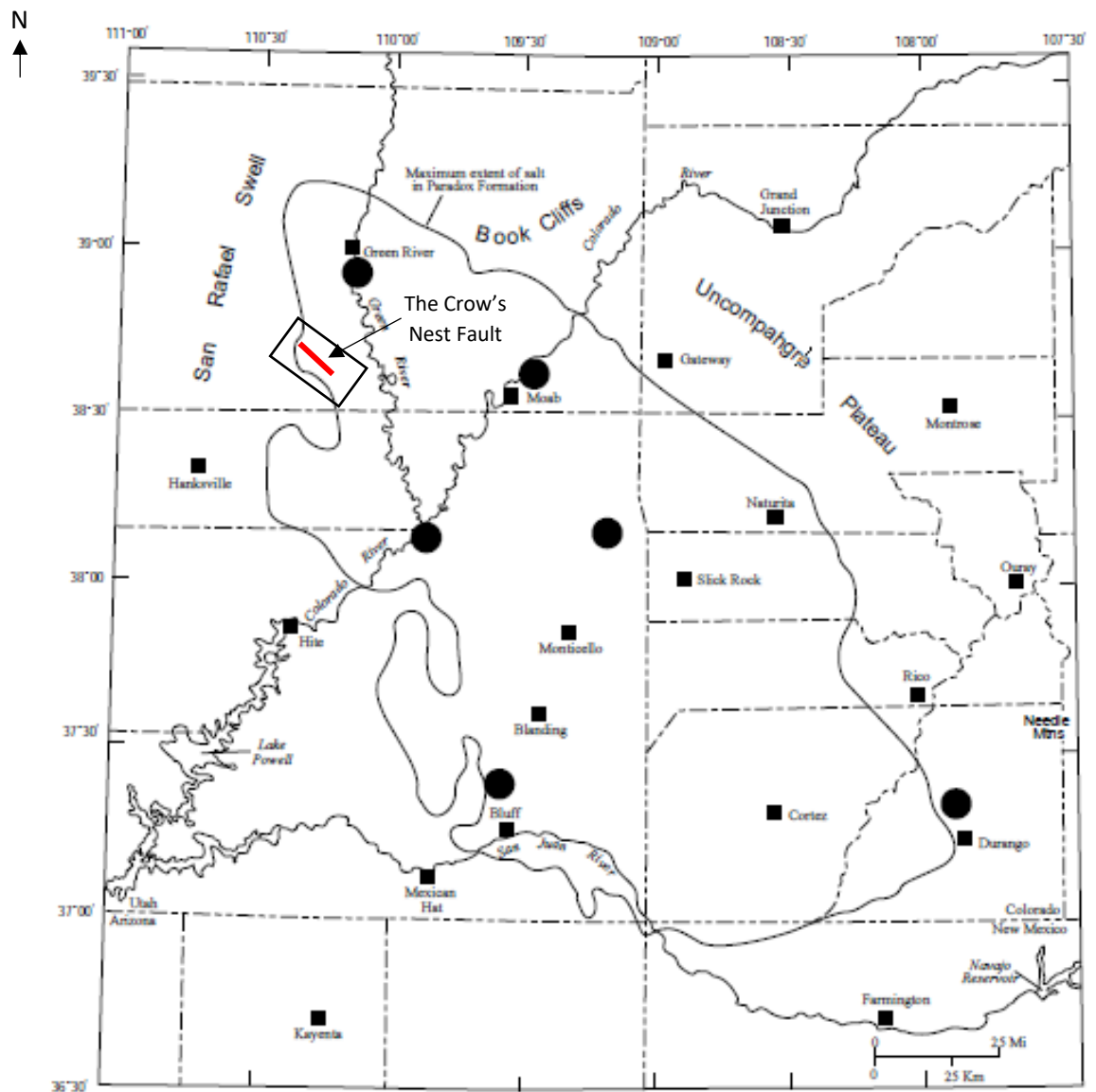
Figure 3.2 – Index map showing the maximum extent of the Paradox Basin as defined by the maximum extent of salt (Condon, 1997). The Crow's Nest Fault is situated to the north-west of this extent.

The Paradox Basin is underlain by an Early Proterozoic basement consisting of metamorphic gneiss, schist and intrusive granites (Nuccio and Condon, 1996). Directly overlying the basement are Pennsylvanian and Permian rocks consisting of carbonates, halites and clastics (Nuccio and Condon, 1996). Between the Triassic and Cretaceous, mostly

sedimentary rocks have been deposited in the region including sandstones, shales and siltstones as well as some limestones.
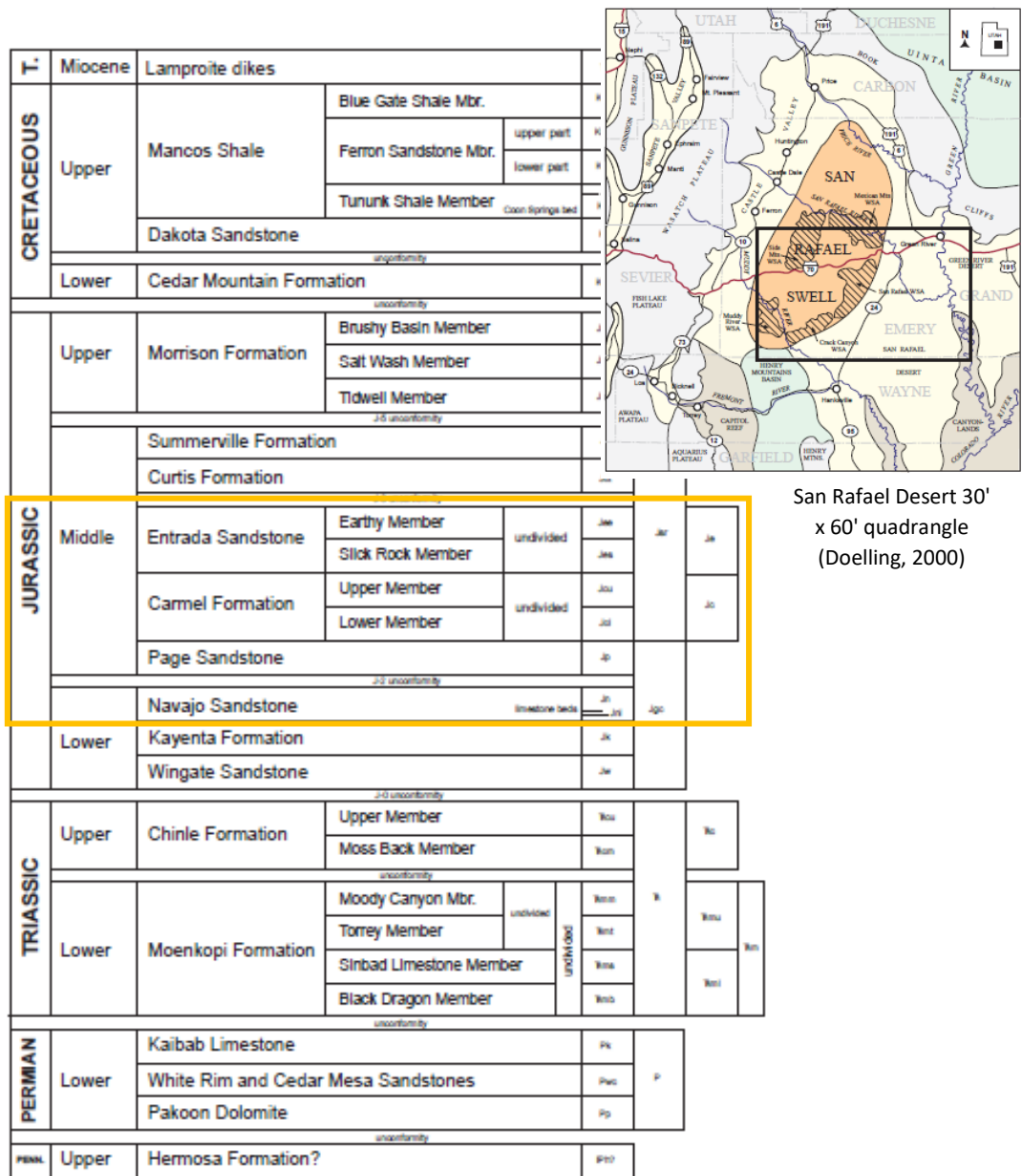
San Rafael Desert 30'
x 60' quadrangle
(Doelling, 2000)

Figure 3.3 – Stratigraphic column of lithologies exposed in the Paradox Basin (from the San Rafael Desert 30' x 60' quadrangle – Doelling, 2000). Rocks exposed at the Crow's Nest Fault are indicated by the yellow rectangle.

Rocks exposed in the field site are Jurassic in age and are indicated in figure 3.3. The maximum burial depth of rocks close to the Crow's Nest Fault are estimated at 3km in the Green River area and up to 7km in the Moab area (Nuccio and Condon, 1996).

North-west trending faults in this region are believed to be influenced from the collapse of salt anticlines during the formation of the Paradox Basin due to Pennsylvanian and Permian uplift of the Uncompahgre Plateau (Doelling et al., 1988; Dockrill and Shipton, 2010).

During the Jurassic, salt migration was influenced by north-west trending faults resulting in cyclic movements and the build-up of 'salt anticlines'. Since the deposition and migration of salt anticlines in the Paradox Basin the region has been folded and faulted. East-west compression occurred between the Late Cretaceous and the Early Tertiary (Baars and Doelling, 1987). Salt movement then continued throughout the Tertiary and resulted in large fault systems developing including the nearby Moab Fault (Foxford et al., 1996; Johansen et al., 2005) and most likely the Crow's Nest Fault.

The Laramide Orogeny formed the Rocky Mountains and resulted in compressional deformation of the Colorado Plateau (Davis, 1999). The San Rafael Swell is one of a number of structures which formed on the Colorado Plateau during the Laramide Orogeny (80-50Ma). The San Rafael Swell is an asymmetrical north-east trending anticline (Hintze, 1988; Davis, 1999) situated south-west of Green River (Baars and Stevenson, 1981; Doelling, 2000).

3.2.2 Faulting in the Paradox Basin

Various other faults within or nearby the Paradox Basin have been extensively studied, including the faults of the Chimney Rock Fault Array and the Moab Fault (figure 3.4). As demonstrated by these other studies, faults have very complex and variable fault architecture and are often segmented which strongly influences deformation style and fault permeability. Features such as these are typically not visible from seismic and borehole data. This study aims to bridge the gap between micro, macro and mega-scale observations by observing the relationship between fault rock, fault architecture and fluid flow in the field.
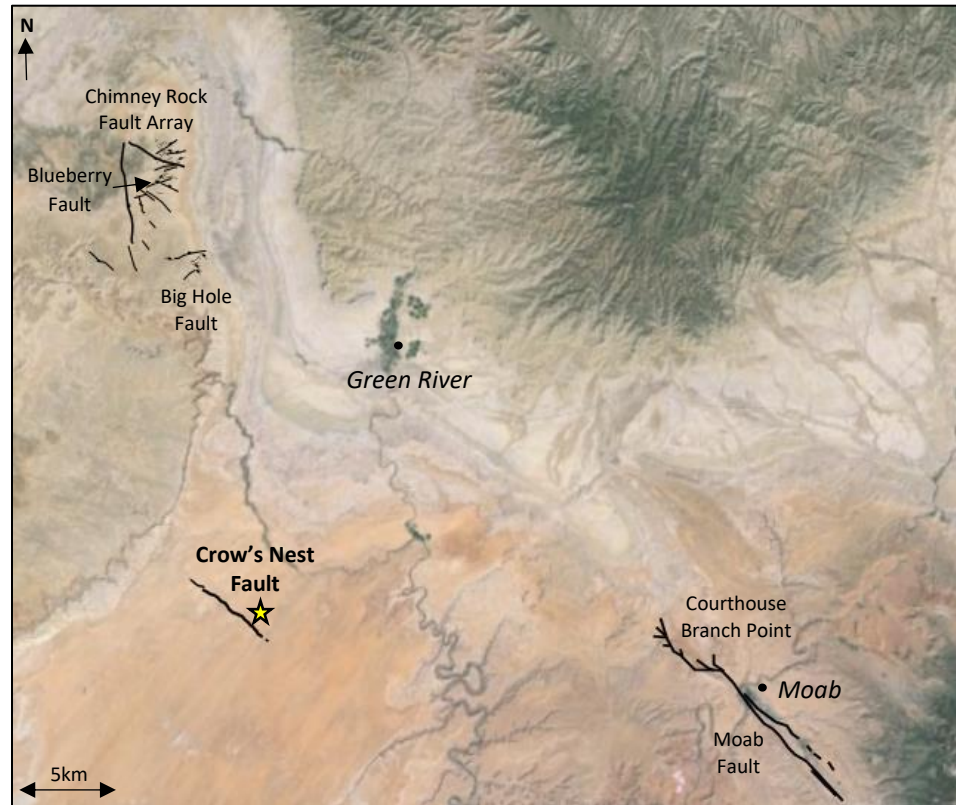
Figure 3.4 – Map of the northern Paradox Basin with the location of the Crow's Nest Fault indicated by a star. The extensively studied Chimney Rock Fault Array (Krantz, 1988; Shipton and Cowie, 2001; Davatzes et al., 2003) the Big Hole Fault and the Blueberry Fault (Shipton and Cowie, 2001) and the Moab Fault (Doelling, 1988; Foxford et al., 1996; Olig et al., 1996; Davatzes et al., 2005; Solum et al., 2005; Eichhubl et al., 2009; Fossen, 2010; Solum et al., 2010) are indicated on the map. Aerial photography from Google Maps 2016.

The Chimney Rock Fault Array (CRFA) (figure 3.4) comprises of a series of normal faults ranging from 100m to 6km in length located on the edge of the northern anticline of the San Rafael Swell (SRS) (figure 3.5) (Davatzes et al., 2003; Shipton and Cowie, 2001; Krantz, 1988). Exposed over an area of 25km^2, the fault array offsets Jurassic Navajo sandstone and the overlying Carmel Formation (Pollard and Fletcher, 2005). It was first thought that the timing of the CRFA formation coincided with the uplift of the SRS during the Laramide Orogeny between 37Ma and 66.4Ma (Krantz, 1988). Davaztes et al., (2003) identified that changes in regional stress and host rock lithology created a transition between two deformation mechanisms crucial in the formation of the CRFA; firstly, the formation of deformation bands and later joint formation. Faults are estimated to have formed between 1.5km and 3km in depth (Krantz, 1988; Shipton and Cowie, 2001; Davatzes et al., 2003).

Early studies by Krantz (1988) indicate that faults at the CRFA exhibit orthorhombic geometry. Faults are traceable along strike for most of their entire length; some faults cross cut one another and other faults are isolated. Shipton and Cowie, (2001) studied two faults in the CRFA in more detail; Blueberry Fault and Big Hole Fault (figure 3.5). Blueberry Fault at 3.6km in length with a maximum throw of 30m exhibits a fault tip which is used as a proxy for the Big Hole Fault tip. Big Hole Fault (BHF) (figure 3.4) is a 4.1km long normal fault with excellent exposure along strike. BHF trends ENE-WSW and dips steeply towards the north-west at approximately 70°. The fault is orientated the same as faults which are dominated by deformation bands in the CRFA (Davatzes et al., 2003) and does not link to any other faults along strike. Along its length, BHF divides into two strands but exposure is poor towards the north-west.

The Moab Fault (figures 3.4 and 3.5) is a near vertical basin-scale normal fault located in central Utah. Aeolian sandstones including the Wingate and Navajo formations in the footwall are juxtaposed against Jurassic and Cretaceous shales and sandstones in the hanging wall (Davaztes et al., 2005). Juxtaposed lithologies include the Navajo, Entrada and Morrison formations in the footwall and the Morrison, Cedar Mountain and Dakota formations in the hanging wall (Eichhubl et al., 2009). It is generally accepted that during the Pennsylvanian the Moab Fault formed as a response to salt tectonism in this region (Doelling, 1988).

The fault is between 45km and 54km in length consisting of three main fault segments. The poorly exposed southern segment is 19km in length. The central segment is also 19km in length and has a maximum throw of 1km (Doelling, 1988; Foxford et al., 1996). The northern segment has an array of complicated branching minor segments and is 16km in length (Olig et al., 1996; Solum et al., 2005, 2010). The two most westerly segments strike predominantly in a north-west orientation. Each fault segment consists of sub-segments which strike parallel to the main fault strands, and are separated by relay ramps. Each sub-segment steps to the right by 50-100m, creating overlap of up to 500m (Davatzes et al., 2005). The Moab Fault (figure 3.5) has a complex and varying fault architecture and many areas of particular structural interest have been studied in detail; Davatzes et al., 2005; Eichhubl et al., 2009; Fossen, 2010).
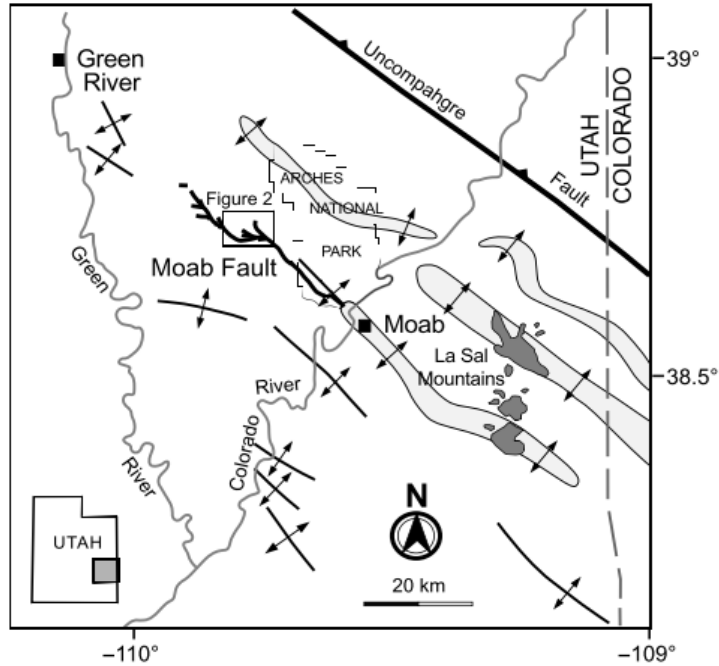
Figure 3.5 - Plan view map showing the Moab fault system, modified from Doelling (1988) and taken from Eichhubl et al., (2009).

3.3 The Crow's Nest Fault

The Crow's Nest Fault consists of four soft linked fault strands (A-D) ranging from 302m to 4.5km in length (figure 3.6). The fault strands dip steeply (70-80°) towards the north-east and expose the Carmel Formation and the Navajo Formation in the footwall and the Earthy Member of the Entrada Formation in the hanging wall.
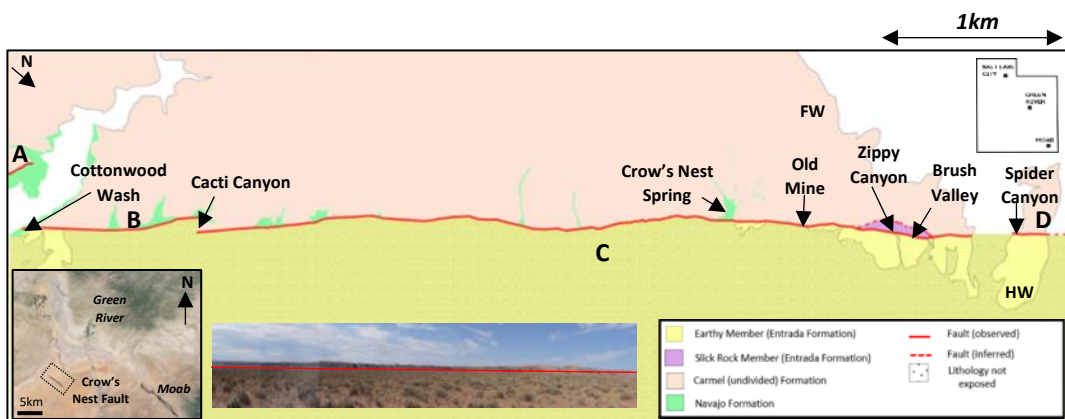
Figure 3.6 - Plan view map of the Crow's Nest Fault showing fault strands A to D. Modified from Doelling (2002).

The longest fault strand (C), exposed for 4.5km shows excellent exposure of the Entrada, Carmel and Navajo formations as canyons dissect the fault across strike. Between fault strands C and D, a lens (Brush Valley lens) has formed which measures 333m along strike and 73m across strike. Along fault strand C, a second lens (Crow's Nest Spring lens) has formed which measures at least 11m across strike. Lenses are defined in this thesis as a unit of rock bounded by two fault strands. The Brush Valley lens is comprised solely of the Slick Rock Member of the Entrada Formation. The Crow's Nest Spring lens is comprised the Carmel Formation. Fault strand A does not appear to link with any other fault strands and fault strand D appears to reach as far as the western edge of the San Rafael Swell. Fault strand B is exposed for 852m. Fault strand C is exposed for just under 4km and does not appear to link with any other fault strands.

In total, seven along-strike exposures of the Crow's Nest Fault have been studied in detail, these are (from south-east to north-west) Cottonwood Wash, Cacti Canyon, Crow's Nest Spring, Old Mine, Zippy Canyon, Brush Valley and Spider Canyon. The relative position of these study sites, their position with respect to the fault plane, and what deformation structures are exposed in these locations, are detailed in section 4.4.

3.4 Sampling and methology

3.4.1 Field mapping

Field mapping was undertaken through the mapping of outcrops and constructing maps of exposed canyons which dissect the fault trace. Canyons which dissect the fault trace were walked through from the hanging wall, for the full length of each exposure, toward the footwall. Canyons were mapped onto graph paper using a tape measure to measure the length of the canyon trace, and a compass clinometer was used to measure the orientation of each bend in the canyon. Changes in lithology, dip/strike measurements and any evidence of deformation structures were noted on the maps. Photographs and samples were taken and GPS readings were dictated straight onto the canyon map for later reference.

GPS readings were taken at points of interest, for example at relay ramps and at lithological boundaries. When taking the photographs, $1m^2$ squares constructed of metre rulers were

laid out on the ground surface at five metre intervals all along the fault and where canyons dissected the fault. To ensure geometrical accuracy when describing exposures, a portable digital printer was used to print photographs which were annotated in the field.

3.4.2 Samples

Hand samples from the host rock were collected in the field using a geological hammer and chisel. Orientated samples were taken where possible. When sampling the host rock, care was taken to collect representative samples. Most of the samples taken were very fragile and had to be packaged in the field. To ensure samples stayed intact, they were bagged up in sealed plastic bags, wrapped firstly in tissue paper, bound with duct-tape and then labelled.

3.4.3 Microanalysis and Image analysis

Hand samples were prepared into thin sections to enable analysis under an optical microscope. Blue dye was used in the resin to highlight the connected porosity in each sample. Thin sections were first analysed using an optical microscope and then using an environmental scanning electron (SEM) microscope to quantify porosity and to look in closer detail at the grain size, mineralogy and any other deformation structures present.

The SEM produces greyscale images where the varying shades in the greyscale relate to the atomic number of the minerals present. Empty pore space/porosity is represented as black and each individual mineral varies from white to dark grey.

To measure the porosity of the samples, the percentage of black pixels by comparison to the total number of pixels, was calculated using the Zeiss software provided with the SEM. This porosity measurement is a 2D calculation. Porosity is a 3D property, hence, some error will be incurred by estimating porosity using a 2D slice. However, the estimation of porosity from thin sections is widely accepted within the literature. Porosity was also estimated using the image analysis software (Image J) to determine the % of blue resin dye present in photos taken under the optical microscope. Porosity estimates were taken from all samples analysed under the optical microscope and the SEM. Rocks with porosities of less than 1-2% could not be measured as the error is greater than the measurement.

Mineralogy was analysed using the SEM by identifying the particles and producing element maps using the Zeiss Sigma field-emission analytical SEM (ZS-SEM). Element maps were produced at resolutions between 1024-800 pixels at 100,000 counts per second. To identify specific minerals, element maps can be made. To determine the elements present in a single grain, X-ray spectra is run to analyse and produce a graph showing the peaks of certain chemical elements found in a specific grain or area. For example, if a specific grain has a high percentage of silica and oxygen present, it is likely to be quartz or have a high quartz content. However, samples prepared for SEM were coated with carbon and this resulted in high levels of carbon being identified on all of the X-ray spectra results.

To deduce the grain size of a particular sample, grains were identified and then measured using the Zeiss software provided with the SEM. To analyse the size of grains in a thin section, the best fit elliptical tool was used on Image J software. Grains were represented by equivalent ellipsoids to estimate the size. This approach was more accurate for grains that were rounded to sub-rounded compared to angular and sub-angular grains. This approach of analysing grain size in thin sections allows for a rapid assessment of multiple samples. Where grain boundaries are distinct in high porosity rocks, the method is more effective than in lower porosity rocks with less distinct grain boundaries. The error for defining grain boundaries is between 1% and 2%. The percentage of error has been estimated from human error. For example, the image analysis software, Image J is entirely accurate when estimating grain size, however, the best fit elliptical tool could not be used as accurately on angular and sub-angular grains or on grains with less distinct grain boundaries. To overcome this, some grains were measured independently and this can lead to small errors of approximately 1-2%.

There are ooids present within the Carmel Formation. Ooids make up the majority of the host rock and are rounded which would likely increase the accuracy to within 1% when analysing the ooids using the best fit elliptical tool on Image J software. However, measuring sub-angular quartz grains would be less accurate when using this tool and so the overall accuracy for analysing the size and shape of grains for the Carmel Formation is likely between 2%-3%. The image analysis software, Image J is entirely accurate with no estimation error, however the human interaction to the software can lead to errors of around 2-3%.

3.5 Host rock lithologies

3.5.1 Introduction

In this section, host rock lithologies are described from field exposures coupled with references from the literature. Lithologies vary over the region due to changes in environmental and geological conditions such as burial depth and diagenesis. Due to the nature of these variations, host rock lithologies will also be described in various locations across southern Utah. In depth microanalysis of each host rock will be discussed.

The host rock lithology exposed at the Crow's Nest Fault includes the Navajo Formation, the Carmel Formation and the Entrada Formation (figure 3.7).

*Not exposed at the CNF
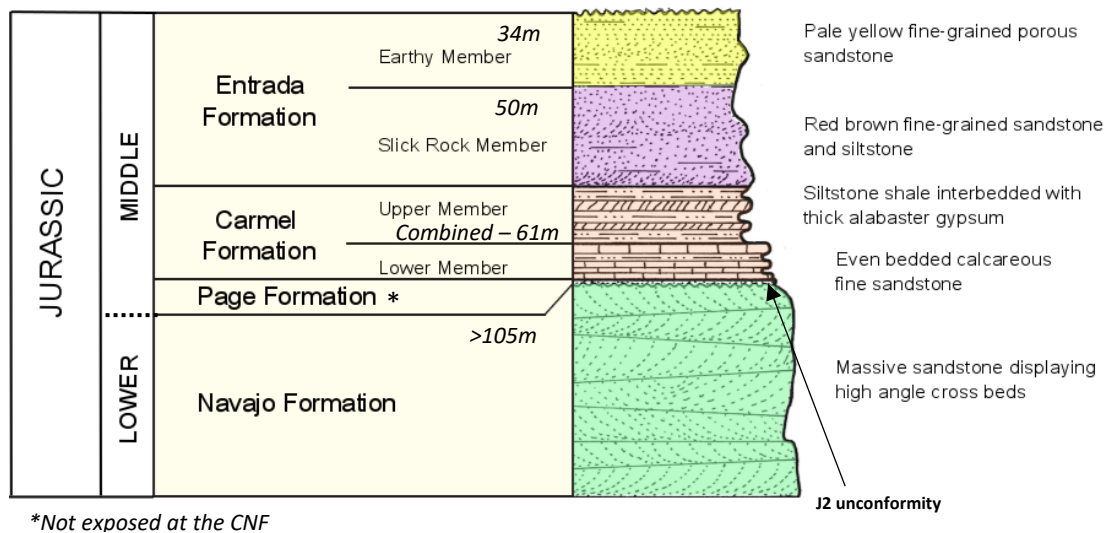
Figure 3.7 – Stratigraphic log showing the lithology exposed along the Crow's Nest Fault, after Trudgill, (2011).

3.6 Entrada Formation

The Entrada Formation outcrops in the hanging wall and the Brush Valley lens of the Crow's Nest Fault. The Earthy Member is exposed throughout the entire hanging wall and is referred to as the Earthy Entrada in this thesis. The Slick Rock Member is exposed only at the Brush Valley lens along fault strand C and is referred to as the Slick Rock Entrada throughout this thesis (figure 3.8).
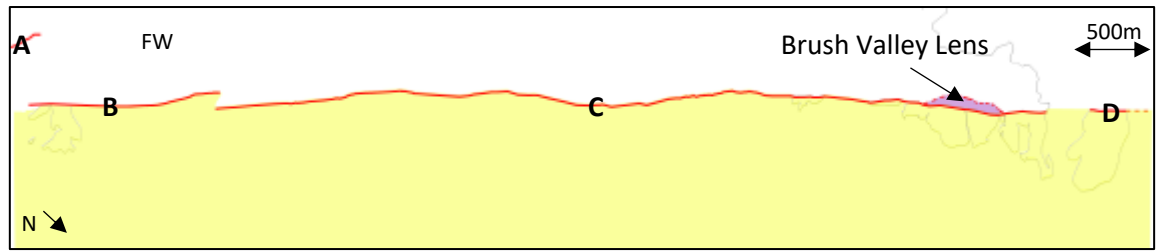
Figure 3.8 – Geological map showing the Earthy Entrada (yellow) and the Slick Rock Entrada (purple) in relation to the fault. There is no exposed Earthy Entrada in the hanging wall or lenses. The Slick Rock Entrada is only exposed in the Brush Valley lens and is not exposed in the footwall and hanging wall. Modified from Doelling, (2002).
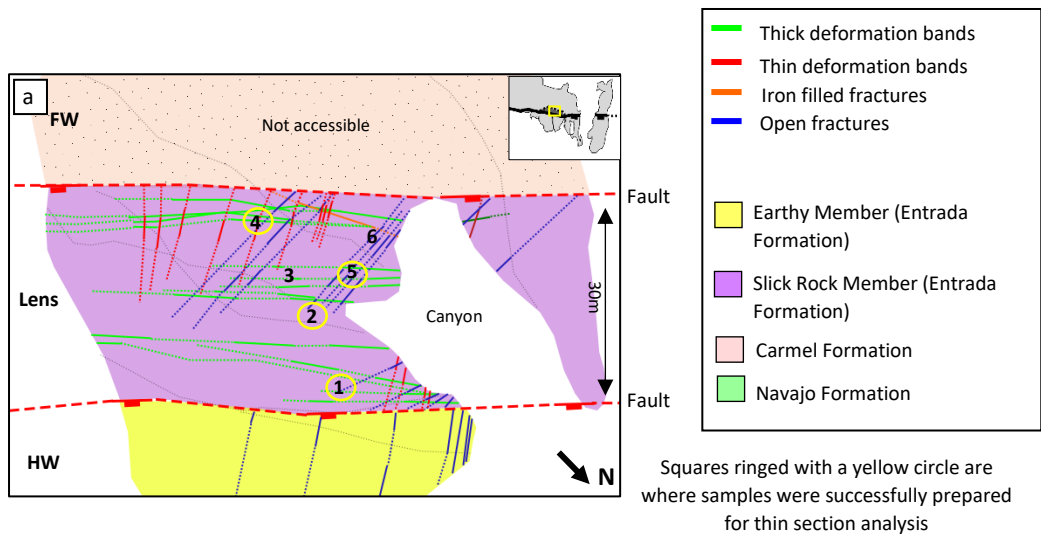
Figure 3.9 – (a) Plan view map of the Brush Valley canyon showing where samples were successfully prepared for thin section analysis. The locations of four samples successfully prepared for thin section analysis are identified.

3.6.1 Description – outcrop and microanalysis

The Entrada Formation has historically been divided into two members; the Earthy Member and the Slick Rock Member based on Doelling, (1988). However, more recently, the Entrada Formation has been reassigned into three new members across southern Utah (Doelling et al., 2000); The Moab Tongue Member, The Slick Rock Member and the Dewey Bridge Member. The Moab Tongue Member has since been reclassified as the overlying Curtis Formation (O'Sullivan, 1981; Johansen et al., 2005). In this study, the Entrada Formation is described using the assignment of members by Doelling, (1988) as this best suited the study area. The Earthy Entrada Member can be roughly correlated to the Moab Tongue Member and the Slick Rock Member remains the same. The Dewey Bridge Member was not laid

down in this area. In the field area the Earthy Member lies unconformably under the Carmel Formation. The Curtis Formation is not present in this area. The combined thickness of the Slick Rock and Earthy Members of the Entrada Formation is approximately 84m.

The Earthy Entrada is composed of red and brown silty sandstones, siltstones and shales, forming smooth rounded outcrops which are often cliff-forming. Along Crow's Nest Fault, the Earthy Entrada is approximately 34m thick. The characteristic red colouration in this member results from the presence of hematite. The member contains thin (0.5-2cm) sheets of gypsum and calcerous shale. The Earthy Entrada weathers to form spherical shapes locally described as 'goblins'. Goblins are formed where localised weathering widens fractures that create weaknesses in the rock. The upper part of the member contains harder, more resistant siltstone to the base of the member.

The Earthy Entrada is widely studied across Utah and can be correlated to the Moab Tongue Member (Eichhubl et al., 2009). The Moab Tongue Member is a fine to medium grained quartz arenite (Eichhubl et al., 2009) with small amounts of clay and iron oxides present (Bright, 2006). The porosity ranges from 21-23% across much of Utah (Bright, 2006) and the permeability ranges from 600 – 5000 mD (Antonellini and Aydin, 1995). Due to its fragile nature and the difficulty with transportation, no samples taken of the Earthy Member met the requirements for creating a thin section.

The Slick Rock Entrada is comprised of resistant sandstone with minor siltstones which are predominantly grey with alternating white and pink layers. The grey sandstone has abundant soft sediment deformation features (Chan et al., 2000). Along Crow's Nest Fault, the Slick Rock Entrada is approximately 50m thick. In the field area, the Slick Rock Entrada is a well sorted sandstone and minor siltstone with grain size ranging from 0.02 – 0.20mm (figure 3.9). This Slick Rock Entrada is comprised mostly of quartz grains (~80%), feldspar (~6%) and clays and lithic fragments (~14%). Quartz grains are sub-rounded and moderately to well sorted. Calcite cement between grains is sporadic (on average, 2% of the total rock) and unevenly distributed. Quartz grains show evidence of fluid inclusions and quartz overgrowths. SEM analysis shows evidence of minor dolomite and kaolinite clays filling in the matrix (figure 3.10).

Regionally, the mineralogy of the Slick Rock Entrada consists of predominantly quartz, feldspar, clays and lithic fragments (Foxford et al., 1996; Bright, 2006), which is identical to

that observed at the Crow's Nest Fault. At the Yellow Cat Graben, the Moab Tongue Member is classified as a quartz arenite with >93% quartz present and 5% feldspar and can be described as a 'clean' sandstone (Bright, 2006). Grain size varies from 0.17mm to 0.28mm and grains are typically sub-rounded (Foxford et al., 1996; Bright, 2006) compared to a mean grain size of 0.11mm at the Crow's Nest Fault. Calcite cement is sporadic in both the Slick Rock Entrada at the Crow's Nest Fault and the Moab Tongue Member at the Yellow Cat Graben.

Grain size average within the Slick Rock Entrada has been calculated from four host rock samples. Four samples of the Slick Rock Entrada were taken from the Brush Valley lens at the Crow's Nest Fault as this is the only location where the host rock is exposed. The use of a single area for sampling, and its location between the two fault strands, is likely to mean that the data is not fully representative of the entire host rock. However, since this was the only exposure, it was not possible to collect from other, more representative locations.

Each sample of the Slick Rock Entrada was analysed under an optical microscope. One sample was also analysed under the SEM (figure 3.10). Mineralogy of the host rock was determined from studying the samples in thin section. EDX spectra was used on the sample analysed under the SEM to confirm the mineralogy. A mean was taken from the four samples for the percentage of each mineral present. The average porosity of the Slick Rock Entrada in the Crow's Nest field area was calculated from four thin sections. Mean porosity was found to be approximately 30%, calculated using five photomicrographs from each of the four thin sections.
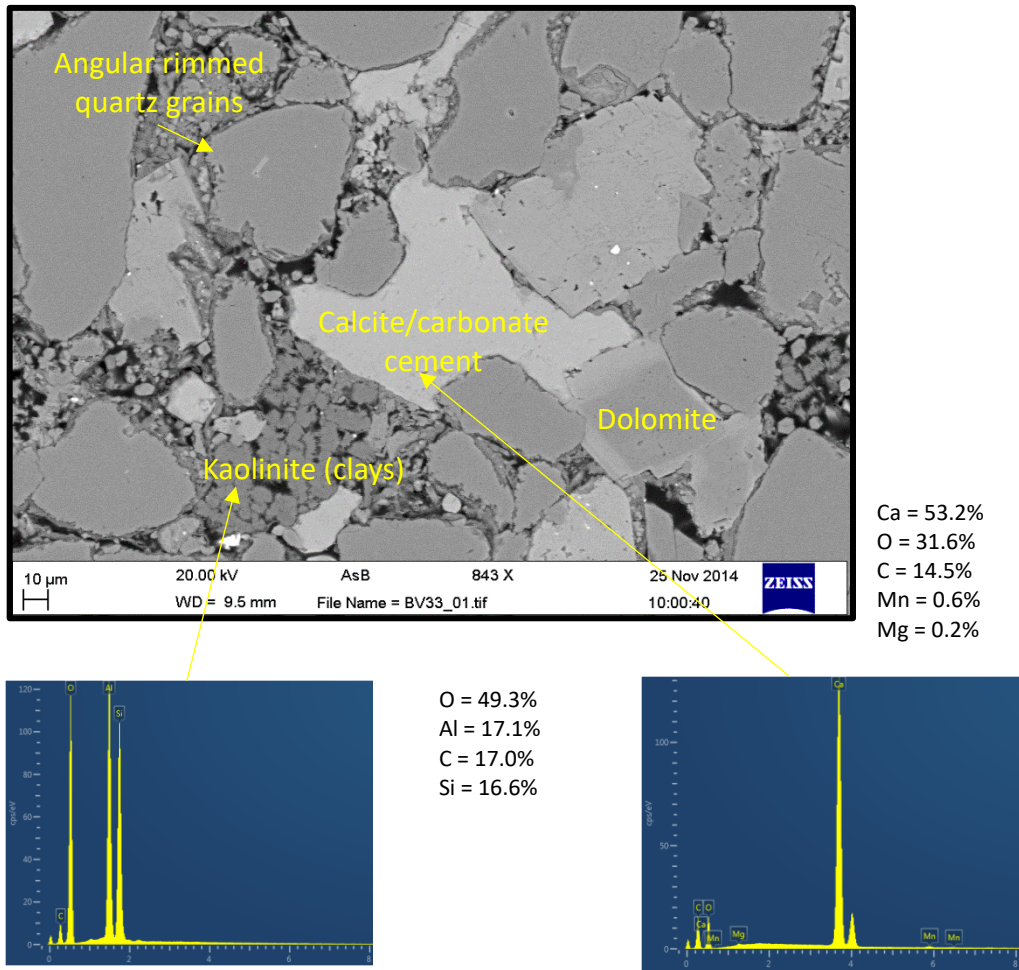
Figure 3.10 – SEM photomicrograph of the Slick Rock Entrada (sample 4) at the Crow's Nest Fault site. Sporadic (sparry) calcite cement and kaolinite are identified by EDX spectra.

Five photomicrographs were taken from each of the four host rock samples analysed. Samples were taken of the host rock at random locations. Photomicrographs were analysed for porosity and grain size using Image J software.

Regionally, porosity of the Slick Rock Entrada ranges widely from 4% to 26.4% (Hood and Patterson, 1984; Antonellini and Aydin, 1994; Bright, 2006) (table 1). The permeability of the Slick Rock Entrada varies from 100-1000 mD (Antonellini and Aydin, 1995).

Lithology	Description	Reference	Porosity	Location
'Slick Rock Entrada' *Comparable to:* Slick Rock Entrada	- Aeolian dune sand inter-bedded with laminated muddy siltstone sabkha beds - Fine to medium grained, well sorted	Antonellini and Aydin, 1994	4 - 15% porosity	Arches National Park
'Slick Rock Entrada' *Comparable to:* Slick Rock Entrada	- Aeolian sandstone interbedded with low permeability sabkha siltstones	Bright, 2006 - PhD thesis	9% porosity	Yellow Cat Graben
'Entrada' *Comparable to:* Slick Rock Entrada	- Shale rich base - Porous sandstone - Highly permeable - Unconfined aquifer unit	Hood and Patterson, 1984	26.4% porosity	Salt Wash Graben (near Little Grand Wash)

Table 1 – Comparison of the different porosity values for the Slick Rock Member of the Entrada Formation across southern-Utah.

The average porosity of the Slick Rock Entrada (~30%), as determined from the field samples, is significantly higher than the 9%-26.4% porosity reported in the literature (table 1). This is likely due to the Slick Rock Entrada only being exposed within a lens at the Crow's Nest Fault.

3.7 Carmel Formation

Towards the south-east of the fault, the Carmel Formation is visible along the middle of fault strands A, B and C as incisions into the footwall and Crow's Nest Spring lens (figure 3.11). Along fault strand C, the Carmel Formation is exposed into the footwall for 300 metres at the Crow's Nest Spring lens locality. Along fault strand D the Carmel Formation is exposed as a ~500m^2 outcrop into the footwall. There is no exposure of the Carmel Formation in the relay ramps or hanging wall.
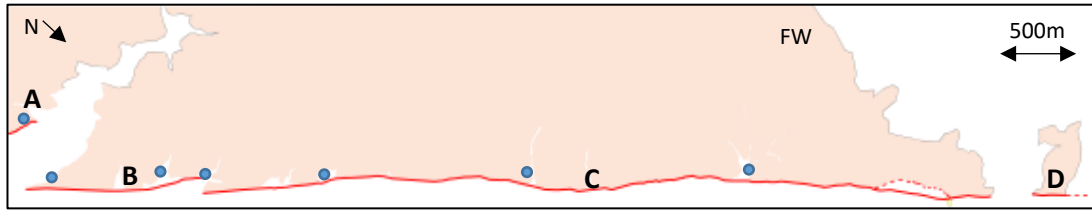
● Location of Carmel Formation is visible in the footwall and lens

Figure 3.11 – Field geological map showing where the Carmel Formation (pink) is visible in the field area. Modified from Doelling (2002).
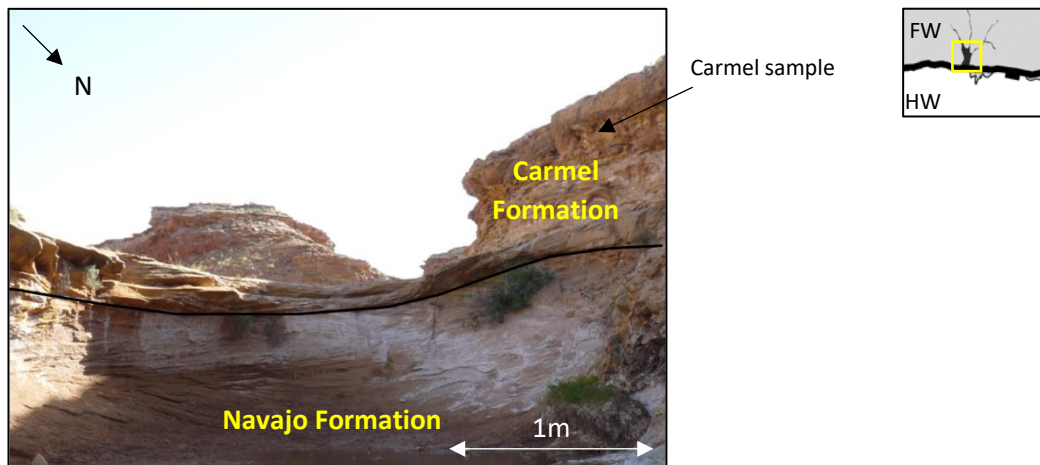
Figure 3.12 – Carmel Formation capping the Navajo Formation at the Crow's Nest Spring lens of the Crow's Nest Fault.

3.7.1 Description – outcrop and microanalysis

Regionally, the Carmel Formation is described as having various compositions including; sandstone, limestone, shale and gypsum (Aydin, 1978). Along the Uinta thrust fault, Parry and Blamey, (2010) describe the Carmel Formation as distinctive red, green and grey siltstones. They note that fine grained sandstone, limestone, mudstone and gypsum are also visible but less distinguishable. Gypsum beds weather to form ledges and red and green beds dominant the base and the top. Beds weather over time to form a yellow or grey outer layer. The Carmel Formation at the Crow's Nest Fault is grey and pale pink in colour.

The Carmel Formation consists of marine siltstones, sandstones and limestones of Middle Jurassic age. The Carmel Formation lies conformably under the Entrada Formation (Slick

Rock Member) and unconformably over the Navajo Formation (J2 unconformity); figure 3.12).

The formation is comprised of an upper and a lower member. However, the Carmel Formation is referred to as a single unit at Crow's Nest Fault because it is difficult to distinguish between the two members. The upper and lower members combined have an observed thickness of approximately 61m in the field area. Thickness has been measured via walking through canyons which cross-cut the fault and expose the Carmel Formation.

Along Crow's Nest Fault, the Carmel Formation is exposed as sandy siltstones with evenly bedded limestones dominated by ooids. Photomicrographs show ~70% ooids/calcium calcite, 28% quartz and 2% lithic fragments such as clays and iron oxides (figure 3.13). Ooid grains are rounded and range from 0.30mm to 0.55mm in diameter. Figure 3.13 shows a quartz grain visible with layers of calcite growing on the perimeter.
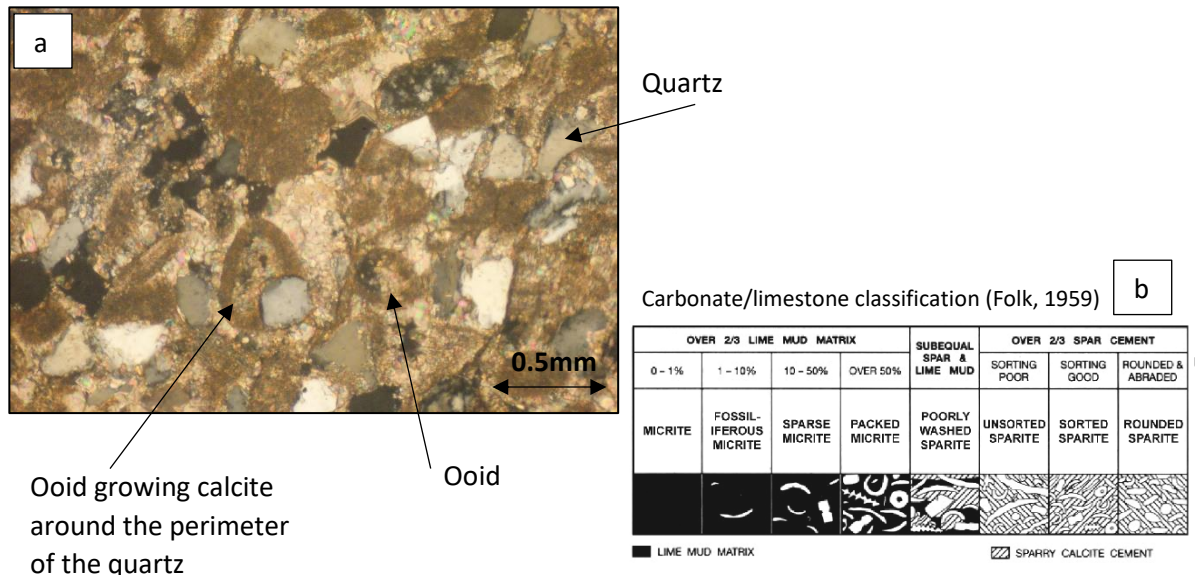
Figure 3.13 – (a) Photomicrograph of the Carmel Formation showing ooids and quartz. (b) The carbonate/limestone classification chart (Folk, 1959).

Quartz grains are sub-rounded to sub-angular and are well sorted. Quartz and ooids are surrounded by a sparry calcite cement which is evenly distributed throughout the entire sample seen in figures 3.13. There is little evidence for any major deformation to the quartz grains with a distinct lack of any fluid inclusions or micro-fracturing. Grain size averages within the Carmel Formation have been generated from two host rock samples using the same methods as used for the Entrada Formation.

Studying the host rock under a light microscope introduces sampling bias where the samples are only studied in the 2D area they were sliced in (figure 3.14).

O = 46.8%
Si = 41.4%
C = 12.2%

Quartz

O = 43.3%   Al= 1.8%
Ca = 34.3%   K = 1.1%
C = 14.2%   Fe = 0.7%
Si = 4.0%   Mg = 0.6%

Carbonate Cement

Ca = 36.8%
O = 35.9%
C = 16.8%
SI = 5.3%
Al = 2.2%
K = 1.8%
Mg = 0.6%
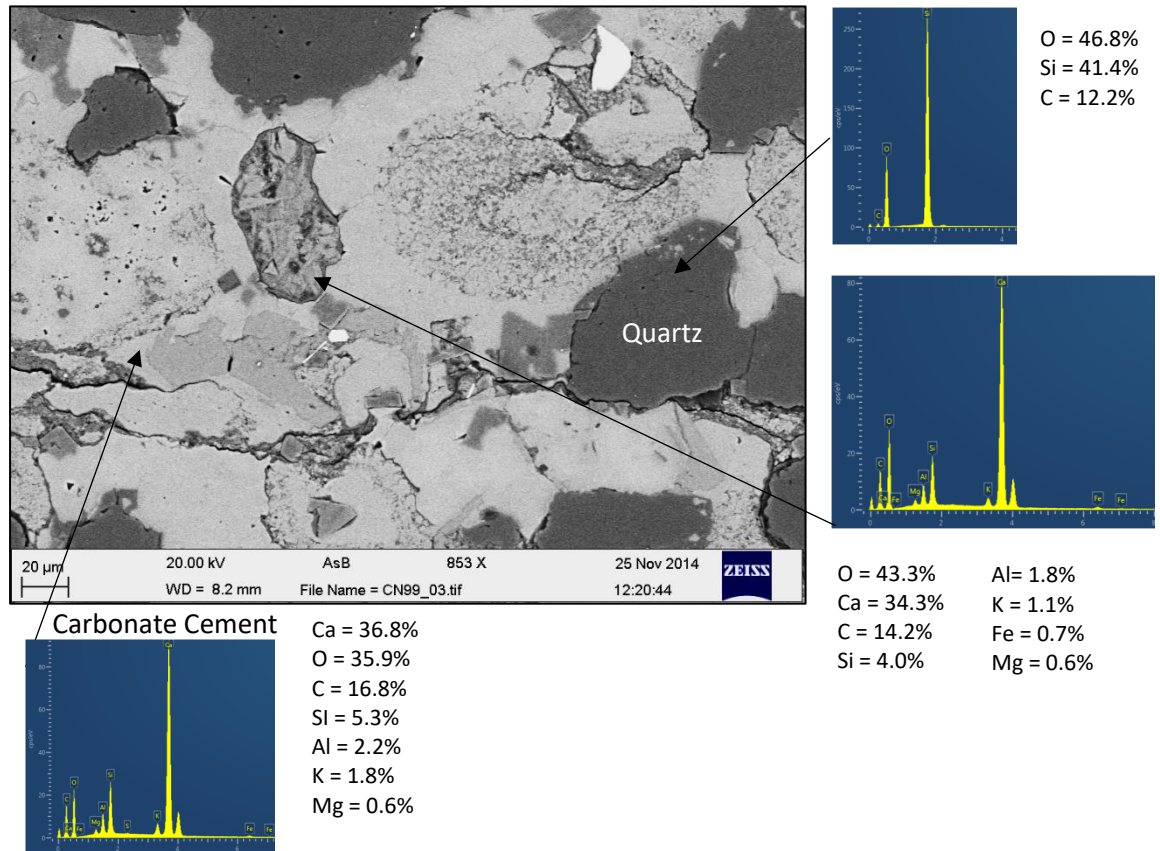
Figure 3.14 – SEM photomicrograph of the Carmel Formation at the Crow's Nest Fault site. Photomicrograph shows evidence of predominantly (sparry) calcite cement between grains of mostly quartz and ooids as evident by the EDX spectra which indicate the element composition.

The SEM indicates the presence of sparry calcite cement (~20%) between a mixture of ooids and quartz. Only one sample was analysed under the SEM and the porosity was calculated using several photomicrographs taken at random. This approach although not statistically significant, gave an overall picture of the sampled host rock. The image analysis software, Image J is entirely accurate with no estimation error, however the human interaction to the software can lead to errors of a couple of percent.

Regionally, there is relatively little information in the literature to compare the mineralogy, grain size, sorting or cementation to the Carmel Formation exposed in the field area. Payne (2011) reports that the porosity of the Carmel Formation is variable and ranges from 0.78% to 15.6% across Utah. The permeability of the Carmel Formation is typically very low,

approximately 0.454mD (data from the Gordon Creek Field, Mountain Carmel Junction, Utah; Payne, 2011).

In the field area, only one sample of the Carmel Formation was successfully prepared for thin section analysis. However, this thin section sample was damaged through transportation. The porosity of the sample is estimated at 9%, however the analysis was only taken from two photomicrographs. The lack of analysis from this sample has led to a higher degree of inaccuracy and smaller representation of the Carmel Formation at the Crow's Nest Fault.

3.8 Navajo Formation

The Navajo Formation outcrops mostly in the footwall of the Crow's Nest Fault (figure 3.15) with the exception of a small $10m^2$ outcrop in the hanging wall at the edge of fault strand B and in the hanging wall at the edge of fault strand A where it is exposed for approximately 150m along strike as cliffs up to 5m high. Along fault strand C, a canyon exposes the Navajo Formation into the footwall for 300 metres at the Crow's Nest Spring locality. There is no exposed Navajo Formation along fault strand D or along any of the relay ramps between the fault strands.
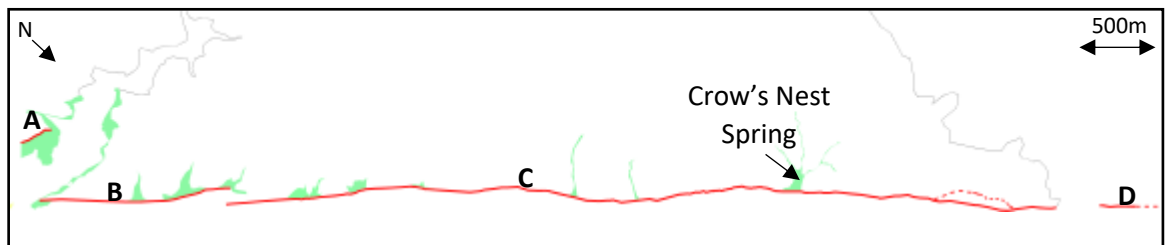
Figure 3.15 – Field geological map showing the exposed (green) outcrop of the Navajo Formation in relation to the fault. Modified from Doelling (2002).

The Navajo Formation has been sampled in two localities at the Crow's Nest Fault; in the footwall of the Crow's Nest Spring locality (figure 3.16) and in the footwall of the Cottonwood Wash locality (figure 3.17).
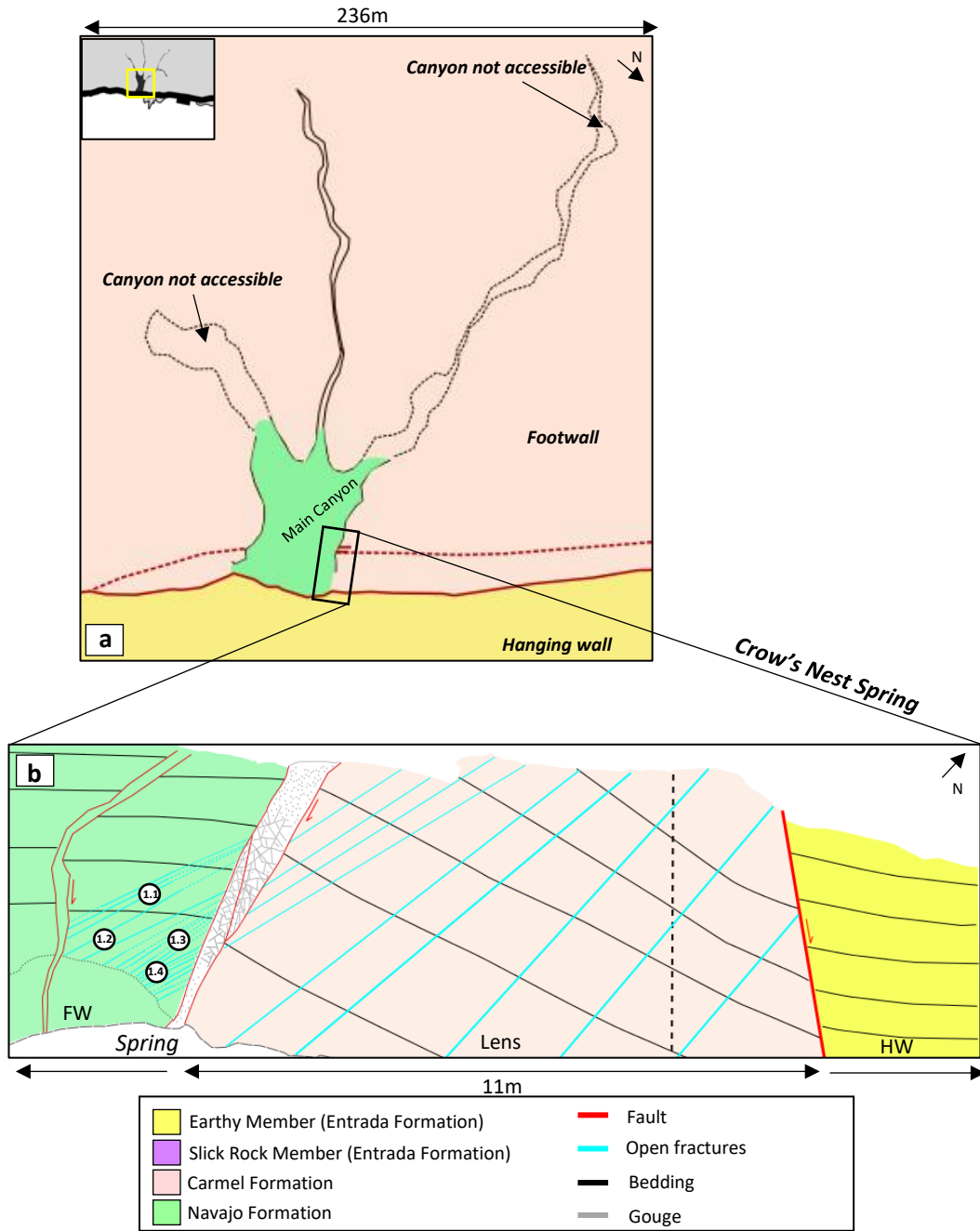
Figure 3.16 – (a) Plan view map of the Crow's Nest Spring locality. (b) Four samples were taken from the Navajo Formation in the footwall at the Crow's Nest Spring locality.
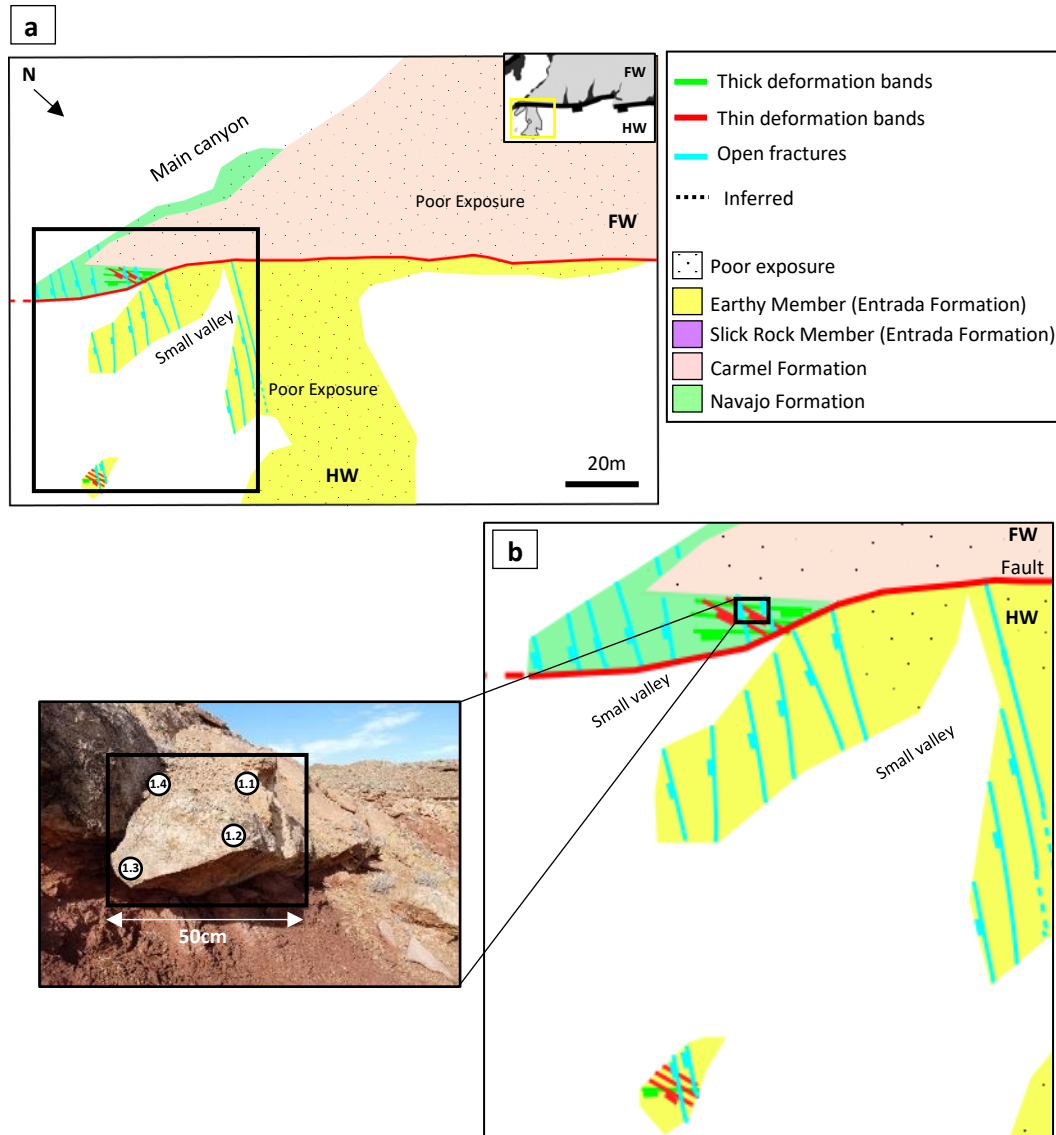
Figure 3.17– (a) Plan view map of the Cottonwood Wash locality. (b) Four samples were taken from the Navajo Formation in the footwall at the Cottonwood Wash locality.

Along the Crow's Nest Fault, the Navajo Formation has a light grey to light brown colour. By comparison, in the Moab area the Navajo Formation is stained with hematite which gives it a honey-brown and red colour (Davaztes et al., 2003). It has been suggested that modern dune deposits such as the Navajo Formation reddened during early diagenesis due to iron released from detrital minerals that oxidised to form hematite cement and grain coatings (Walker, 1975; Walker et al., 1978, 1981, Turner, 1980; Parry et al., 2004). This lack of redness within the Navajo Formation has also been observed at other locations in Utah; Beitler et al., (2003) attribute it to iron removal via bleaching fluids.

3.8.1 Description – outcrop and microanalysis

The Navajo Formation is a massive aeolian unit and inter-dune unit which forms smooth cliffs and rounded topped outcrops. The Navajo Formation is overlain unconformably by the Carmel Formation and lies conformably over the Kayenta Formation (figure 3.7). The Navajo Sandstone forms part of the Glen Canyon Group of the Lower Jurassic along with the Wingate Sandstone and Kayenta Formation. In this field area, the Navajo Formation has an exposed thickness of 105m, however the base is not exposed. Over the rest of southern-Utah the thickness of the Navajo Formation ranges from 135-200m (Doelling, 1988).

Along Crow's Nest Fault, the Navajo Formation is a quartz arenite with ~90% quartz, 3% feldspar and limited trace values (~2%) for clay and iron oxides present (figure 3.18). With such a high quartz content, the Navajo Formation can be classed as a particularly 'clean' sandstone. The Navajo Formation is a very fine (0.15 – 0.25mm) to medium (0.20 – 0.45mm) grained sandstone. Grain size average within the Navajo Formation was generated from four host rock samples and using the same methods as used for the Entrada Formation and Carmel Formation. The host rock samples were collected in two locations; along the middle of a fault strand next to the Crow's Nest Spring lens and at the Cottonwood Wash locality in the footwall. The average grain size is ~0.25mm estimated from four analysed samples in both localities studied and the grains are well rounded and moderately to well-sorted.

Average percentages of minerals (using the SEM):

Quartz = **90%**
Feldspar = **3%**
Lithic fragments/clay = **2%**

0.45mm

Carbonate cement is more evenly distributed surrounding finer grains (~10% - 3%)
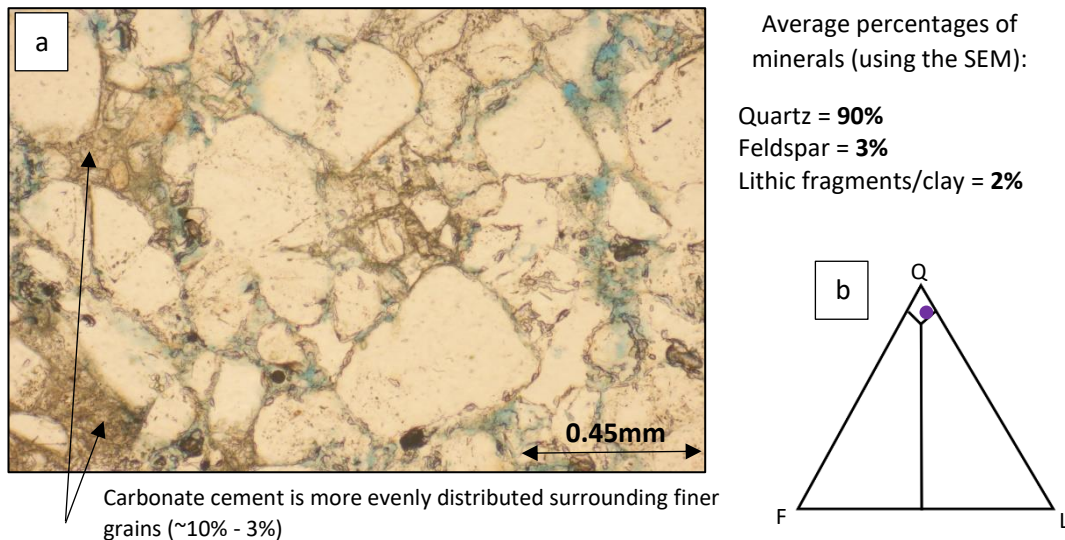
Figure 3.18 – (a) Photomicrograph of the Navajo Formation (sample 1.2) showing well sorted grains in a moderate to well sorted grain distribution. Blue resin dye indicates pore space within the host rock. (b) Average (from four samples) percentage of the host rock mineralogy.

Regionally, the mineralogy of the Navajo Formation consists of predominantly quartz and minor feldspar, clays and lithic fragments which is identical to that observed at the Crow's Nest Fault (Bright, 2006; Fossen et al., 2011). The Navajo Formation observed at the Yellow Cat Graben, Utah by Bright, (2006) is classified as a quartz arenite with 89% quartz and 4-6% feldspar. Grain size varies from 0.1 – 0.25mm and are typically sub-rounded and well sorted (Bright, 2006) compared to grains which range between 0.15 - 0.25mm at the Crow's Nest Fault. Studies of Navajo dune sets at the Buckskin Gulch, Utah by Fossen et al., (2011) found that quartz in dune cross strata were well rounded and very well sorted.

Calcite cement is unevenly distributed in the Navajo Formation exposed at the Crow's Nest Fault. By comparison, the cementation is variable in the Navajo Formation regionally; Fossen et al., (2011) found that the amount of cement was generally small at the Buckskin Gulch and Bright, (2006) found that finer grained sandstone was more cemented than coarser grained sandstone at the Yellow Cat Graben. Variability in cement distribution could likely be a function of fluid alteration of the rock or burial depth.

Regionally, porosity of the Navajo Formation ranges widely from 10% to 30% (Cooley et al., 1969; Shipton and Cowie, 2001; Fossen et al., 2011) (table 2). The permeability of the Navajo Formation varies from 5-3000mD (Shipton et al., 2002) which is likely to be a result of the variation in grain size distribution and resulting cementation. The average porosity of the Navajo Formation at the Crow's Nest Fault was calculated from four thin sections at the Cottonwood Wash locality and four thin sections at the Crow's Nest Spring locality. Mean porosity was found to be 15.9% at the Crow's Nest Spring locality, 22.6% at the Cottonwood Wash locality and a total mean of 19.3%. All samples are in the upper range of values for porosity but they are within the previously observed range.

Lithology	Description	Reference	Porosity	Location
Navajo	Aeolian sandstone, planar to cross bedded, medium to fine grained, well sorted and well-rounded sandstone	Shipton and Cowie, 2001	19.2%	Big Hole Fault, Utah
Navajo	Very well sorted, porous sandstone	Fossen et al., 2011	20-25%	Buckskin Gulch, East Kaiba Monocline, Utah
Navajo	Fine to medium grained, high porosity sandstone	Cooley et al., 1969	10-30%	Laramide uplifts on the Colorado Plateau in south-ern Utah

Table 2 – Porosity data for the Navajo Formation regionally throughout Utah.

3.9 Summary

Host rock lithologies in the field area consist of mostly quartz rich, well sorted sandstones, minor siltstones and limestones. Exposed lithologies are moderately to highly porous (15.9% - 30%). The Slick Rock Entrada has the smallest grain size in the field area (0.02-0.20mm) and the highest porosity (~30%). The Navajo Formation has a moderately high porosity (up to 22.6%) but with a slightly larger grain size distribution (0.15 – 0.45mm). The Carmel Formation is the only lithology with a limestone component. This is reflected with a lower ~9% average porosity in addition to increased cementation.

The distribution and percentage of calcite cement varies between the different lithologies, but also within the same lithologies at different locations. For example, the Navajo Formation in the footwall at the Cottonwood Wash locality has an average porosity of 22.6% whereas the Navajo Formation in the footwall at the Crow's Nest Spring locality has an average porosity of 15.9%. The variability in cementation can alter the pore space and subsequently porosity and permeability of a rock.

Chapter 4

Deformation Mechanisms and Fault Architecture

4.1 Introduction

This chapter presents field evidence for the deformation structures exposed within the fault zone at the Crow's Nest Fault and the factors that influence the style of deformation.

The types of deformation structures present are identified in section 4.2. The methods and modes of sampling are outlined in section 4.3. Individual study sites identified on the basis of good exposure along strike and through eroded valleys across the fault are described in more detail in section 4.4. The composition of fault gouge is outlined in section 4.5. At each study site the orientation, frequency and distribution of deformation structures has been examined in detail and overall trends are outlined in section 4.6. In section 4.7, microanalysis of deformation structures including detailed descriptions and cross cutting relationships are analysed. Section 4.8 explores the field evidence for the spatial and temporal relationship of deformation structures including evidence of cementation and porosity. An interpretation is given in section 4.9 with a summary in section 4.10.

4.1.1 Crow's Nest Fault

Seven individual sites have been studied at the Crow's Nest Fault. These include (from south-east to north-west); Cottonwood Wash, Cacti Canyon, Crow's Nest Spring, Old Mine, Zippy Canyon, Brush Valley and Spider Canyon (figure 4.1). The study sites were chosen on the basis of good exposure, position within the fault zone, deformation style and where possible, are formed by canyons which cross cut the fault.
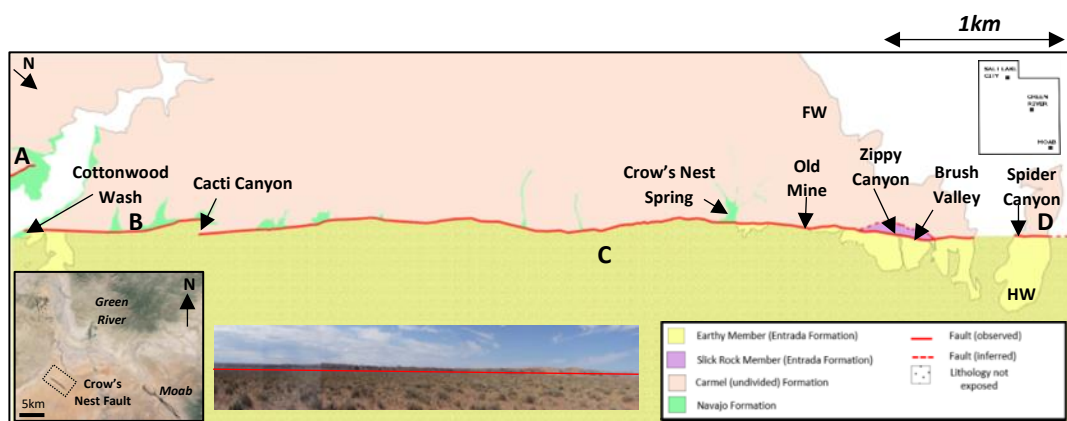
Figure 4.1 - Plan view map of the Crow's Nest Fault showing fault strands A to D. Modified from Doelling (2002).

4.1.2 Fault displacement

Figure 4.2 shows throw range for the Crow's Nest Fault calculated from offsets, by assuming the maximum and minimum reported thicknesses of the offset stratigraphic units. Observed maximum and minimum throw at the sites which have good exposure include; Cottonwood Wash, Crow's Nest Spring, Old Mine, Zippy Canyon, Brush Valley and Spider Canyon.

Calculating the throw range used the estimated stratigraphic thicknesses presented in section 3.5 to construct cross sections using the Carmel Formation as a marker where exposed. The throw was then calculated using structure contours from the Interim Geologic Map of the San Rafael Desert 30' x 60' Quadrangle, Emery and Grand Counties, Utah (Doelling, 2002) for the hanging wall and footwall of the same marker horizon across the fault in order to estimate vertical displacement, as shown in figure 4.3. Field data was used to double check measurements from the map. Where canyons cut through the fault but were not accessible, observed throw was estimated from a combination of field observations and Google Earth aerial imagery and the estimated throw was plotted onto the graph as shown in figure 4.2. The rationale for this method was solely due to the lack of exposure along strike along the middle of the fault strands. Crow's Nest Fault has excellent exposure at the ends of the fault strands, but the middle of the fault strands are poorly exposed unless a canyon cross-cuts the fault.

Although the above methods introduce error through the assumption that all strata are planar on either side of the fault (Shipton and Cowie, 2001), the combination of methods used to estimate throw reduce error significantly. For example, stratigraphic thicknesses estimated by Doelling, (1988) are presented as a range within a lower and upper bound. Stratigraphic thickness for lithology in the field can be better estimated knowing this range and cross referencing thickness to what is observed in the field area which is able to increase accuracy where possible. Where lithology is not well exposed in the field area, it is better approximated using Google Earth imagery. The combination of these different methods reduces error to a very minimal level.

The calculated throw at the Crow's Nest Fault ranges from 4m to 110m (figure 4.2). The throw profile for Crow's Nest Fault shows a linear increase towards the middle of fault strand C, where the maximum throw is 110m, then a decrease in throw at the fault tips to a maximum observed throw of 20m at the Brush Valley study site, close to the north-western

tip of fault strand C. At the end of fault strand D at the Spider Canyon study site there is a decrease in observed throw to a maximum of 10m and at the end of fault strand B there is a maximum throw of 11m at the Cottonwood Wash study site.

Fault does continue off the mapped 6km length as seen in Doelling, (2002)
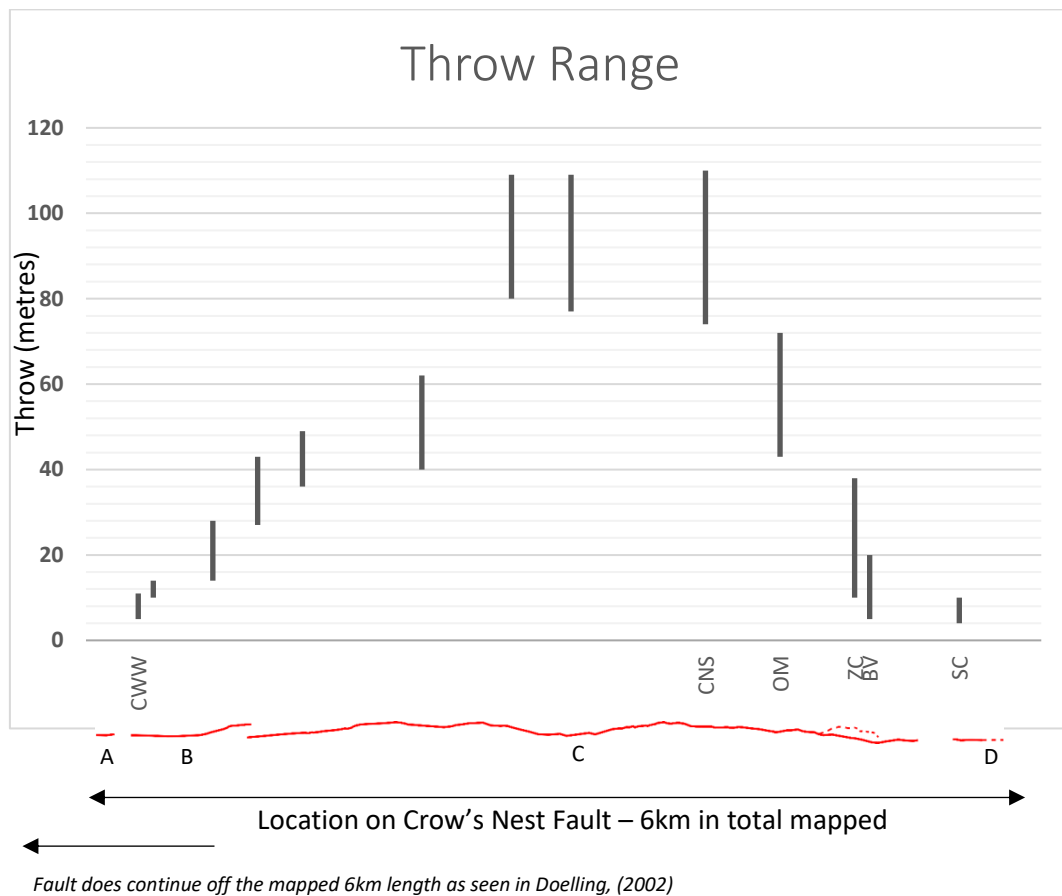
Figure 4.2: Throw range calculated from offsets assuming the maximum and minimum reported thicknesses of the offset stratigraphic units. The maximum observed throw along Crow's Nest Fault is 110m.

The observations of throw, along with field observations showing a segmented fault geometry, suggest that the fault segments are behaving like a linked fault with a throw profile that shows maximum displacement at the middle of the fault and decreasing throw towards the fault tips (Cowie and Scholz, 1992). The fault tips at Crow's Nest Fault are not exposed at the surface but the decrease in throw towards what appears to be the ends of the fault strands suggests they are likely buried under the surface nearby.
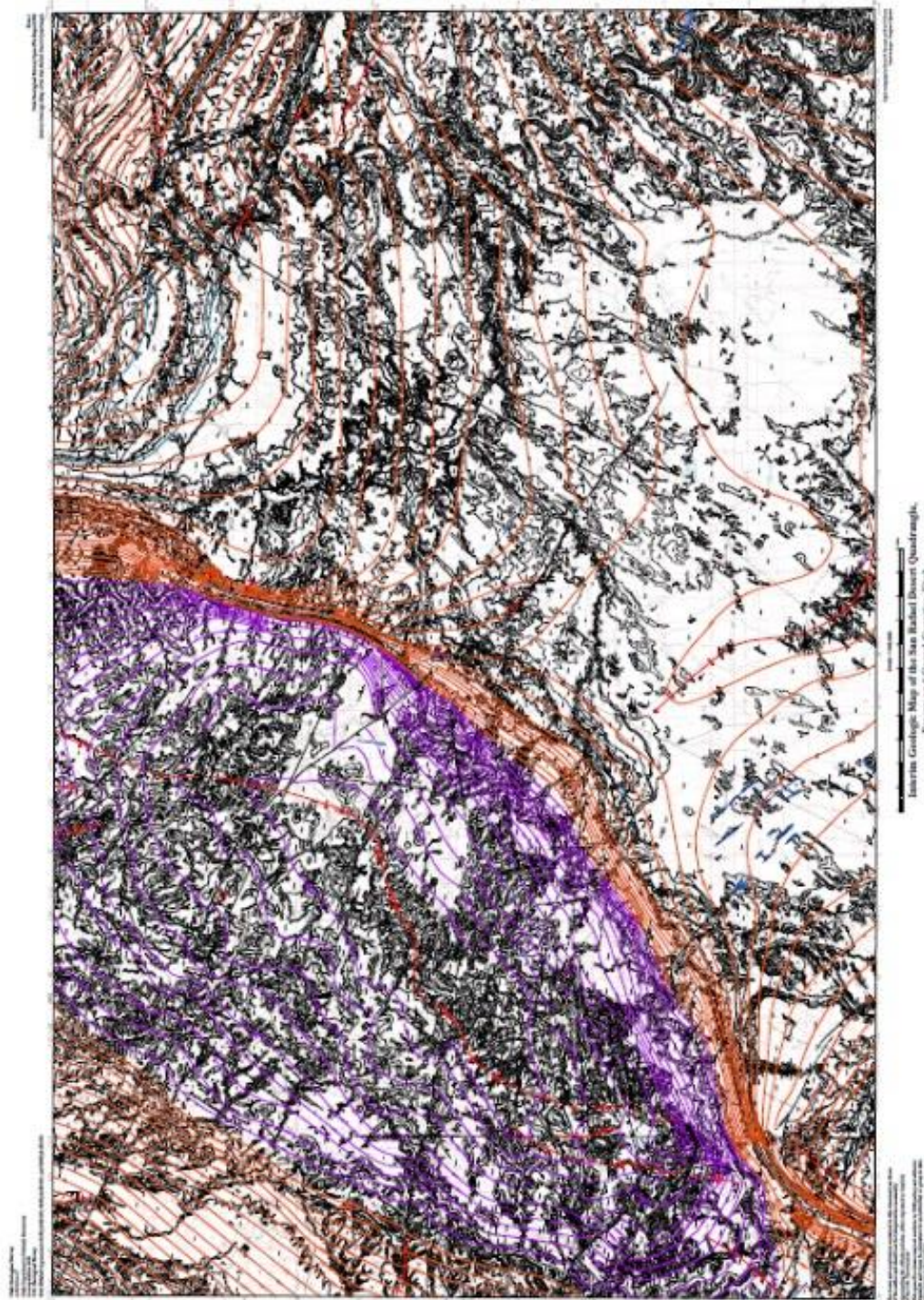
Figure 4.3. - The Interim Geologic Map of the San Rafael Desert 30' x 60' Quadrangle, Emery and Grand Counties, Utah (Doelling, 2002) with structure contours present.

4.2 Deformation structures

The damage zone at Crow's Nest Fault is composed of four principal deformation structures; thick deformation bands, thin deformation bands, iron-rich fractures and open fractures (figure 4.4). The fault core at Crow's Nest Fault is exposed as fault gouge. Fault gouge is observed in multiple locations across the fault and is discussed in more detail in section 4.5 for each individual study site where it is exposed.
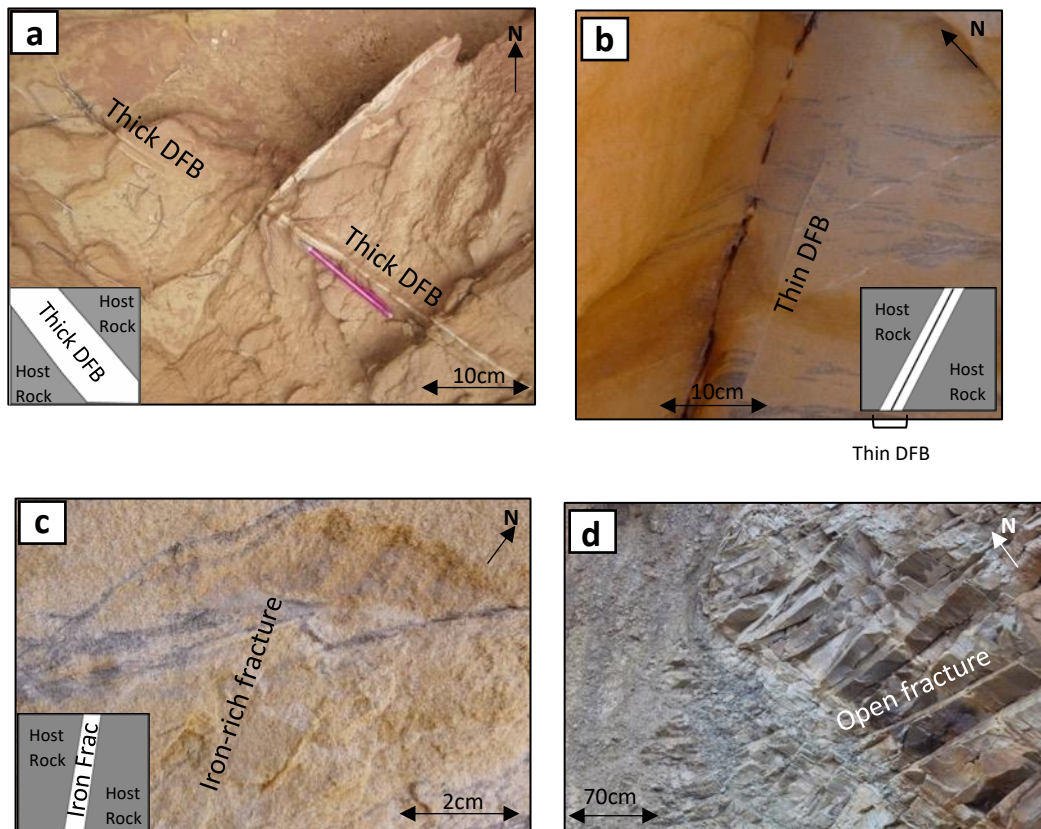
Figure 4.4 – At Crow's Nest Fault there are four deformation structures which are exposed within the fault zone, these include (a) thick deformation bands, (b) thin deformation bands, (c) iron-rich fractures and, (d) open fractures.

In the damage zone, deformation bands appear as pale coloured, usually white or cream, prominent ribs which are raised above the surface by about 0.5 mm to 2mm. Deformation bands at Crow's Nest Fault show identical characteristics to cataclastic bands as defined by Aydin and Johnson, (1978); fracturing of sand grains lead to grain failure and collapse resulting in the reduction of porosity in the deformation band. Evidence for these characteristics is further discussed in section 4.4.

Two types of deformation bands are exposed in the field area and are distinguished by their thickness. 'Thick' deformation bands are ~0.5-1cm in width and are observed subparallel to the main fault trace (figure 4.4a). 'Thin' deformation bands are 0.3-0.4mm in width and are perpendicular to the main fault trace (figure 4.4b).

Two populations of later cross cutting fractures are observed; iron-rich fractures and fractures. Iron-rich fractures show evidence of iron infilling under thin section and are orientated north-south (figure 4.4c). Fractures without any iron filling are termed here as 'open fractures' and are mainly perpendicular to the fault trace (figure 4.4d).

4.3 Methods and sampling of deformation structures

4.3.1 Field methodology

The frequency and distribution of deformation bands and fractures at Crow's Nest Fault was studied by extensive field mapping. Deformation band and fracture intensity were measured by examining the location and extensiveness of individual deformation structures through a series of scanlines and the placement of measured 'squares'. For the purpose of this study, the 'intensity' of the deformation structures refers to the number of bands or fractures in a given area, divided by the area they are exposed in. Each deformation structure was counted as a single entity but bands and fractures which branch off are not counted as additional individual structures (figure 4.5).

These thin deformation bands are defined as one single band. This is because they appear to have branched off the same structure.

These two fractures are defined as two fractures because they do not appear to branch off one another within the exposed area.

These fractures were not exposed outside of this area, however they may branch together where the exposure is poor and this is not exposed within the sample

Figure 4.5 – An example of exposed deformation structures showing how fractures and deformation bands are defined within this thesis. If a structure appears to branch off with another structure, they are classed as a single entity, but if they do not then they are defined as individual structures.

Within this thesis, deformation structures are defined using this method because it characterises structures, which are often branching, as a single structure. There have been many studies surrounding deformation structures, particularly about deformation bands which suggest such structures often branch from a single deformation structure (Johansen et al., 2005; Fossen at el., 2007). This method may lead to an overestimation of deformation structures, however, this was thought to be the most practical method.

To reduce sampling bias, further analysis could be undertaken using circular scanlines. However, areas of limited exposure can produce bias. For example, there is limited exposure in a lot of the hanging wall within the field area and only one exposure of deformation bands is present. It is unclear if this is due to the lack of exposure in the hanging wall, or factors such as localised porosity differences which highly influence whether the rock will deform by fracturing or by deformation banding.

When studying deformation structures in the field, observations are limited to methods which study structures on a 2D level even though these structures are 3D. This issue introduces bias within any method used to sample the frequency of these structures.

Parameters used to quantitatively estimate fracture frequency within a given area include trace intensity, trace density and mean trace length, these are outlined in figure 4.6 (Mauldon et al., 2000). Trace intensity is defined as the mean total trace length of fractures per unit area (figure 4.6a) (Mauldon et al., 2000). Trace density is defined as the mean number of fracture trace centres per unit area (Figure 4.6b) (Mauldon et al., 2000). The mean trace length is defined as the mean fracture trace length of individual fracture traces within an individual population (Figure 4.6c) (Mauldon et al., 2000).

 In this thesis, trace intensity has been estimated for all deformation structures. Dividing the number of traces by the total area is the most practical and least biased estimate of the trace intensity compared to the other two methods. For example, trace density relies on finding the trace centre and trace length relies on knowing how long a deformation structure is, both of which are difficult to attain in areas of limited exposure. Not all areas where deformation structures are measured in the field area are of an equal size and so trace density may lead to over or under estimations.
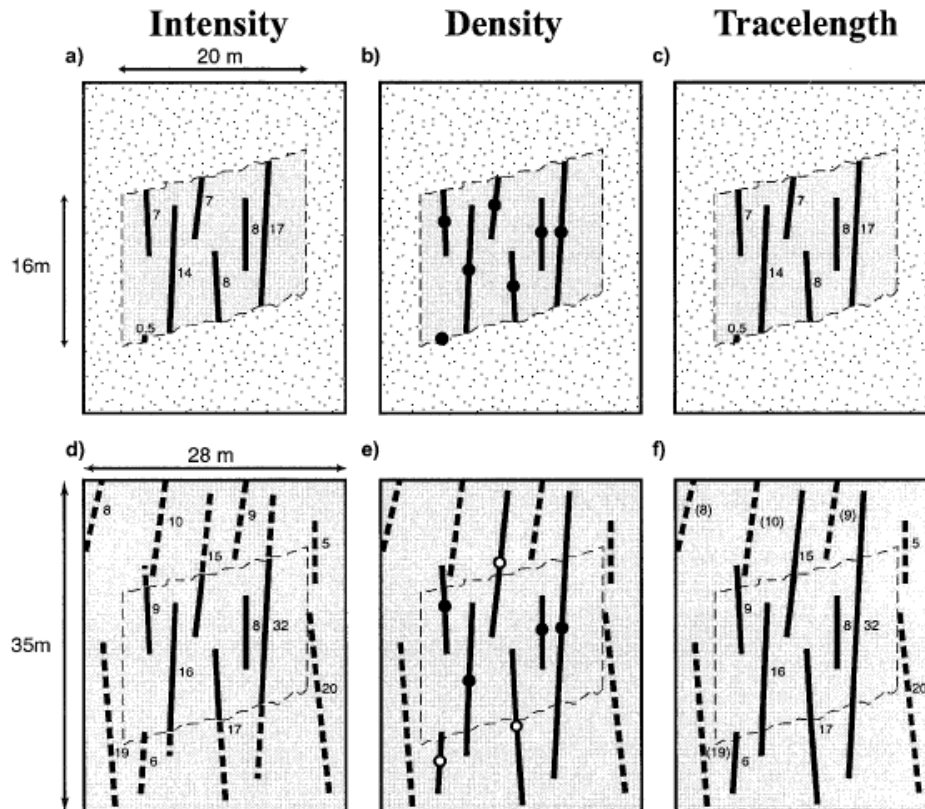
Figure 4.6 – Parameters used to estimate fracture frequency by (a) trace intensity, (b) trace density and (c) mean trace length (Mauldon et al., 2000).

When using trace density as a parameter, it is often difficult and unrealistic to identify the trace centre of each structure because the centre is often unknown or not exposed. This method has not been used in this thesis because of the limited exposure of some study sites would have introduced more bias to the sampling method.

In the same way as estimating the trace density, calculating the mean trace length is unrealistic because the total length of a trace is often not visible at this site. This method was deliberately not used here because exposures are limited and this would result in a length bias toward shorter mean trace lengths.

For estimating the trace intensity for deformation structures (deformation bands) at Crow's Nest Fault, there were two main methods of sampling; linear scanlines to measure both across and along strike trace intensity and measuring the trace intensity of 'representative' samples.

Where canyons cross cut the fault, maps were constructed of the canyons by walking along an orientated tape measure to map out the architecture of the canyon. Whilst mapping, deformation structures orientated below 180° to the tape measure were plotted onto the canyon map directly including any orientations and cross cutting relationships. Once the canyon map was constructed, the deformation structures within the canyon and across the fault were logged onto the map.

At sites where there were no exposed canyons cross cutting the fault, maps were constructed by walking from the furthest exposure in the hanging wall towards the fault and documenting the frequency, orientation and location of deformation structures. Deformation band intensity was then calculated by counting the deformation bands oriented 180° or less to the orientation of the tape measure and dividing this number by the total exposed area by walking from the north-east to the south-west along the strike of the fault. To deduce the along strike trace intensity, the same method was repeated and the localities were walked along in the footwall and lenses.

Where there are a number of localities close together there may be some overlap between the measured areas of the exposures which can lead to overestimation of trace frequency. To reduce this bias, clear boundaries between site localities were determined prior to fieldwork by studying the exposures from aerial photography imagery on Google Earth.

The use of linear scanlines as a method for determining deformation structure frequency has been previously deployed in Utah along the Moab Fault by Johansen et al., (2005). They showed this method resulted in a more accurate representation of trace intensity with deformation bands and joints, compared to random sampling. However, linear scanlines have a bias toward sampling structures perpendicular to the scanline. To reduce bias, circular scanlines could be undertaken within this area in the future to reduce any overestimations of trace intensity, length and orientation bias.

Where deformation structures were well exposed, a plastic ruler was constructed into a square and placed on the outcrop. Photographs of the exposed deformation structures were taken within the measured square and where possible, photographs were printed off using a portable printer and annotated within the field. Placing measured squares on the exposed outcrops where deformation structures were present allowed for a more accurate representation of the exposed areas when annotating field sketches and making detailed measurements of the deformation structures in the field.

For example, at the Zippy Canyon site, only an area measuring 72cm x 24cm out of the total exposed 58m x 4m of the lens had any deformation bands present. Placing a square around the area exposing these deformation bands allowed for a highly detailed look into the deformation bands present and gave a better indication of where the deformation bands were exposed at this location. The placement of the different squares is shown in figure 4.5 and the results of the deformation structure frequency is discussed further in section 4.6.4. This method was used everywhere in the field area apart from at the Brush Valley locality.

Due to the high frequency of deformation structures at the Brush Valley locality, a different approach to sampling was undertaken that was more time efficient. Instead of measuring the trace intensity of all deformation structures in the exposed area and dividing this value by the area, 'representative' samples of the deformation structures were taken from the Brush Valley locality. This was undertaken by using plastic rulers measured into squares of varying sizes (see figure 4.5) placed on the outcrop so that the trace intensity could be deduced from that square by dividing the number of traces by the total area exposed. This method helped to normalise the trace intensity to enable a comparison to other sites at the Crow's Nest Fault.

In evaluating the method used at Brush Valley, it is clear that there is some bias present. In the Brush Valley site, six individual squares were chosen on the basis of being in a well exposed area with a high frequency of deformation structures. In doing so, this method has likely led to an overestimate of the trace intensity at this site.

In each locality the size of the exposed area varies. The implication of this is that larger areas may have a higher chance of there being a higher number of exposed deformation structures compared to areas which are less well exposed. By dividing the number of deformation structures exposed by the area, this reduces the area bias. However, localities which are exposed as canyons which cross cut the fault may be more likely to expose a greater frequency of deformation structures compared to localities that are not.

4.3.2 Microanalysis of fault gouge at Crow's Nest Fault

Samples of fault gouge were taken from each location and studied under a scanning electron microscope (SEM). Only one sample of each different type of gouge was analysed using the SEM and each sample may not be representative of the entire fault gouge.

Mineralogy was identified through a series of element maps and the mineralogical composition was estimated through looking at each slide and estimating the percentage of each mineral by sight. This was repeated for five times on each slide, looking at different parts of the thin section and establishing an average composition.

Element maps are used to show a spatial distribution of elements within a sample by different elements being highlighted in different colours on a map. Element maps were generated at 100,000 counts per second at a resolution of 512-400 pixels. For each sample, 10 to 15 photomicrographs were imaged at a scale of 350 pixels to produce element maps. Average percentages of each mineral were calculated from the element maps.

The smallest grains may be under-counted and if the grains are all the same mineral then that mineral may become under-represented. This leads to a small amount of bias for some higher resolution minerals when using this method. To improve the accuracy of determining mineralogical composition of the fault gouge samples, a combination of point counting and elemental mapping should be used.

4.4 Outcrop descriptions - field locations

4.4.1 Cottonwood Wash

The Cottonwood Wash site is located on the south-easterly end of fault strand B where a canyon cuts the Crow's Nest Fault (figure 4.7). On its north-western edge, the canyon exposes a 25m wide by 15m high section into the fault footwall. The footwall is composed of Navajo Formation sandstone, capped by the lower part of the Carmel Formation.   The hanging wall Entrada formations are incised by two small valleys.
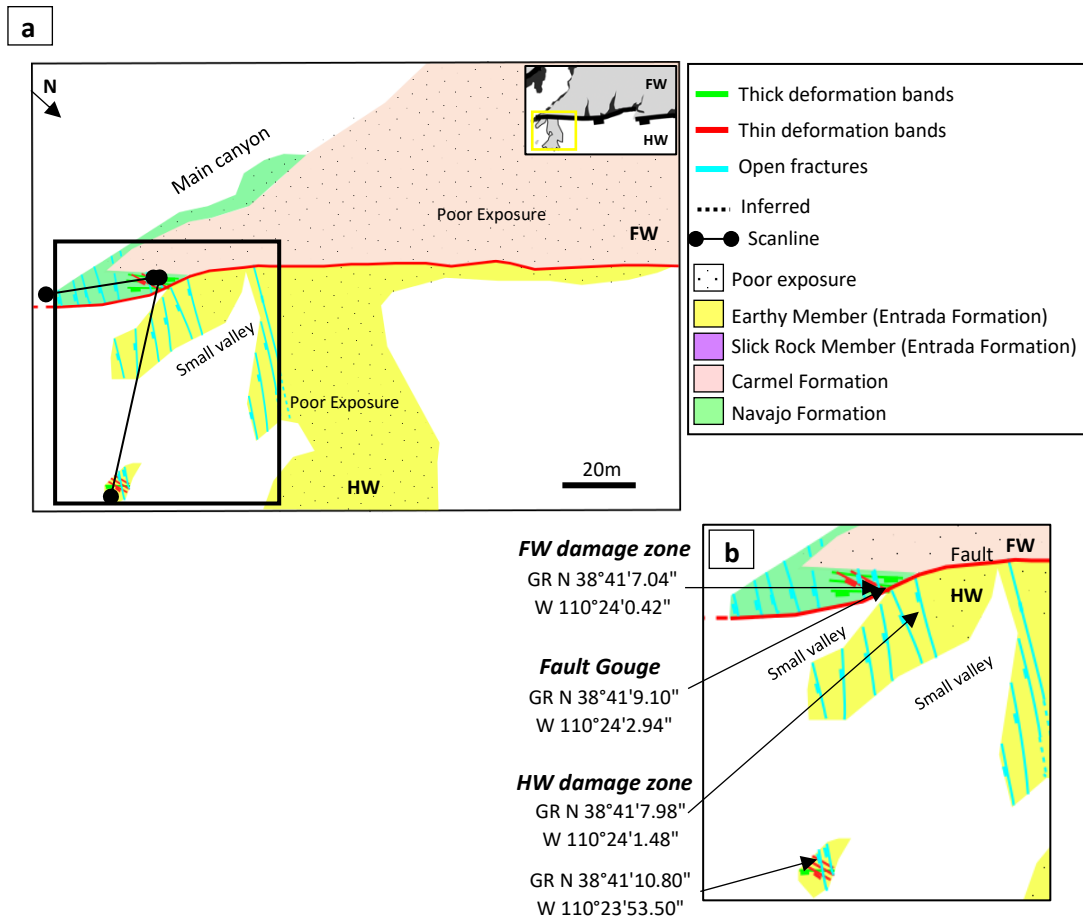
Figure 4.7 – Map of the Cottonwood Wash locality in plan view, the footwall includes the Carmel Formation and Navajo Formation and the hanging wall is exposed as the Earthy Entrada. Thick and thin deformation bands and open fractures are exposed in the footwall and hanging wall. Where geology is white on the map, no exposure is observed.

The fault zone at Cottonwood Wash is observed along the north edge of the canyon. The footwall damage zone is composed of the Navajo Formation which contains fractures and deformation bands, both of which increase in frequency approaching the fault core (figures 4.7 & 4.8). The hanging wall damage zone is composed of fractured Earthy Entrada. A 20cm thick band of purple-green incohesive fault gouge is observed at GR N 38°41'9.10" W 110°24'2.94" which maintains its thickness for 3m along strike.

Although the Cottonwood Wash footwall is exposed in a 25m by 15m canyon wall, only an area measuring 10m x 5m is deformed. The footwall damage zone is only exposed in the Navajo Formation in an area measuring 30m x 21m. There is only one outcrop in the footwall which contains deformation bands measuring 50cm by 34cm and this can be seen in figure 4.7b. The remainder of the damage zone includes open fractures only.

The hanging wall at Cottonwood Wash is exposed twice, firstly as an area measuring 73m x 24m at GR N 38°41'7.98" W 110°24'1.48" to GR N 38°41'8.90" W 110°23'58.83" and secondly as an area measuring 42m x 33m at GR N 38°41'10.80" W 110°23'53.50", both of which are shown in figures 4.7 and 4.8. The hanging wall damage zone at the first exposure includes open fractures only in the Earthy Entrada. At the second exposure, the damage zone is only exposed as a 40cm^2 area in the Earthy Entrada which includes thick and thin deformation bands and open fractures.

Linear scanlines were taken at the Cottonwood Wash locality in the footwall and hanging wall to determine the fracture intensity with respect to the fault (figure 4.7 and 4.9). In the hanging wall, the number of fractures per metre generally increases towards the fault, from a minimum value of 1.1 fractures per metre at a distance of 75m from the fault core to a peak value of 5.2 fractures per metre adjacent to it. There are local smaller peaks in fracture density at around 52 m and 35 m from the fault zone.

The footwall is exposed for a maximum of 30m perpendicular to the fault. Fractures are only present in the first 10m of the exposed footwall, beyond this there are no fractures. The number of fractures per metre increases towards the fault from zero to 4.4 fractures per metre 0-5m from the fault. The absence of any fractures for distances >10m from the exposed footwall suggests that fractures are fault related and the damage zone is 10m wide at this location.
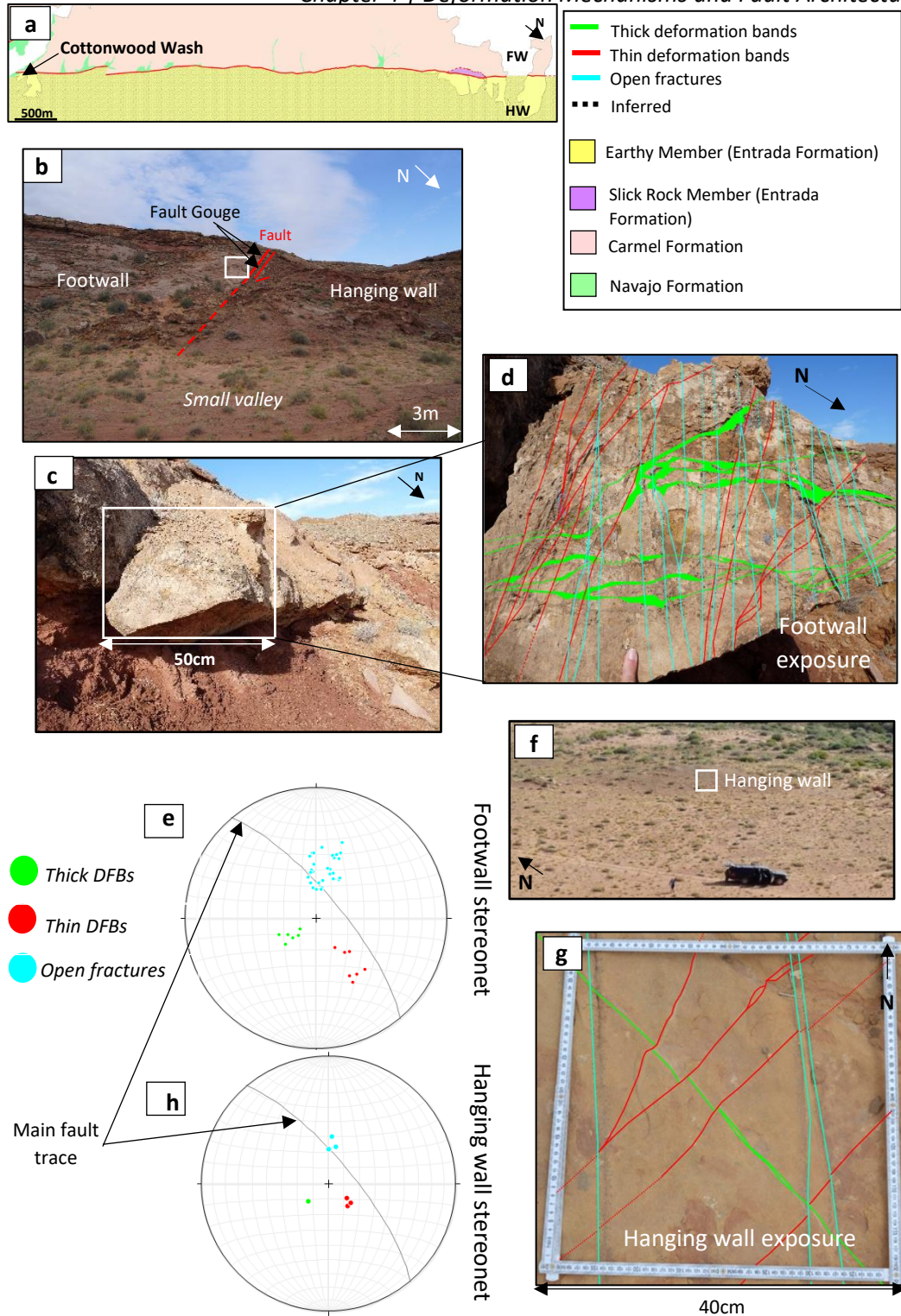
Figure 4.8 – (a) Map of Crow's Nest Fault, (b) the fault in outcrop, (c) outcrop where deformation bands are exposed in the footwall, (d) close up of deformation bands exposed in the footwall, (e) stereonet of deformation bands an fractures in the footwall, (f) where the deformation bands are exposed in the hanging wall, (g) deformation bands and fractures in the field and (h) stereonet of deformation bands and fractures in the hanging wall.
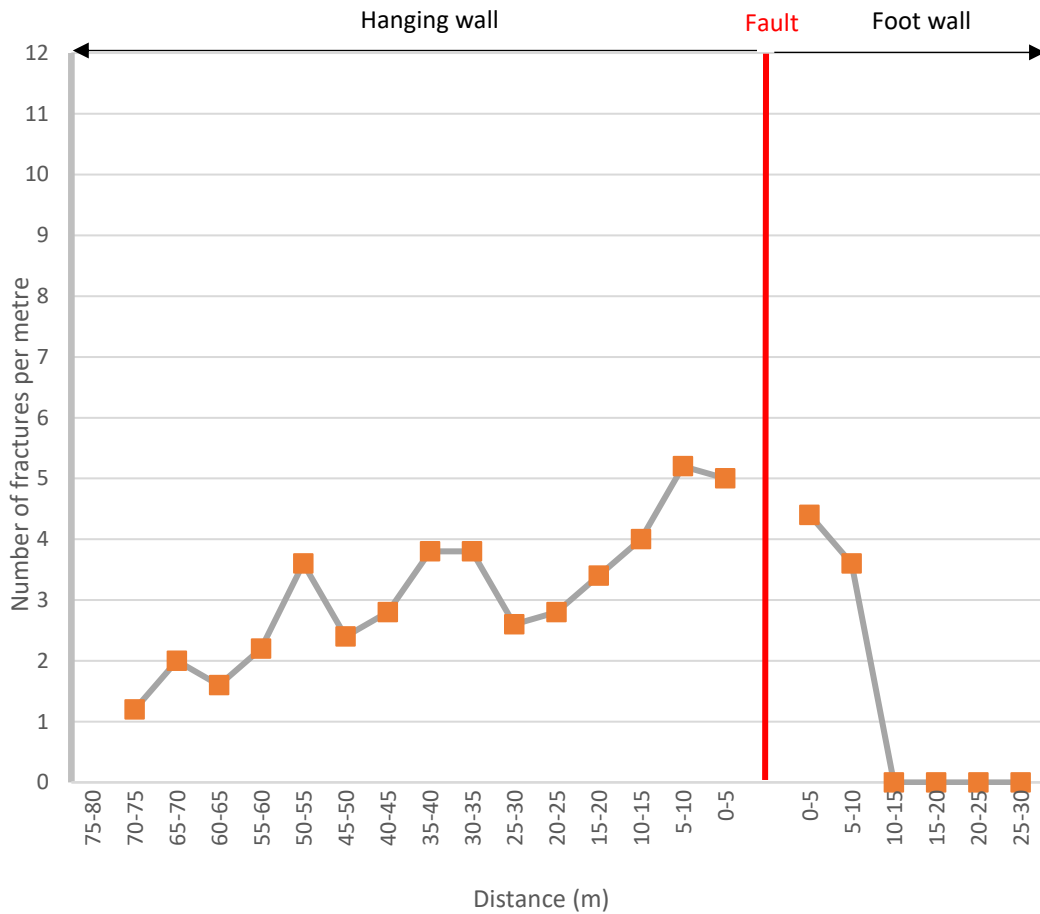
Figure 4.9 – Fracture intensity graph showing the number of fractures increasing towards the fault core at Cottonwood Wash locality. Scanline is orientated east-west.

4.4.2 Cacti Canyon

Cacti Canyon site is located on the south-eastern end of fault strand C where a canyon cuts the Crow's Nest Fault (figure 4.10). On its north-western edge, the canyon exposes a 54m wide by 14m high section into the footwall. The footwall is composed of Navajo Formation, capped by the lower part of the Carmel Formation. The hanging wall is not well exposed at this site.

The fault zone damage zone is observed along the north-western edge of the canyon only. The footwall damage zone is exposed in the Navajo Formation in an area measuring 27m x 14m (figures 4.11b). The footwall damage zone contains thick and thin deformation bands and no fractures.
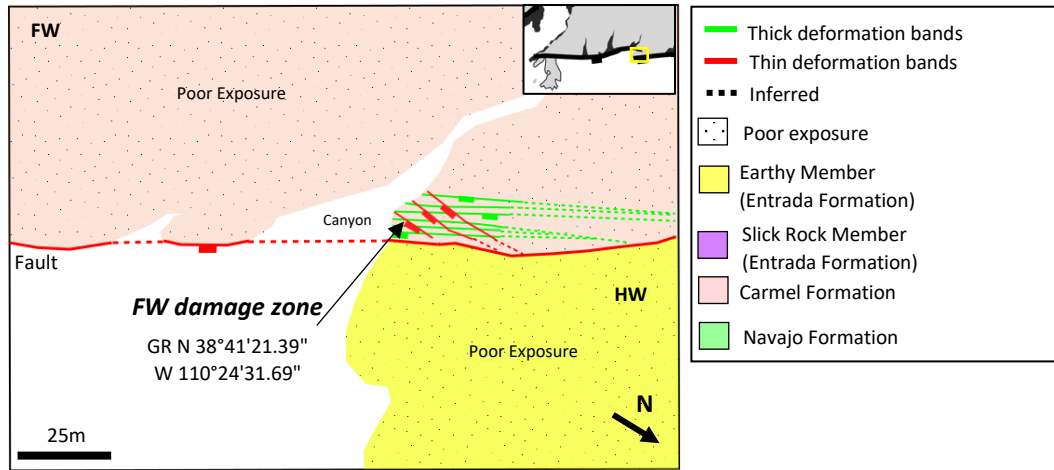
Figure 4.10 – Map of Cacti Canyon site in plan view. Thick and thin deformation band are exposed in the Navajo Formation of the footwall. Exposure is poor in the hanging wall but is composed of the Earthy Entrada.
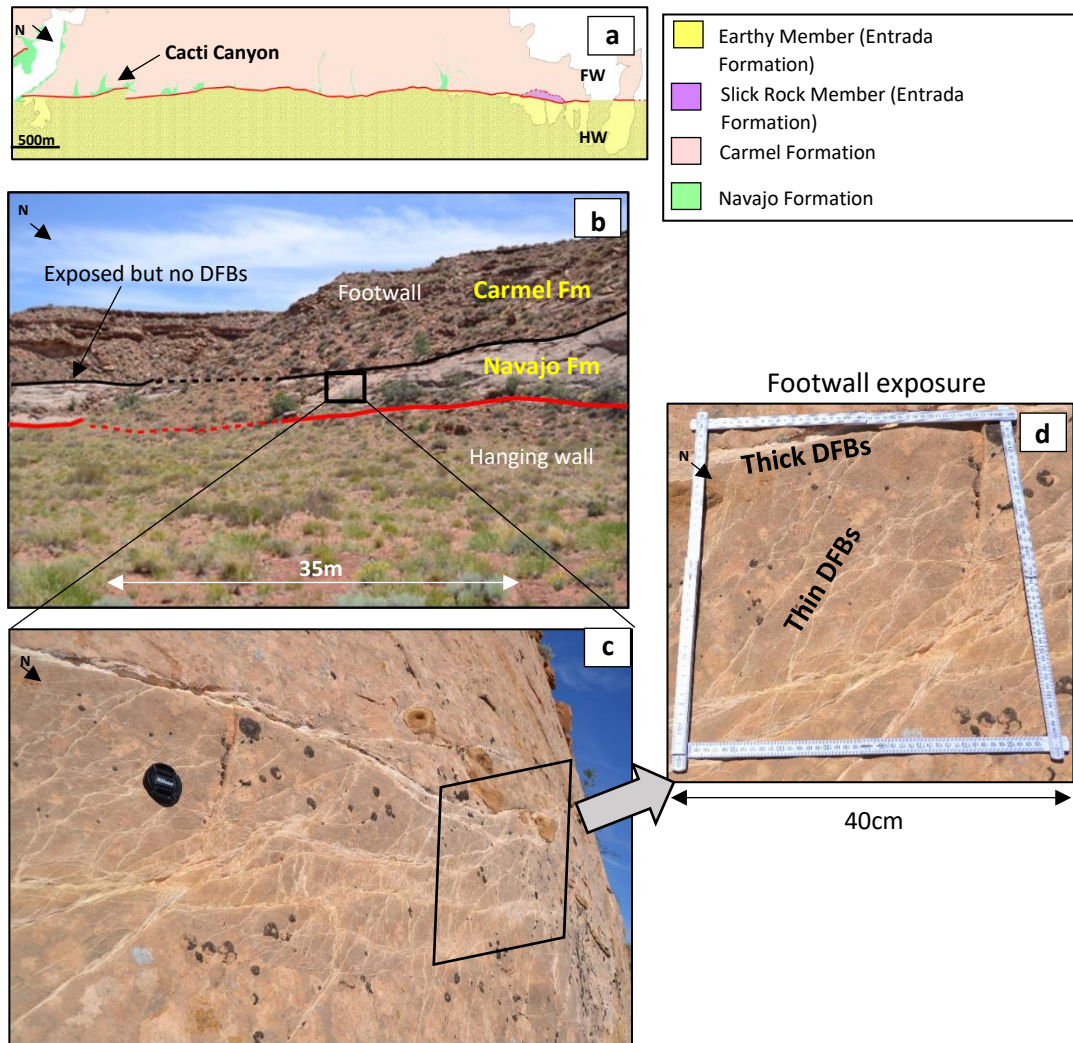
Figure 4.11 – (a) Map of the Crow's Nest Fault showing the location of Cacti Canyon, (b) photograph showing the footwall and hanging wall at Cacti Canyon, (c) and (d) show the exposure of the thick and thin deformation bands in the field.

4.4.3 Crow's Nest Spring

Crow's Nest Spring, the site of an old prospect pit, is located midway along fault strand C where a wide river canyon cuts through the fault (figure 4.12). The canyon branches out into three narrow canyons up to 15m wide that get narrower into the footwall. At its widest, the main canyon is 35m in width, exposing Navajo Formation and Carmel Formation in the footwall and Entrada Formation in the hanging wall. A stratigraphic log was made along the middle canyon which is well exposed for 480m to the south-south west of the main fault trace, exposing the Upper Carmel Formation, Lower Carmel Formation and the Navajo Formation (figure 4.13).

The footwall damage fracture frequency increases approaching the fault core (figure 4.14). The 11m wide lens within the fault zone is composed of fractured Navajo and Carmel Formation bound by two slip surfaces separating the lens from the footwall and hanging wall. The hanging wall damage zone is composed of the Earthy Entrada but is not well exposed. There are no deformation bands present at this location.

The main fault core is defined by a 50cm thick band of purple-grey incohesive fault gouge, which maintains a constant thickness for at least 5m along strike and is observed at GR N 38°42'8.68" W 110°26'23.55. A second parallel exposure of fault gouge is observed at GR N 38°42'8.57" W 110°26'23.84, however this is not well exposed or accessible.
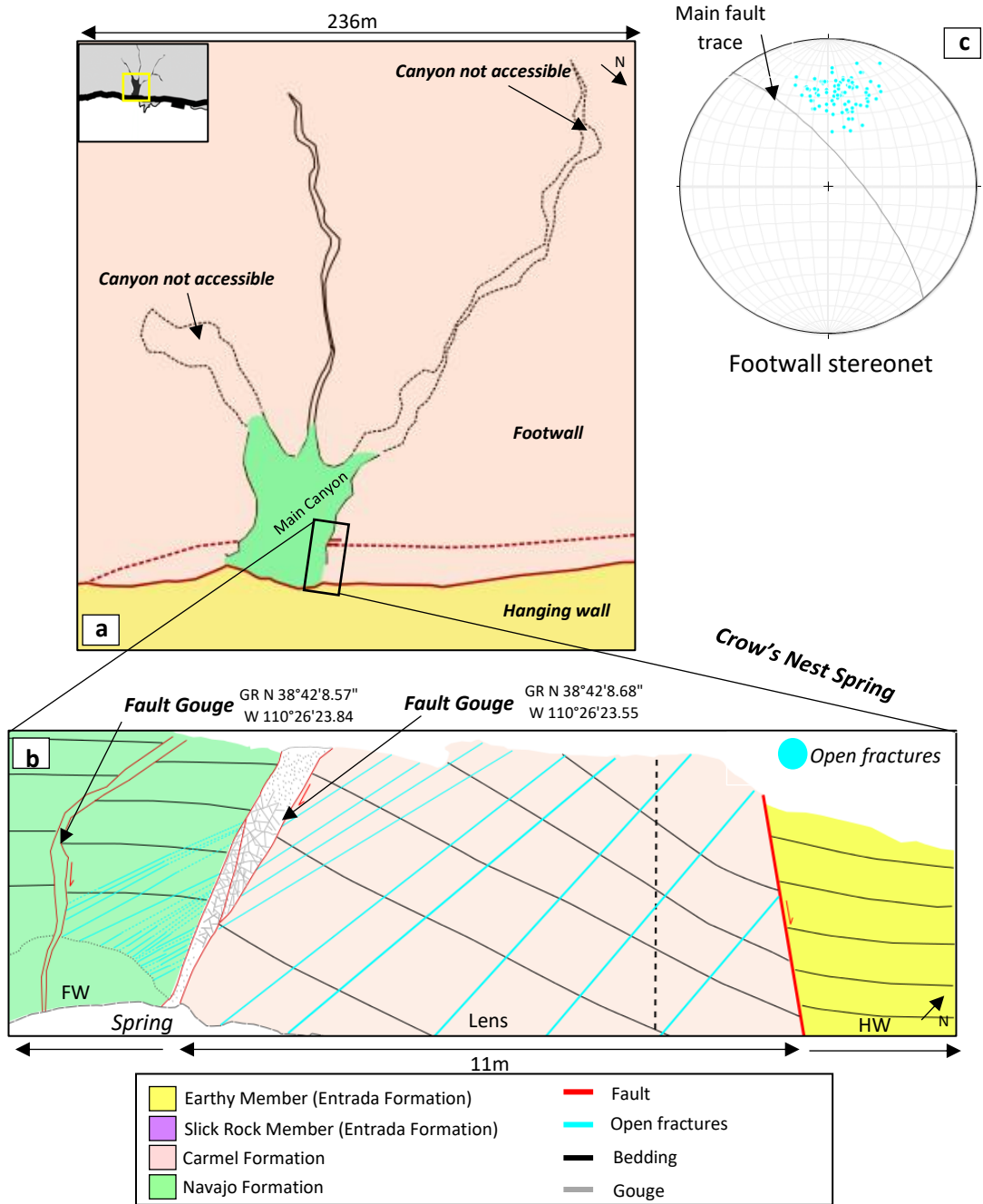
Figure 4.12 - (a) Plan view map of the Crow's Nest Spring locality, (b) Looking face on at the fault zone including the fault gouge and (c) a stereonet showing the orientation of the fractures with respect to the fault.
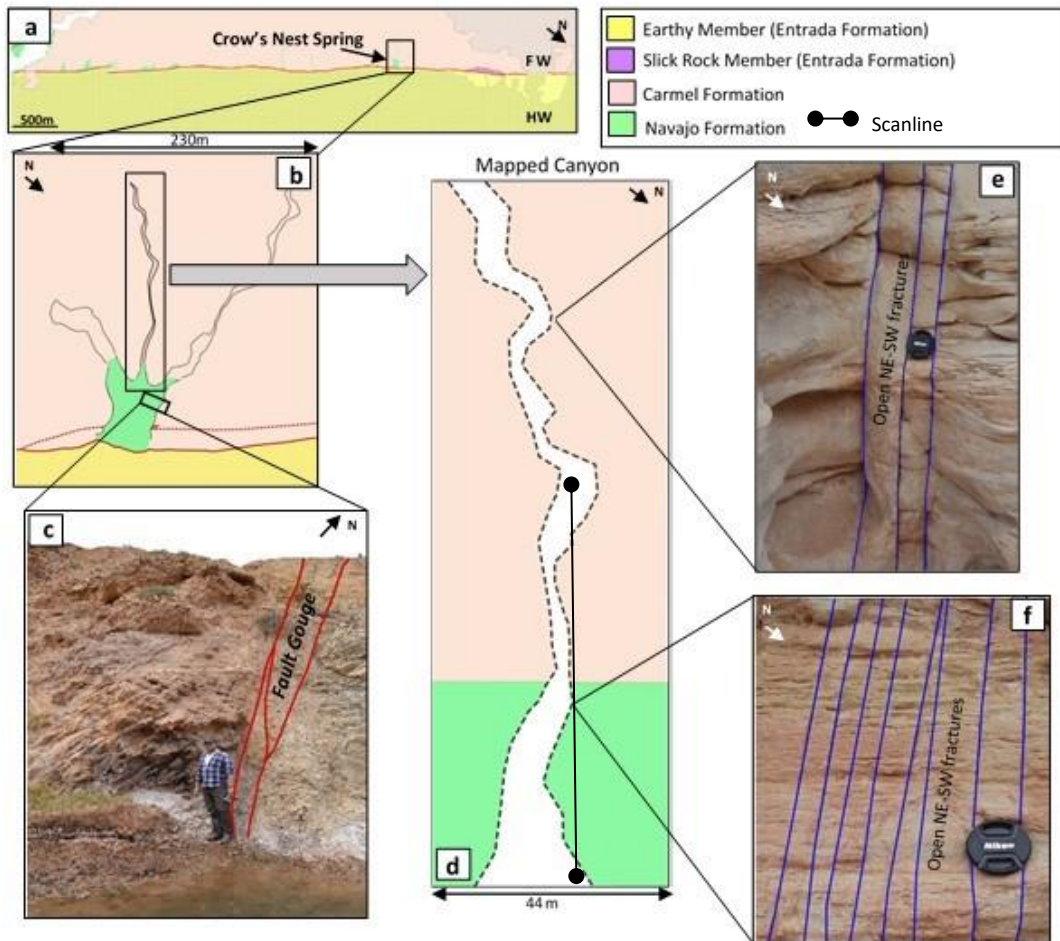
Figure 4.13 – (a) Map of the Crow's Nest Fault indicating the Crow's Nest Spring site, (b) a plan map of the Crow's Nest Spring site, (c) a photograph showing the fault zone at the Crow's Nest Spring site, (d) A plan map of the mapped canyon going towards Crow's Nest Fault, (e) open fractures in the Carmel Formation and (f) open fractures in the Navajo Formation.

Linear scanlines were taken at the Crow's Nest Spring locality in the lens and footwall to determine the fracture intensity with respect to the fault (figure 4.13 and 4.14). There are 8.1 fractures per metre up to 5m away from the fault closest to the hanging wall and 7.8 fractures per metre 5m away from the slip surface closest to the footwall.

The footwall is exposed in a 480m long canyon. However, fractures are only exposed for 175m perpendicular to strike. For the remaining distance that is exposed in the footwall, fractures are not observed. 5m into the footwall there are 8 fractures per metre and this decreases steadily to 3 fractures per metre at 110-115m into the footwall. At 115m into the footwall, fractures taper off to 0.5-1.5 fractures per metre until 175m away from the fault where they die out. The last 60m of the footwall where fractures are exposed is likely

background fracturing as the number of fractures per metre remains relatively constant, never increasing to more than 1.5.
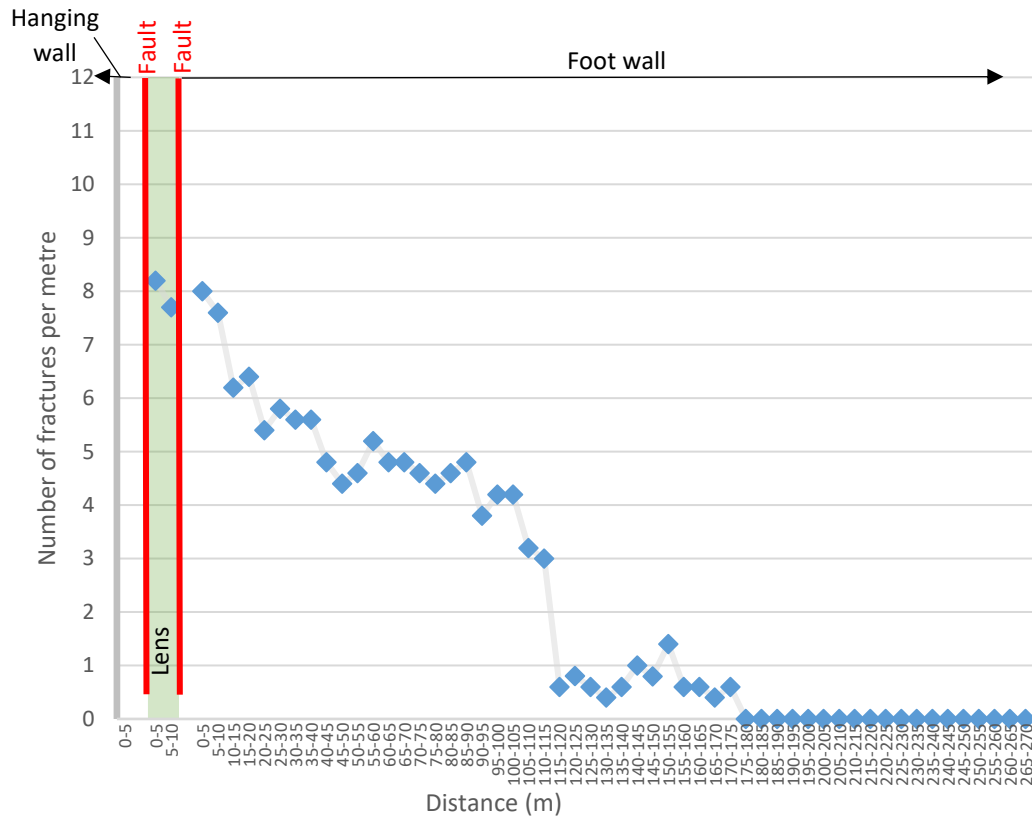
Figure 4.14 - Fracture intensity graph showing the number of fractures increasing towards the fault core at Crow's Nest Spring locality.

4.4.4 Old Mine

The Old Mine site is located on the north-westerly end of fault strand C and is an abandoned site which was of interest to miners (figure 4.15). In the footwall, the site is exposed within a 47m x 17m high cliff composed of the Navajo Formation and capped by the Carmel Formation (figure 4.16). The hanging wall is composed of the Earthy Entrada.

FW damage zone
GR N 38°42'23.51"
W 110°26'44.31"
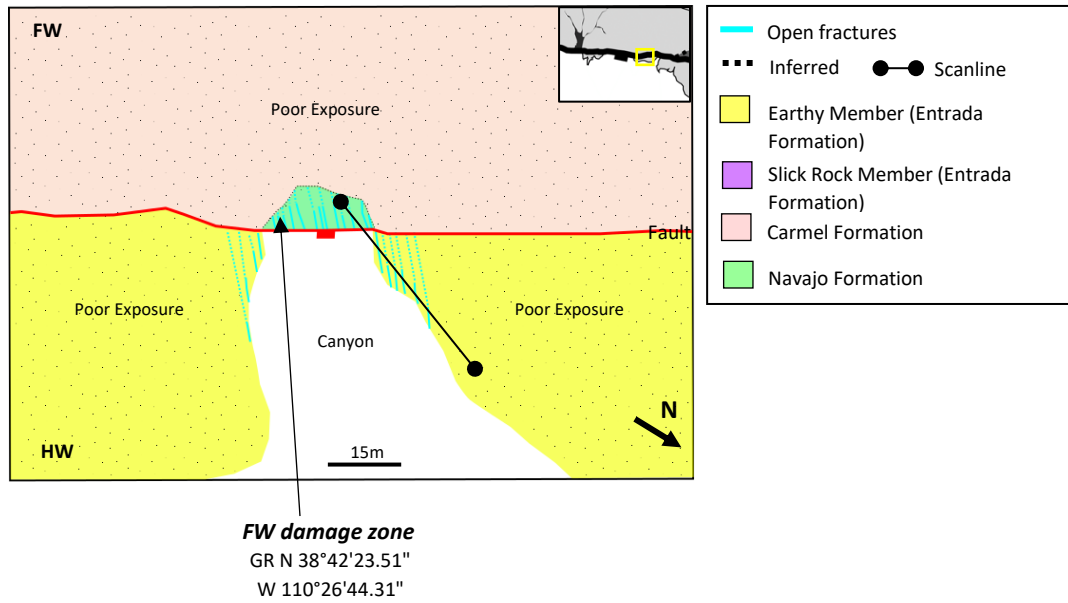
Figure 4.15 – Map of the Old Mine site. Fractures are exposed in the Slick Rock Entrada Formation and Carmel Formation in the footwall and in the Earthy Entrada Formation in the hanging wall.

The footwall damage zone is composed of fractured Navajo Formation and Carmel Formation and breccia (GR N 38°42'22.88" W 110°26'44.33") (figure 4.16); fractures increase in frequency towards the main fault trace (figure 4.18). The hanging wall damage zone is composed of fractured Earthy Entrada. The fault core (gouge) is not exposed at this locality.

Although the Old Mine site is exposed as a canyon measuring 47 in height x 17m in width, the footwall damage zone is only exposed in the Carmel Formation in an area measuring 14m x 15m. The footwall damage zone, composed of fractures and breccia (figure 4.18), is situated at GR N 38°42'23.51" W 110°26'44.31". The remainder of the damage zone is exposed within a high cliff which is not accessible.
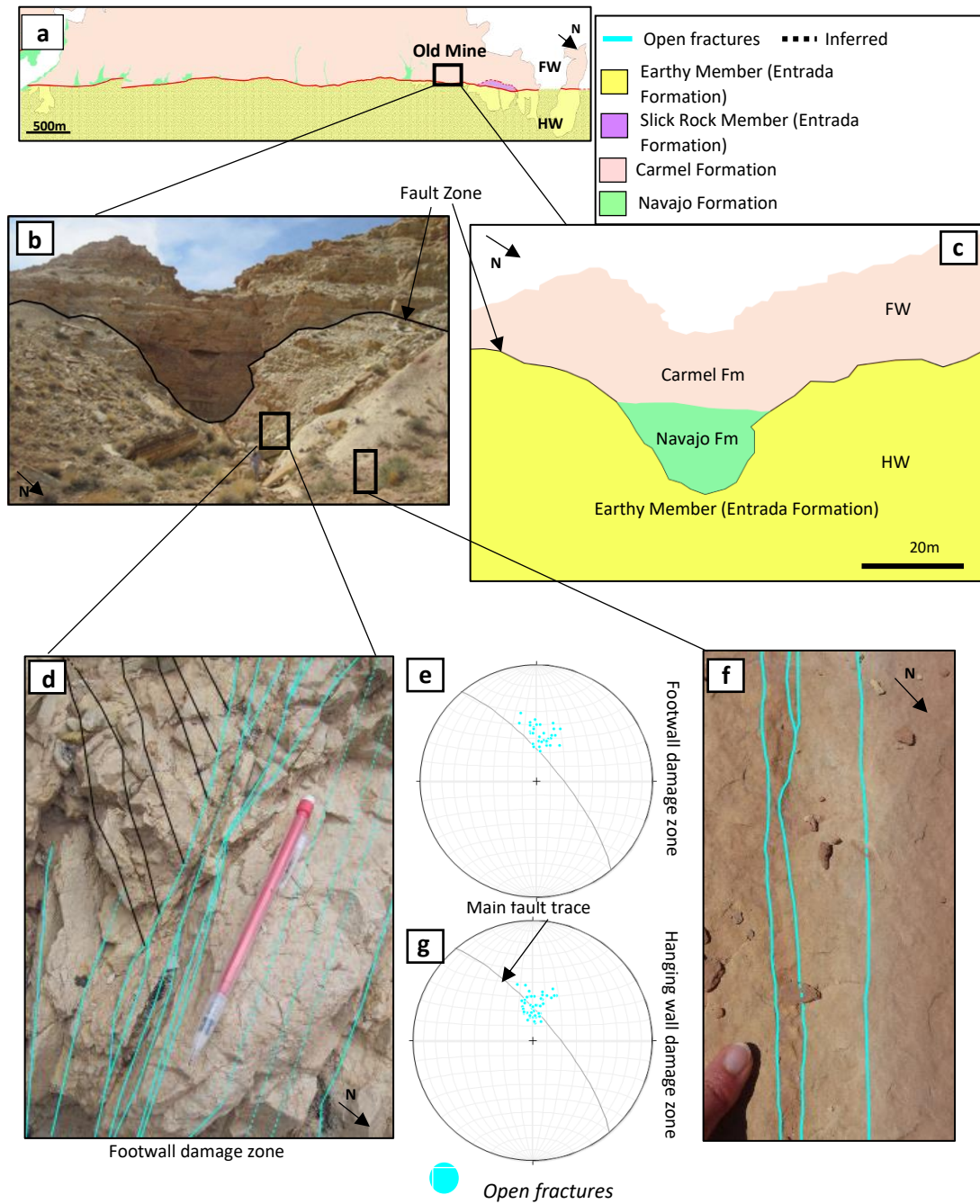
Figure 4.16 – (a) Map of the Crow's Nest Fault indicating where the Old Mine site is situated, (b) photograph of the Old Mine site, (c) annotated photograph of the Old Mine site includes the Carmel and Navajo formations. The footwall damage zone (d) and hanging wall damage zone (f) are heavily fractured and this can be viewed by the stereonets in (e) and (g).
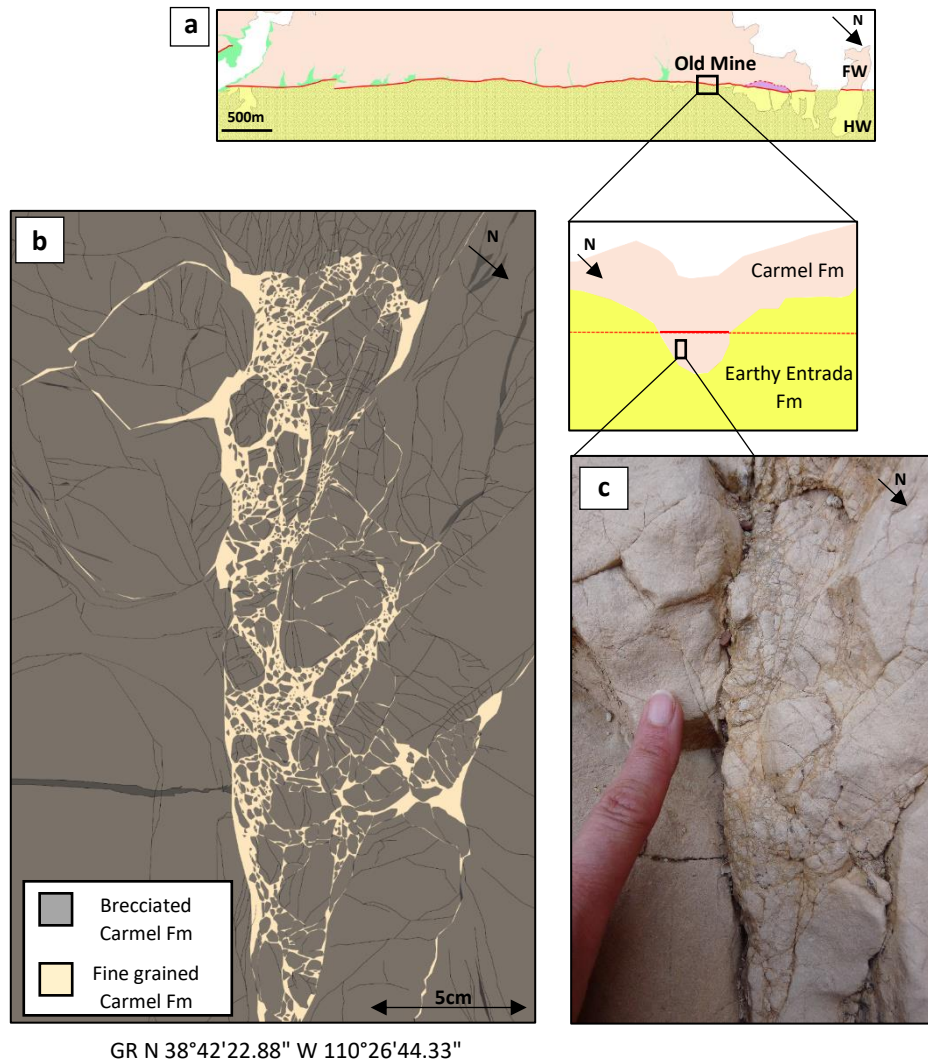
Figure 4.17 – (a) Map of the Crow's Nest Fault indicating the location of the Old Mine site. (b) and (c) show an area in the footwall where the host rock has become brecciated.

Linear scanlines were taken at the Old Mine locality in the footwall and hanging wall to determine the fracture intensity with respect to the fault (figure 4.15 and 4.18). Both the hanging wall and footwall show a positive relationship between the number of fractures exposed per metre and an increase in distance towards the fault. Between 0-5m into the hanging wall, there are 8 fractures per metre exposed. Whilst some variability is observed, the fracture intensity falls fairly steadily from this value to 4 fractures per metre at 45-50m into the hanging wall, where the hanging wall exposure ends. In the footwall, there are 11 fractures exposed per metre at <5m away from the fault and this decreases sharply to 8.4 fractures per metre at 10-15m into the footwall where the exposure ends.
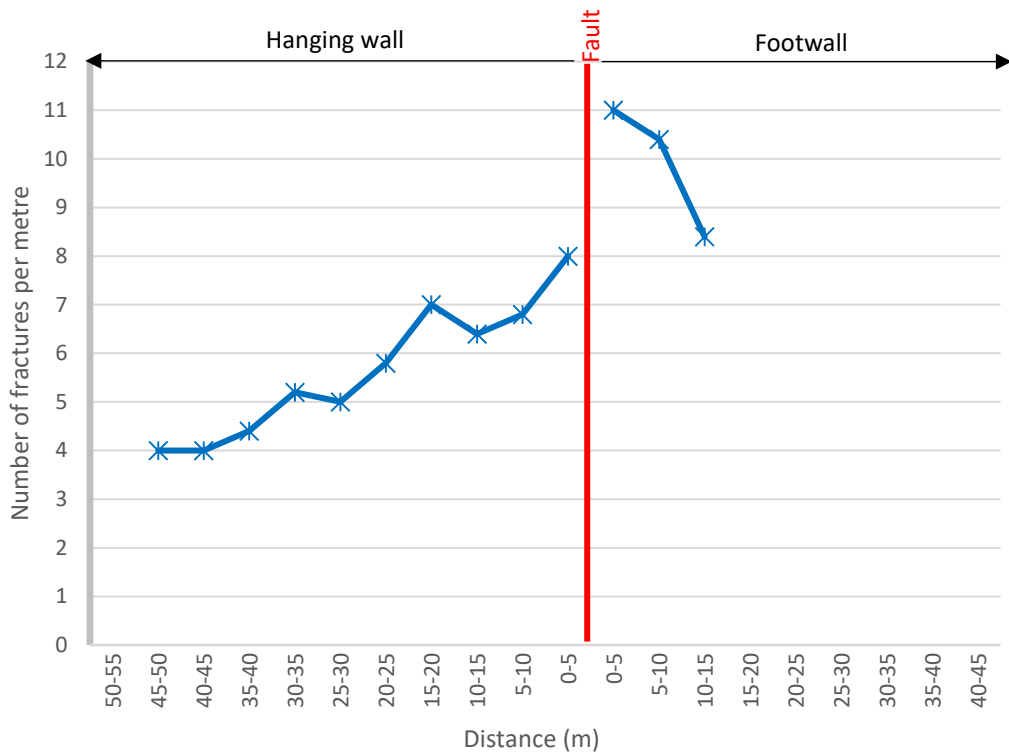
Figure 4.18 - Fracture intensity graph showing the number of fractures increasing towards the fault core at Old Mine locality.

4.4.5 Zippy Canyon

The Zippy Canyon site is located on the north-westerly end of fault strand C (figure 4.19). The canyon is exposed for 58m in length and has a maximum width of 4m. It cuts the fault through a sandstone lens (see section 2.2.3) and there is no exposure to the footwall (figure 4.21). The lens is composed of the Slick Rock Entrada. The hanging wall is composed of the Earthy Entrada and is expressed as locally weathered 'goblins'.

The lens damage zone contains deformation bands. The hanging wall damage zone is composed of fractures which increase in frequency towards the fault (figure 4.20).

Deformation bands are only present in a small area measuring 72cm by 24cm in the lens and this is situated at GR N 38°42'30.69" W 110°26'55.65". Much of the exposure where the hanging wall meets the lens is covered by fallen rock.

The hanging wall damage zone is exposed for an area measuring at 21m x 33m at GR N 38°42'31.26" W 110°26'55.04" and includes open fractures only.
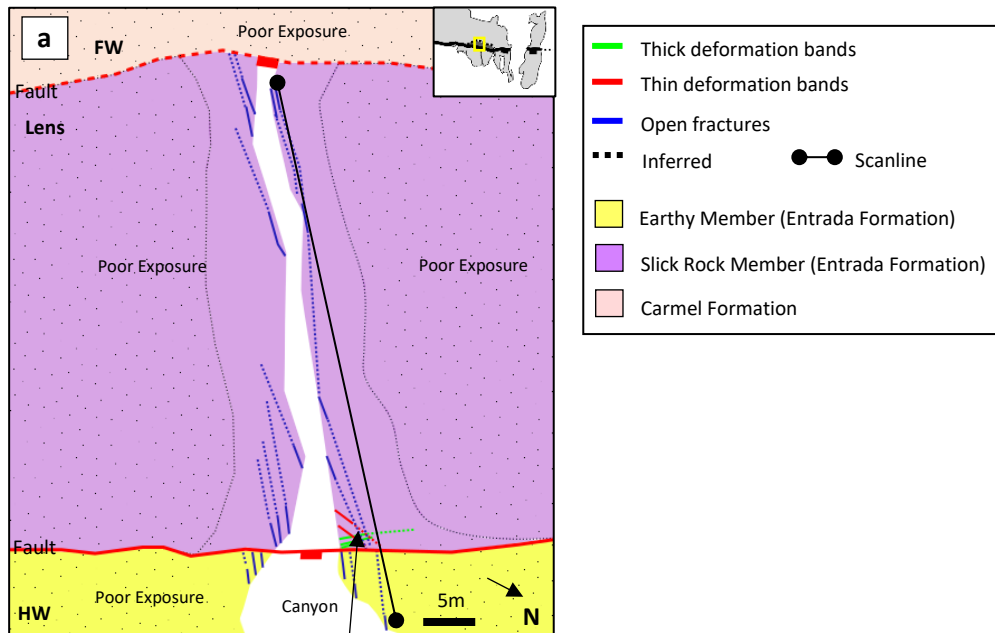
Exposed DFBs in the lens
GR N 38°42'30.69" W 110°26'55.65"

Looking south-west into the canyon standing in the hanging wall, looking into the lens

Figure 4.19 – (a) Map of the Zippy Canyon site in plan view. (b) Looking into the canyon from the hanging wall.
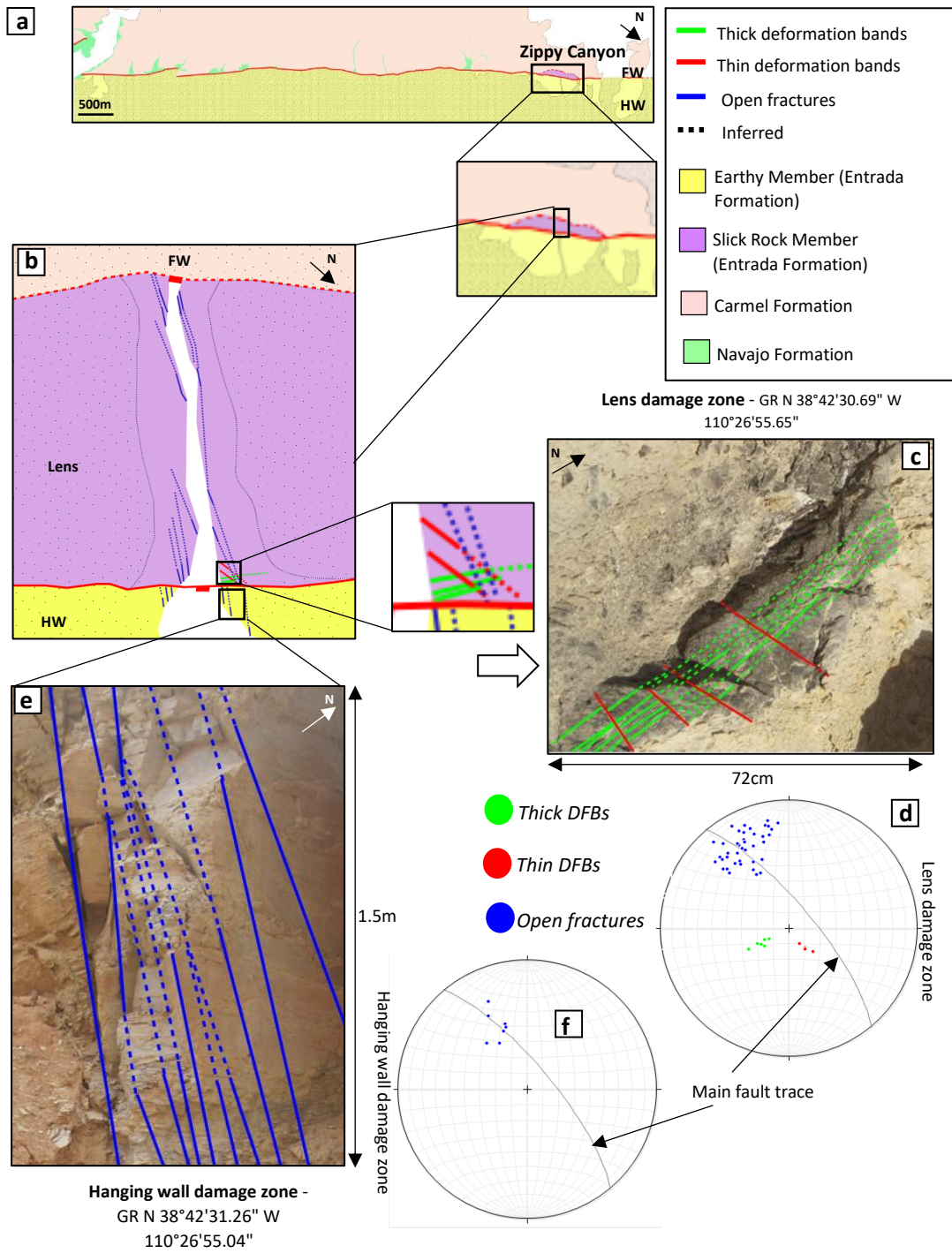
Figure 4.20 – (a) Map of the Crow's Nest Fault indicating where the Zippy Canyon site is located, (b) plan view of the Zippy Canyon indicating where (c) deformation bands are located in the lens and (e) fractures are located in the hanging wall. (d) and (f) are stereonets representing the fractures and deformation bands in the hanging wall and lens.

Figure 4.21 - Fracture intensity graph showing the number of fractures increasing towards the fault core at Zippy Canyon locality.

In the hanging wall there is a slight increase in fracture intensity from 2 to 3 fractures per metre as distance to the first fault strand decreases from 15-20m to 0-5m (figure 4.21). Compared to fracture intensity at the rest of the Crow's Nest Fault, these values are low for the hanging wall damage zone and could suggest that these fractures are not fault related. Alternatively, this may be a consequence of the presence of a second fault strand, with most damage zone deformation being accommodated within the lens.

The lens is bound by two slip surfaces; one closest to the hanging wall and one closest to the footwall. There are 5.9 fractures per metre and after a slight decrease, fracture intensity in the lens increases steeply as the second fault strand is approached, rising to a peak value of 9 fractures per metre.

4.4.6 Brush Valley

The Brush Valley site is located on the most north-westerly end of fault strand C (figure 4.22). The canyon is located between the main fault trace and the breached relay ramp,

where a lens has been formed (figure 4.22b). On its south-western edge, the canyon exposes a 29m wide by 52m high section into the lens adjacent to the footwall. On its north-eastern side, the canyon exposes a 13m wide by 19m high section into the lens adjacent to the hanging wall. The lens is composed of the Slick Rock Entrada. The hanging wall is the Earthy Entrada. The footwall is composed of the Carmel Formation but it is not accessible from the canyon.

Figure 4.22 - Map of the Brush Valley site. Open fractures, iron-rich fractures and thick and thin deformation bands are exposed in the Slick Rock Entrada in the lens and open fractures are exposed in the Earthy Entrada in the hanging wall.

At the Brush Valley site, the fault zone is observed along both the south-western edge and the north-eastern edge of the canyon and both are composed of a damage zone and fault gouge. In the lens, the damage zone is composed of the Slick Rock Entrada which contains deformation bands (figures 4.24; 4.26) and iron-rich fractures, both of which increase in frequency towards the fault core which is exposed as fault gouge. The hanging wall damage zone is composed of fractured Earthy Entrada. Fault gouge is composed of a 50cm thick band of purple-grey incohesive fault gouge, which maintains its thickness for at least 48m along strike. Fault gouge is exposed twice at GR N 38°42'32.02" W 110°26'57.59", again at N 38°42'32.59" W 110°26'58.44" (figure 4.23).

Although Brush Valley is exposed as two sections measuring 29m x 52m to the south-west and 13m x 19m to the north-east, due to the sheer number and geometric complexity of the damage features, the lens was characterised by detailed mapping of six 20cm^2, 40cm^2 or 1m^2 squares (figure 4.24) in the south-western canyon due to the excellent exposure.

This approach allowed for more effective use of limited fieldwork time and led to a more detailed description of the geometrically complex deformation structures at this location.

The hanging wall at Brush Valley is exposed as a 131m x 124m area, however only an area of 44m x 35m is well exposed and accessible, this area includes open fractures only. The remainder of the area is covered by wind-blown sediment.
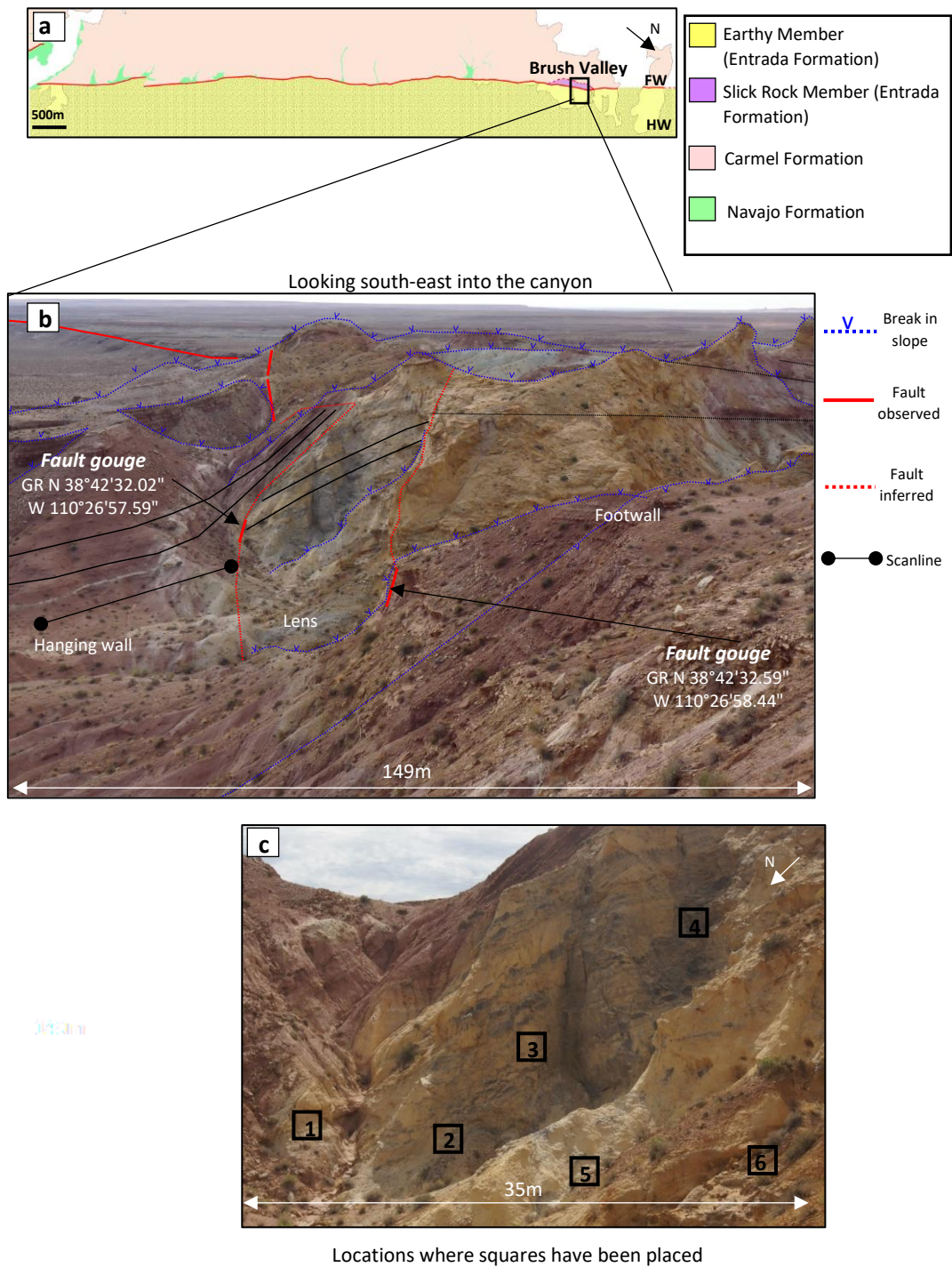
Figure 4.23 – (a) Map of the Crow's Nest Fault indicating where the Brush Valley site is locate. (b) demonstrates where the lens, hanging wall and footwall are situated at the Brush Valley site and (c) indicates where samples 1-6 were taken from the locality.
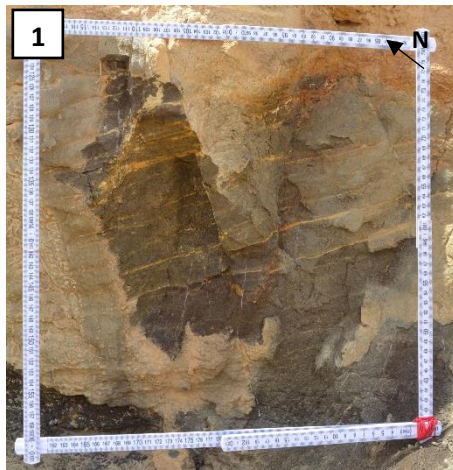
Square 1 - 40cm x 40cm at GR N 38°42'32.44" W 110°26'58.48"
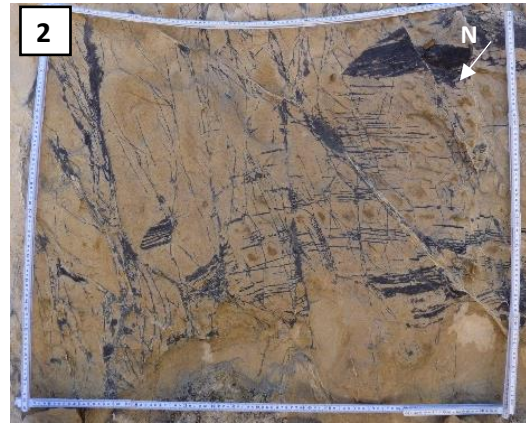
Square 2 - 1m x 1m at GR N 38°42'32.24" W 110°26'58.89"

Square 3 - 1m x 1m at GR N 38°42'32.11" W 110°26'58.96"

Square 4 - 1m x 1m at GR N 38°42'32.24" W 110°26'58.89"
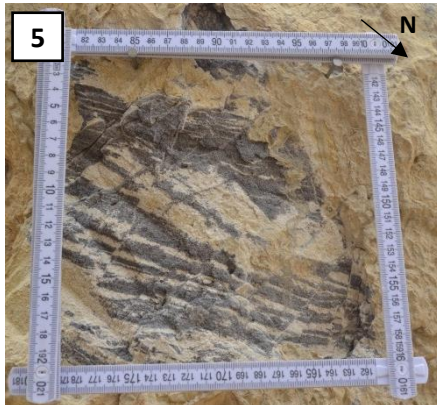
Square 5 – 20cm x 20cm at GR N 38°42'32.10" W 110°26'59.27"
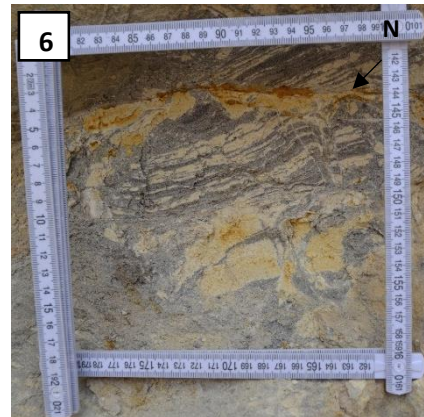
Square 6 – 20cm x 20cm at GR N 38°42'32.28" W 110°26'59.62"

Figure 4.24 – Squares 1-6 indicate where the samples were taken from the Brush Valley locality.
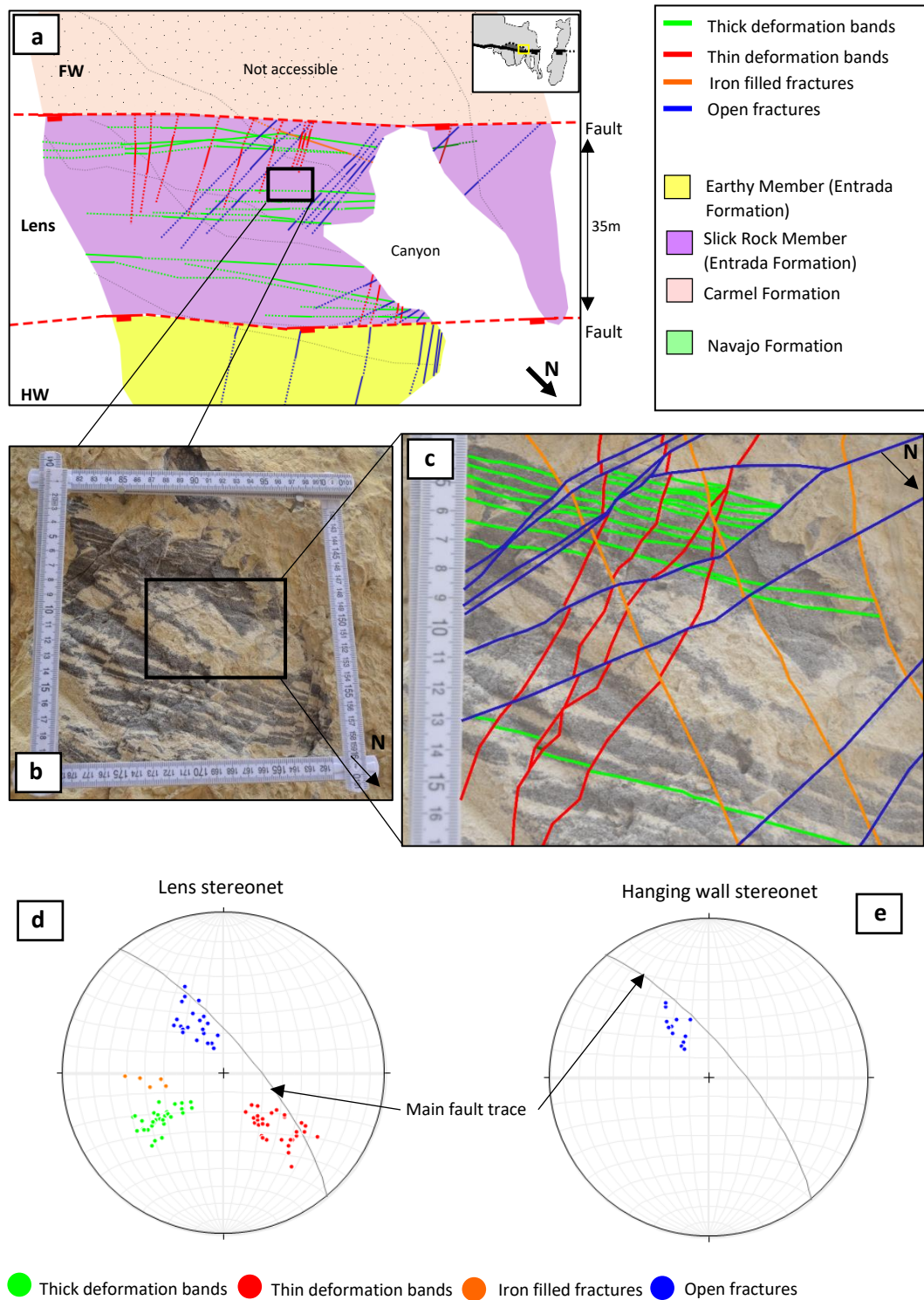
Figure 4.25 – (a) Map of the Brush Valley locality. (b) and (c) show the cross cutting relationships of deformation bands and fractures in square 5 orientated data are represented in stereonets in (d) and (e) showing the orientations of the structures with respect to the main fault trace.

Figure 4.26 - Fracture intensity graph showing the number of fractures increasing towards the fault core at Brush Valley locality.

In the hanging wall the number of fractures per metre rises gradually as the fault is approached, from 1.1 fractures per metre 20-25m from the fault to 2.9 fractures per metre adjacent to the fault (figure 4.26). Similar to the Zippy Canyon locality, fracture intensity in the hanging wall is relatively low. Again, this may be due to the presence of a second fault strand, since within the lens, fracture intensity is high; increasing in value adjacent to both the slip surfaces. As in the case of Zippy Canyon, fracture intensity is at its highest (8.4 fractures per metre) within the lens, adjacent to the southern fault strand.

4.4.7 Spider Canyon

The Spider Canyon site is located on the south-easterly end of fault strand D where a canyon cuts the Crow's Nest Fault (figure 4.27). The canyon measures 18m in width by 105m in length and on its south-westerly edge, exposes a 35m wide by 71m long high section into the fault footwall. The footwall is composed of the Carmel Formation. The hanging wall is composed of the Earthy Entrada.

Footwall damage zone
GR N 38°42'44.74" W 110°27'21.27"
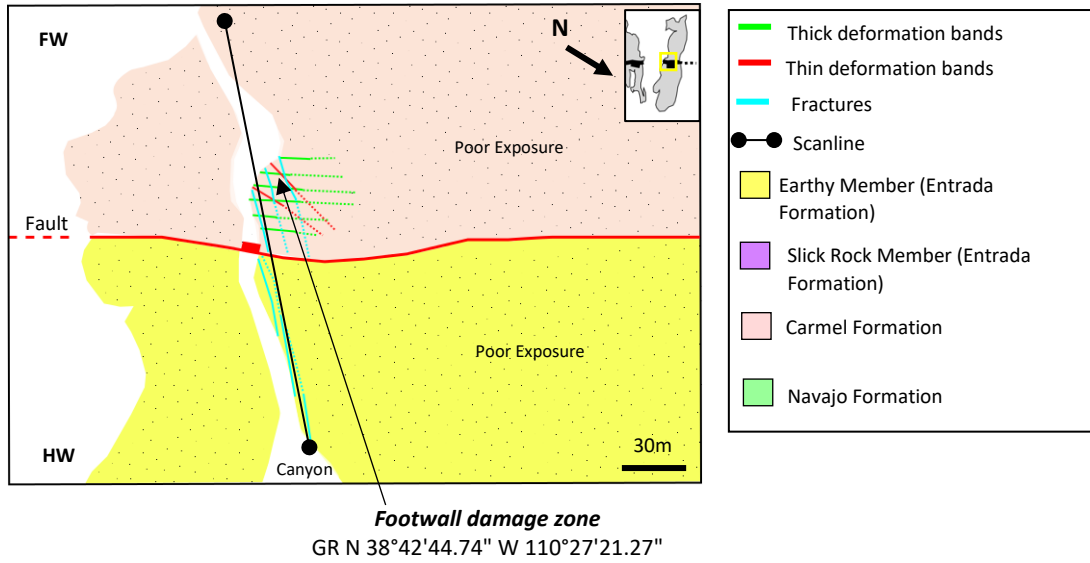
Figure 4.27 – Map of the Spider Canyon site in plan view. Open fractures, and thick and thin deformation bands are exposed in the Slick Rock Entrada in the footwall and open fractures are exposed in the Earthy Entrada in the hanging wall.

The fault zone at the Spider Canyon site is observed along the north-western edge of the canyon. Only the damage zone is exposed. The fault core (gouge) is not exposed at this locality. The footwall damage zone is composed of fractured Carmel Formation and thick and thin deformation bands, all of which increase in frequency towards the main fault trace (figure 4.28). The hanging wall damage zone is composed of fractured Earthy Entrada Formation.
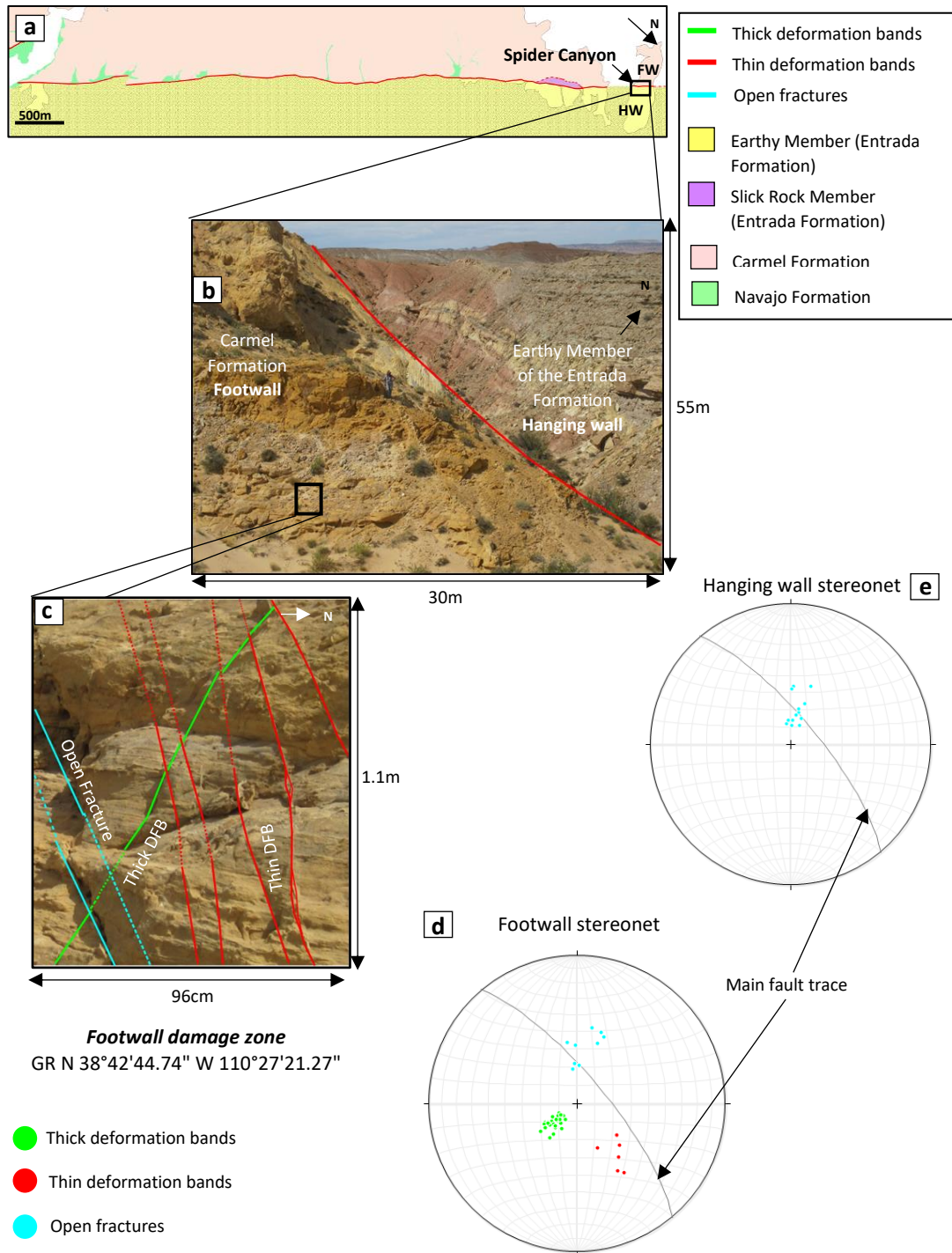
Figure 4.28 – (a) Map of Crow's Nest Fault indicating the Spider Canyon site (b) The footwall and hanging wall at Spider Canyon. (c) Photograph showing the deformation bands and fractures in the footwall. (d) and (e) are stereonets showing the deformation structures in the footwall and hanging wall.

Although Spider Canyon has an exposed high section into the footwall measuring 35m x 171m, the footwall damage zone is only exposed in the Carmel Formation as an area measuring 12m x 145m.

The hanging wall at Spider Canyon measures 106m by 202m, however most of the hanging wall is not well exposed. Hanging wall that is exposed measures 18m by 74m and is composed of fractured Earthy Entrada.
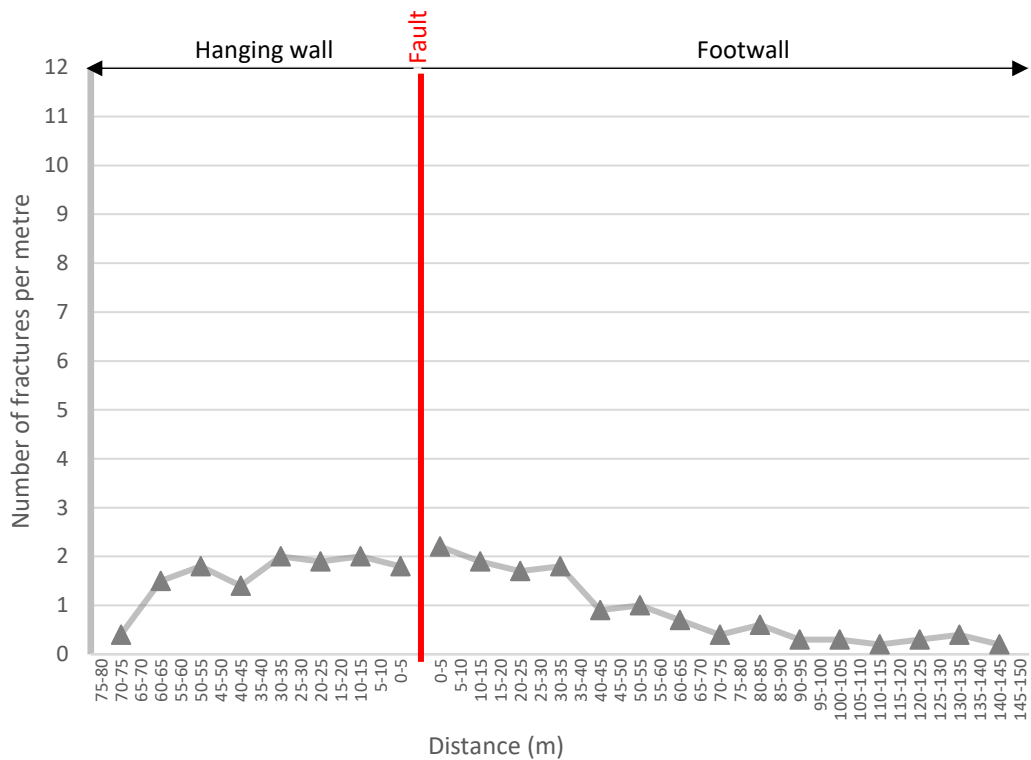
Figure 4.29 - Fracture intensity graph showing the number of fractures only slightly increasing towards the fault core at the Spider Canyon locality.

Both the hanging wall and footwall show a gradual rise in the fracture intensity, to a value of around 2 fractures per metre, as the distance to the fault decreases (figure 4.29). The fracture intensity drops to a background value of around 0.4 factures per metre at 70-75m from the fault on either side, corresponding to a damage zone width of approximately 150m. Fractures in the footwall at the Spider Canyon locality are open and unfilled, however fractures in the hanging wall have been bleached. This is discussed further in chapter 5. The rise in fracture intensity approaching the fault suggests that all fractures, both bleached and unbleached, are fault related.

4.5 Fault gouge

4.5.1 Fault gouge at Crow's Nest Fault

Where the fault is well exposed along strike, fault gouge is exposed, suggesting that fault gouge is likely continuous along strike. Fault gouge is exposed along the fault at the following localities; Cottonwood Wash, Crow's Nest Spring and Brush Valley (figure 4.30).
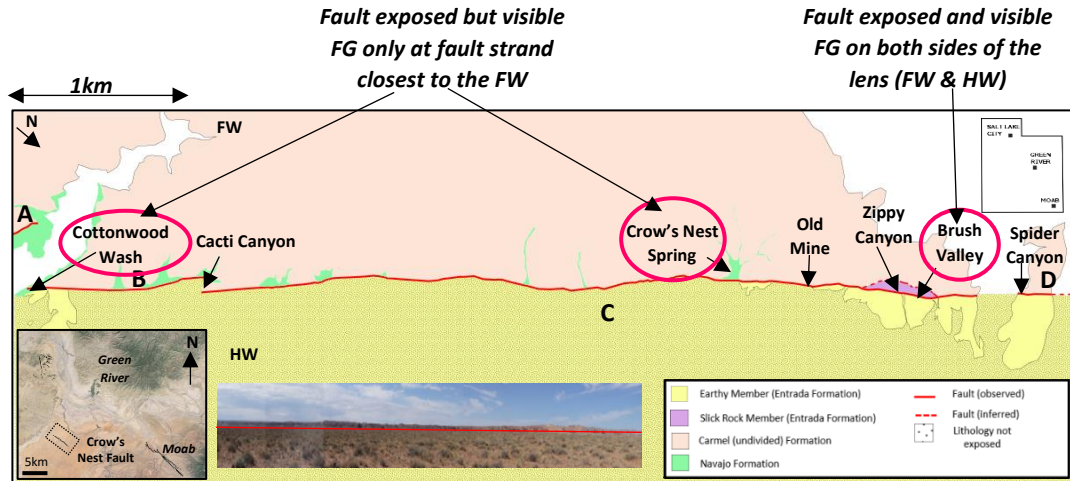
Figure 4.30 – Plan view map of the Crow's Nest Fault indicating the locations of exposed fault gouge at the Cottonwood Wash locality, the Crow's Nest Spring locality and the Brush Valley locality.

Figure 4.31 shows where the fault gouge is exposed at the Crow's Nest Fault, which fault strand it is associated with and the maximum thickness of the gouge at each exposure.
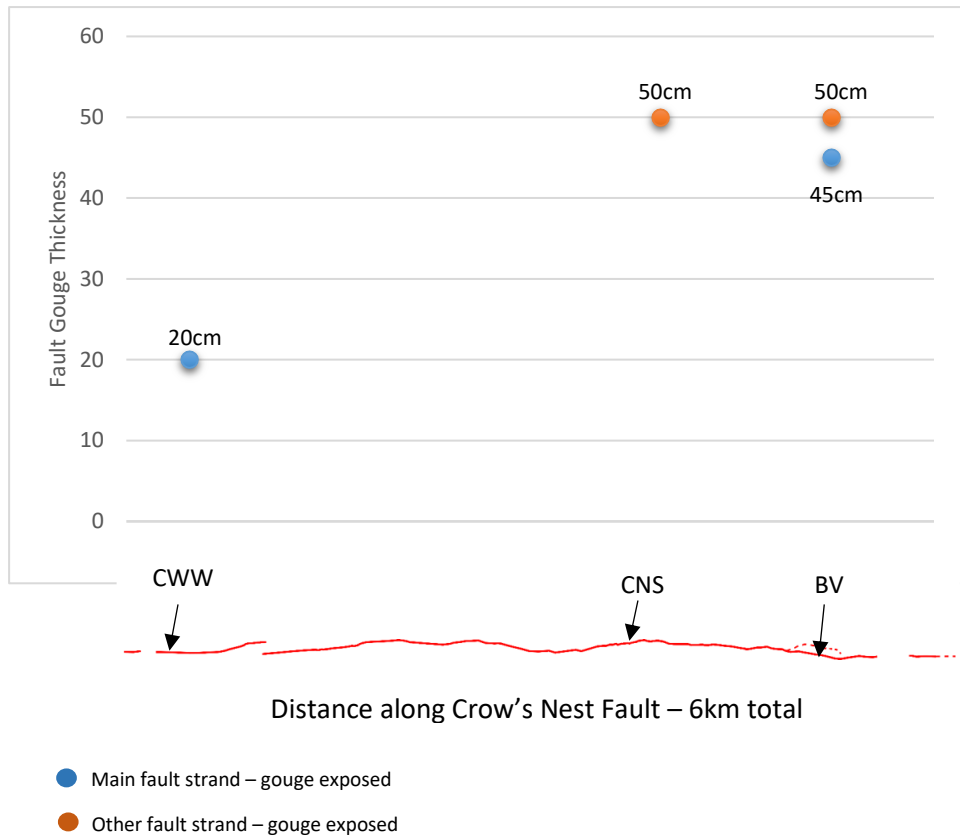
Figure 4.31 – Graph showing the maximum fault gouge thickness along strike at the Crow's Nest Fault.

At the south-easterly end of fault strand B, fault gouge is exposed at the Cottonwood Wash locality between the Carmel Formation and Navajo Formation of the footwall (figure 4.32). Gouge is highly localised and is only exposed for 1.5m along strike (figure 4.32). Gouge is made up of pink, pale yellow and brown coloured stripes which vary in thickness from 0.5cm – 4.5cm. The maximum total thickness of the fault gouge is 50cm. The gouge is brittle and contains a moderte planar fabric which is parallel to the fault.
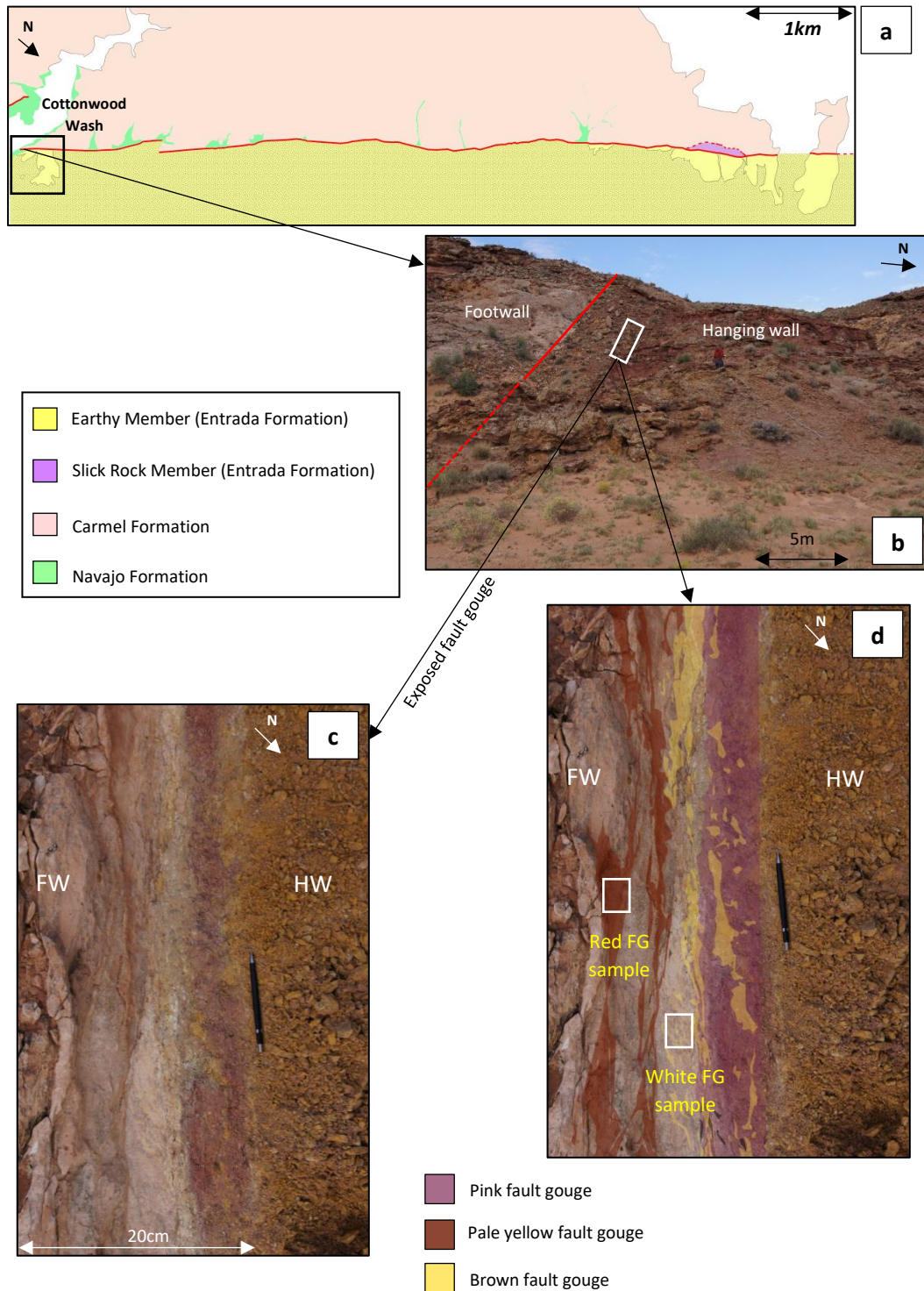
Figure 4.32 – (a) Map of the Crow's Nest Fault with the Cottonwood Wash locality indicated. (b) Photograph showing the location of the exposed fault gouge between the Navajo Formation and the Carmel Formation in the footwall. (c) Photograph of the exposed fault gouge at the Cottonwood Wash locality. (d) Annotated photograph of the exposed fault gouge shows pink, pale yellow and brown stripes of clays. The location of samples prepped for SEM are indicated.

Gouge appears hard and compacted with fine grained (0.3cm – 0.7cm) layers. Within the pink gouge, rounded quartz grains (0.5cm – 0.7cm) are held within a fine grained matrix which is too fine grained to observe in the field. Pale yellow gouge consists of rounded to sub-rounded quartz (0.4cm – 0.5cm) within a fine to very fine grained matrix. Brown gouge is more brittle then the rest of the gouge and appears to have fewer rounded quartz grains (<0.4cm) within a fine grained matrix which appears a darker shade of brown.

Samples of both the pink and pale yellow gouge from Cottonwood Wash were analysed under the SEM. The pink gouge has pockets of rounded quartz grains (0.5cm – 0.7cm) surrounded by a matrix of finer grained (20µm - 60µm) sub-angular to angular quartz, gypsum and clays such as illite (figure 4.36). The presence of illite was detected throughout the sample using EDS analysis (figure 4.33c). Throughout the sample there is evidence of cracks within quartz grains which appear parallel to the orientation of the planar larger (0.5cm – 0.7cm) pockets of quartz (figure 4.33).

The pale yellow gouge was very crumbly and less intact than the pink gouge (figure 4.34a). There are again large rounded quartz grains visible to the naked eye, which are up to 0.5cm in size. Under the SEM, the pale yellow gouge sample exhibits a fine grained matrix of sub-angular to angular illite (30µm - 70µm) and quartz grains (70µm - 90µm) with some larger (0.4cm – 0.6cm) rounded quartz grains (figure 4.34b).

From the element maps, an estimated mineral composition for the fault gouge samples is; 70% quartz, 25% illite, 3% gypsum and 2% feldspar (pink gouge) and 60% quartz, 30% illite, 6% feldspar and 4% gypsum (pale yellow gouge). The pink gouge appears to have a strong fabric of larger (0.5cm – 0.7cm) rounded quartz grains within a fine grained matrix (20µm - 60µm) dominated by sub-angular to angular quartz, gypsum and clays such as illite. In comparison, the pale yellow gouge shows a lack of a distinct fabric with a fine grained matrix of sub-angular to angular illite (30µm - 70µm) and quartz grains (70µm - 90µm) but only some larger (0.4cm – 0.6cm) rounded quartz grains present.

1.6cm

a

Fine grained clay dominated matrix

Larger, rounded quartz

b

Gypsum grains in between larger grains in the low stress pockets

c

Illite - clay in pockets, same orientation as large quartz pockets.

Cracks appear parallel to the orientation of the pockets of low stress/larger and rounded grains (Quartz)
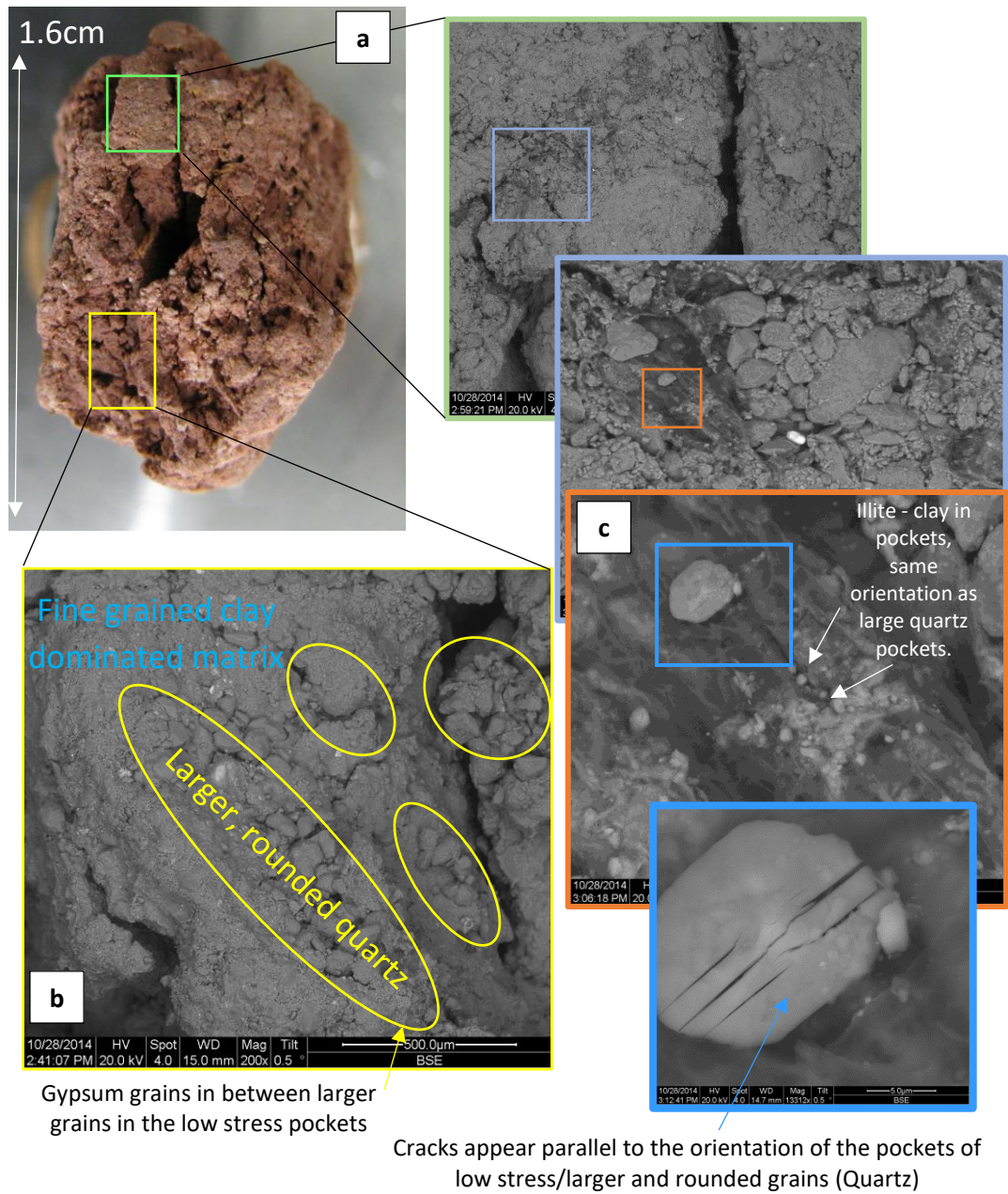
Figure 4.33– (a) Sample of the pink fault gouge at the Cottonwood Wash locality prepared for SEM analysis. (b) Under SEM the gouge shows evidence for pockets of rounded quartz grains up to 0.7cm in size within a fine grained matrix of illite, feldspars and gypsum. (c) Quartz grains show evidence of cracks which appear perpendicular to the pockets of quartz.
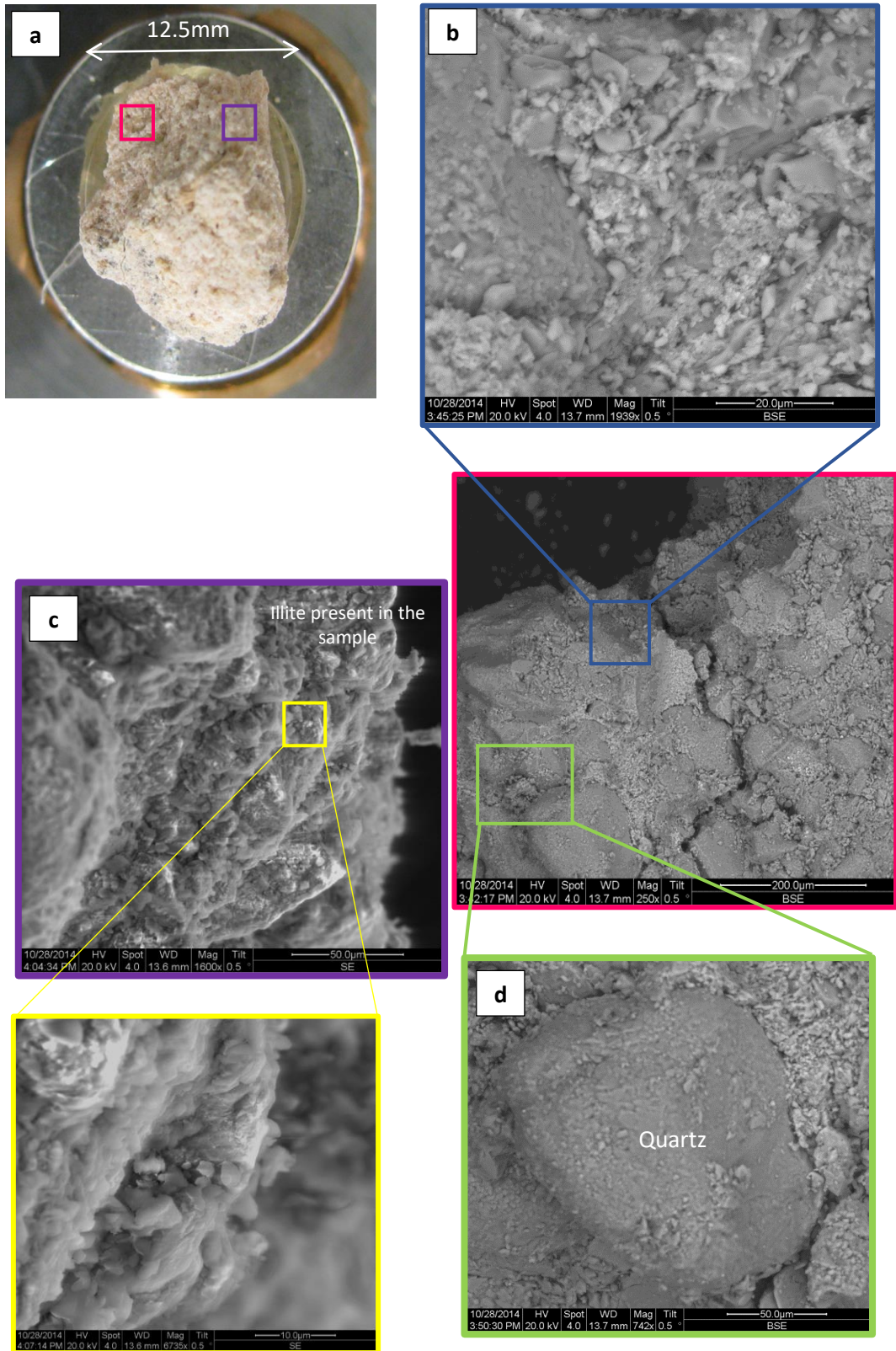
Figure 4.34– (a) Sample of the pale yellow fault gouge at the Cottonwood Wash locality prepared for SEM analysis. (b) Under the SEM there is evidence for rounded quartz grains within fine grained matrix. (c) Illite present in the sample and quartz. (d) Quartz appears rounded under SEM.

3km south-east from the end of fault strand C and in the centre of the fault strand, fault gouge is exposed at the Crow's Nest Spring locality (figure 4.35). Fault gouge is exposed twice between the Navajo Formation in the footwall and the Carmel Formation in the lens.

Fault gouge is exposed continuously for 12m along strike but is only accessible for 6m (figure 4.35c). Fault gouge is exposed in two separate exposures which are 1m in width apart, however the most south-easterly fault gouge is not accessible to sample.

Gouge appears hard and compact, is orange and grey and varies in thickness from 2cm to 50cm. The gouge contains a weak planar fabric which is parallel to the fault and consistent with the orientation of thick deformation bands observed elsewhere in the field area. Gouge is very fine grained and too small to measure with the naked eye.
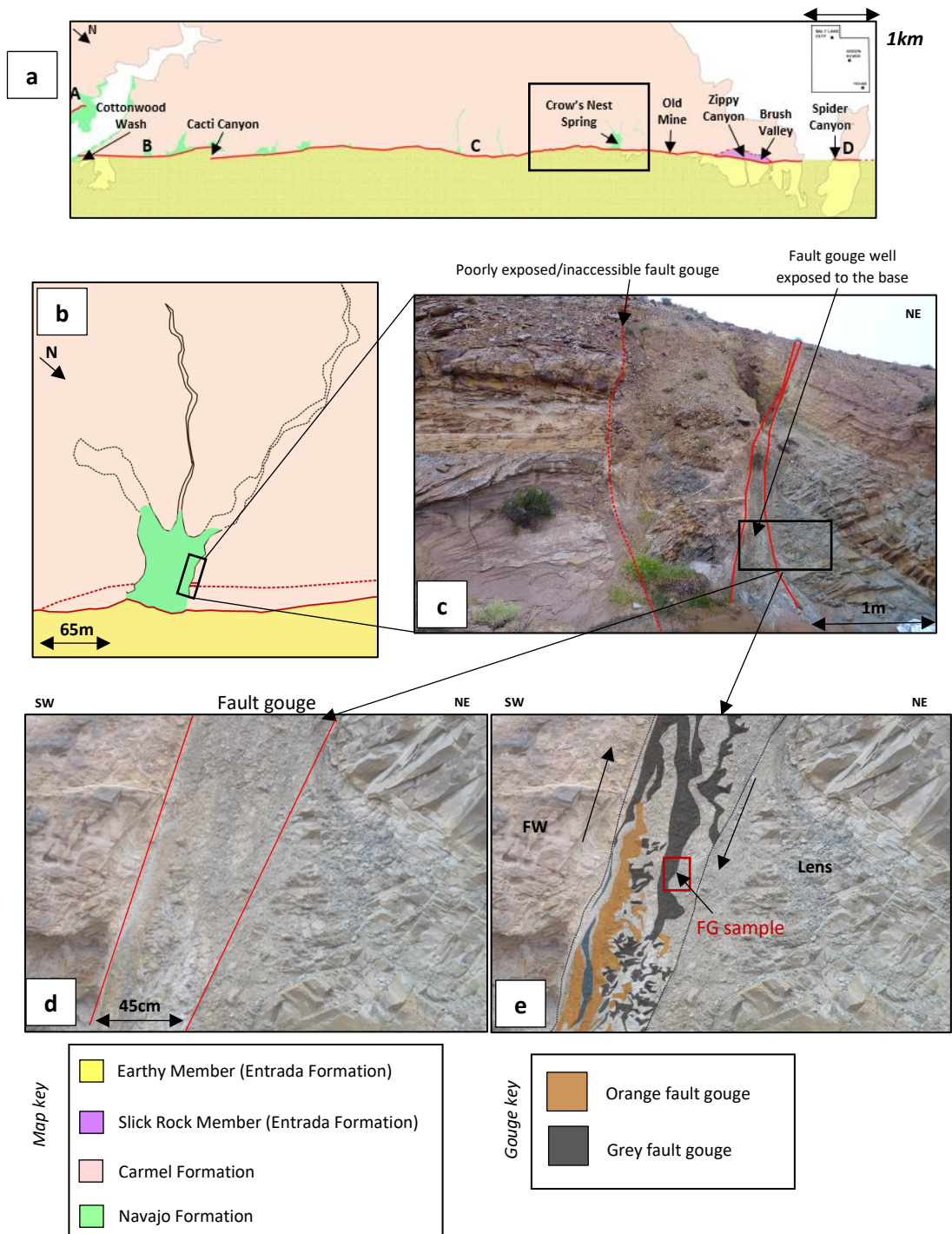
Figure 4.35 – (a) Map of the Crow's Nest Fault with the Crow's Nest Spring locality indicated. (b) Schematic plan view cartoon of the Crow's Nest Soring locality, a canyon which dissects the fault. (c) Photograph showing the location of the exposed fault gouge in the Navajo Formation of the lens (d) Photograph of the exposed fault gouge at the Crow's Nest Spring locality. (e) Annotated photograph of the exposed fault gouge shows tan/orange and grey stripes of clay. The location of the sample prepped for SEM analysis is indicated.

Samples of orange and grey gouge were analysed under the SEM. Orange gouge is dominated by a mostly larger (50-100μm) rounded quartz mineralogy within a finer grained (10-20μm) sub-angular to angular matrix dominated by illite, quartz and feldspar (figure 4.36). The presence of illite was detected throughout the sample using EDS analysis. Grains in both the orange and grey gouge are poorly sorted and there is no strong fabric present, although a weak linear fabric was observed in outcrop.

From the use of element maps, a best estimation of the mineral composition for both fault gouge samples was made; 75% quartz, 20% illite, and 5% feldspar (orange gouge) and 55% quartz, 40% illite, and 5% feldspar (grey gouge).
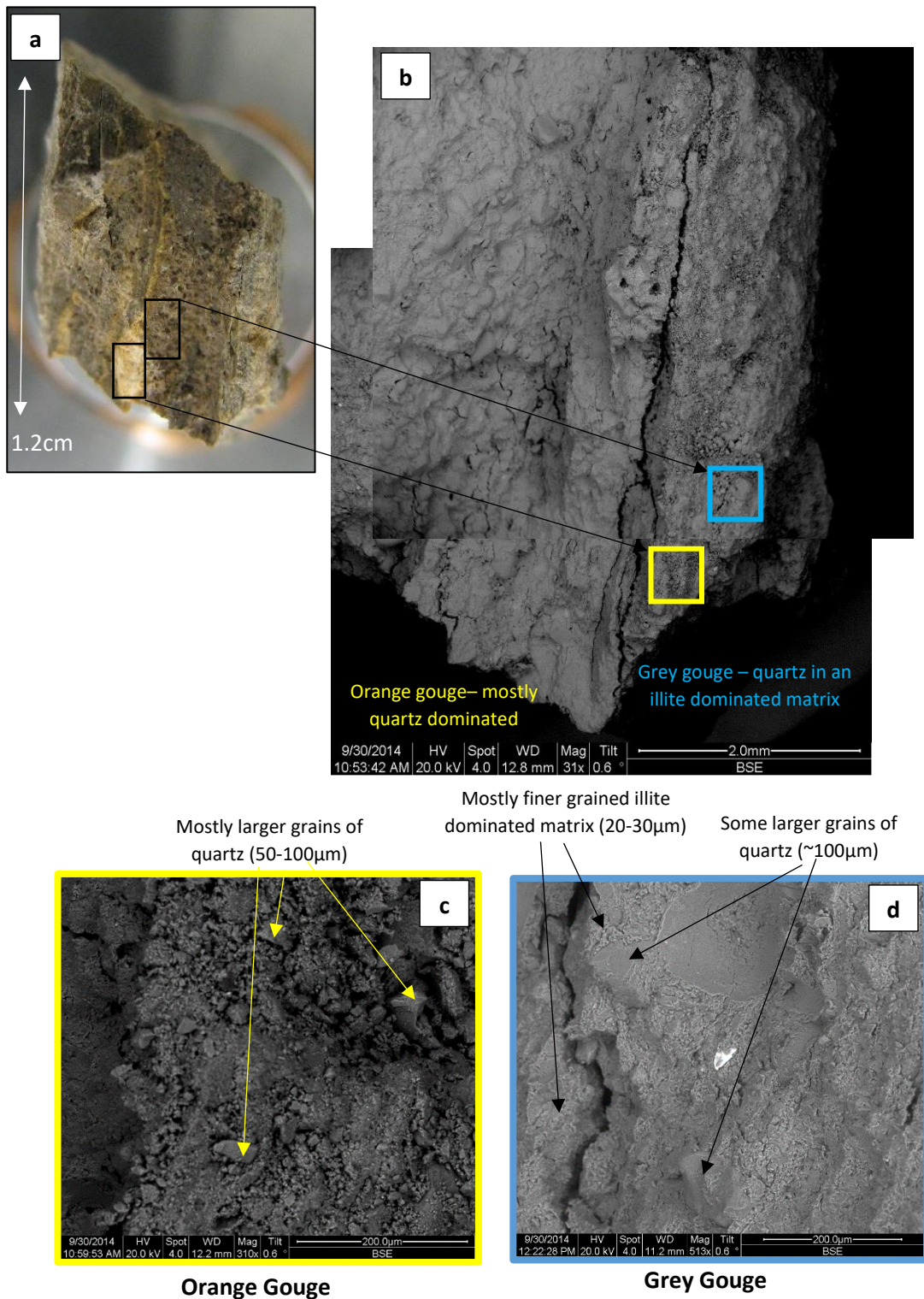
Figure 4.36 – (a) Sample of fault gouge from the Crow's Nest Spring locality prepared for SEM analysis. (b) SEM micrograph showing the orange and grey gouge. (c) Orange gouge is dominated by a quartz rich mineralogy (50-100µm) with an illite and quartz matrix whereas grey gouge (d) tend to be dominated by a fine grained illite and quartz rich matrix (20-30µm) with some larger (~100µm) quartz grains.

At the most north-westerly end of fault strand C, fault gouge is exposed at the Brush Valley locality in two locations; cutting the Slick Rock Entrada within the lens and the Earthy Entrada in the hanging wall and dividing the Slick Rock Entrada in the lens from the Carmel Formation in the footwall (figure 4.37). The fault is well exposed at this site, however the north-eastern part of the lens is a steep cliff face and not accessible. Where gouge is exposed and accessible, it is continuous along strike for 2m.

Both exposed fault gouge is made up of light grey and dark grey coloured stripes which vary in thickness from 0.4cm – 3cm. The maximum total thickness of the fault gouge is 50cm where gouge divides the lens from the hanging wall and 45cm where the gouge divides the lens from the footwall. The gouge contains a moderate linear fabric which is parallel to the fault and the darkest gouge appears concentrated more in the centre.

Gouge appears brittle and powdery and the light gouge appears altered/bleached. Light grey gouge consists of sub-rounded quartz (0.3cm – 0.5cm) in a fine grained dark matrix (<0.2cm), dark grey gouge appears very fine grained with some larger sub-rounded quartz present (~0.4cm). Light and dark gouge indicates a linear texture with dark gouge mostly in the centre of the gouge (figure 4.38).
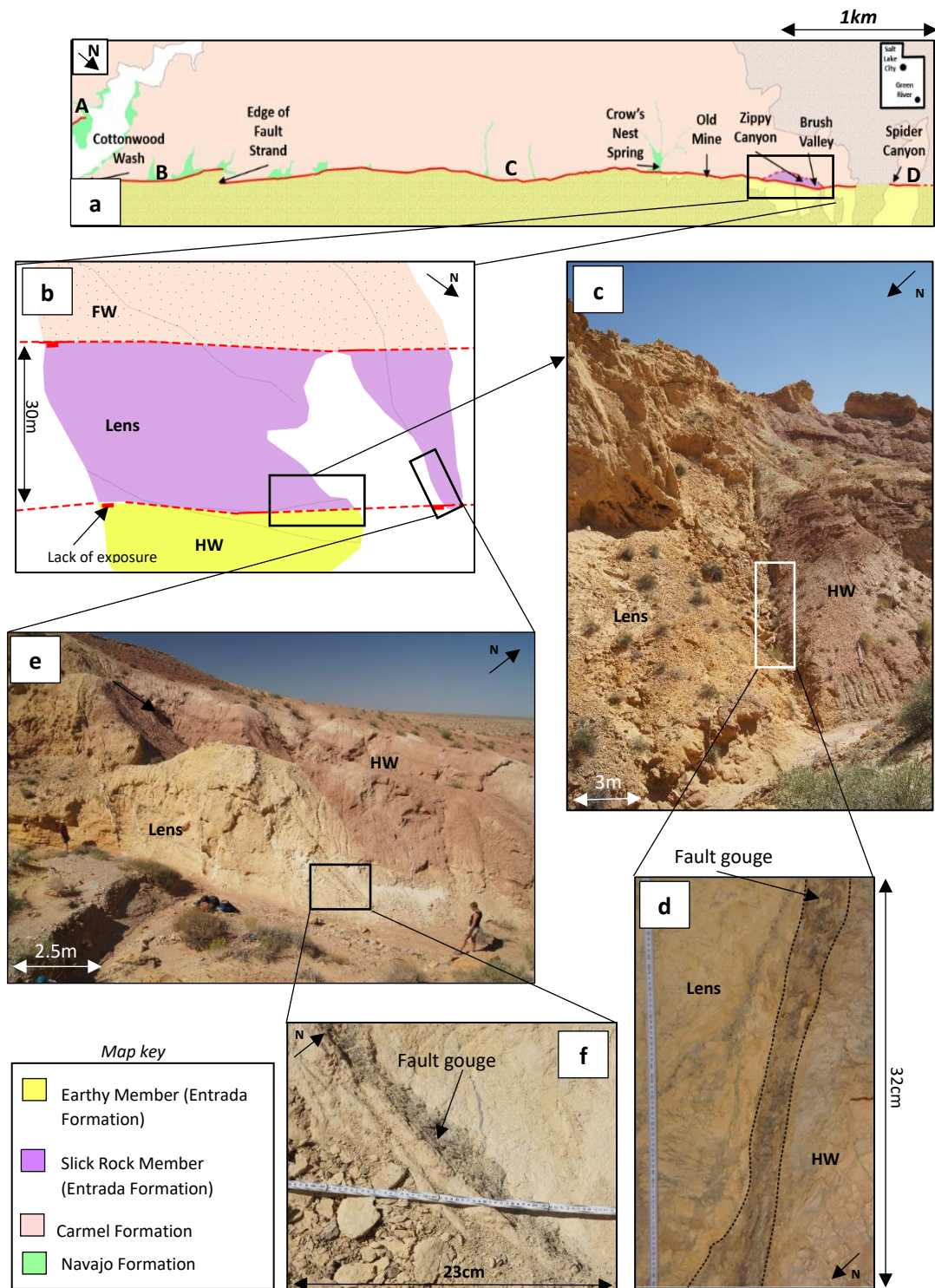
Figure 4.37 – (a) Map of the Crow's Nest Fault indicating the Bush Valley locality. (b) Plan view cartoon map of the Brush Valley locality. (c) Photograph indicating the location of the fault gouge within the lens and (d) and up close photograph of the exposed fault gouge. (e) Photograph indicating the location of the fault gouge at the edge of the lens and (f) an up close photograph of the exposed fault gouge.
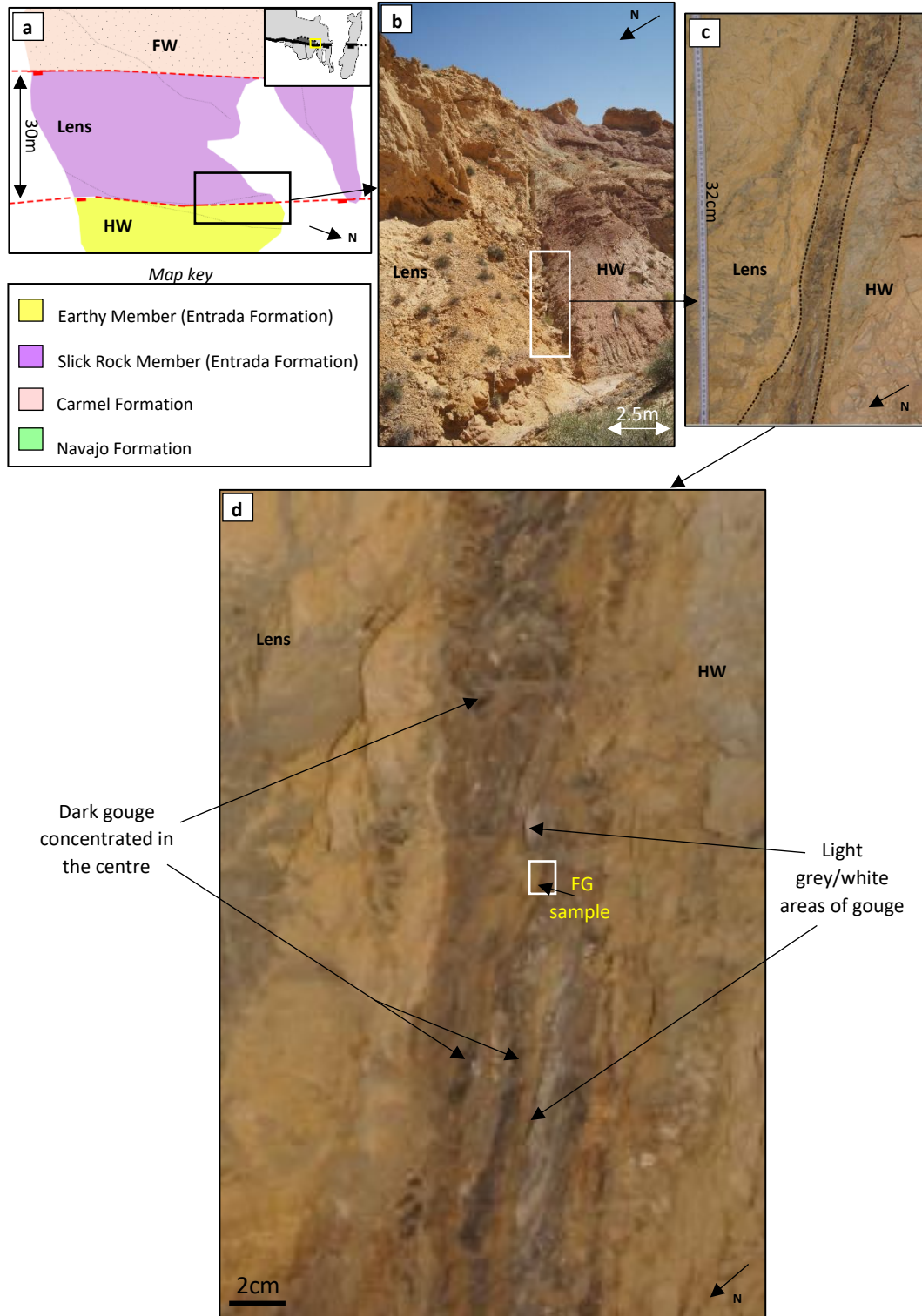
Figure 4.38 – (a) Map of the Brush Valley locality where fault gouge is exposed (b), (c). Fault gouge consists of dark grey and light grey/white stripes of gouge which appears brittle and powdery (d). The location where the sample of fault gouge was extracted is indicated in (d).

At the Brush Valley locality, samples of the light grey and dark grey fault gouge were analysed under the SEM. Light gouge is powdery and soft, consisting of pockets of rounded quartz grains (100-150μm) surrounded by a fine grained matrix (10-40μm) of illite, feldspar, quartz and gypsum (figure 4.39).
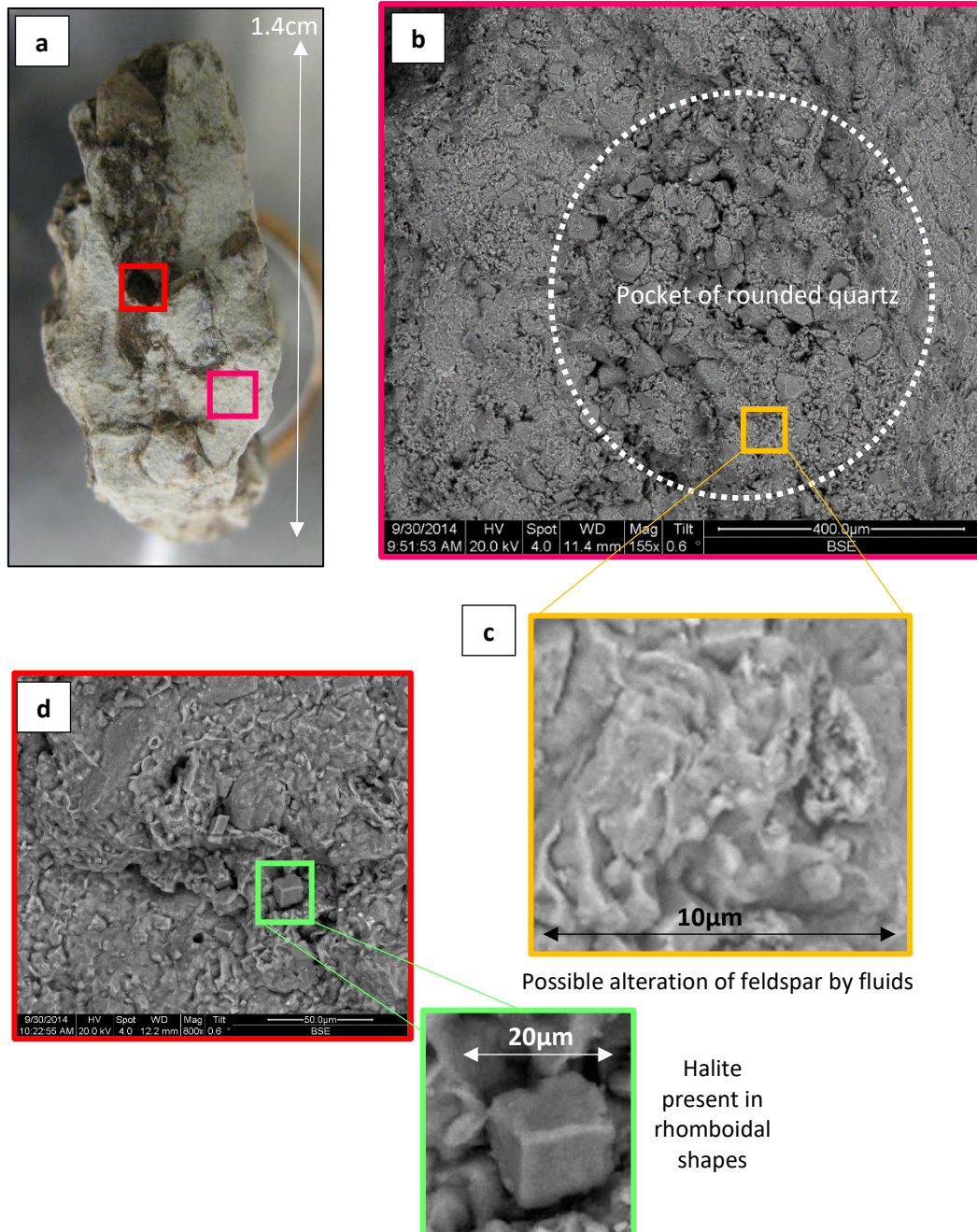
Figure 4.39- (a) Sample of fault gouge at the Brush Valley locality prepared for SEM analysis. (b) Lighter grey gouge analysed and (c) shows possible alteration of feldspar by fluids. (d) Analysis of the dark grey gouge showing halite present in rhomboidal shapes.

The feldspar in the matrix appears altered by comparison to unaltered feldspar which generally displays characteristic striations and conchoidal cleavage (Zhu et al. 2006, figure 4.40). This could be as a result of fluid interacting with the light grey gouge, entering through the higher porosity areas within the rounded pockets of quartz.
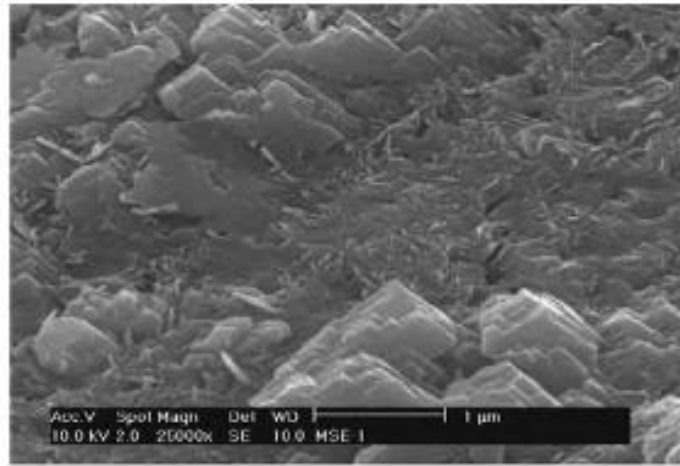
Figure 4.40 – Photomicrograph of K-feldspar from the Navajo Formation, Black Mesa, Arizona which shows prominent, characteristic cleavage which is not observed in the K-feldspar in the Brush Valley fault gouge (Zhu et al., 2006).

To determine whether there were any fluid events associated with the fault gouge, cathodoluminescence (CL) could be used. CL works by reflecting differences in trace element compositions, for example Fe or Ca of fluids which have precipitated and this process may also determine if there are varying growth rates for different minerals. This is discussed further in Chapter 7.

The dark grey gouge is made up of a fine grained matrix (<10µm) dominated by illite, feldspar, quartz and gypsum. Within the matrix, larger (20-30µm) rhomboidal calcite crystals are observed, that show no evidence of grain crushing or micro fracturing. This suggests they are likely to be post-faulting, as otherwise they would have experienced cataclasis. Similar, rhomboidal calcite crystals have been observed infilling stylolites in the damage zone of the Pirgaki Fault Zone, Greece and are thought to be as a result of a change in fluid composition, likely caused by episodic fluid flow along the fault zone (Géraud et al., 2006).

From the use of element maps, a best estimation of the mineral composition for both fault gouge samples was made; 60% quartz, 20% illite, 15% feldspar and 5% gypsum (light grey gouge) and 40% quartz, 30% illite, 20% calcite and 10% feldspar (pale yellow gouge).

4.5.2 Interpretation of fault gouge and comparison to elsewhere

Fault gouge mineralogy at the Crow's Nest Fault is dominated by quartz (~60-75%) and illite (~20-25%) with minor feldspar (~2-10%), calcite (~20%) and gypsum (~4-5%). Grain size ranges from 10µm to 0.6cm. Gouge is typically dominated by rounded to sub-rounded quartz within a fine grained clay matrix and minor feldspar, calcite and gypsum.

In outcrop, gouge tends to show a weak to moderate planar fabric. Under the SEM, the dominant fabric is areas of rounded quartz within a fine-grained matrix. When sheared, quartz rich gouge tends to result in intense cataclasis and grain size reduction. However, clays are able to promote the preservation of larger quartz grains; in gouge which has 30-40% clays present, clay matrix tends to take up most of the shear strain by slipping between the quartz grains (Crawford et al., 2008).

Increasing clay content typically results in a sharp decrease in permeability (Manzocchi et al., 1999). However, studies of clay gouge content and permeability by Crawford et al., (2008) indicated that the lowest permeability within a fault gouge is at 30-40% clay content (figure 4.41). It is thought that solution-precipitation processes are responsible for this reduction in permeability (Nakatani and Scholz, 2004).
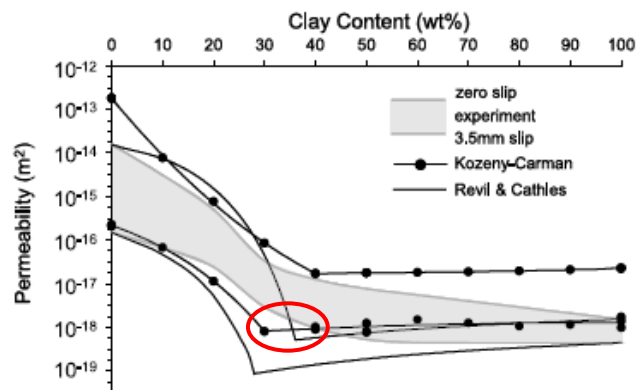
Figure 4.41 – With increasing clay content within a fault gouge, the permeability will decrease. However, the lowest permeabilities are usually in fault gouge with a clay content of 30-40% (Crawford et al., 2008).

Clay content of fault gouge at the Crow's Nest Fault is estimated to be 20-25% which would suggest a low permeability in the range of $10^{-17}m^2$ based on figure 4.41.

Engelder, (1974) stated that the primary cause for the formation of a quartz dominated fault gouge is due to cataclasis. Gouge at the Crow's Nest Fault is dominated by cataclasis, however there is evidence of post deformational mineralisation at Brush Valley (dark grey) gouge. The presence of rhomboidal calcite in the light grey gouge must be post deformational because cataclasis would not permit the preservation of such euhedral crystals.

The presence of altered feldspar alongside rhomboidal calcite suggests that diagenesis has occurred in the fault gouge at Brush Valley. The gouge at the Brush Valley locality is striped with light and grey layers which both show evidence of diagenesis. This suggests that the gouge between the lens and hanging wall could have behaved as a baffle to fluid flow; the presence of post-faulting calcite growth indicate the fault may have behaved as a conduit to flow, however the presence of clays indicate the fault behaved as a barrier to flow.

There is a lack of evidence for diagenesis in the fault gouge at the Cottonwood Wash and Crow's Nest Spring locations, however, the presence of high porosity pockets of rounded quartz grains could have the potential to allow fluid flow within the gouge if they became interconnected through fracturing or a further slip event.

In the pink gouge at the Cottonwood Wash locality there is evidence of fractured quartz grains perpendicular to the orientation of the pockets of rounded quartz. The orientation of micro-fracturing in quartz dominated gouge is thought to give an indication for the orientation of the stress field that the gouge formed in (Engelder, 1974). However, to infer the orientation, the sample needs to be orientated, which was not possible at the Crow's Nest Fault. However, if micro-fracturing happened early on and then grain rotation happened through shearing, then this could have opened up a pathway for fluid connectivity.

One striking difference between the Brush Valley, Crow's Nest Spring and Cottonwood Wash localities is the visible presence of hydrocarbons (see Chapter 5). The Brush Valley and Crow's Nest Spring localities have hydrocarbons present at the surface but the Cottonwood Wash locality does not. The fault gouge at the Brush Valley and Crow's Nest Spring localities is dark grey whereas the fault gouge at the Cottonwood Wash locality is pink and pale yellow. This suggests that the grey colouration of the gouge at the Brush Valley and Crow's Nest Spring localities could be due to the presence of hydrocarbons.

Unfortunately, due to the carbon coating of the thin section slides, it was not possible to accurately detect any difference between carbon content between the fault gouge at the different sites.

The fault gouge characteristics at the Crow's Nest Fault are similar to those reported for other faults in Utah. For example, fault gouge at the Big Hole Fault is intermittent and highly localised along a major slip surface, is pale yellow and pink, and is also associated with locations with a high concentration of deformation bands (Shipton and Cowie, 2003). However, fault gouge at the Big Hole Fault has negligible clay content and the fault is self-juxtaposed.

Gouge at the Crow's Nest Spring site is continuous along strike between the footwall and lens but although the fault is well exposed, there is an absence of gouge between the lens and hanging wall. Gouge at the Big Hole Fault is highly localised and varies in thickness from 2cm to 50cm which is the same as that seen at the Crow's Nest Spring fault gouge.

Fault gouge at the Big Hole Fault is always associated with mineralisation and is powdery to the touch. The presence of iron oxides and calcite within the gouge suggests that the fault gouge may have acted as a conduit to fluid flow. In comparison, the fault gouge at the Crow's Nest Spring site shows no indication of mineralisation and instead, contains ~20% illite which suggests it more likely acted as a barrier or baffle to flow.

At the Yellow Cat Graben, fault gouge is formed where the low porosity (~9%) Slick Rock Entrada Formation in the footwall is juxtaposed against the higher porosity (21-23%) overlying Moab Tongue Entrada Formation in the hanging wall (Bright, 2006). The resulting fault gouge is continuous along the length of the fault. The Slick Rock Entrada has deformed mostly by fractures and the Moab Tongue is dominated by deformation bands. It is suggested that the occurrence of fault gouge is related to a change in deformation style in the low porosity Slick Rock Entrada.

Host rock and deformation style at the Brush Valley lens site is similar to that observed at Yellow Cat. At the Brush Valley site, fault gouge is formed where the high porosity (~30%) Slick Rock Entrada is juxtaposed against the low porosity (~10-15%) Earthy Entrada. There are both deformation bands and fractures in the Slick Rock Entrada, but the dominant mechanism appears to be through deformation banding. The Earthy Entrada is deformed by fracturing only.

At both the Yellow Cat Graben and Crow's Nest Fault, there appears to be a relationship between host rock lithology and how strain is accommodated. Within the literature there have been many studies which have looked at this relationship including; Dunn et al., (1973) and Wong et al., (1997). These studies have estimated that porosity can control how a rock deforms; deformation by banding tends to occur in rocks of >15% porosity and rocks <15% porosity will preferentially deform by fracturing.

Fault gouge at the Crow's Nest Fault is rich in illite (~20%). However, the surrounding protolith/damage zone contains ~10-15% less clay then the fault gouge. This suggests that the clay within the fault gouge could not have formed entirely through mechanical incorporation of the protolith (Solum et al., 2005). For clays to have formed, there must either have been an element of fault authigenesis, or the clay could have come from the layers that have been dragged past, for example clays in the Slick Rock Entrada and Carmel Formation. Fault gouge at the Big Hole Fault and Yellow Cat Graben have negligible clay content and the faults are self-juxtaposed.

Fault gouge at the Moab Fault in Utah is more enriched in illite (~40%) than the Crow's Nest Fault relative to the % of clays within the protolith/damage zone (Solum et al., 2005). It is thought that the percentage of clays present within a fault gouge is related to the percentage of mudstone the sequence is moving past. For example, shale rich gouge is present when a sequence moves past which has >c.20% of mudstone present (Foxford et al., 1998).

At the Crow's Nest Fault, the fault gouge cuts through the Navajo Formation, Carmel Formation and the Entrada Formation. Of these unaltered protoliths, only the Entrada Formation and Carmel Formation have any significant clay content present. However, the assumption that the percentage of clay content in the gouge directly corresponds to an average clay content within the host rock would assume homogenous mixing and no diagenesis of the displaced rock units. Therefore the variations in clay content between the fault gouge at the Moab Fault and at the Crow's Nest Fault can be attributed to heterogeneous mixing and diagenesis, both of which are difficult to predict.

The Moab Fault juxtaposes the Moab Tongue Sandstone against the Honaker Trail Formation, a mudstone and sandstone mix. In comparison, the Crow's Nest Fault juxtaposes mostly 'clean' sandstones and sandstones with minor siltstones and limestones present.

Fault gouge at the Crow's Nest Fault has stripes of darker, more clay rich material. The presence of stripes is unusual and not commonly seen in faults. The clay rich stripes appear to be fault parallel suggesting that the Crow's Nest Fault behaved as a barrier to across fault flow.

4.6 Distribution and timing of deformation structures

4.6.1 Orientations of deformation structures

Orientations of the deformation structures were measured everywhere along the fault that were well exposed and accessible. Most of the deformation bands in the damage zone are either sub-parallel or perpendicular to the fault strands and have the same strike. The modal dip of thick deformation bands falls between 35° – 40° (figure 4.42a) and the modal dip of thin deformation bands also falls between 35° – 40° (figure 4.42b).
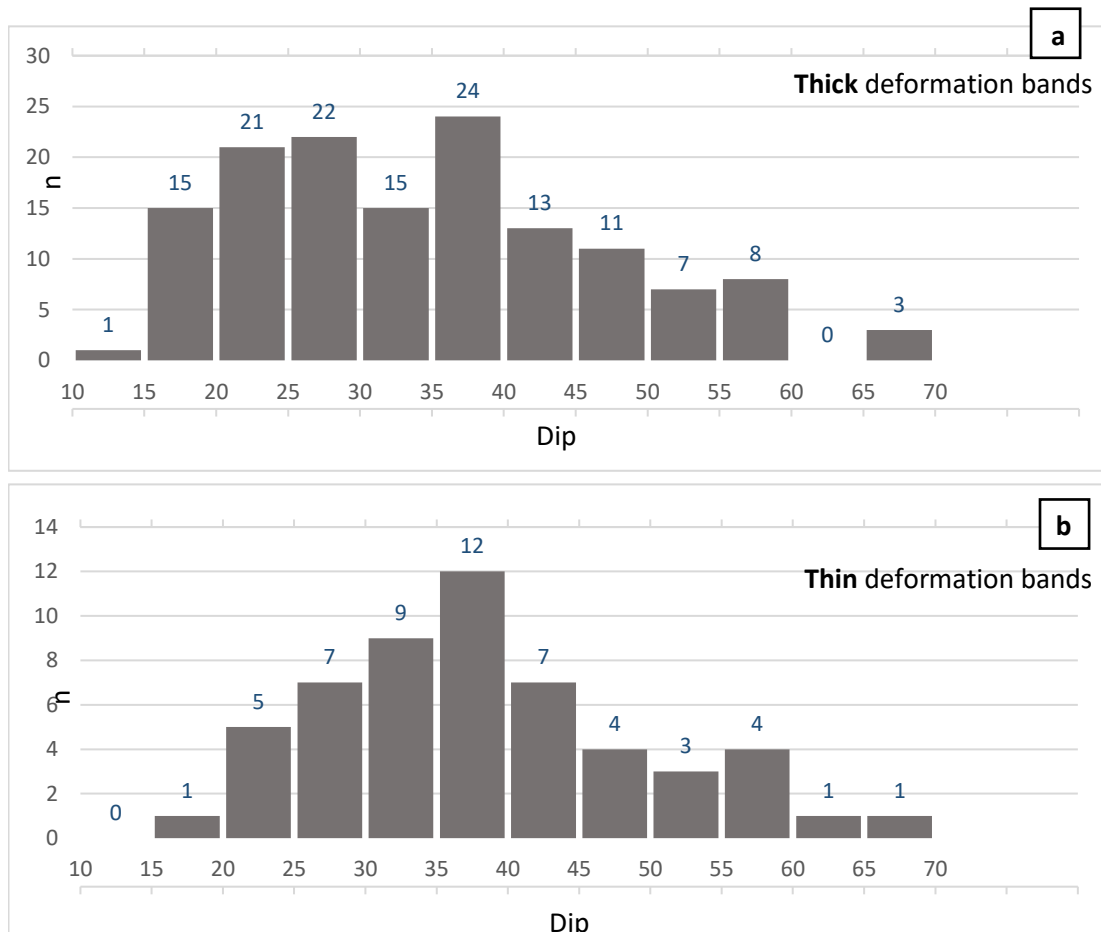
Figure 4.42 – Distribution of the dip of deformation structures at Crow's Nest Fault; (a) Thick deformation bands have a mean dip of 34.2° and (b) Thin deformation bands have a mean dip of 38.3°

Figure 4.43 shows stereonets of both the thick and thin deformation bands, with those from the lens at Brush Valley plotted separately from the hanging and footwall in each case. The thick deformation bands strike sub-parallel to the fault and have a mean dip for all measured bands (in the footwall, Brush Valley lens and hanging wall combined) of 34° taken from a total of 140 bands (figure 4.43a). In the hanging wall the mean dip is 34° and in the footwall the mean dip is 29° compared to a steeper mean dip of 39° in the Brush Valley lens.

The strike of the thin deformation bands is almost perpendicular to the fault (and to the thick deformation bands). They have a mean dip for all measured thin deformation bands of 38°, in the footwall, Brush Valley lens and hanging wall combined, with a total of 54 bands measured (figure 4.43b). In the hanging wall the mean dip is 35° and in the footwall the mean dip is 37° compared to a slightly steeper mean dip of 42° in the Brush Valley lens.

Iron-rich fractures are only found at the Brush Valley site and have a mean dip of 38.8^o north-east (figure 4.44a). Iron-rich fractures strike sub-parallel to the fault, similar to thick deformation bands and dip slightly steeper than the thick deformation bands. Iron-rich fractures dip roughly the same as thin deformation bands but strike perpendicular to the fault and to the thick deformation bands.

Open fractures in the footwall and hanging wall are on average orientated perpendicular to the thick deformation bands and the main fault trace with a mean dip of 44° to the south and strike towards the west from a measured sample of 181 fractures. In the lens, fractures dip more steeply to the south-east with a mean dip of 48° (figure 4.44b). In the hanging wall, open fractures dip on average 44° and strike 116 to the south-west compared to in the footwall where open fractures dip on average 42° and strike 65 to the south-east.
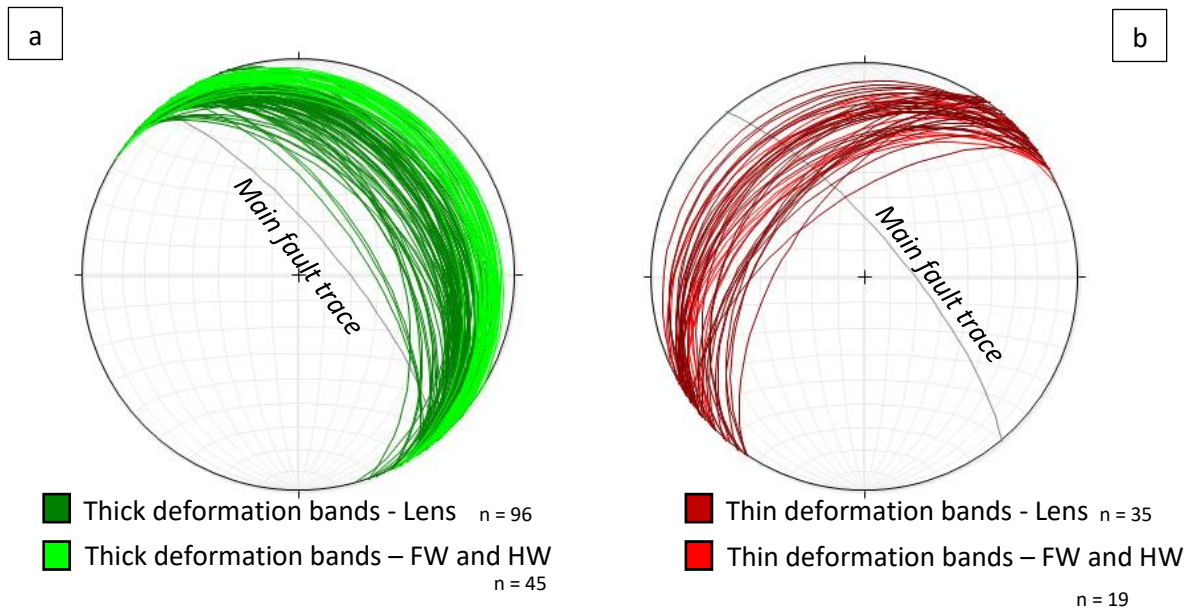
Figure 4.43 (a) Stereonet showing the difference in dip/dip direction for thick deformation bands in the lens compared with the footwall and hanging wall. (b) Stereonet showing the difference in dip/dip direction for thin deformation bands in the lens compared with the footwall and hanging wall.
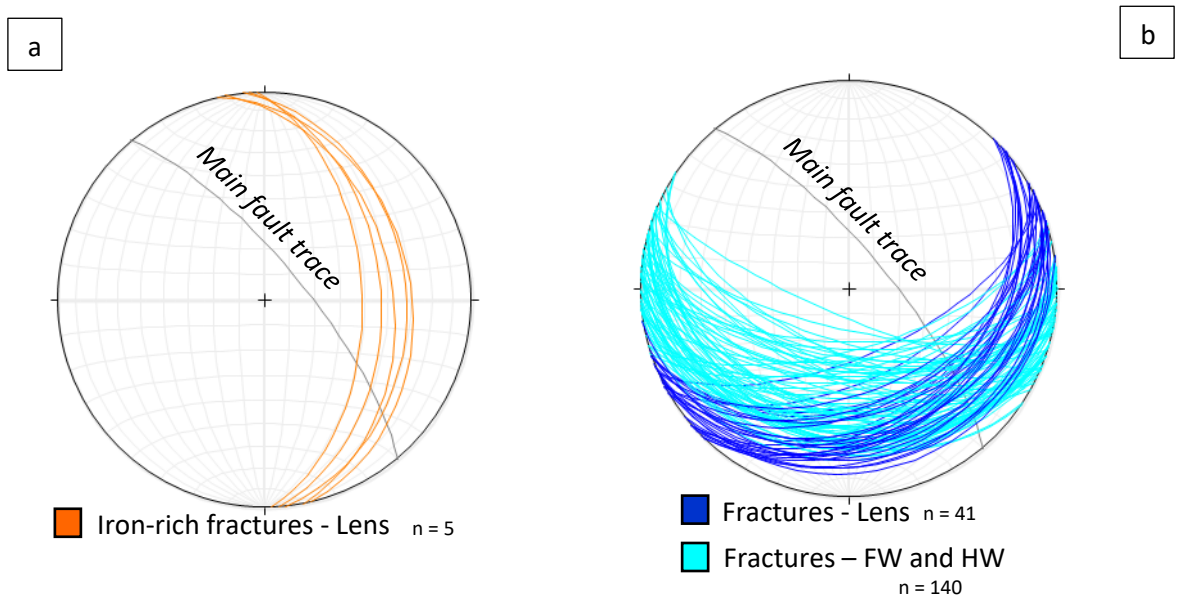
Figure 4.44 (a) Stereonet showing the dip/dip direction for iron-rich fractures in the lens at the Brush Valley location. (b) Stereonet showing the difference in dip/dip direction for unfilled fractures in the lens compared with the footwall and hanging wall.

4.6.2 Relative timing of deformation structures

Relative timing of deformation structures in the damage zone has been constrained by cross-cutting relations both in the field and microscopically. This enables a chronology of deformation to be established.

Thick deformation bands are overprinted by thin deformation bands in the field and so represent the oldest deformation structures present. Field cross cutting relationships show that thin deformation bands are overprinted by iron-rich fractures. Iron-rich fractures are only present in small numbers at the Brush Valley location (figure 4.45). Fractures that are not filled with iron are the youngest deformation structures present in the field area. These fractures are perpendicular to the fault and are exposed in the hanging wall, footwall and lens. This evidence is consistent with fracturing postdating deformation bands in this region as seen at the nearby Moab Fault and Big Hole Fault (Davaztes and Aydin, 2003; Shipton and Cowie, 2003; Johansen et al., 2005).
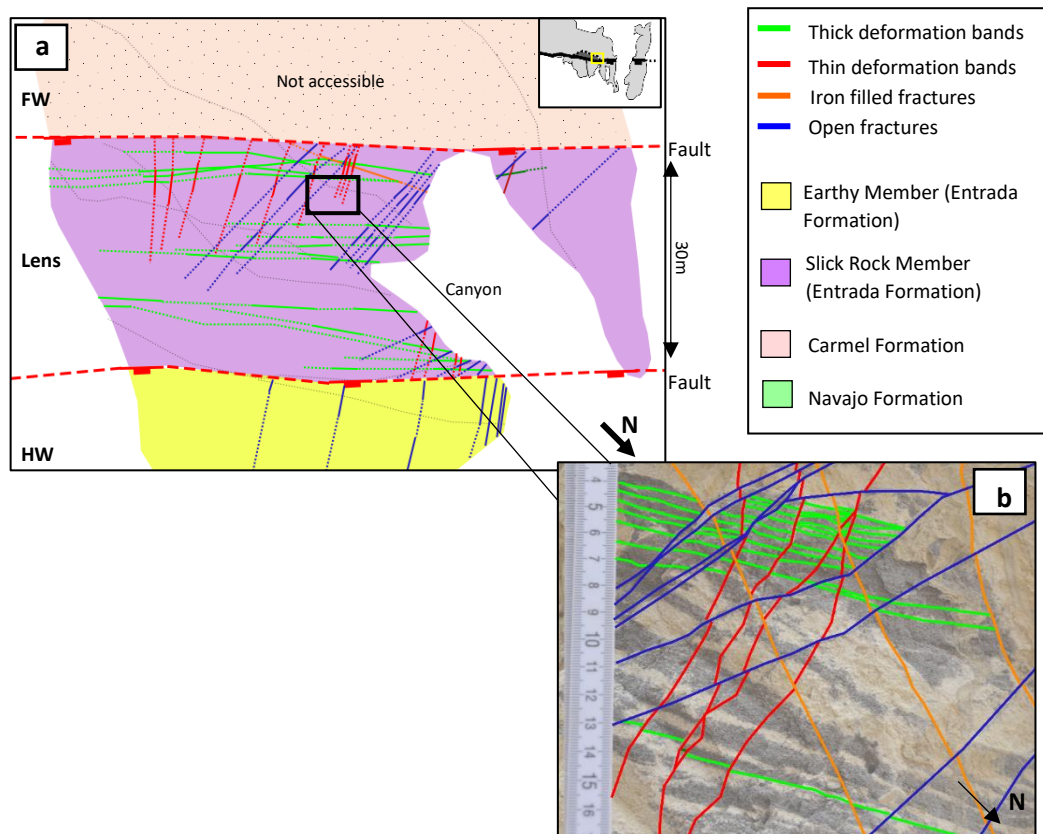
Figure 4.45 – (a) Plan view map of the Brush Valley site and (b) shows the cross cutting relationships of the deformation structures present within the lens.

4.6.3 Frequency and distribution of deformation structures

Thick deformation band intensity is highest within the lens or close to the fault (e.g. at the Cottonwood Wash site which is within the footwall) and decreases in the footwall away from the Brush Valley lens (figure 4.46). The Cottonwood Wash site is the only location where thick deformation bands are found in the hanging wall; only one thick deformation band is exposed at Cottonwood Wash in a total exposed hanging wall measuring 115m x 57m (table 3).
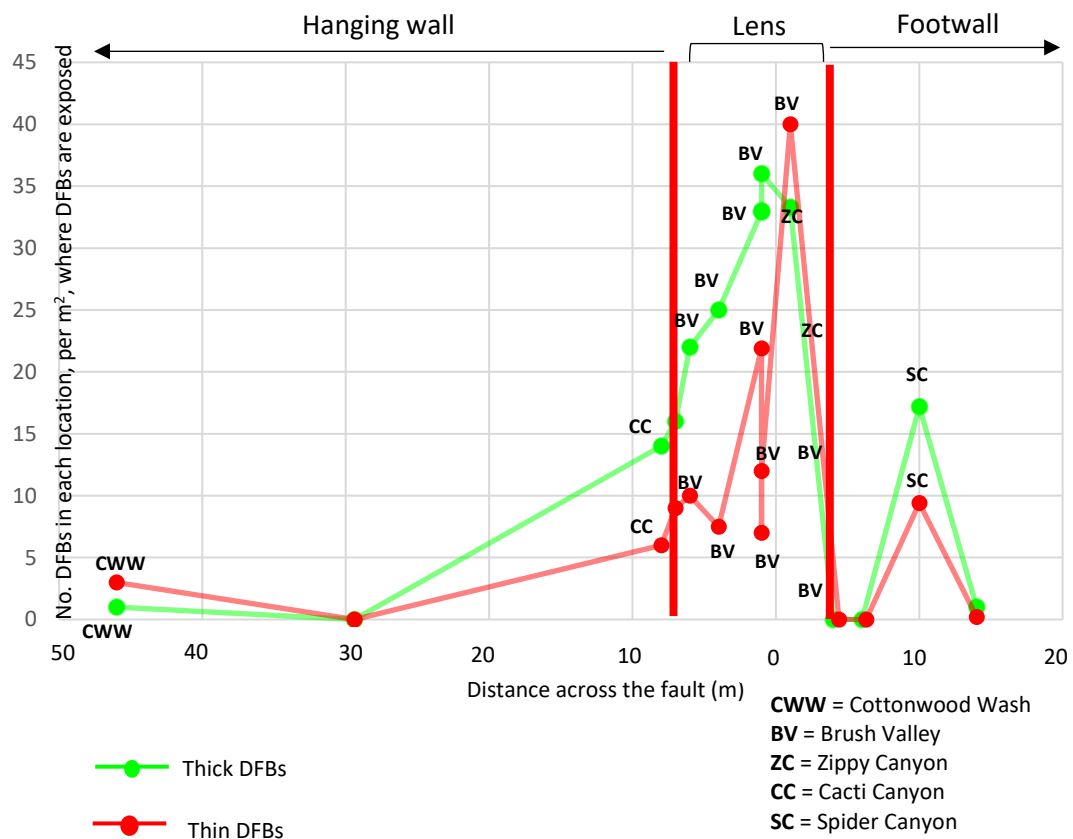
Figure 4.46 - Frequency of the deformation bands *across* the Crow's Nest Fault. Thick and thin deformation bands frequencies mirror one another in the hanging wall and footwall.

Everywhere along the fault where thick deformation bands are exposed, thin deformation bands are also present. The intensity of thin deformation bands is highest at the fault, peaking at 33 bands per m^2 at the Cottonwood Wash site and then decreasing into the footwall thereafter. In every location there is a higher intensity of thick deformation bands than there are thin deformation bands, apart from in the hanging wall and footwall at the

Cottonwood Wash site where there are more thin deformation bands exposed (figure 4.47).

Location on Crow's Nest Fault – 6km total length
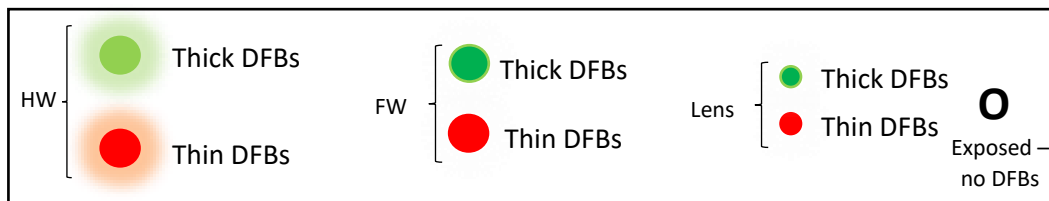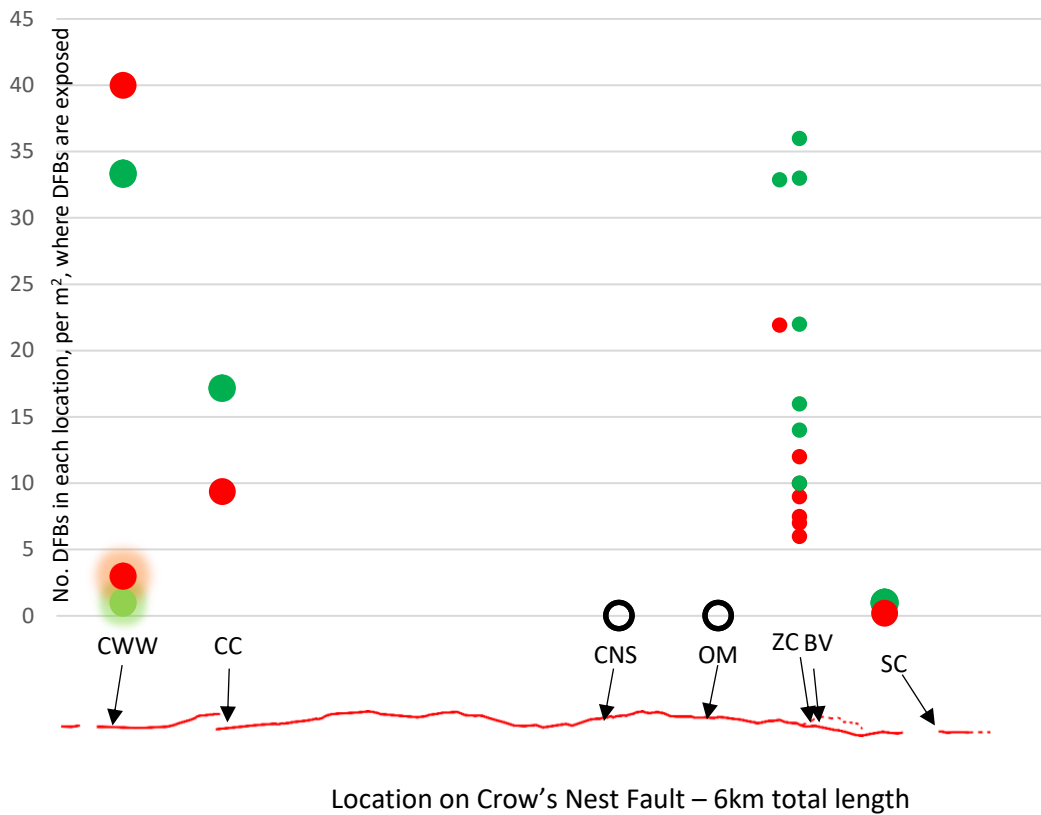
CWW = Cottonwood Wash   **CC** = Cacti Canyon   **CNS** = Crow's Nest Spring   **OM** = Old Mine
ZC = Zippy Canyon   **BV** = Brush Valley   **SC** = Spider Canyon

Figure 4.47 – Frequency of deformation bands *along* the Crow's Nest Fault. Although deformation bands are isolated in patches along the fault, thick and thin deformation bands are concentrated along the ends of the fault strands and within the lens at fault strand C. At the Spider Canyon locality, there are areas 14m into the footwall but projected into the fault. Where there are exposed areas but no deformation bands are observed, these are represented as open circles.

Study site	Position on the fault	Total area exposed	Area exposed with deformation bands	% of total area exposed with deformation bands observed	Total number of deformation bands
Cottonwood Wash	Hanging wall	115m x 57m	40cm x 40cm	0.002%	Thick = 1 Thin = 3
Cottonwood Wash	Footwall	25m x 15m	50cm x 30cm	0.04%	Thick = 5 Thin = 6
Cacti Canyon	Footwall	54m x 14m	1.6m x 1.2m	0.14%	Thick = 33 Thin = 18
Crow's Nest Spring	Footwall	480m x 45m	0	0	0
Old Mine	Footwall	47m x 17m	0	0	0
Zippy Canyon	Lens	58m x 4m	76cm x 24cm	0.07%	Thick = 6 Thin = 4
Brush Valley (Square 1)	Lens	29m x 52m	40cm x 40cm	0.06%	Thick = 22 Thin = 10
Brush Valley (Square 2)	Lens	29m x 52m	1m x 1m	0.06%	Thick = 9 Thin = 3
Brush Valley (Square 3)	Lens	29m x 52m	1m x 1m	0.06%	Thick = 33 Thin = 7
Brush Valley (Square 4)	Lens	29m x 52m	1m x 1m	0.06%	Thick = 16 Thin = 9
Brush Valley (Square 5)	Lens	29m x 52m	20cm x 20cm	0.06%	Thick = 14 Thin = 6
Brush Valley (Square 6)	Lens	29m x 52m	20cm x 20cm	0.06%	Thick = 19 Thin = 9
Spider Canyon	Footwall	35m x 71m	8m x 7m	2.25%	Thick = 30 Thin = 6

Table 3 – Localities studied at Crow's Nest Fault including the total area exposed and the area exposed where deformation bands are present.

Iron-rich fractures are only exposed in a $2m^2$ area of the Brush Valley location in the lens. Elsewhere iron oxide stains the host rock but no other structures along the fault are visibly filled with iron. Open fractures that are not filled with iron oxide or any other mineral are exposed everywhere along the fault in the hanging wall, footwall and lens. Along most of the fault, fractures remain unfilled but at the Crow's Nest site, fractures are filled with hydrocarbon at fracture junctions. At the Old Mine site there is evidence of hydrocarbons infilling some fractures.

Beyond the damage zone at the Crow's Nest Fault, 1-2 fractures per 10 metres are visible as natural background fracturing (figure 4.47). Locations close to the ends of fault strands, as shown by figure 4.48 show an increase in fracturing towards the fault and then decrease away from the damage zone. However, the Crow's Nest Spring locality has a gradual decrease in fracturing away from the fault for 90 metres into the footwall but then a steep drop off in intensity where natural background fracturing resumes at 90 metres into the footwall. The highest frequency of fractures are found in the lenses and in the first 15 metres into the footwall. Away from the fault and into the footwall the frequency of fractures decreases towards the north-east from an average of 9-10 per five metres to a background frequency of 1-2 fractures per ten metres. Fractures taper away from the fault in the hanging wall from maximum of 8 fractures per five metres at 5 metres away from the fault to less than 1 fracture per five metres at a background level approximately 70 metres south-west of the fault.
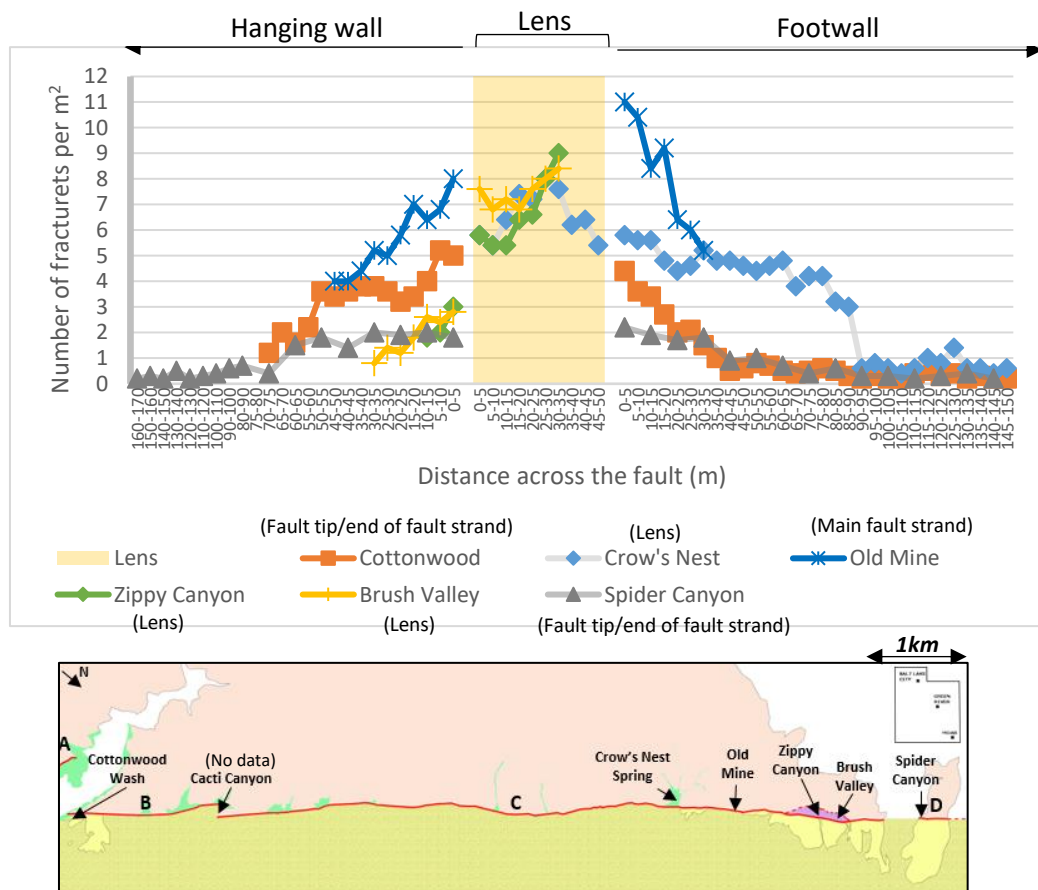
Figure 4.48 – Fracture frequency along Crow's Nest Fault is greatest within the lens at fault strand C and within the first 15 metres of the footwall.

Although linear scanlines were used to estimate deformation band frequency at the Crow's Nest Fault, the Brush Valley locality was analysed by scanlines in the hanging wall and by using squares in the lens (section 4.3). The use of different methods to analyse trace frequency could lead to an overestimation of trace intensity in the lens of the Brush Valley locality.

4.6.4 Large scale structures and how they formed

Up to ten bedding measurements were taken at each locality in the footwall, lens and hanging wall. Outside the fault zone, there is very limited exposure and bedding measurements can only be estimated from Google Earth aerial imagery.

Along the fault where the hanging wall is exposed, bedding is fairly flat lying and generally dips 10° towards the north. The hanging wall is not well exposed along the fault but bedding data has been measured from the Cottonwood Wash locality and can be seen in figure 4.49.
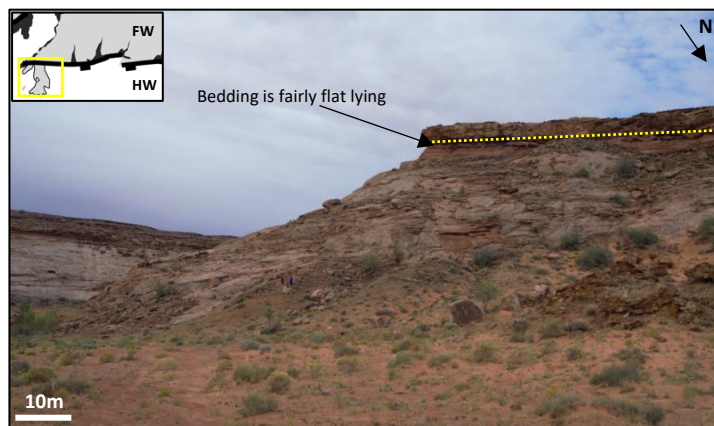
Figure 4.49 – Bedding in the hanging wall at the Cottonwood Wash is fairly flat lying.

Where the hanging wall is exposed at the Brush Valley locality, the hanging wall bedding begins to steepen from an average of 35° at 12m from the fault zone to approximately 50° towards the fault zone. This was not accessible by foot so bedding data has been estimated from photographs taken in the field (figure 4.50).
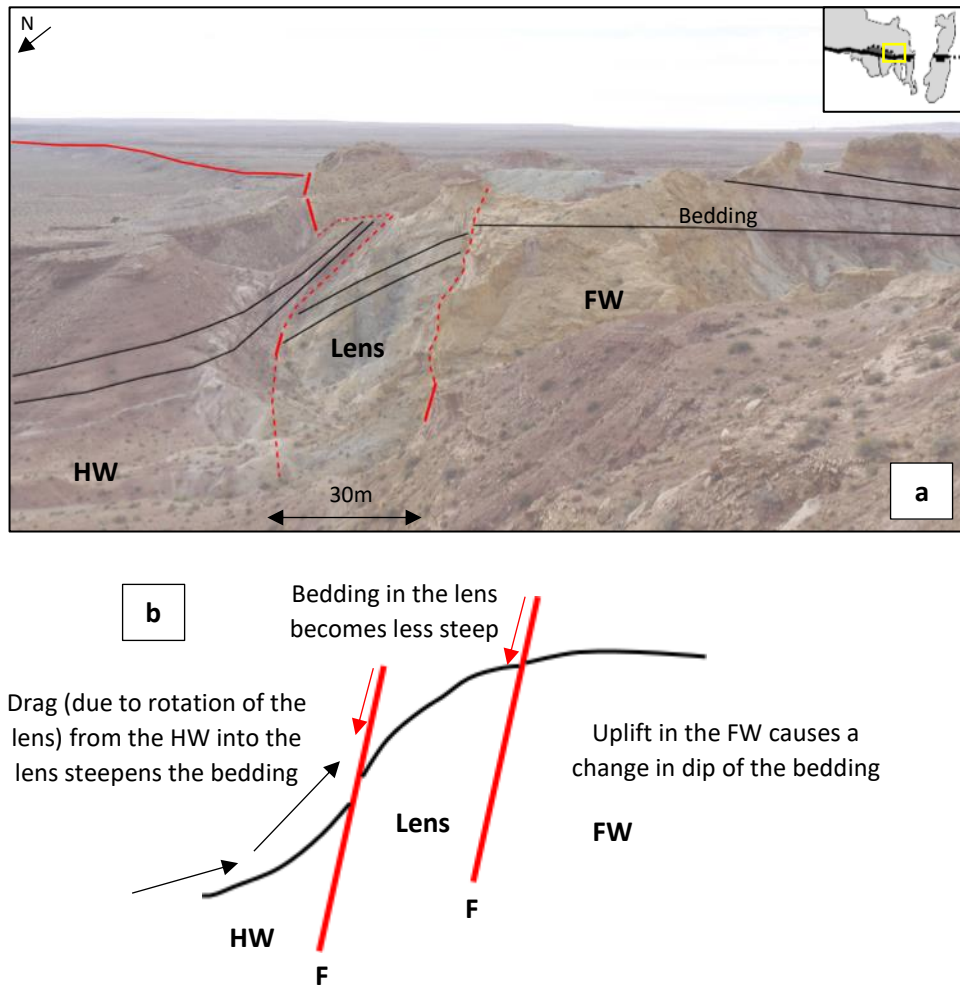
Figure 4.50
   (a) Annotated photo of the Brush Valley location showing the change in bedding through the hanging wall, lens and footwall.
   (b) Bedding steepens from the hanging wall into the lens where it then shallows out. In the footwall uplift causes additional change in the bedding dip. Regionally the eastern flank of the San Rafael Swell dips 45-80° so bedding has become less steep in the footwall in comparison.

Steepening of the bedding in the hanging wall is only observed at the Brush Valley locality in the hanging wall 10m away from the fault zone and could be a result of the lens formation. There is a lens at the Crow's Nest Spring locality but the hanging wall is not well exposed so any changes in bedding from the hanging wall at that locality were not estimated.

Within the Brush Valley lens, bedding is less steep than the hanging wall at ~20° (figure 4.51).

Figure 4.51
- (a) Plan view of the fault showing a distance of 1km between the Brush Valley and Crow's Nest Spring localities.
- (b) Plan view map synthesising the locations of the bedding data in the lens with respect to the fault.
- (c) Stereonet showing bedding data for the four data sets in the lens.

Location	Bedding Data (Dip/Strike)	Position in relation to the fault (m from FW)
Brush Valley lens (1)	43/209	25m from the FW
Brush Valley lens (2)	33/188	20m from the FW
Brush Valley lens (3)	17/207	14m from the FW
Crow's Nest Spring lens (4)	40/144	19m from the FW

To determine the degree of rotation the Brush Valley lens has undergone as a result of faulting, the bedding data in the lens has been rotated incrementally and then applied back onto the original bedding that is observed in the field today (figures 4.52a and 4.52b).

Location	Bedding Data (Dip/Strike)	Position in relation to the fault (m from FW)
Brush Valley lens (1)	43/209	25m from the FW
Brush Valley lens (2)	33/188	20m from the FW
Brush Valley lens (3)	17/207	14m from the FW
Crow's Nest Spring lens (4)	40/144	19m from the FW

Figure 4.52
    (a) Stereonet showing the rotated lens bedding data.
    (b) Stereonets showing lens bedding data un-rotated by 20 degrees.
The main fault trace is shown on the stereonets to show how the bedding changes with relation to the orientation of the fault. All bedding data is shown in the table.

Figure 4.52b shows the bedding data for the Brush Valley lens and Crow's Nest Spring lens match the current orientation when they are rotated 20° around the fault axis. Although the hanging wall is not well exposed at the Crow's Nest Spring locality, the bedding was

likely rotated ~20° as observed at the Brush Valley lens as it all part of the same fault system.

The lenses at the Crow's Nest Fault are probably the cores of a breached relay ramp. For a relay ramp to form there must be some degree of rotation (Peacock and Sanderson, 1994; Cartwright and Mansfield, 1998). When a relay ramp forms, the bedding in the lens was most likely rotated and distorted due to the propagation of the fault tips and formation of complex structures in the relay ramp.

In many relay ramps horizontal rotation leads to the lens tilting (Peacock and Sanderson, 1994). However, the lens at Brush Valley lens at the Crow's Nest Fault rotates around a horizontal axis (figure 4.53). This could be explained by a possible folding event at 90 degrees to the fault which was directly related to the formation and growth of the relay ramp. Evidence of rotation being accommodated in the lens is observed as intense deformation banding in the Brush Valley lens.
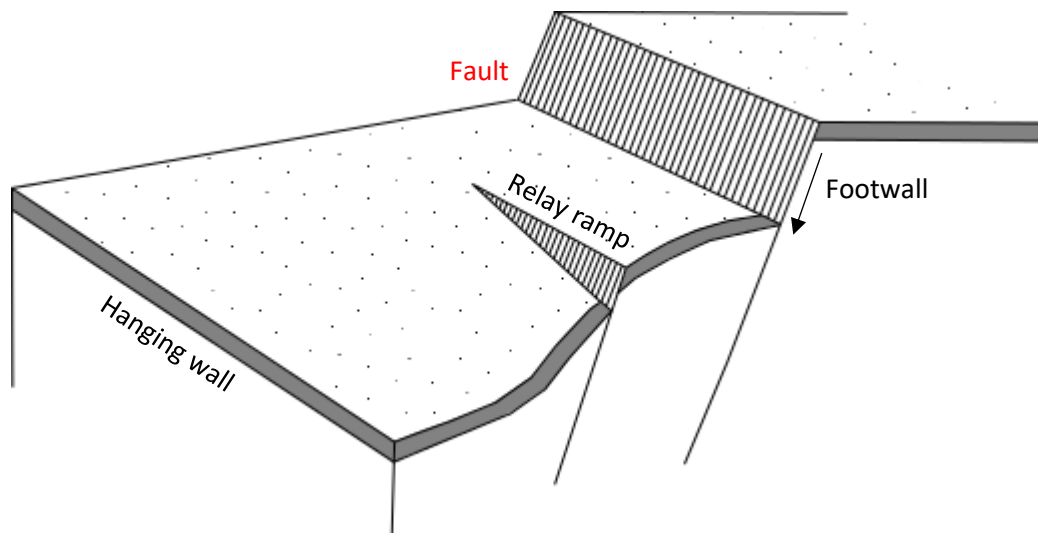
Figure 4.53 – Model of the Crow's Nest Fault which shows the development of the relay ramp with respect to the hanging wall and footwall.

Bedding in the lens depends upon its position in relation to the relay ramp structure (table 6). The relationship between the bedding data and the position in relation to the fault shows that bedding gets steeper when closer to the hanging wall (figures 4.54a, 4.54b and 4.54c). Into the lens, bedding is not consistent because of the folding caused by formation of the relay ramp.

As outlined in section 4.2, thick deformation bands at the Crow's Nest Fault are the first deformation structures to have formed. To determine whether thick deformation bands formed pre-faulting and pre-rotation of the lens, it is important to determine whether bedding rotation of the lens matches that of thick deformation bands.

To test this hypothesis, the same rotation of 20° was applied to the to the thick deformation bands which are exposed in the Brush Valley lens and thick deformation bands in the footwall (figure 4.54). Thick deformation band data within the footwall has been collected from the Cottonwood Wash, Cacti Canyon and Spider Canyon sites.
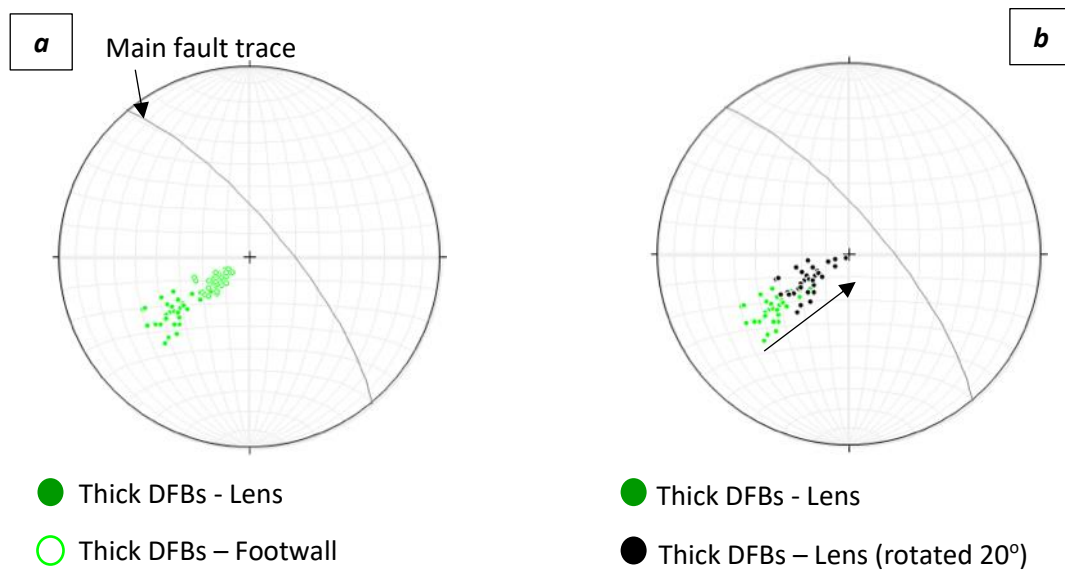
Figure 4.54 – (a) Stereonet showing thick dfbs in the lens (solid dark green) and the footwall (hollow light green. (b) Stereonet showing thick dfbs in the lens (solid dark green) have rotated 20° parallel to the fault (solid black) which now fit directly over the thick dfbs in the footwall indicating that thick dfbs are likely pre-faulting.

Both thick deformation bands in the lenses and footwall strike ~320° but the mean dip of thick deformation bands in the lens is 55° compared to a mean dip of 20° in the footwall. When thick deformation bands in the Brush Valley lens are rotated 20° around a horizontal axis parallel to the fault (75/320), they fit exactly onto the data points for the thick deformation bands in the footwall (figure 4.55). This suggests that thick deformation bands likely formed pre-faulting and pre-rotation of the lens.

Cross cutting relationships in the field and under thin section suggest thin deformation bands formed after thick deformation bands. Thin deformation bands inside and outside of

the lens have the same orientation. This suggests that thin deformation bands formed after the Brush Valley lens was formed.
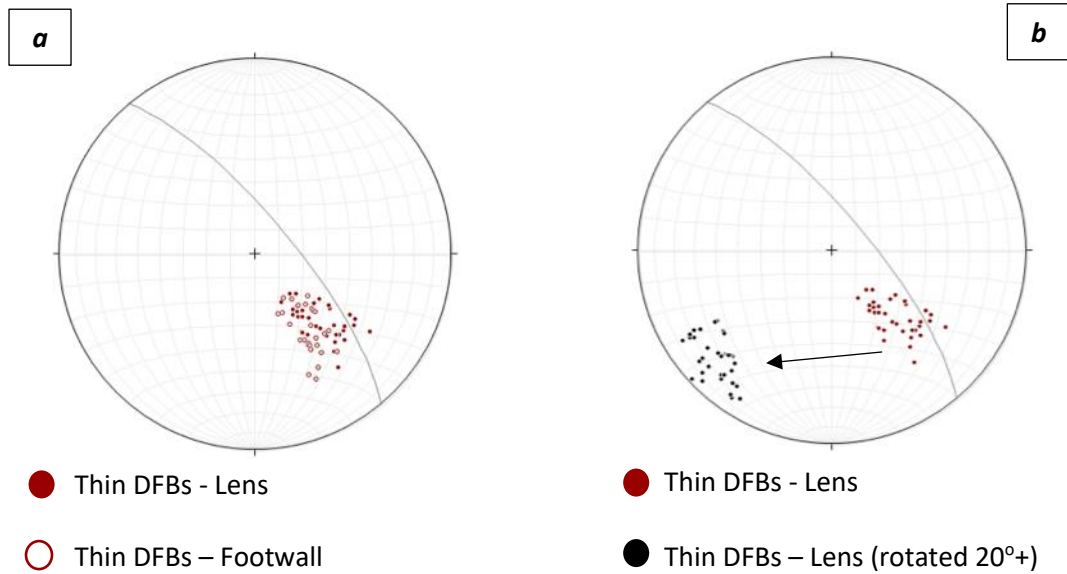
Figure 4.55 (a) Stereonet showing thin dfbs in the lens (solid dark red) and the footwall (hollow dark red). (b) Stereonet showing thin dfbs in the lens (solid dark red) and thick dfbs that have been rotated 20°+ parallel to the fault (solid black) do not fit directly on top of one another suggesting the thin deformation bands are post-faulting.

Fracture populations within and outside the lenses do not match. The same principle was applied to fractures, however, when rotated 20° parallel to the fault, the fractures do not fit onto the cluster of data for the footwall (figure 4.56). There is a difference between the populations, both in strike and in dip. Fractures inside the lens have an average dip of 33° and strike of 55 compared to fractures outside in the footwall which dip on average 59° and a strike of 102°.

a

b

● Fractures - Lens

● Fractures - FW

● Fractures - Lens

● Fractures – Lens (rotated 20°)
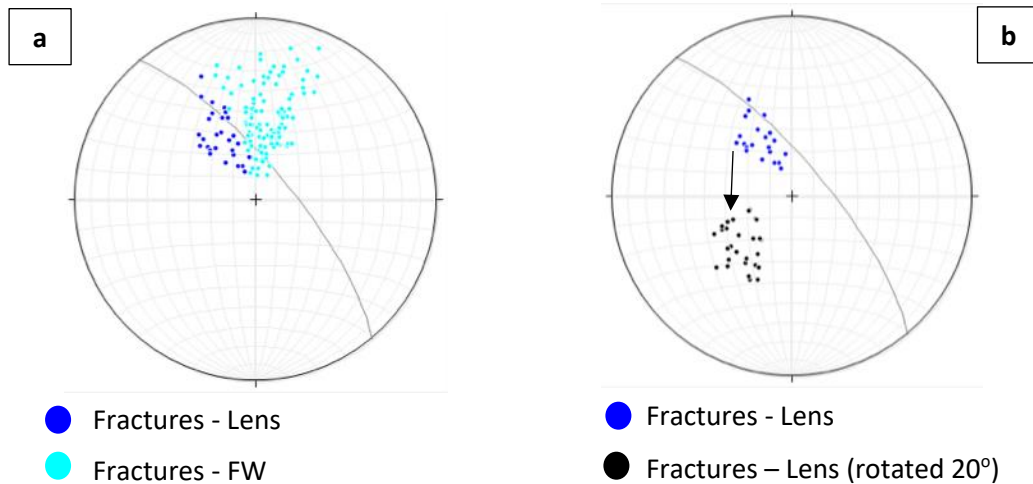
Figure 4.56 (a) Stereonet showing fractures in the lens (solid dark blue) and the footwall (solid light blue). (b) Stereonet showing fractures in the lens (solid dark blue) and fractures that have been rotated 20° parallel to the fault (solid black) do not fit directly on top of one another and this suggests it is likely the fractures are post-faulting.

Iron-rich fractures are only exposed in the Brush Valley lens and cross cutting relations suggest they are post-faulting in age. Iron-rich fractures on average strike 350 and dip 46°. Compared to open fractures they are north-south orientated compared to north east-south west orientated and dip more steeply than open fractures in the Brush Valley lens.

The change in orientation of fracturing could be due to a number of reasons, for example; pre-existing weakness within the host rock, sudden or multiple uplifts. Although only exposed localised within the Brush Valley lens, iron-rich fractures could be situated elsewhere along the fault but are not well exposed elsewhere.

4.7 Microanalysis

Thin sections were prepared using standard methods. To analyse thick and thin deformation bands, samples were prepared for analysis from each of the six studied squares at the Brush Valley site. Due to the fragile nature of the host rock at this site, only four out of the six samples were successfully prepared for thin section analysis (figure 4.57b).

In each sample, five different areas of the same sample were analysed for grain size using the Image J software with thresholds reset each time. To analyse the photomicrographs, grain boundaries of each mineral were defined by adjusting the colour threshold of each

photomicrograph. Once the threshold has been set, the photomicrograph is analysed using the 'Analyse Particles' function on Image J.

The standard deviation and the average grain size were calculated for each photomicrograph for the Slick Rock Entrada host rock at the Brush Valley locality. Analysing a number of photomicrographs from each square reduced error and increased accuracy. To improve accuracy further, more photomicrographs and samples could be analysed.

Grain size analysis using this method uses 2D thin sections to analyse 3D entities; grains. In rocks which are highly anisotropic, for example in fault rocks, this can lead to errors. The image analysis method used at the Crow's Nest Fault can be considered accurate to ~6-7% based on the calculated standard error of the mean. This is an easy and efficient method for analysing high porosity rocks such as aeolian sandstones as grain boundaries are more prominent.

Prior to analysis, thin section samples were injected with blue resin dye (epoxy resin) which infills vacant pore space and represents 'modern day porosity' (figure 4.61). This method is widely used within the literature as it allows discrimination between open pore space, cement and grains (Gardner, 1980; Mair et al., 2000; Johansen et al., 2005). In this study, the blue resin dye is edited to appear red within the Image J software in order to show a clear contrast between porosity, grains and cement (figure 4.61).

Where pore spaces are filed with black or brown material, this is defined as 'filled porosity'. Pore spaces which are filled with brown material have been identified through energy dispersive spectroscopy (EDS) as iron oxide. However, it has not been possible to uniquely identify the black material. The black material is carbon rich and likely hydrocarbon, however the thin sections were coated in carbon during thin section preparation which gives each sample an existing high percentage of carbon when analysed under the SEM. The black material could possibly be magnetite, however magnetite has a high Fe content compared to that of the black material so it should have been identified. Further studies could include analysing entire samples under XRD for identification. However, based on field observations and existing literature, for the purposes of this study the black material is referred to as a hydrocarbon rich material. By combining the modern day and filled porosity estimations, a total porosity for each photomicrograph can be analysed (figure 4.61).

Porosity of the samples was analysed by calculating the total number of pixels within each photomicrograph. This number is then compared to the porosity of the photomicrograph. The photomicrograph must first be scaled to replicate the true scale of the sample. As there is no standard tool to accurately distinguish porosity from minerals and cement, each photomicrograph has to be manually edited to enhance the contrast between each feature. For each photomicrograph, the colour threshold is adjusted to determine the porosity (black pixels) from the rest of the image (white pixels). Once the threshold has been established, the particles can be analysed and a porosity measurement can be calculated. The same process was used to determine the cement within in each photomicrograph.

When analysing porosity, air bubbles are included within the porosity measurements. Air bubbles can get trapped through sample preparation if air becomes trapped within the pores when flooding the sample with blue epoxy resin, or when the cover slip is glued onto the slide.

For each sample analysed, five photomicrographs were then analysed. After analysing four or five samples the results of the porosity and cement percentages were producing very similar results. Five was found to be the optimum number between having a good sample selection, reducing any errors and being time efficient. Other porosity analysis studies throughout Utah have looked at similar numbers of samples and photomicrographs (Johansen et al., 2005; Bright, 2006). Analysing twenty micrographs at each locality gives a good overall representation of the host rock at each of the three localities studied as it reduces most anomalies and human error.

Thin deformation bands have been analysed in the same way that thick deformation bands have been analysed for grain size distribution. Five photomicrographs of each sample were analysed containing both the host rock and the thin deformation bands to determine the average grain size and standard deviation for each.

4.7.1 Host rock porosity at the Crow's Nest Fault

Samples of host rock exposed at the Crow's Nest Fault have been taken from the Navajo Formation and the Slick Rock Entrada. Samples of the Navajo Formation were taken from the footwall of the Cottonwood Wash locality and from the footwall of the Crow's Nest

Spring locality. Samples of the Slick Rock Entrada were taken from the lens at the Brush Valley locality.

Host rock porosity for the Slick Rock Entrada and Navajo Formation exposed at the Crow's Nest Fault have been estimated through thin section analysis.

Table 4 outlines the samples and photomicrographs analysed for porosity of the Slick Rock Entrada and the Navajo Formation at the Crow's Nest Fault. It is important to note that host rock exposed in the Brush Valley lens at the Crow's Nest Fault has been altered and does not represent the Entrada Formation elsewhere.

Host rock lithology	Number of samples and photomicrographs	Mean total porosity	Mean filled porosity	Mean modern porosity
Navajo Formation (Cottonwood Wash – footwall)	No. samples = 4 No. photomicrographs of each sample = 5	22.6%	6.8%	15.8%
Navajo Formation (Crow's Nest Spring – footwall)	No. samples = 4 No. photomicrographs of each sample = 5	15.9%	11.2%	4.4%
Slick Rock Entrada (Brush Valley – lens)	No. samples = 4 No. photomicrographs of each sample = 5	30%	13.7%	16.5%

Table 4 – Porosity of the Slick Rock Entrada and Navajo Formation at the Crow's Nest Fault.

4.7.2 Thick deformation bands

Thick deformation bands have a microstructure which is dominated by larger (50µm mean) un-deformed quartz grains within a fine grained matrix of (18µm mean) quartz fragments (figure 4.58). Some areas of fine grained matrix within the deformation band are too small to see in thin section and appear as dark brown areas in optical photomicrographs (figure 4.59; 4.60). There are very few scattered un-deformed quartz grains which leads to a strong bimodal grain size distribution.
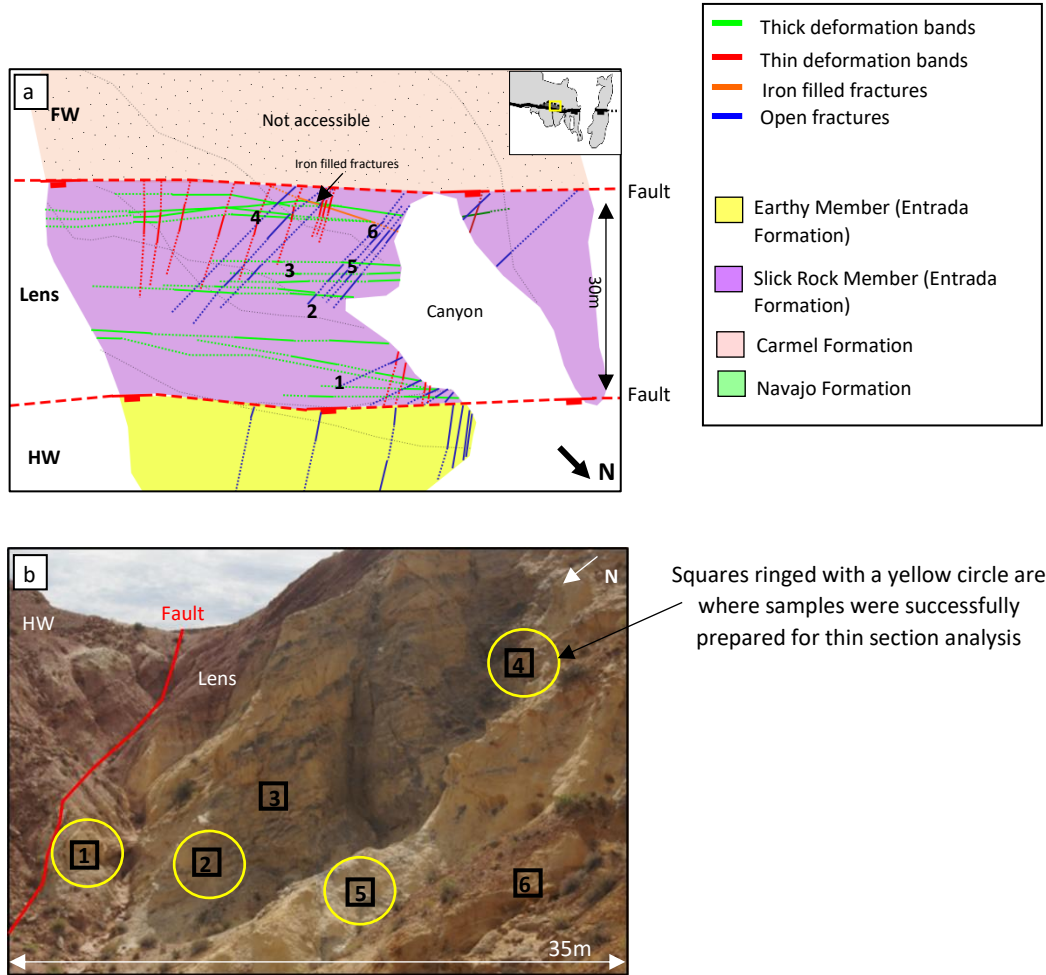
Figure 4.57 – (a) Plan view map of the Brush Valley canyon and (b) indicates which four samples were successfully prepared for thin section.

Square 2 - 1m x 1m at GR N 38°42'32.24" W 110°26'58.89"
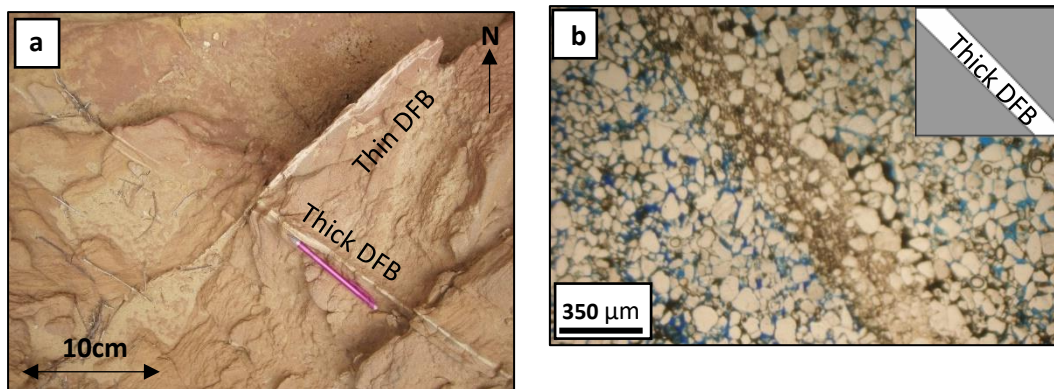
Figure 4.58 – (a) An outcrop photograph showing a thick deformation band cross cut by a thin deformation band. (b) A photomicrograph showing a thick deformation band. Sample is taken from square 2 at the Brush Valley locality.

Figure 4.59 – Photomicrograph of a thick deformation band in thin section from square 2 at the Brush Valley site. The thick band shows evidence of intense grain crushing and lack of open pore space compared to the surrounding porous host rock.

Square 1 - 40cm x 40cm square at GR N 38°42'32.44" W 110°26'58.48" **Square 2** - 1m x 1m square at GR N 38°42'32.24" W 110°26'58.89"

Large undeformed quartz grains

Intense grain crushing (Thick DFB)

Square 4 - 1m x 1m square at GR N 38°42'32.24" W 110°26'58.89"

Large undeformed quartz grains

Intense grain crushing (Thick DFB)

Open pore space surrounding quartz grains

Thick DFB

Square 5 – 20cm x 20cm square at GR N 38°42'32.10" W 110°26'59.27"

Figure 4.60 – (a) Square 1 shows evidence of large undeformed quartz grains in the host rock which surround intense grain crushing in the thick deformation band as seen in (b), (c) and (d). (e) shows evidence of a thick deformation band surrounded by a host rock with open pore space.

133

The results of the grain size analysis for the un-deformed quartz grains which make up the host rock are shown in table 5.

Sample	Average grain size (1)	Average grain size (2)	Average grain size (3)	Average grain size (4)	Average grain size (5)	Average grain size of square 1	Standard Deviation (of 1-5)	Standard Error of the mean	Standard Error as % of mean
Square 1	50µm	63µm	69µm	54µm	55µm	58.2µm	7.66	3.42	5.89
Square 3	47µm	65µm	63µm	55µm	46µm	55.2µm	8.78	3.92	7.12
Square 4	67µm	43µm	51µm	58µm	56µm	55µm	8.86	3.96	7.20
Square 5	63µm	44µm	57µm	50µm	46µm	52µm	7.90	3.53	6.80

Table 5 – Grain size analysis of un-deformed quartz grains in the Slick Rock Entrada Formation at the Brush Valley locality.

The average grain size of un-deformed quartz grains in the host rock is 55.1µm in the Slick Rock Entrada at the Brush Valley locality.

Due to the fine grained nature of the deformed quartz within the thick deformation bands, the image analysis software could not distinguish the size of most of the deformed quartz grains as they were too small to measure.

Although most grains (~70%) were less than 20 µm and hence too fine grained to be analysed using Image J software, the remaining 30% of the deformed quartz grains were between 20-80µm.

Although present in the field area, deformation bands could not be distinguished under thin section within samples from the Navajo Formation. Deformation bands exposed in the Navajo Formation were highly weathered on the surface and this may have affected the sample preparation.

At the Cottonwood Wash and Crow's Nest Spring localities, four samples of the Navajo Formation were deemed sufficient due to the size of the area exposed. However, a further two samples of the Slick Rock Entrada were collected from the Brush Valley locality but these were too fragile to be prepared for thin section analysis.

Figure 4.61c shows that the host rock has abundant empty pore spaces surrounding the rounded to sub-rounded quartz grains. Where the thick deformation band is present, there is very little observable pore space (figure 4.61b).
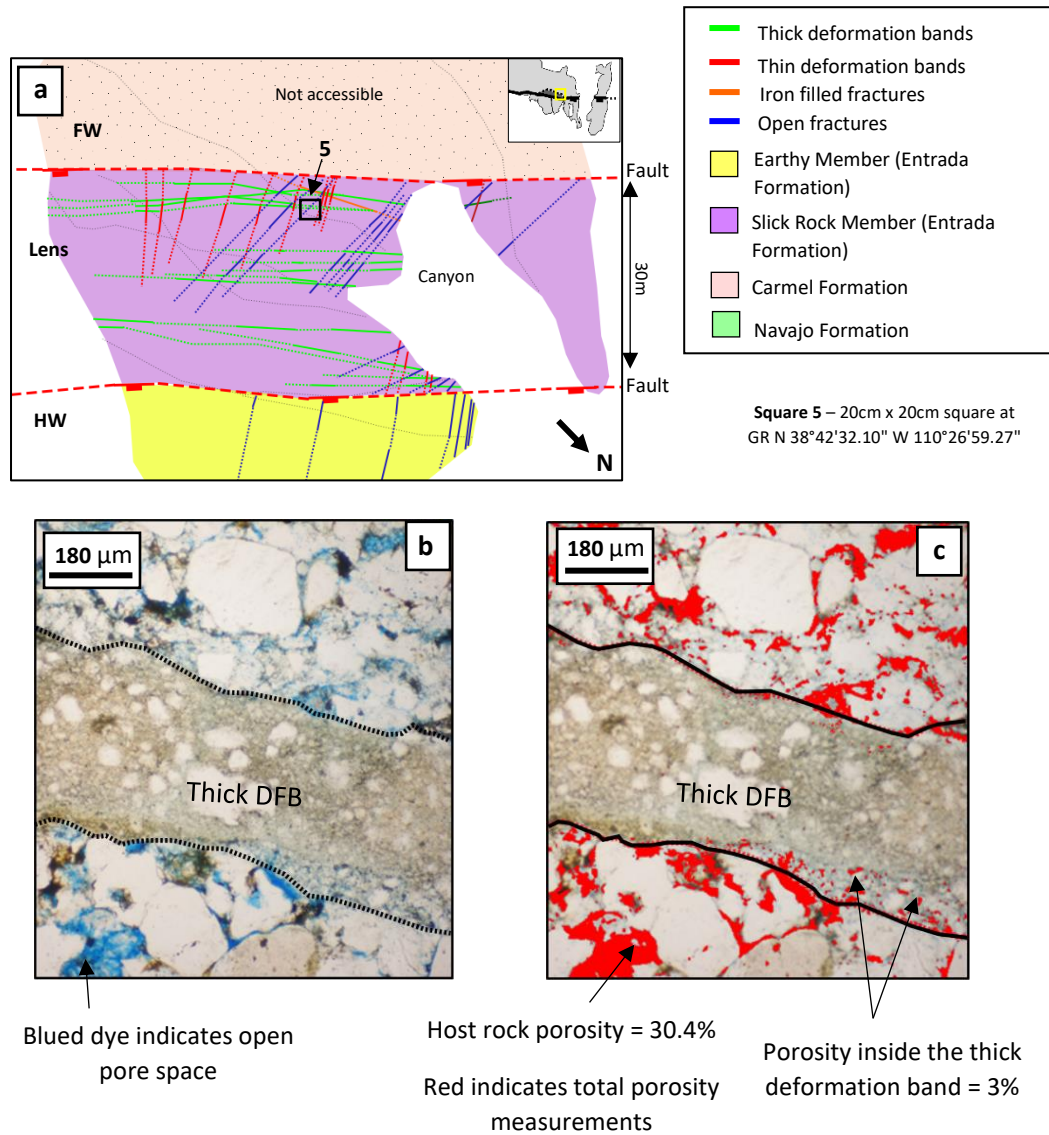
Figure 4.61 – (a) Plan view map of the Brush Valley lens site. (b) A photomicrograph showing blue dye within the host rock which indicates open pore space and (c) the open pore space is indicated as red to measure the porosity using Image J software.

The modern day porosity, filled porosity and total combined porosity of thin sections taken from squares 1, 2, 4 and 5 at the Brush Valley site are given in Table 4. For each square sampled, five photomicrographs were analysed making a total of 20 samples; averages, standard deviations and standard error for each sample/square was formulated (table 6).

The results of the porosity estimations for both the thick deformation bands and the surrounding host rock can be seen in table 6.

Sample/square	Modern day porosity (%) Host rock*	Filled porosity (%) Host rock*	Total porosity (%) Host rock*	Total porosity (%) Thick DFB*
Square 1	16.2	13.8	30.0	2.7
Square 2	16.2	13.4	29.6	2.0
Square 4	17.2	13.4	30.6	2.0
Square 5	16.4	14.0	30.4	3.0
Average	**16.5**	**13.7**	**30.0**	**2.5**
Standard deviation	0.5	0.3	0.4	0.5
Standard error (SE)	0.2	0.2	0.2	0.3
SE / mean	1.4%	1.1%	0.7%	10.4%

Table 6 – Porosity estimations of the thick deformation bands and surrounding Slick Rock Entrada host rock at the Brush Valley lens site. *Average of five samples taken at each square.

The results of the porosity calculations show that the host rock at the Brush Valley site is highly porous with an average total porosity of 30% and a standard deviation of 0.4. In each sample, the modern day porosity is higher than the filled porosity by 2-4%. Thick deformation bands are measured to have a very low total porosity of 2-3%, due to grain crushing and grain reorganisation (Mair et al., 2000).

There is an error of up to ~1.4% when analysing the host rock porosity based on the calculated standard error of the mean. The error of the thick deformation band total porosity is much higher at ~10.4% as porosity estimates have been rounded to the nearest integer because of the small grain sizes being more difficult to analyse using Image J software. Even though there is a small (0.2%) standard error of the mean, dividing this number by a small mean results in a higher error %.

4.7.3 Thin deformation bands

Thin deformation bands have a microstructure that is dominated by mostly larger relatively uniformly sized quartz grains (35µm) with a zone of discontinuous intense quartz crushing through the centre of the band. Samples of thin deformation bands were taken from the same squares as the thick deformation bands (locations in figure 4.4.6). Thin deformation bands show evidence for fracturing along the band both in the field and under thin section (figure 4.62).

Square 5 – 20cm x 20cm square at GR N 38°42'32.10" W 110°26'59.27"
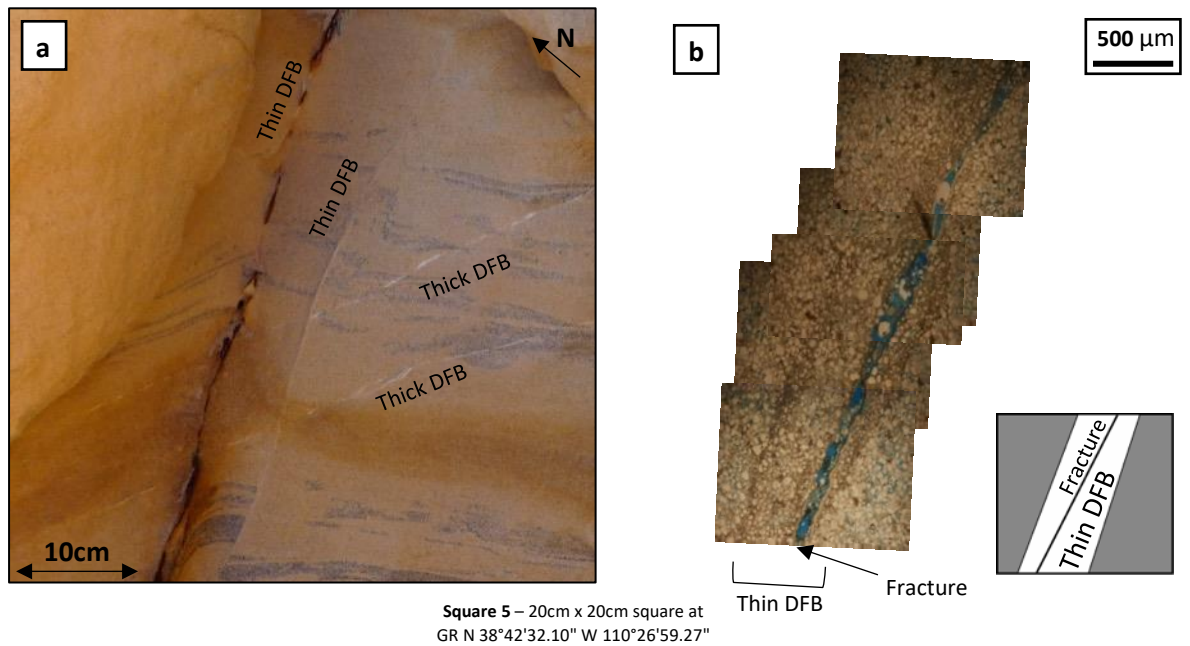
Figure 4.62 - (a) Outcrop photograph location showing cross cutting relationship of deformation structures. (b) Photomicrograph showing a thin deformation band with a later fracture almost parallel to the thin deformation band.

Similar to thick deformation bands, thin deformation bands are pre-dominantly quartz rich which is too fine grained to determine an average grain size using Image J software (figure 4.62). Similar to the thick deformation bands there is a bimodal distribution within the thin deformation bands.

Approximately 60-65% of deformed quartz within thin deformation bands was too fine grained to be measured using the Image J software (less than 10µm). The overall average grain size was 22µm with a standard deviation of 2.3.

As shown in figure 4.63, there is no blue dye resin (modern day porosity) or evidence of filled porosity within the thin deformation bands, indicating a lack of open pore space

within the band. However, the surrounding, undeformed host rock shows evidence of modern day and filled porosity with limited amounts of calcite cement (~3%).
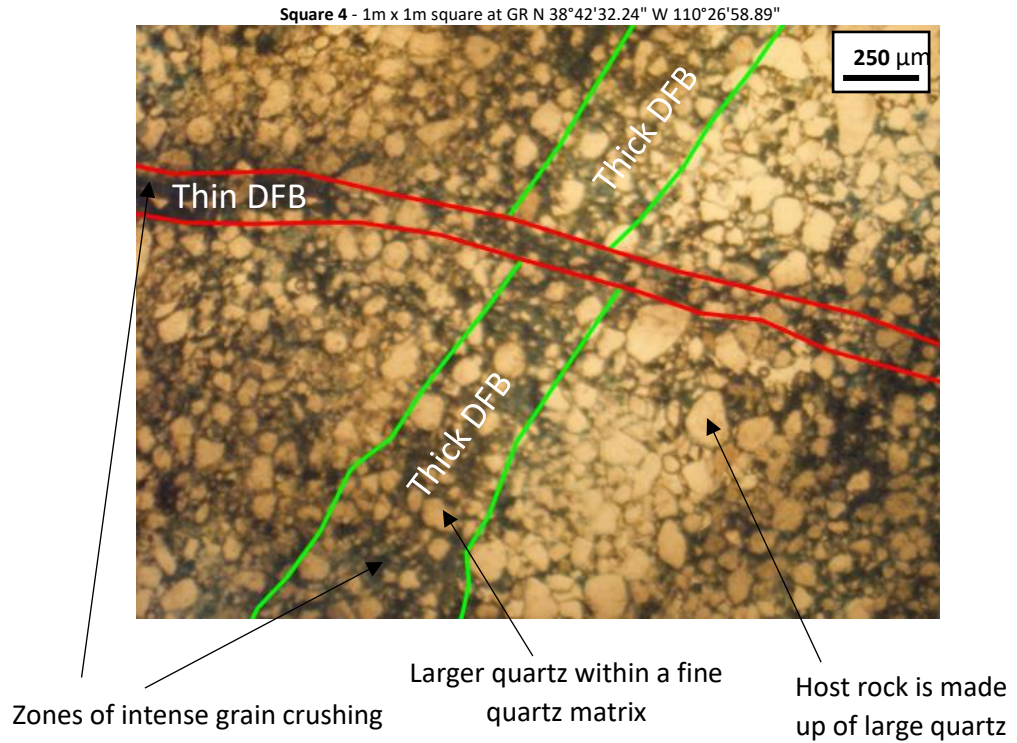
Figure 4.63 – Photomicrograph location showing a thick deformation band being cross cut by a thin deformation band.

The results of the porosity analysis can be observed in table 7.

Sample/square	Modern day porosity Host rock*	Filled porosity Host rock*	Total porosity **Host rock***	Total porosity **Thin DFB***
Square 1	16.2	13.8	30.0	4.0
Square 2	16.2	13.4	29.6	2.0
Square 4	17.2	13.4	30.6	5.0
Square 5	16.4	14.0	30.4	3.0
Average	**16.5**	**13.7**	**30.0**	**3.5**
Standard deviation	0.5	0.3	0.4	1.3
Standard error (SE)	0.2	0.2	0.2	0.6
SE / mean	1.4%	1.1%	0.7%	18.4%

Table 7 – Porosity estimations of the thin deformation bands and surrounding Slick Rock Entrada Formation host rock at the Brush Valley lens site. *Average of five samples taken at each square.

A comparison of the thick and thin deformation bands shows them to have average total porosities of 2.5% and 3.5% respectively. Thin deformation band margins are more diffuse compared to thick deformation bands. Table 8 presents a comparison of the characteristics exhibited of thick deformation bands compared to thin deformation bands.

Thick deformation bands	Thin deformation bands
• Thickness = ~0.5-1cm • Sub-parallel to the fault • Strongly bimodal grain size distribution • Defined margins • Degree of grain crushing is approximately constant throughout band • Less anastomosing geometries	• Thickness = 0.3-0.4mm • Perpendicular to the fault • More uniform grain size distribution • Diffuse margins • Intense grain crushing in centre of deformation band • More anastomosing geometries

Table 8 – Table defining the diagnostic features between thick and thin deformation bands.

Studies of thick and thin deformation bands at Courthouse Branch Point, Moab by Johansen et al., (2005) show a similar series of deformation structures present to those observed at Crow's Nest Fault. Analysis of these deformation structures in thin section suggests that cohesive grain contacts inhibited the reorganisation of grains and this resulted in the host rock ultimately failing by cataclasis, resulting in the switch from thick to thin deformation bands. However, both thick and thin deformation bands at the Crow's Nest Fault show evidence of cataclasis. The thick deformation bands show no clear gouge zone in the middle of the band, however the thin deformation bands show evidence for discontinuous intense grain crushing, localised towards the centre of the band.

It is worth noting that there is a size difference to how deformation bands manifest themselves in the field, compared to how they are observed in thin section. For example, thick deformation bands appear 400-500µm thick in thin section but when observed in the field, appear as 0.5-1cm wide bands. This is likely due to further clusters of deformation bands observed under thin section which are not observed in the field, or it may be that deformation bands have intense zones of grain crushing which are not visible in the field.

Grain size distribution is an important factor which can influence porosity reduction in deformation bands Marone and Scholz, (1989). During prolonged deformation, smaller grains (~10μm) are less likely to fail than larger grains (~25-50μm). With increasing deformation, grain rolling and grain rotation, large grains reduce in size and a fine grained gouge develops. However, once formed, the fine grained gouge dominates the deformation band and cataclasis becomes a less important process (Johansen et al., 2005).

4.7.4 Iron-rich fractures

Photomicrographs confirm that iron-rich fractures cross cut thick deformation bands (figure 4.64). The thickness of iron-rich fractures is up to ~70μm. Iron-rich fractures contain larger quartz grains (up to 200μm) and smaller quartz fragments (<20μm) which are sub-rounded to rounded in a matrix of iron. The edges of the iron-rich fractures are distinct (figure 4.65).

Figure 4.64 – (a) Iron-rich fractures offset thick deformation bands in the field. (b) Photomicrograph showing the offset of thick deformation bands by iron-rich fractures. Iron infills the fracture in between quartz.
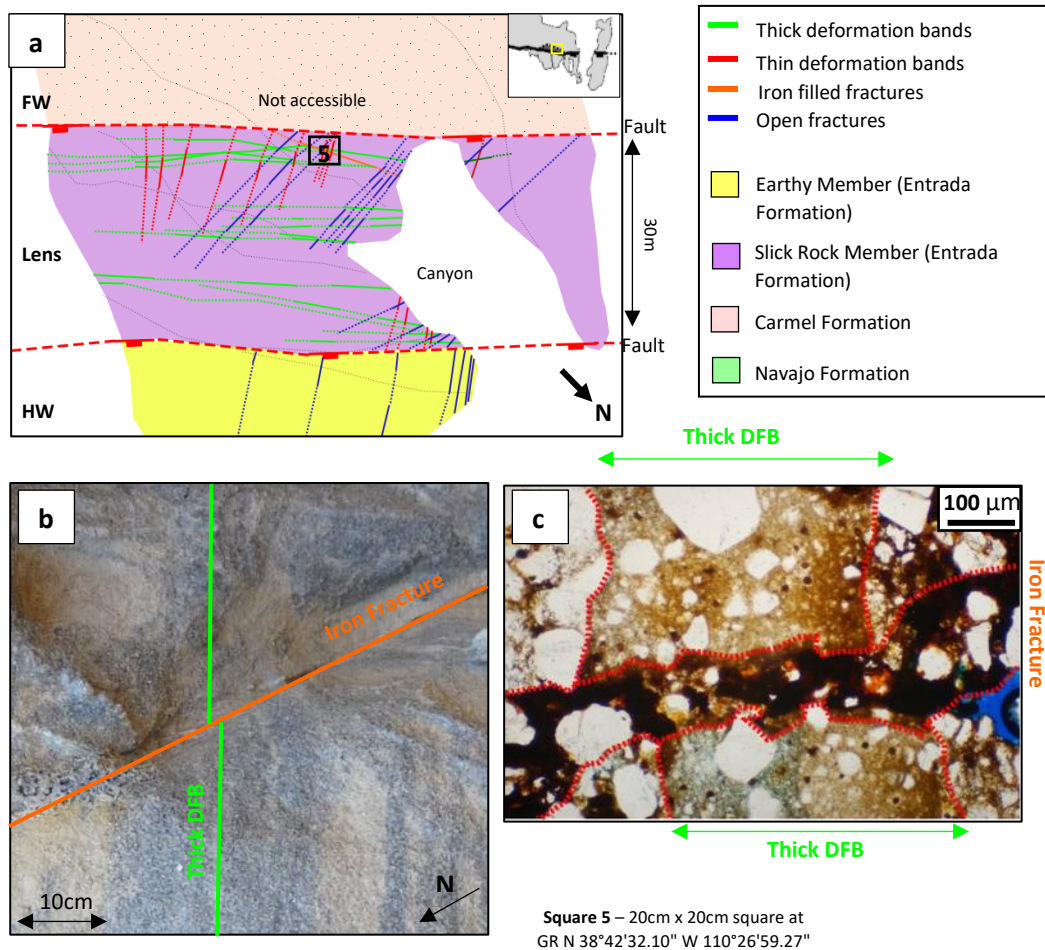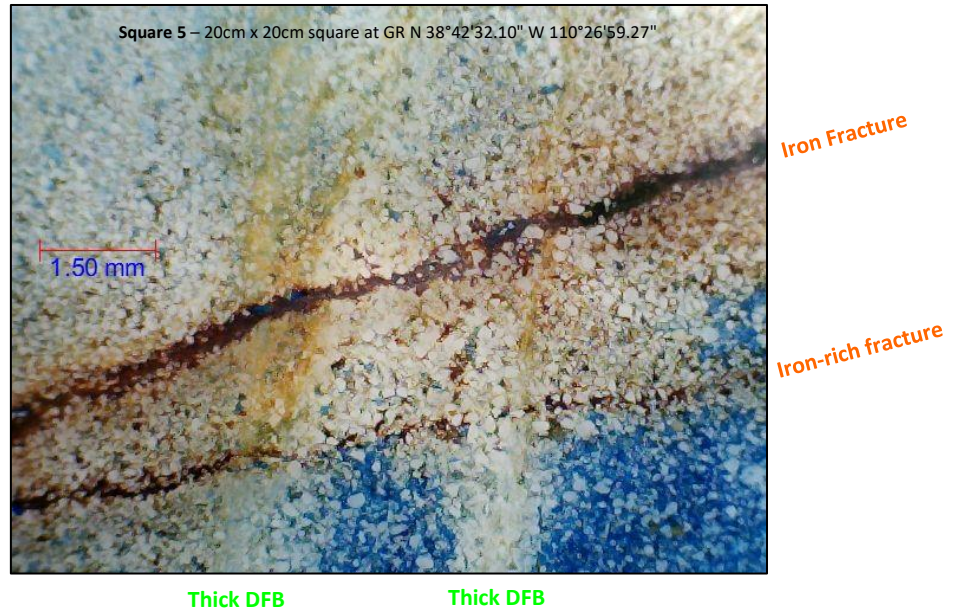
Figure 4.65 – Photomicrograph showing two iron-rich fractures cross cutting two thick deformation bands. The host rock surrounding the deformation structures is highly porous compared to the structures themselves as indicated by the blue resin present between grains.

4.7.5 Open fractures

Photomicrographs show evidence of fractures characterised by a lack of infilling where blue resin dye has filled the empty pore spaces. Within the fractures, some larger quartz grains (40-50μm) are visible. The margins of the fractures are diffuse in some areas and more distinctive in others. As seen in figure 4.66b, where a fracture cross cuts a thin deformation band, the fracture has more distinctive margins where it cuts through a more intense zone of cataclasis. Where grain crushing is less intense, the fracture has more irregular margins.

Square 1 - 40cm x 40cm square at GR N 38°42'32.44" W
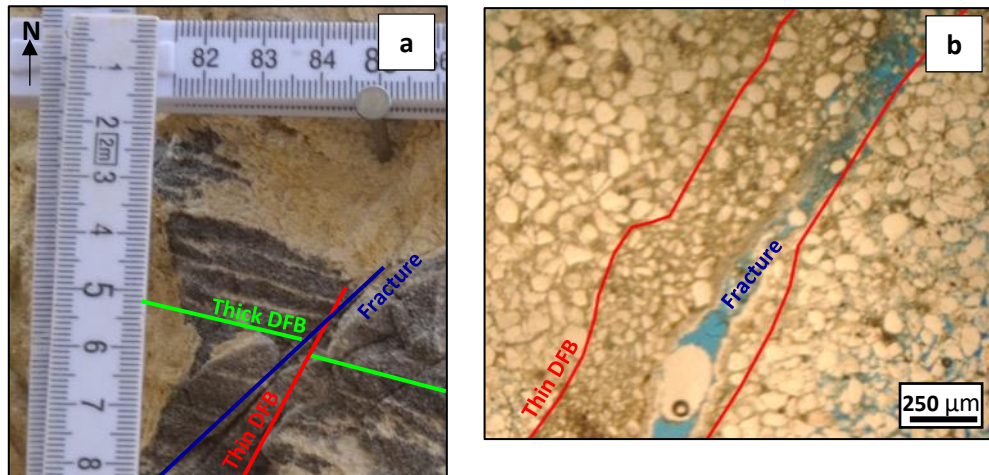
Figure 4.66 – (a) Exposed host rock in the lens (Brush Valley location) shows cross cutting evidence between deformation structures. (b) Cross cutting relations under thin section shows evidence for unfilled fractures overprinting thin deformation bands.

4.8 Evidence of cementation and porosity

4.8.1 Cementation and porosity of host rock at the Crow's Nest Fault

Sampling of the host rock was restricted by the exposure at sampling sites (figure 4.67). For example, the Navajo Formation is poorly exposed at the Cottonwood Wash locality within the footwall and this limited the number of samples collected. At the Crow's Nest Spring locality, only altered Navajo Formation is exposed in the footwall and so a comparison to unaltered rock was not possible.

The Slick Rock Entrada is only exposed at the Brush Valley locality. In this locality, exposure is further limited by steep cliff exposure. Host rock is fragile and crumbly at this locality and this resulted in a number of samples collected being unsuitable for thin section preparation. All host rock at this locality appeared altered and no exposures of unaltered Slick Rock Entrada are observed elsewhere at the Crow's Nest Fault.
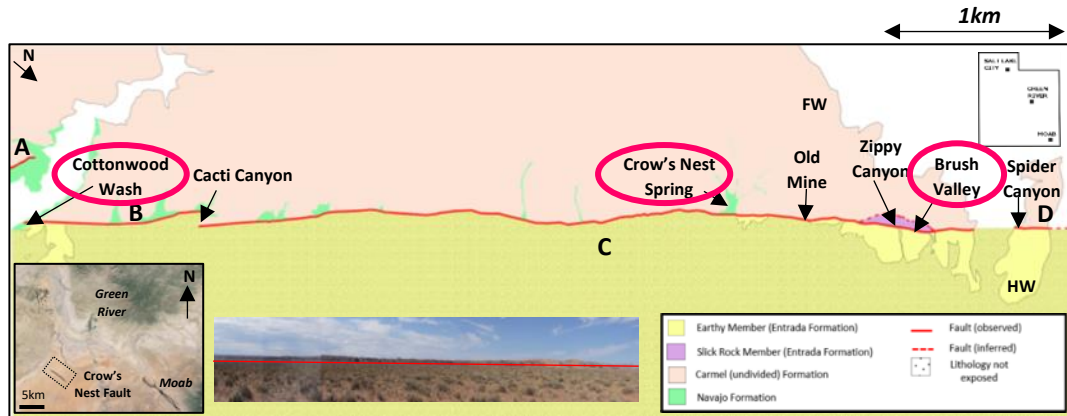
Figure 4.67 - Plan view map of the Crow's Nest Fault showing fault strands A to D and indicating the locations where samples have been taken and analysed for porosity; the Cottonwood Wash locality, the Crow's Nest Spring locality and the Brush Valley locality. Map modified from Doelling (2002).

Sampling at all three sites was taken where there was good exposure. This method may have resulted in sampling bias of the 'best' samples, where features were distinct and favourable for thin section analysis. To overcome this, care was taken to collect samples from a variety of exposed host rock locations spread out across each locality in an attempt to reduce sampling bias.

Thin section slides were produced from hand samples collected in the field, and then analysed under a scanning electron microscope (SEM). Once under the SEM, photomicrographs have been taken of the thin section slides at random which were analysed using Image J.

The Cottonwood Wash locality is located on the south-eastern tip of fault strand B. The Navajo Formation is exposed in the footwall and four samples were taken where deformation bands are exposed in a small 50cm by 34cm outcrop at GR N 38°41'7.04" W 110°24'0.42" (figure 4.68).
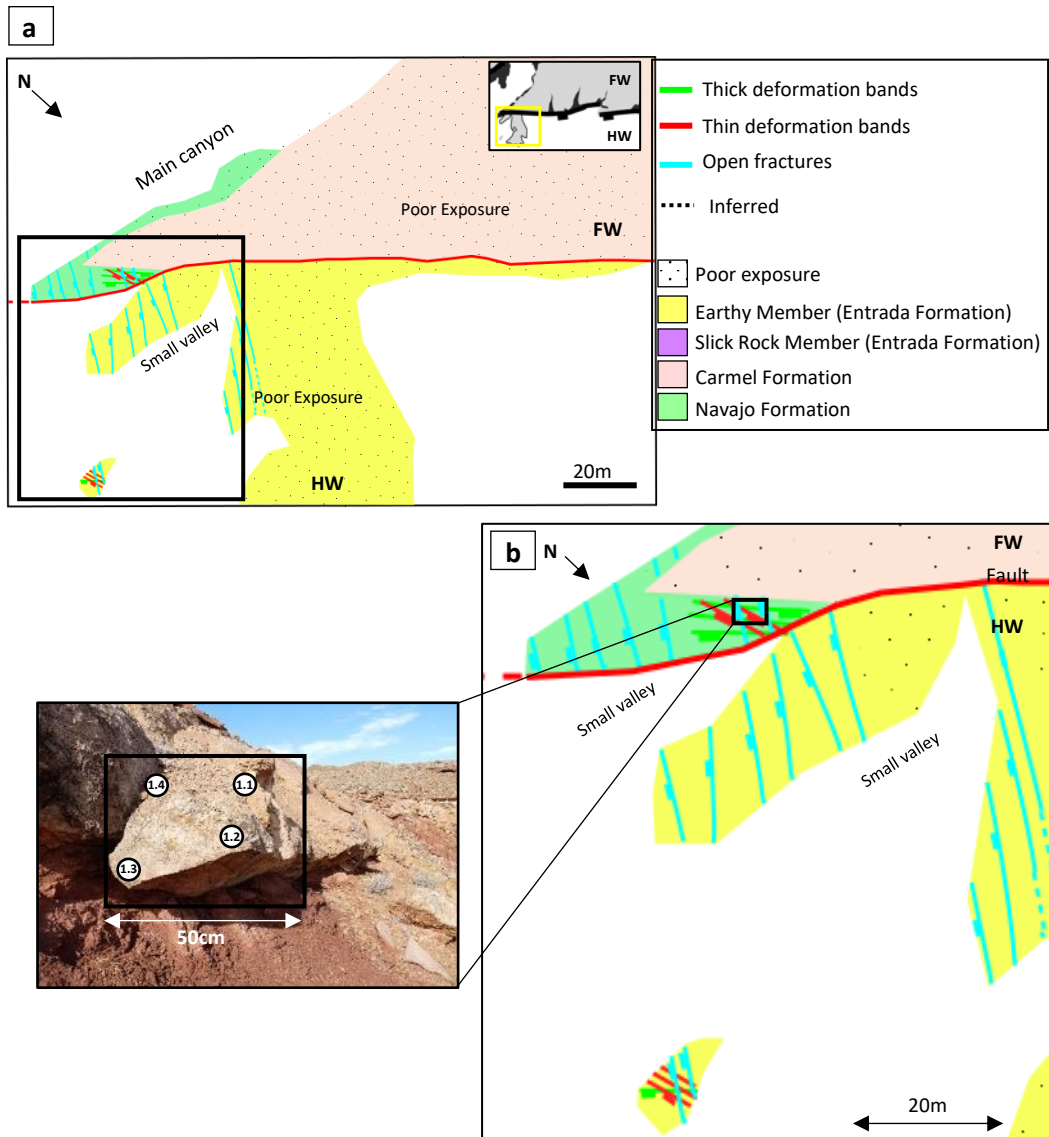
Figure 4.68– (a) Plan view map of the Cottonwood Wash locality. (b) Four samples were taken from the Navajo Formation in the footwall at the Cottonwood Wash locality.

Samples CWW 1.1, 1.2, 1.3 and 1.4 were each placed under the SEM and five photomicrographs were then taken from each sample and analysed for porosity (figure 4.69).

Sample: CWW 1.1   GR N 38°41'7.01" W110°24'0.61"
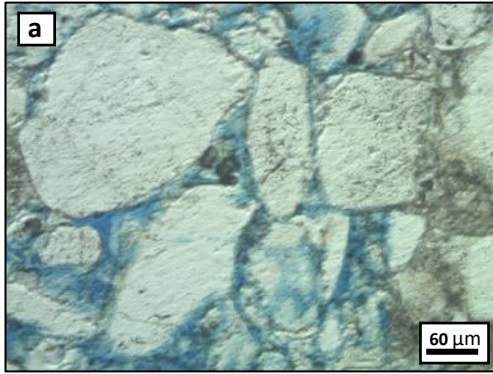
Original photomicrograph
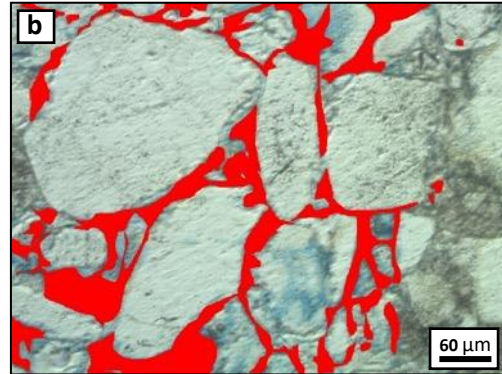
Total porosity* = 22.4%

Sample: CWW 1.2   GR N 38°41'6.95" W110°24'0.52"
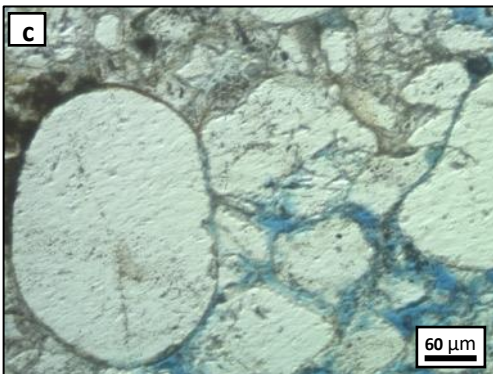
Original photomicrograph
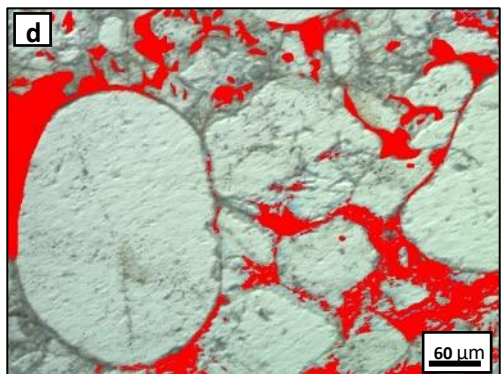
Total porosity* = 21.6%

Sample: CWW 1.3   GR N 38°41'6.91" W110°24'0.28"
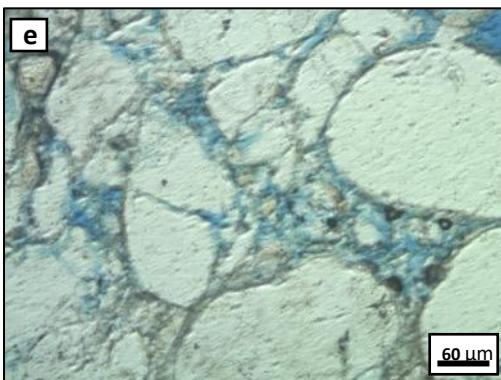
Original photomicrograph
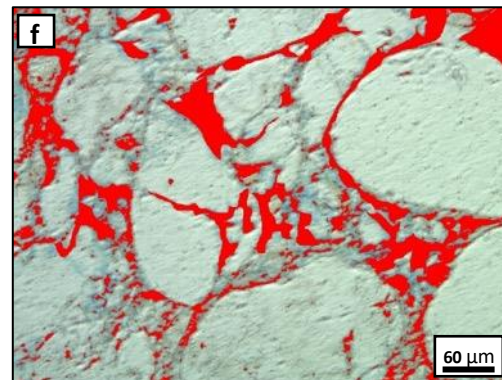
Total porosity* = 23.8%

Sample: CWW 1.4   GR N 38°41'6.85" W110°24'0.00"
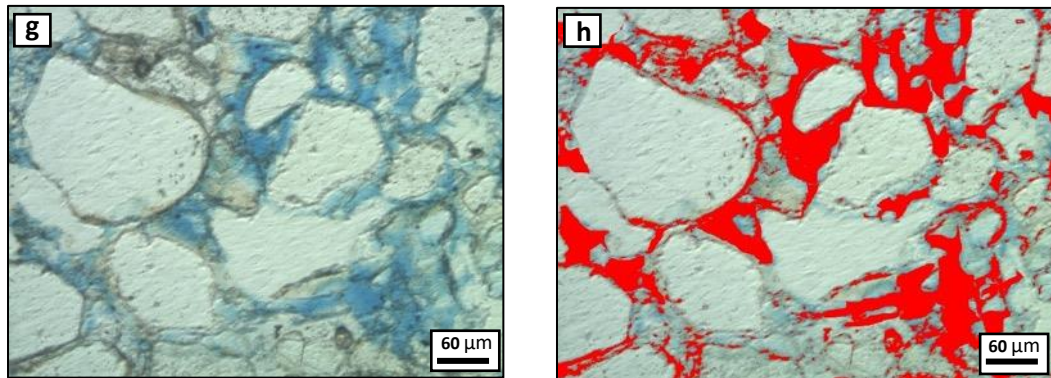
Original photomicrograph

Total porosity* = 22.4%

Figure 4.69 – Samples of the Cottonwood Wash locality which have been analysed for porosity; CWW 1.1 (a), (b), CWW 1.2 (c), (d), CWW 1.3 (e), (f), CWW 1.4 (g), (h).
* Total porosity = taken from the average of five photomicrographs per one sample.

Table 9 outlines the porosity data from the Cottonwood Wash locality.

Sample (photomicrograph)	Modern porosity	Filled porosity	Total porosity	Cement?*	DFBs present at the site?
CWW 1.1 (1)	14%	7%	21%	2%	Yes
CWW 1.1 (2)	18%	6%	24%	1%	Yes
CWW 1.1 (3)	19%	8%	27%	3%	Yes
CWW 1.1 (4)	13%	7%	20%	2%	Yes
CWW 1.1 (5)	15%	5%	20%	2%	Yes
Average at CWW 1.1	15.8%	6.6%	22.4%	2%	Yes
CWW 1.2 (1)	13%	8%	21%	3%	Yes
CWW 1.2 (2)	16%	6%	22%	2%	Yes
CWW 1.2 (3)	14%	5%	19%	4%	Yes
CWW 1.2 (4)	12%	9%	21%	2%	Yes
CWW 1.2 (5)	19%	6%	25%	2%	Yes
Average at CWW 1.2	14.8%	6.8%	21.6%	2.6%	Yes
CWW 1.3 (1)	14%	7%	21%	1%	Yes
CWW 1.3 (2)	18%	8%	26%	3%	Yes
CWW 1.3 (3)	15%	10%	25%	2%	Yes
CWW 1.3 (4)	18%	6%	24%	1%	Yes
CWW 1.3 (5)	15%	8%	23%	3%	Yes
Average at CWW 1.3	16%	7.8%	23.8%	2%	Yes
CWW 1.4 (1)	18%	3%	21%	3%	Yes
CWW 1.4 (2)	16%	6%	22%	4%	Yes
CWW 1.4 (3)	15%	4%	19%	1%	Yes
CWW 1.4 (4)	16%	9%	25%	1%	Yes
CWW 1.4 (5)	17%	8%	25%	2%	Yes
Average at CWW 1.4	16.4%	6%	22.4%	2.2%	Yes
Cottonwood Wash average	15.8%	6.8%	22.6%	2.2%	Yes

Table 9 – Porosity data from the Cottonwood Wash locality.
Including calcite, dolomite and clays.

As shown in table 9, the average modern day porosity for the Navajo Formation at the Cottonwood Wash locality is 15.8%, with an average of 6.8% filled porosity. Calcite cement, dolomite and clays constitute the filled porosity of the Navajo Formation, as identified through EDS (figure 4.70). The percentage of calcite cement, dolomite and clays remains low at only 2.2% on average at this locality.
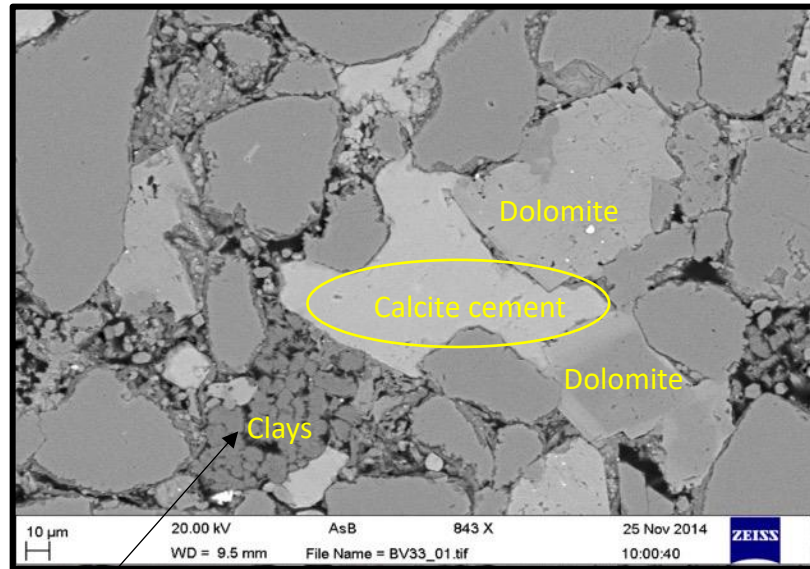
Kaolinite, as identified through EDS (Energy Dispersive Spectroscopy)

Figure 4.70 – In the space between the quartz there is evidence of calcite cement, dolomite and clays which have been identified through EDS analysis.

Sample: CNS 1.1   GR N 38°42'8.66" W110°26'24.12"

Original photomicrograph

Total porosity* = 14.6%

Sample: CNS 1.2   GR N 38°42'8.60" W 110°26'24.03"

Original photomicrograph

Total porosity* = 14.4%

Sample: CNS 1.3   GR N 38°42'8.58" W110°26'24.01"

Original photomicrograph

Total porosity* = 20%

Sample: CNS 1.4   GR N 38°42'8.63" W110°26'23.97"

Original photomicrograph
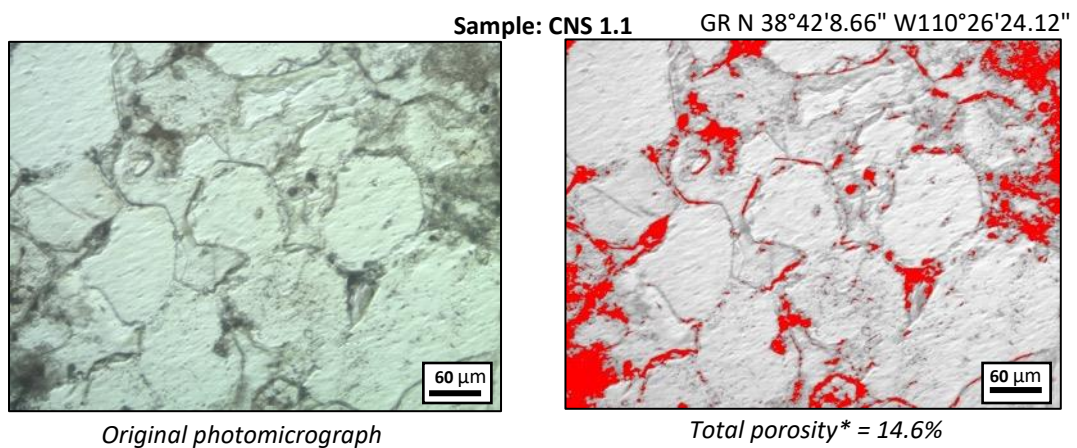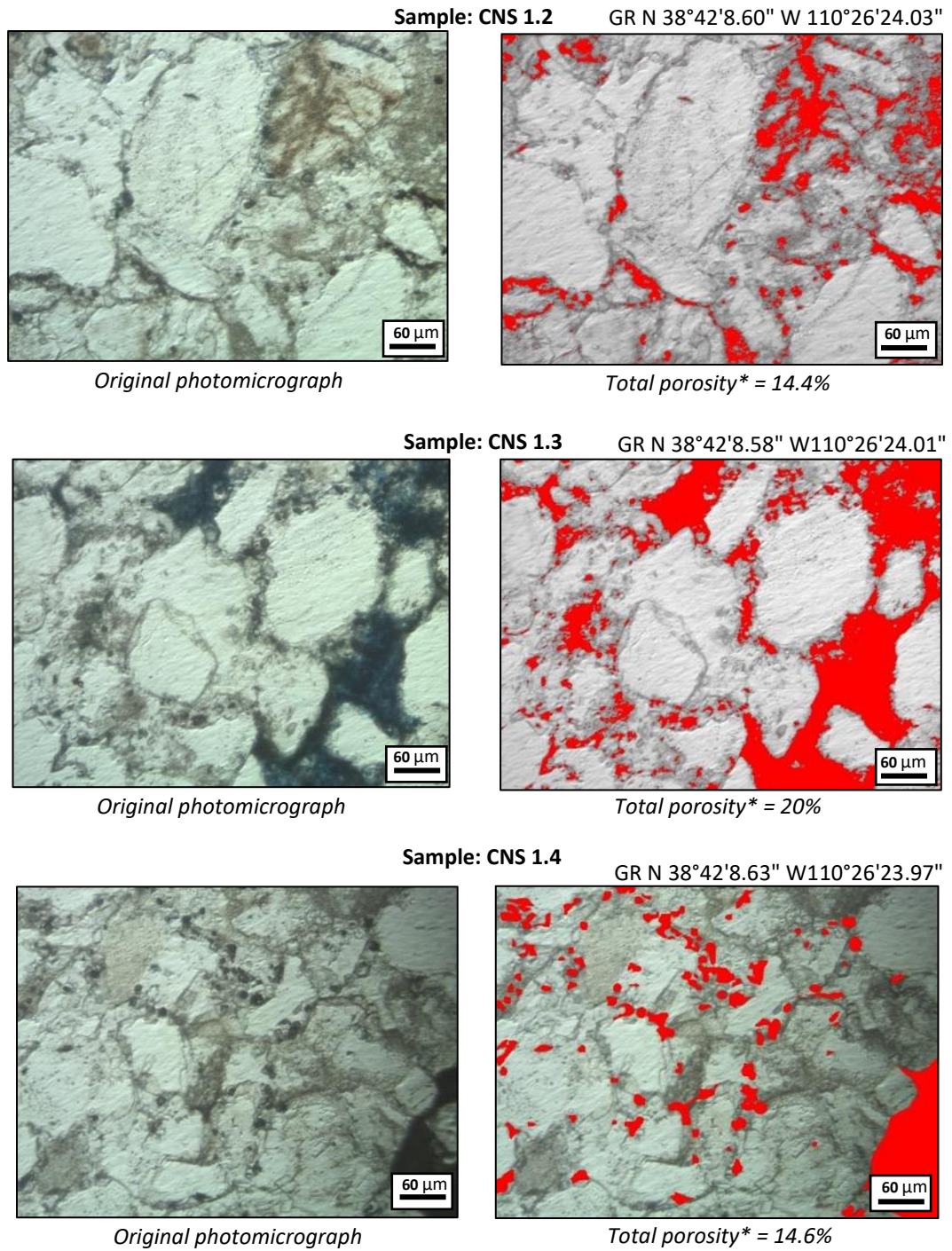
Total porosity* = 14.6%

Figure 4.71 – Samples of the Crow's Nest Spring locality which have been analysed for porosity; CNS 1.1 (a), (b), CNS 1.2 (c), (d), CNS 1.3 (e), (f), CNS 1.4 (g), (h).
* Total porosity = taken from the average of five photomicrographs per one sample.

Table 10 outlines the porosity data from the Crow's Nest Spring locality.

Sample (photomicrograph)	Modern porosity	Filled porosity	Total porosity	Cement?*	DFBs present at the site?
CNS 1.1 (1)	1%	8%	18%	12%	No
CNS 1.1 (2)	2%	12%	14%	14%	No
CNS 1.1 (3)	1%	10%	11%	10%	No
CNS 1.1 (4)	2%	14%	16%	12%	No
CNS 1.1 (5)	2%	12%	14%	13%	No
Average at CNS 1.1	1.6%	11.2%	14.6%	12.2%	No
CNS 1.2 (1)	4%	10%	14%	11%	No
CNS 1.2 (2)	6%	11%	17%	13%	No
CNS 1.2 (3)	2%	14%	16%	9%	No
CNS 1.2 (4)	2%	9%	11%	12%	No
CNS 1.2 (5)	2%	12%	14%	8%	No
Average at CNS 1.2	3.2%	11.2%	14.4%	10.6%	No
CNS 1.3 (1)	10%	11%	21%	9%	No
CNS 1.3 (2)	12%	8%	20%	12%	No
CNS 1.3 (3)	8%	12%	20%	8%	No
CNS 1.3 (4)	10%	8%	18%	7%	No
CNS 1.3 (5)	11%	13%	21%	7%	No
Average at CNS 1.3	10.2%	10.4%	20%	8.6%	No
CNS 1.4 (1)	1%	14%	15%	10%	No
CNS 1.4 (2)	2%	12%	14%	10%	No
CNS 1.4 (3)	2%	11%	13%	14%	No
CNS 1.4 (4)	5%	13%	18%	12%	No
CNS 1.4 (5)	3%	10%	13%	8%	No
Average at CNS 1.4	2.6%	12%	14.6%	10.8%	No
Crow's Nest Spring average	4.4%	11.2%	15.9%	10.5%	No

Table 10 – Porosity date from the Crow's Nest Spring locality.

Including calcite dolomite and clays.

As shown in table 10, the average modern day porosity for the Navajo Formation at the Crow's Nest locality is low at only 4.4%. Filled porosity comprises slightly more with 11.2% of filled porosity on average. In total, the average total porosity of the Navajo Formation at this locality is moderate to high at 15.9%. However, unlike the Navajo Formation at the Cottonwood Wash locality, calcite cement comprises a slightly higher % of the sample with 10.5% on average at this locality.

Sample: Square 1   GR N 38°42'32.44" W 110°26'58.48"
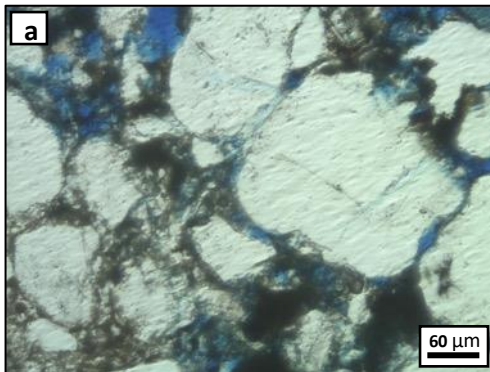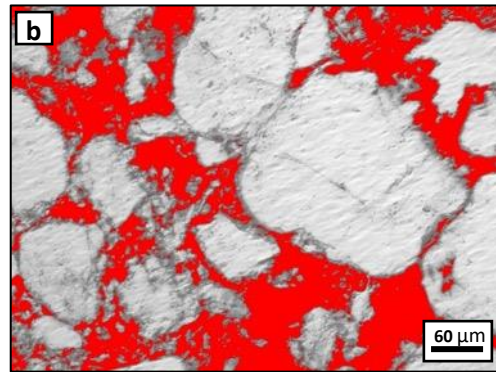
Original photomicrograph   *Total porosity* = 30%*

Sample: Square 2   GR N 38°42'32.24" W 110°26'58.89"
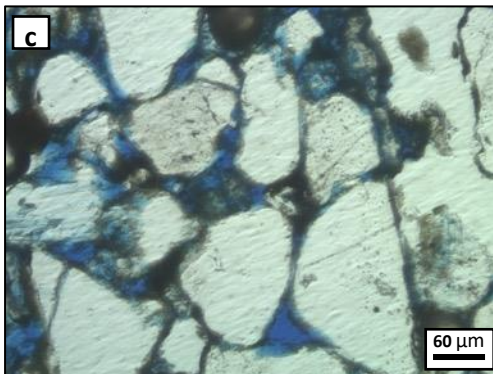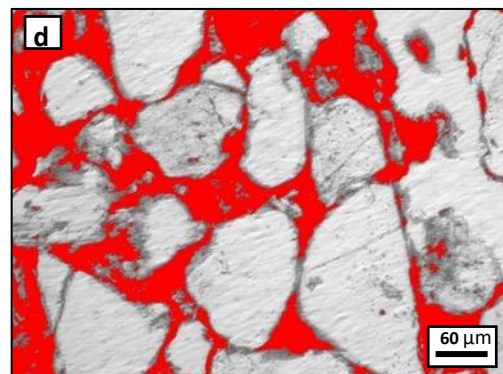
Original photomicrograph   *Total porosity* = 29.6%*

Sample: Square 4   GR N 38°42'32.24" W 110°26'58.89"
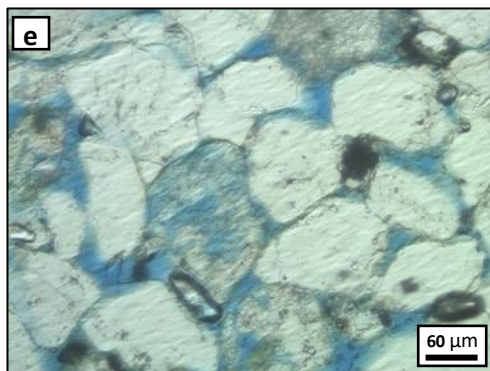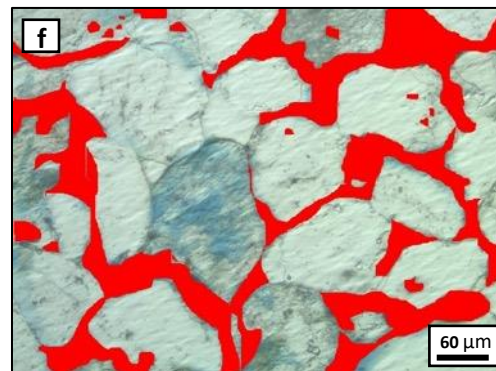
Original photomicrograph   *Total porosity* = 30.6%*

151

Sample: Square 5   GR N 38°42'32.10" W 110°26'59.27"

Original photomicrograph
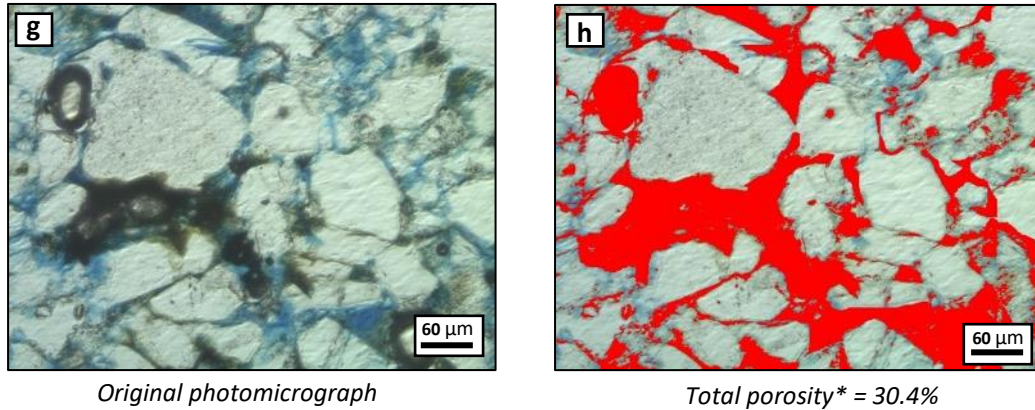
Total porosity* = 30.4%

Figure 4.72 – Samples of the Brush Valley locality which have been analysed for porosity; Square 1 (a), (b), Square 2 (c), (d), Square 4 (e), (f), Square 5 (g), (h).
*Total porosity = taken from the average of five photomicrographs per one sample

Table 11 outlines the porosity data from the Brush Valley locality.

Sample (photomicrograph)	Modern porosity	Filled porosity	Total porosity	Cement?*	DFBs present at the site?
Square 1 (1)	17%	12%	29%	1%	Yes
Square 1 (2)	20%	11%	31%	3%	Yes
Square 1 (3)	15%	16%	31%	2%	Yes
Square 1 (4)	15%	13%	28%	2%	Yes
Square 1 (5)	14%	17%	31%	1%	Yes
Average at Square 1	16.2%	13.8%	30%	1.8%	Yes
Square 2 (1)	17%	15%	32%	2%	Yes
Square 2 (2)	19%	14%	33%	1%	Yes
Square 2 (3)	15%	14%	29%	1%	Yes
Square 2 (4)	13%	11%	24%	4%	Yes
Square 2 (5)	17%	13%	30%	4%	Yes
Average at Square 2	16.2%	13.4%	29.6%	2.4%	Yes
Square 4 (1)	16%	13%	29%	2%	Yes
Square 4 (2)	19%	10%	29%	3%	Yes
Square 4 (3)	15%	17%	32%	1%	Yes
Square 4 (4)	21%	12%	33%	1%	Yes
Square 4 (5)	15%	15%	30%	3%	Yes
Average at Square 4	17.2%	13.4%	30.6%	2%	Yes
Square 5 (1)	14%	14%	28%	3%	Yes

Square 5 (2)	19%	16%	35%	1%	Yes
Square 5 (3)	18%	11%	29%	5%	Yes
Square 5 (4)	15%	13%	28%	2%	Yes
Square 5 (5)	16%	16%	32%	1%	Yes
Average at Square 5	16.4%	14%	30.4%	2.4%	Yes
Brush Valley average	16.5%	13.7%	30%	2%	Yes

Table 11 – Porosity date from the Brush Valley locality.
*Including calcite, dolomite and clays.

As shown in table 11, the average modern day porosity for the Slick Rock Entrada Formation at the Brush Valley locality is moderate at 16.5%. Filled porosity comprises slightly less with 13.7% of filled porosity on average. The total porosity of the Slick Rock Entrada at this locality is high at 30%. However, calcite cement is low at only 2% on average as a % of the total sample.

Overall, there is evidence of local variations in the porosity and % of calcite cement present in the Navajo Formation at the Crow's Nest Fault (table 12). Where deformation bands are exposed in the Navajo Formation, the porosity is higher compared to where there are no deformation bands present. At the Crow's Nest Spring locality there are no deformation bands exposed and the average porosity is 15.9% compared to an average porosity of 22.6% at the Cottonwood Wash locality where deformation bands are exposed. Additionally, where deformation bands are exposed at the Cottonwood Wash site, calcite cement is sparse (2.2% on average) compared to the Crow's Nest Spring site where deformation bands are not found and there is more calcite cement present (10.9% on average).

Location (Lithology)	Modern porosity	Filled porosity	Total porosity	Calcite cement?*	DFBs present at the site?
Cottonwood Wash (Navajo)	15.8%	6.8%	22.6%	2.2%	Yes
Crow's Nest Spring (Navajo)	4.4%	11.2%	15.9%	10.5%	No
Brush Valley (Slick Rock, Entrada)	16.5%	13.7%	30%	2%	Yes

Table 12 – Porosity date from all studied localities at the Crow's Nest Fault.
*Including dolomite and clays.

4.8.2 Comparison of cementation and porosity of host rock elsewhere in Utah

Across the rest of Utah, the Navajo Formation has been extensively analysed for porosity measurements (table 13).

Lithology	Description	Reference	Porosity	Location	DFBs present?	Measured technique
Navajo	Aeolian sandstone, planar to cross bedded, medium to fine grained, well sorted and well-rounded sandstone	Shipton and Cowie, (2001)	19.2%	Big Hole Fault, Utah	Yes	Image analysis of BSEM images using two software packages; Erdas Imagine and Optimas.
Navajo	Very well sorted, porous sandstone	Fossen et al., (2011)	20-25%	Buckskin Gulch, East Kaiba Monocline, Utah	Yes	Image analysis of SEM images and ambient-porosity laboratory measurements conducted on plugs taken along linear scanlines.
Navajo	Fine to medium grained, high porosity sandstone	Cooley et al., (1969)	10-30%	Laramide uplifts on the Colorado Plateau in south-ern Utah	Yes	Water pumping tests through drill cores.
Navajo	**Very fine grained, massive aeolian sandstone**	**This thesis**	**22.6%** ***Total porosity***	**Cottonwood Wash (FW)– Crow's**	**Yes**	**Image analysis of SEM images using**

				Nest Fault		Image J software.
Navajo	**Very fine grained, massive aeolian sandstone**	**This thesis**	**15.9% *Total porosity***	**Crow's Nest Spring (FW)-Crow's Nest Fault**	**No**	**Image analysis of SEM images using Image J software.**

Table 13 – Porosity data for the Navajo Formation compiled from studies of exposures within Utah.

Throughout Utah, the Navajo Formation commonly deforms by deformation banding (Shipton and Cowie, 2001; Johansen et al., 2005; Bright, 2006; Fossen et al., 2011). However, there were no deformation bands found in the Navajo Formation at Crow's Nest Spring. The Navajo Formation elsewhere in Utah tends to have a higher porosity (up to 30%) where deformation bands are exposed compared to an average of 15.9% at the Crow's Nest Spring locality. Additionally, there is a higher percentage of calcite cement at Crow's Nest Spring 10.5% compared to 2.2% on average at Cottonwood Wash. This suggests a likely relationship between deformation banding and porosity. Ideally further porosity analysis should be undertaken for un-deformed Navajo Formation at the Crow's Nest Spring locality to compare the porosity and calcite cement, however, no un-deformed Navajo Formation was exposed at the Crow's Nest Spring locality to do so.

Across the rest of Utah, the Slick Rock Entrada has been extensively analysed for porosity measurements (table 14).

Lithology	Description	Reference	Porosity	Location	DFBs present?	Measured technique
'Slick Rock Entrada'	- Aeolian sandstone interbedded with low permeability sabkha siltstones	Bright, (2006) - PhD thesis	9%	Yellow Cat Graben, Utah	Yes	Image analysis of BSEM images using Scion Image Analysis software
'Moab Member' *Equivalent to:*	- Aeolian dune sand inter-bedded with laminated	Antonellini and Aydin, (1994)	4 - 28%	Arches National Park	Yes	Image analysis of BSEM images and mini

Slick Rock Entrada	muddy siltstone sabkha beds - Fine to medium grained, well sorted					permeameter
'Moab Member' *Equivalent to:* Slick Rock Entrada	- Aeolian dune sand inter-bedded with laminated muddy siltstone sabkha beds - Fine to medium grained, well sorted	Antonellini and Aydin, (1994)	20-25%	Moab Fault	Yes	Image analysis of BSEM images and mini permeameter
'Moab Member' *Equivalent to:* Slick Rock Entrada	- Flood plain and fluvially deposited mudstones, siltstones, and sandstones	Johansen et al., (2005)	1-17%	Courthouse Branch Point, Moab fault	Yes	Image analysis of BSEM images
'Entrada' *Equivalent to:* Slick Rock Entrada	- Shale rich base - Porous sandstone - Highly permeable - Unconfined aquifer unit	Hood and Patterson, (1984)	26.4%	Salt Wash Graben (near Little Grand Wash)	No	Water saturated into core plug samples

Slick Rock Entrada	Well sorted sandstone and minor siltstone	This thesis	29.25% *Total porosity*	Brush Valley (lens) Crow's Nest Fault	Yes	Image analysis of SEM images

Table 14 – Porosity data for the Slick Rock Entrada compiled from studies of exposures within Utah.

Throughout Utah, the porosity of the Slick Rock Entrada is variable (Antonellini and Aydin, 1994; Johansen et al., 2005; Bright, 2006). For example, the Slick Rock Entrada at the Yellow Cat Graben, 20 miles south-west of the Crow's Nest Fault has an estimated porosity of 9% (Bright, 2006) (figure 4.73). Compared to the Slick Rock Entrada exposed at the Brush Valley locality where calcite cement is sparse, the Slick Rock Entrada has an iron oxide matrix at the Yellow Cat Graben, resulting in a less fragile rock then observed at Brush Valley.

It is important to note that there are a wide range of methods used to estimate porosity such as image analysis of SEM images, lab tests and the use of a mini permeameter. Different porosity tests will have varying levels of accuracy, bias and limitations which may lead to slight over and under estimations of porosity. However, it is clear to see from the porosity analysis of host rock taken from areas where there are varying frequencies of deformation bands present, that deformation structures are highly influenced by porosity.

Bright, (2006) estimated porosity at the Yellow Cat Graben using BSEM scales of x30 or x35 magnification which resulted in a 1% porosity error. As the observations from this thesis used the same methods they also had a 1% porosity error. However, porosity measurements of the Slick Rock Entrada were taken on x10 to x15 magnification and thus the 1% error was of a larger measurement so carries a larger absolute error by approximately 2-3 times. Nevertheless, most of the samples of the Slick Rock Entrada at the Brush Valley site are highly porous (up to 30%) and so this was not a major issue for this study.
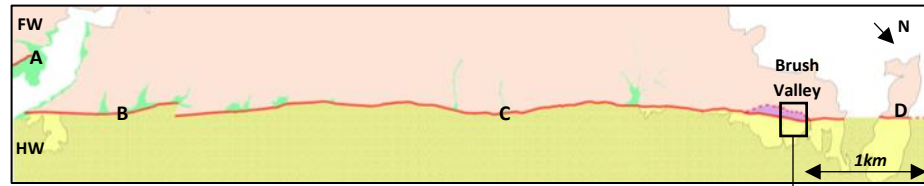
Brush Valley site, Crow's Nest Fault
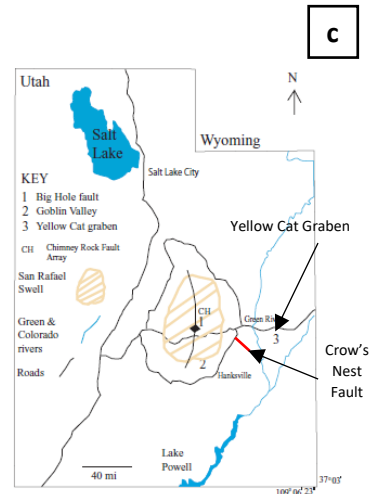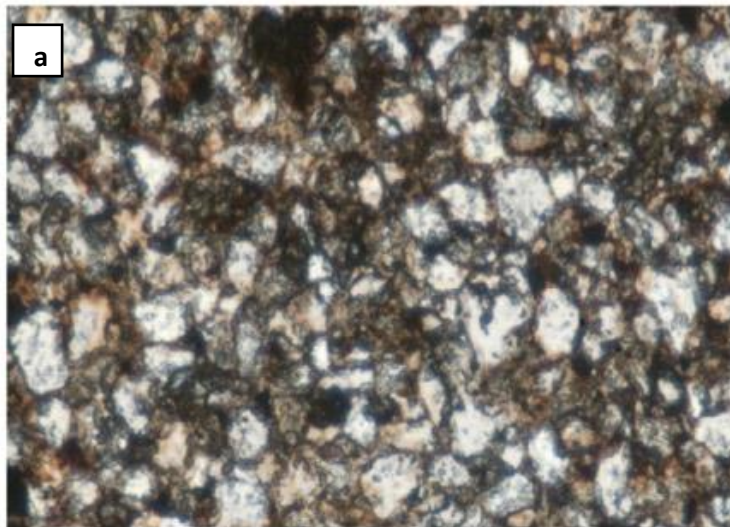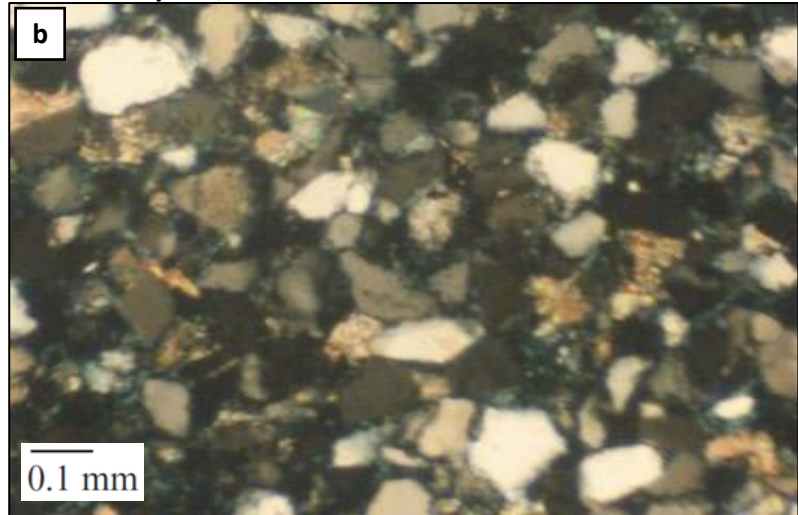
Yellow Cat Graben, Utah (Bright, 2006)

Figure 4.73 – (a) Photomicrograph of the Slick Rock Entrada Formation shows evidence of a cemented lithology at the Yellow Cat Graben (Bright, 2006) compared to (b) the Slick Rock Entrada Formation at Crow's Nest Fault which is a low cement rock. (c) Indicates the proximity of the Yellow Cat Graben to Crow's Nest Fault which is approximately 20 miles south-west (Bright, 2006).

At the Arches National Park, studies of the Slick Rock Entrada suggest porosity values as low as 4% and as high as 28% (Antonellini and Aydin, 1994). Porosity variations for the Slick Rock Entrada could be explained by the sedimentology. Samples of the Slick Rock Entrada at the Yellow Cat Graben were taken from an area rich in siltstone and had an average porosity of 9% compared to Antonellini and Aydin (1994) who studied samples from aeolian dune sets which yielded porosities of up to 28% (Bright, 2006).

Antonellini and Aydin, (1994) analysed the porosity of the Slick Rock Entrada at the Arches National Park through image analysis and the use of a mini permeameter. The use of the two devices was chosen to reduce inaccuracies related to averaging. For example, the use of core plugs for a sandstone rich in deformation bands will likely result in sampling the deformation bands which in turn affects the host rock porosity value. By using a mini permeameter and image analysis software, the pore geometry can be better characterised to help evaluate the effects on sealing potential, and to increase the accuracy of porosity analysis.

The use of image analysis software by Antonellini and Aydin, (1994) was undertaken in the same way as analysis at the Crow's Nest Fault and therefore would fit within the same error bounds. Results from Antonellini and Aydin, (1994) suggest a coupling relationship between host rock porosity on deformation mechanisms and deformation mechanisms influencing host rock porosity.

At Courthouse Branch Point, Moab Fault, porosity of the Entrada Formation ranges from 1-17% (Johansen et al., 2005). Small areas of unaltered rock have a maximum porosity of 17%, whereas rock which has been subject to high levels of quartz dissolution and precipitation yields porosities of 1%. Elsewhere along the Moab Fault porosity is much higher with averages of 20-25% (Antonellini and Aydin, 1994) which suggests that porosity is more variable at fault intersections at the Moab Fault. There is no evidence of quartz precipitation Brush Valley locality and in contrast to Courthouse Branch Point, there is evidence of dissolution of calcite cement instead which has resulted in a high, 30% average porosity.

At the Salt Wash Graben, near Little Grand Wash, the average porosity for the Entrada Formation is 26.4% (Hood and Patterson, 1984). This porosity value is similar to the 30% average calculated for the Brush Valley, however the methods used in analysing are very different. Porosity was calculated by pumping water through core plug samples. In doing

so, the % of moisture within each core sample is measured by volume and then the porosity can be calculated. As with core sampling, there are always limitations with gaining a representation of samples as cores only focus on a very limited area.

4.9 Interpretation

For the co-existence of deformation bands (thick and thin) to be situated within the same rock, there must be a decrease in porosity. This could occur due to an increase in burial and compaction, through fluid interaction with the host rock (Fossen et al., 2007) or through changes in stress (Davatzes and Aydin, 2003).

At the Crow's Nest Fault, where there are deformation bands present, porosity is on average 6.7-14.1% higher than where there are no deformation bands present (table 2). For example, the porosity of the Navajo Formation is 6.7% higher at the Cottonwood Wash locality where there are thick and thin deformation bands present compared to where there are no deformation bands present at the Crow's Nest Spring locality and the porosity is only 15.9% compared to 22.6%.

Elsewhere in Utah the porosity of the Navajo Formation varies from ~10-30% regionally as shown in table 13 (Cooley et al., 1969; Dunn et al., 1973; Shipton and Cowie, 2001; Beitler et al., 2003; Fossen et al., 2011) and the porosity of the Slick Rock Entrada varies from 4-28% as shown in table 14 (Hood and Patterson, 1984; Antonellini and Aydin, 1994; Johansen et al., 2005; Bright, 2006).

Studies of deformation banding and fracturing within the same rock unit at the Courthouse Branch Point, Moab Fault show evidence for a switch from thick bands to thin bands to later fracturing. Johansen et al., (2005) suggest that the switch from thick to thin deformation banding is due to a decrease in porosity. However, fracturing at the Courthouse Branch Point has strengthened the host rock through mineralisation, whereas fracturing at the Crow's Nest Fault has altered and weakened the rock. Instead, the switch from deformation banding to fracturing at the Crow's Nest Fault more closely follows studies by Davatzes and Aydin, (2003) whereby a period of uplift has caused the change in deformation style.

As a rock deforms by banding, the strength of a rock increases whilst the porosity starts to decrease up to a point where the rock can only deform by fracturing. As observed at the Crow's Nest Fault, first generation deformation bands (thick bands) have a maximum

thickness of 1cm. In comparison, second generation deformation bands (thin bands) have a maximum thickness of 0.4mm. Over time as the frequency of thick bands increased, the host rock becomes more compacted which reduces the porosity significantly so there is less room for grain rolling and reorganisation associated with deformation band formation.

At the Crow's Nest Fault, porosity is higher close to the fault tips and at the Brush Valley lens. This could be due to an increase in porosity post-faulting due to migration of fluids to the surface and the dissolution of calcite cement, or that fault strands stopped growing at areas of high porosity. The host rock is highly porous (up to 30%) at fault tips and within the Brush Valley lens, there is very little calcite cement (~2%) and deformation bands are exposed. Away from the fault strand ends, the host rock is less porous (15.9%), well cemented and there are no deformation bands exposed (table 12).

Deformation bands at the Crow's Nest Fault likely formed everywhere along the fault but are only observed where exposure is good at fault tips and lenses. It is therefore likely that no deformation bands were observed along the main fault strands because there is a lack of good exposure along the main fault strands.

Iron-rich fractures are only found at the Brush Valley lens site. Open fractures are found everywhere at Crow's Nest Fault but the highest frequency of open fractures is situated at the Crow's Nest Spring lens site. Iron-rich fractures are only found at the Brush Valley location in the lens. These fractures are orientated north-south and dip on average 46° towards the north-west and towards the hanging wall.

Changes in fracture orientation are likely due to the differences in mechanical strength of the Brush Valley lens compared to the footwall and hanging wall. Within the Brush Valley lens, the host rock appears crumbly, fragile and weak. Prior to fracturing, fluid flow likely migrated through the Brush Valley lens which could have weakened the rock.

4.10 Summary

There are four types of deformation structures present at the Crow's Nest Fault; thick deformation bands, thin deformation bands, iron-rich fractures and open fractures. From analysing cross cutting relationships in the field and under thin section, the timing of the structures has been constrained.

Thick deformation bands are the oldest deformation structure to form at Crow's Nest Fault. Back rotation of the bedding within the Brush Valley lens has been used to deduce that thick deformation bands formed before the tilting of the bedding within the lens. These structures are likely precursors to fault formation. From cross cutting relations, thin deformation bands are the next deformation structure to form followed by iron-rich fractures and then open fractures.

Thick deformation bands and thin deformation bands are always found together. Thick and thin deformation bands are only found at the ends of fault strands or within the sandstone lens at the Brush Valley and Zippy Canyon sites. There is only one exposure of deformation bands in the hanging wall and this is likely due to local variations in porosity of the Entrada Formation. Studies of faults in Utah suggest that deformation bands can form in isolated patches, as linked systems and on both sides of a fault (Aydin and Johnson, 1983; Fossen and Hesthammer, 1997). Factors which affect the number of deformation bands forming during slip include burial depth, grain size, porosity and cementation (Fossen et al., 2007).

At the Crow's Nest Fault, thick deformation bands are subparallel to the fault and on average dip 55° towards the north in the lens and 20° towards the north in the footwall. Thin deformation bands are perpendicular to the fault and dip between 12° and 61° towards the north.

In summary, host rock porosity is 6.7-14.1% higher on average where there are deformation bands exposed compared to where there are no deformation bands present. Deformation bands are exposed at fault tips and within the sandstone lens at the Brush Valley site. Where deformation bands are exposed, not only is porosity higher but there is approximately 8% less calcite cement compared to host rock where there are no deformation bands exposed. Porosity controls whether the host rock deforms by fracturing or through the formation of deformation bands.

Chapter 5

Evidence of Paleo Fluid Flow

5.1 Introduction

This chapter presents evidence for modern and paleo fluid flow at the Crow's Nest Fault. Evidence of fluid flow includes hydrocarbons, iron oxide staining, nodules and iron-rich fractures, bleaching and the dissolution of calcite cement and water flow.

Section 5.2 outlines the different types of fluid flow evidence exposed at the Crow's Nest Fault. The location and distribution of fluid flow evidence with respect to the fault zone is outlined in section 5.3. In section 5.4 the origins and chemistry of fluids in the basin are discussed. A summary outlining the evidence for the origin of the modern and paleo fluid flow at the Crow's Nest Fault is discussed in section 5.5.

5.2 Fluid flow features

This section presents evidence for fluid flow at the Crow's Nest Fault. Through a combination of field observations and microanalysis, the different types of fluid flow evidence observed at the Crow's Nest Fault are described and characterised. Sampling methods and host rock samples used to analyse fluid flow within this chapter are the same as those used in chapter 4. Methodology and rationale of sampling is outlined in section 4.3.

5.2.1 Modern hydrocarbons

Hydrocarbons are exposed in three ways at the Crow's Nest Fault; as hydrocarbons which stain the host rock (figures 5.1a and 5.1b), as hydrocarbons which seep from fracture junctions in the host rock (figures 5.1c and 5.1d) and as hydrocarbons which infill fractures (figure 5.1e and 5.1f).
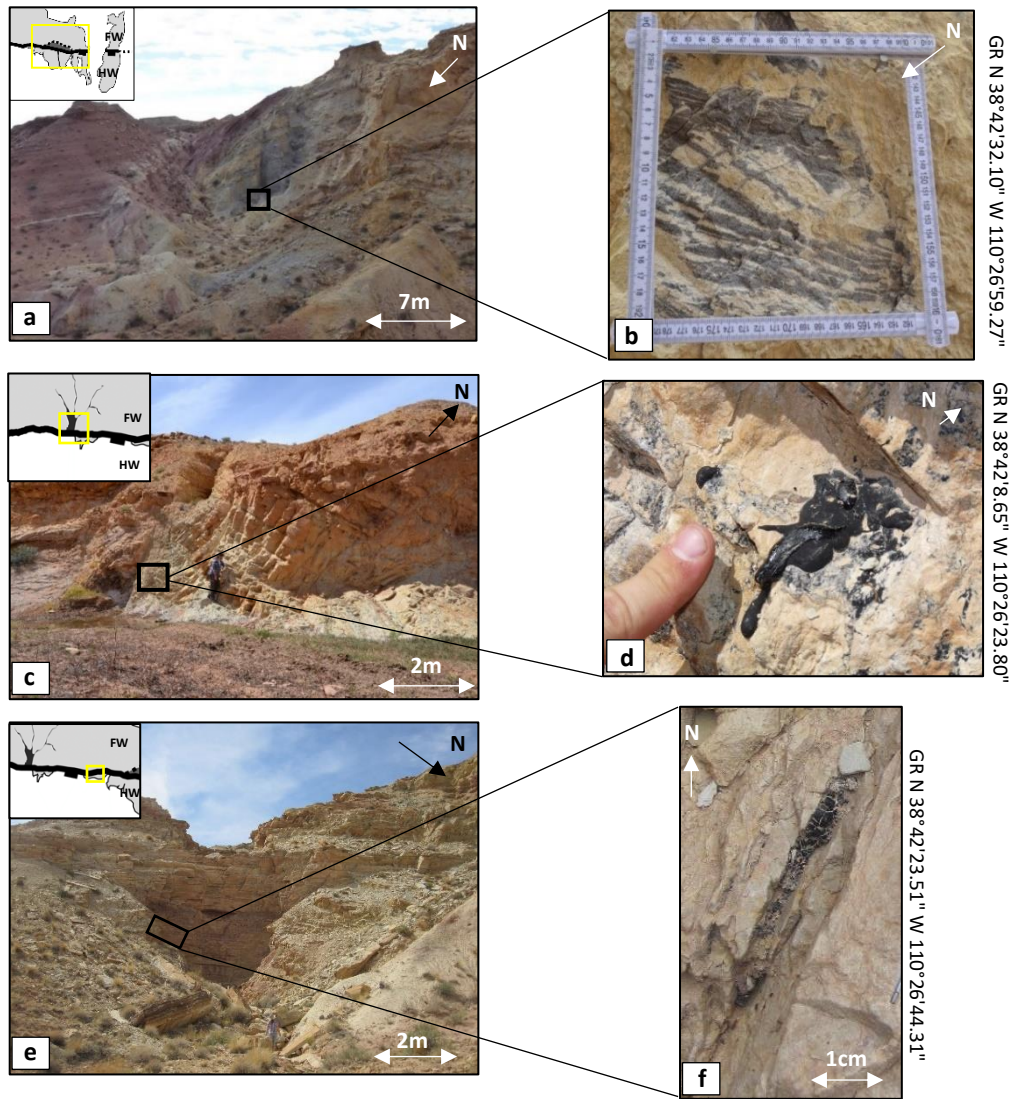
Figure 5.1 – At Crow's Nest Fault, hydrocarbons are exposed in three ways; as hydrocarbons staining within the host rock (a & b), as modern day hydrocarbons which seep out of fracture junction (c & d) and as hydrocarbons which infill fractures (e & f).

In the field, hydrocarbons are observed as black and dark grey material which stains the host rock as seen in figures 5.2a and 5.2b.
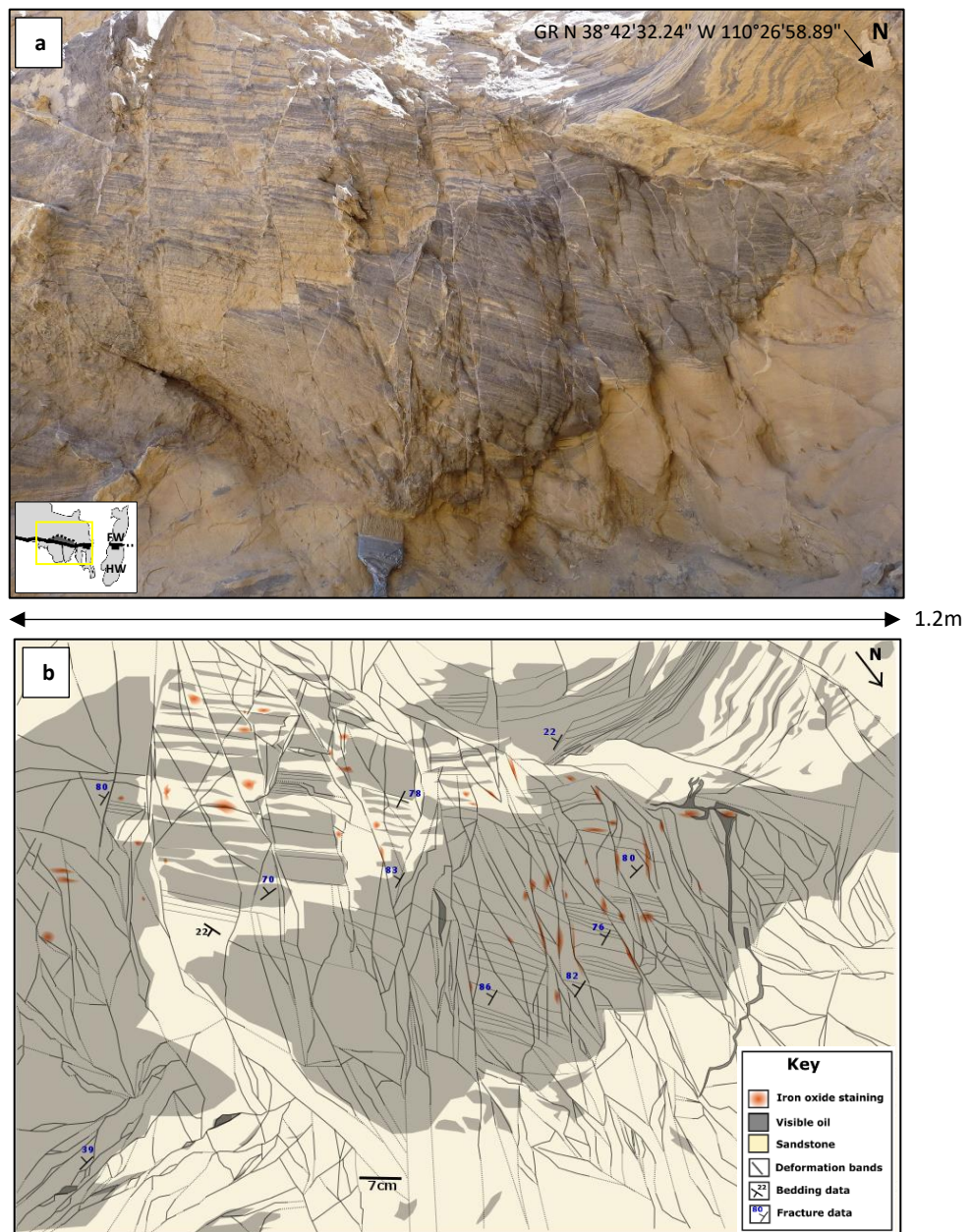
Figure 5.2 – (a) Photograph showing hydrocarbon staining within the host rock. (b) Interpretation shown by figure 5.2b showing the relationship of deformation bands with iron oxide staining and hydrocarbon staining.

Hydrocarbons that stain the host rock are observed in isolated or continuous patches ranging in size from ~1cm to 9m. Where hydrocarbons stain the host rock, the host rock appears less cemented and more fragile than the surrounding host rock (figure 5.3).

GR N 38°42'32.12" W 110°26'58.18"

Host rock stained by hydrocarbons appears more crumbly/fragile

Host rock which has not been stained by hydrocarbons appears less crumbly/fragile
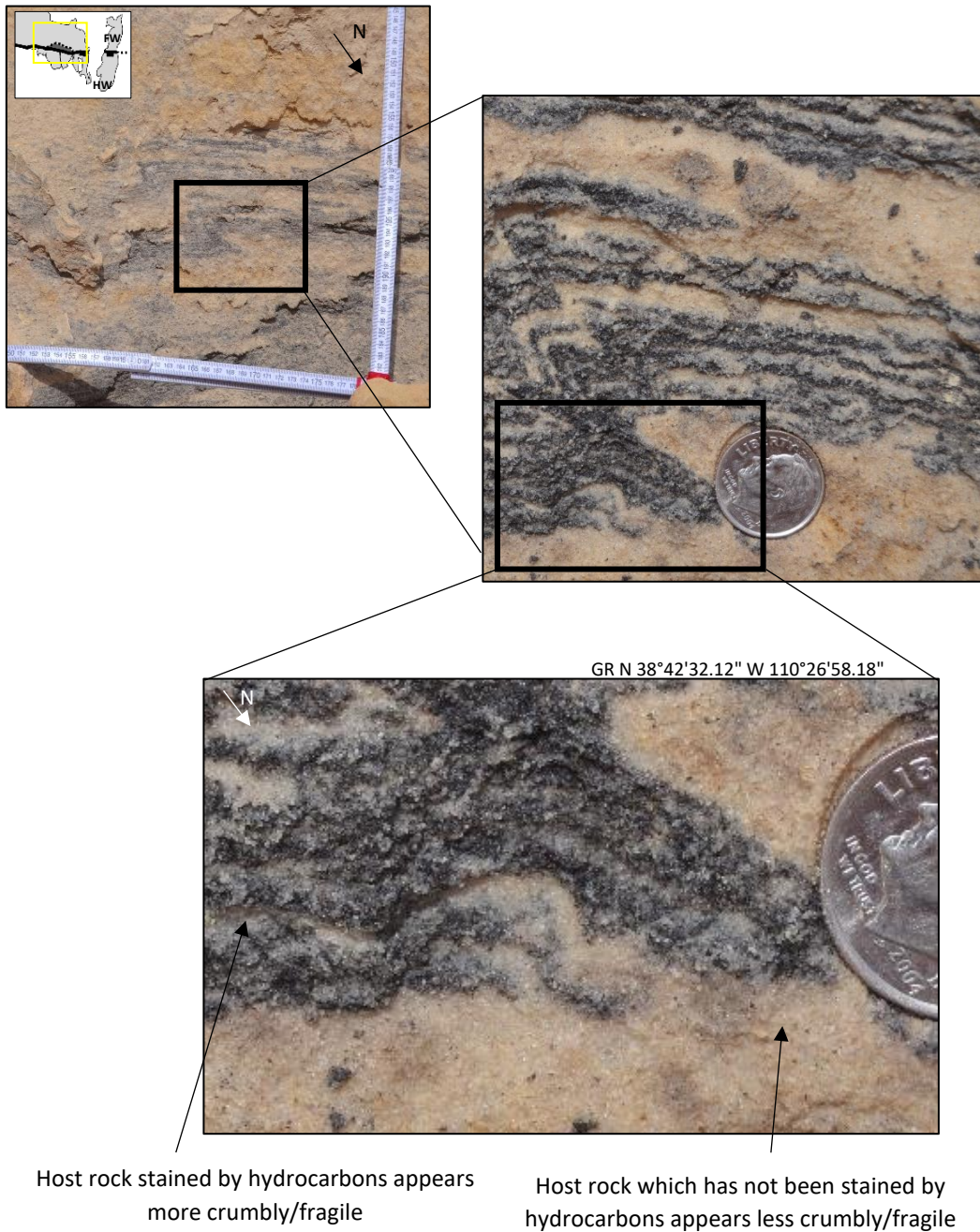
Figure 5.3 – Where the host rock is stained by hydrocarbons, the rock appears more crumbly, fragile and less cemented compared to the surrounding host rock. Photo of the Slick Rock Entrada at the Brush Valley lens locality.

Samples of the Slick Rock Entrada at the Brush Valley lens locality have been analysed under thin section. Possible hydrocarbons have been identified through EDS and the methodology and rationale for this is outlined in section 4.3. Hydrocarbons are observed coating quartz grains and infilling vacant pore spaces (figure 5.4a and 5.4b).

GR N 38°42'31.67" W 110°26'58.42"
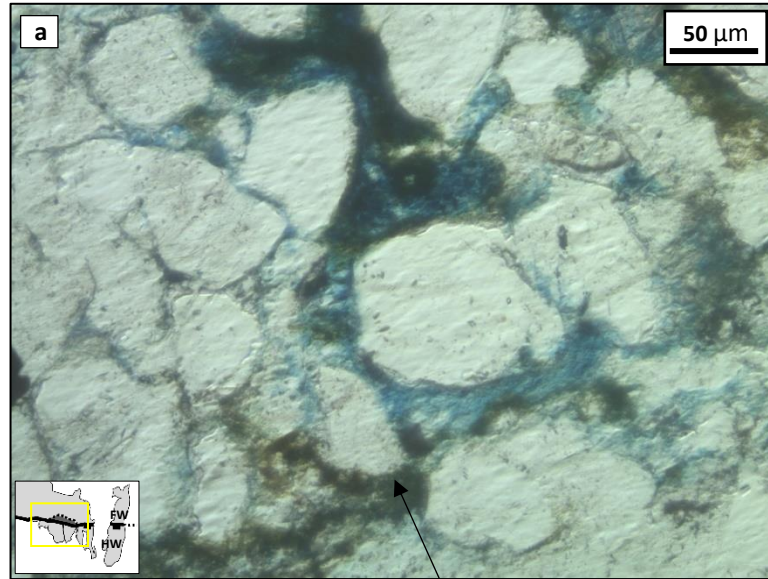
Coating of hydrocarbons surrounding the quartz

GR N 38°42'31.93" W 110°26'58.56"
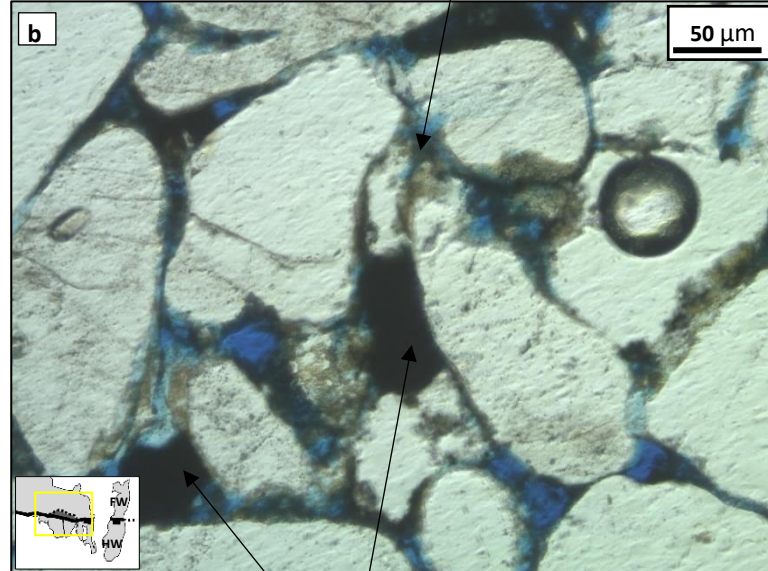
Hydrocarbon infilling open pore space

Figure 5.4 – Photomicrographs of the Slick Rock Entrada showing hydrocarbon coating around quartz grains (a) and infilling vacant pore space (b).

In the rest of Utah, there is little evidence for hydrocarbons present within the Slick Rock Entrada. Where the Slick Rock Entrada does not show evidence of hydrocarbons coating quartz grains and infilling pore space, pore space is occupied by calcite cement and an iron oxide matrix as shown in figure 5.5 (Bright, 2006).
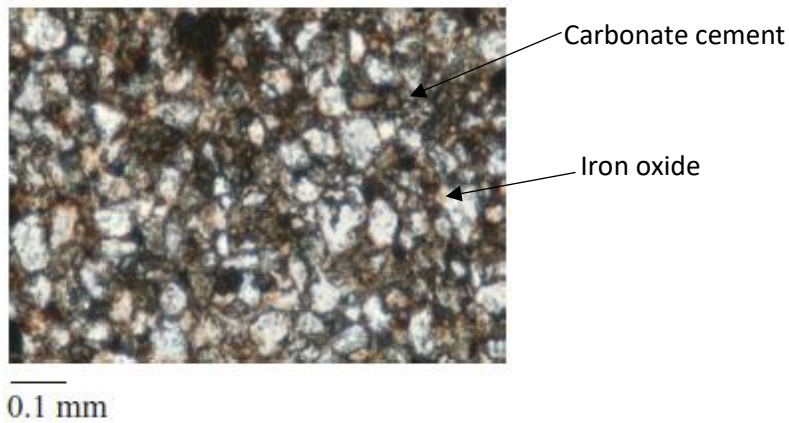
Figure 5.5 – Photomicrograph of the Slick Rock Entrada taken from the Yellow Cat Graben, Utah which shows a lack of hydrocarbon staining and instead, calcite and iron oxide rich material infilling pore space and coating quartz grains (Bright, 2006).

For hydrocarbons to have coated quartz grains and infilled pore space, calcite cement must have been removed to allow space for the hydrocarbons to infill the rock. This is likely due to cement dissolution and this is discussed in more detail in section 5.2.3.

Modern day hydrocarbons which seep out of fracture junctions are only observed within the Carmel Formation within the Crow's Nest Spring lens and in the Navajo Formation within the footwall at Crow's Nest Spring locality. Hydrocarbons are observed seeping out of the host rock where two or more fractures meet at fracture junctions (figure 5.6a). Hydrocarbons are observed as black, viscous liquid with a high shine and are sticky to the touch (figures 5.6 b, c, d).

Modern day hydrocarbons which infill fractures are only observed within the Navajo Formation within the footwall at the Old Mine locality. Hydrocarbons that infill fractures are black and hardened with a high shine but are not sticky to the touch (figure 5.8c).

GR N 38°42'8.65" W 110°26'23.75"
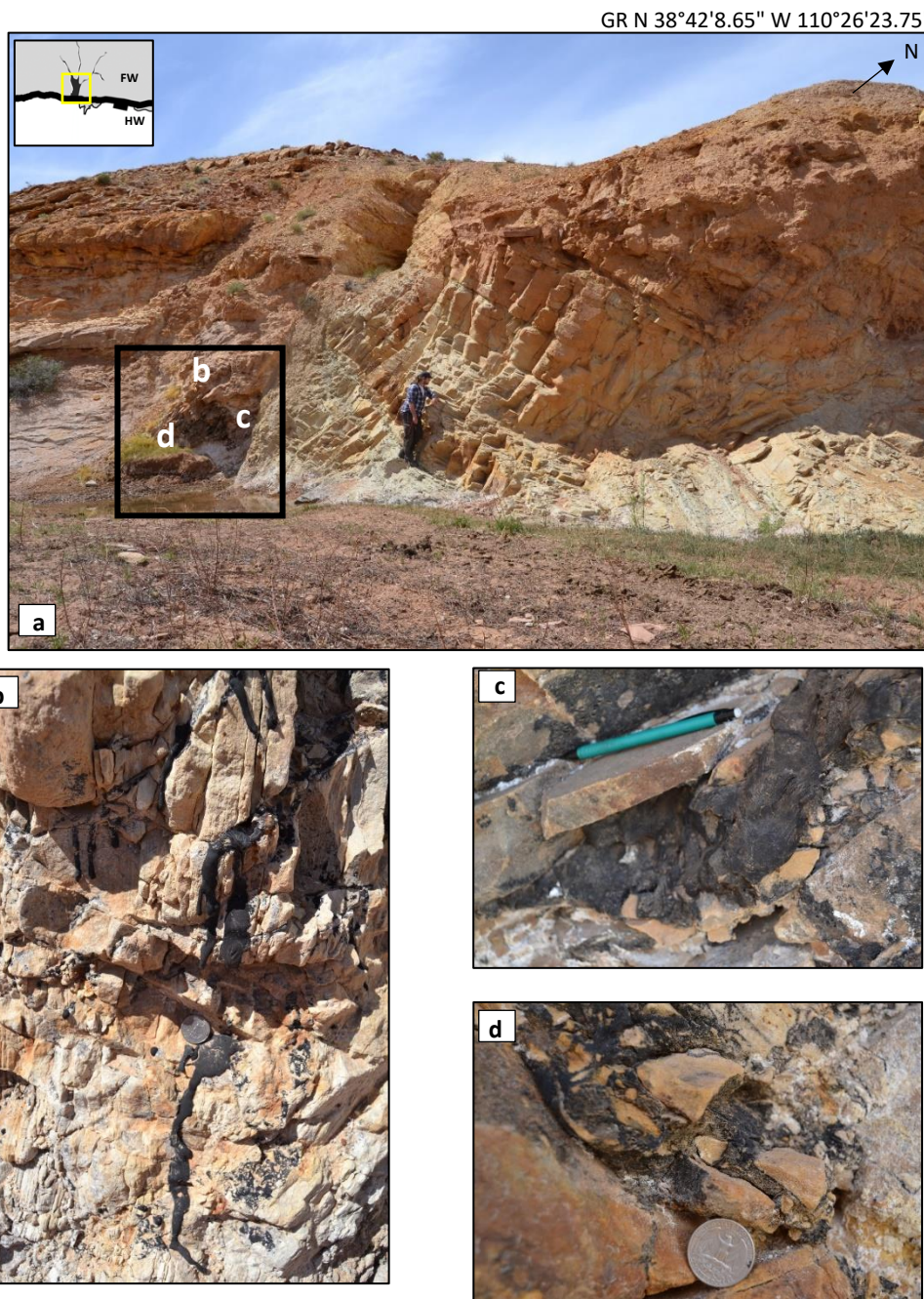
Figure 5.6 – Hydrocarbon seeping from the Navajo Formation at the Crow's Nest Spring site (a). Hydrocarbons appear viscous and seep from fracture junctions (b, c, d).

In thin section, there is evidence for hydrocarbons infilling some vacant pore space between grains in the Navajo Formation within the footwall (figure 5.7c).
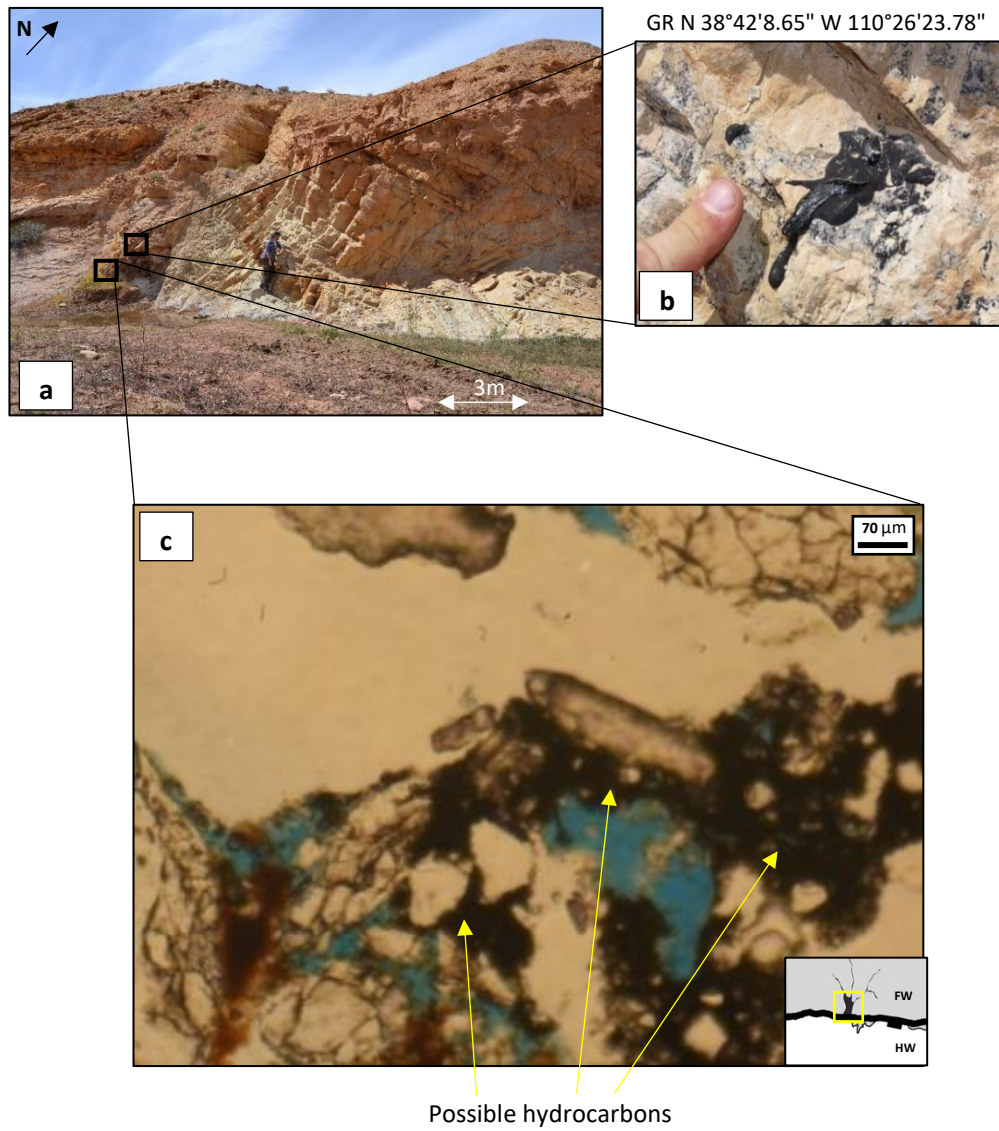
Figure 5.7 – Hydrocarbon seeping from the Navajo Formation is observed at the Crow's Nest Spring site (a, b). Photomicrograph showing a sample from the host rock, (not a fracture junction) where hydrocarbon staining concentrates in pores (c).

Fracture infilled with hydrocarbons

Fractures infilled with hydrocarbons

GR N 38°42'23.51" W 110°26'44.31"
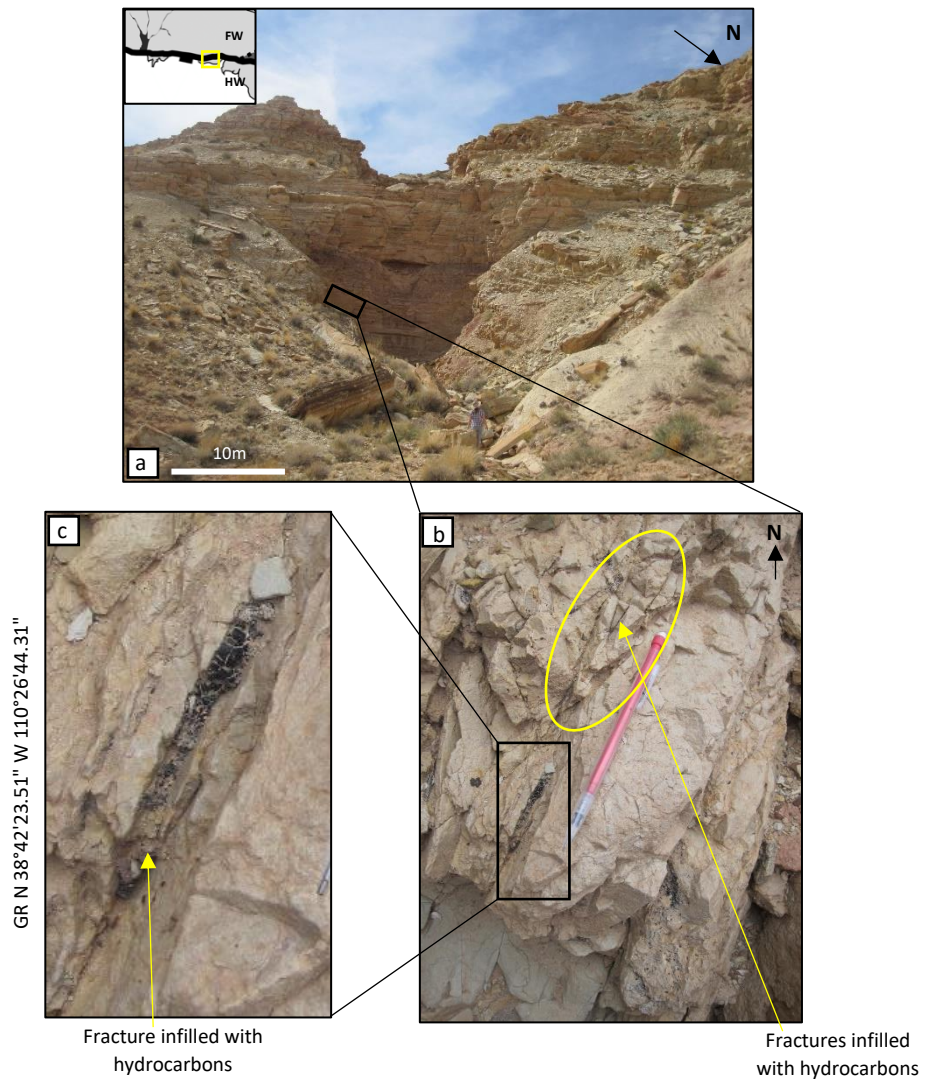
Figure 5.8 – Hydrocarbons are exposed at the Old Mine Site (a). Hydrocarbons infill fractures in the Navajo Formation of the footwall and appear hardened (b, c).

5.2.2 Iron oxide staining, nodules and fractures

Iron oxide is observed at the Crow's Nest Fault in three ways; as iron oxide nodules, iron oxide staining and iron-rich fractures (figure 5.9).
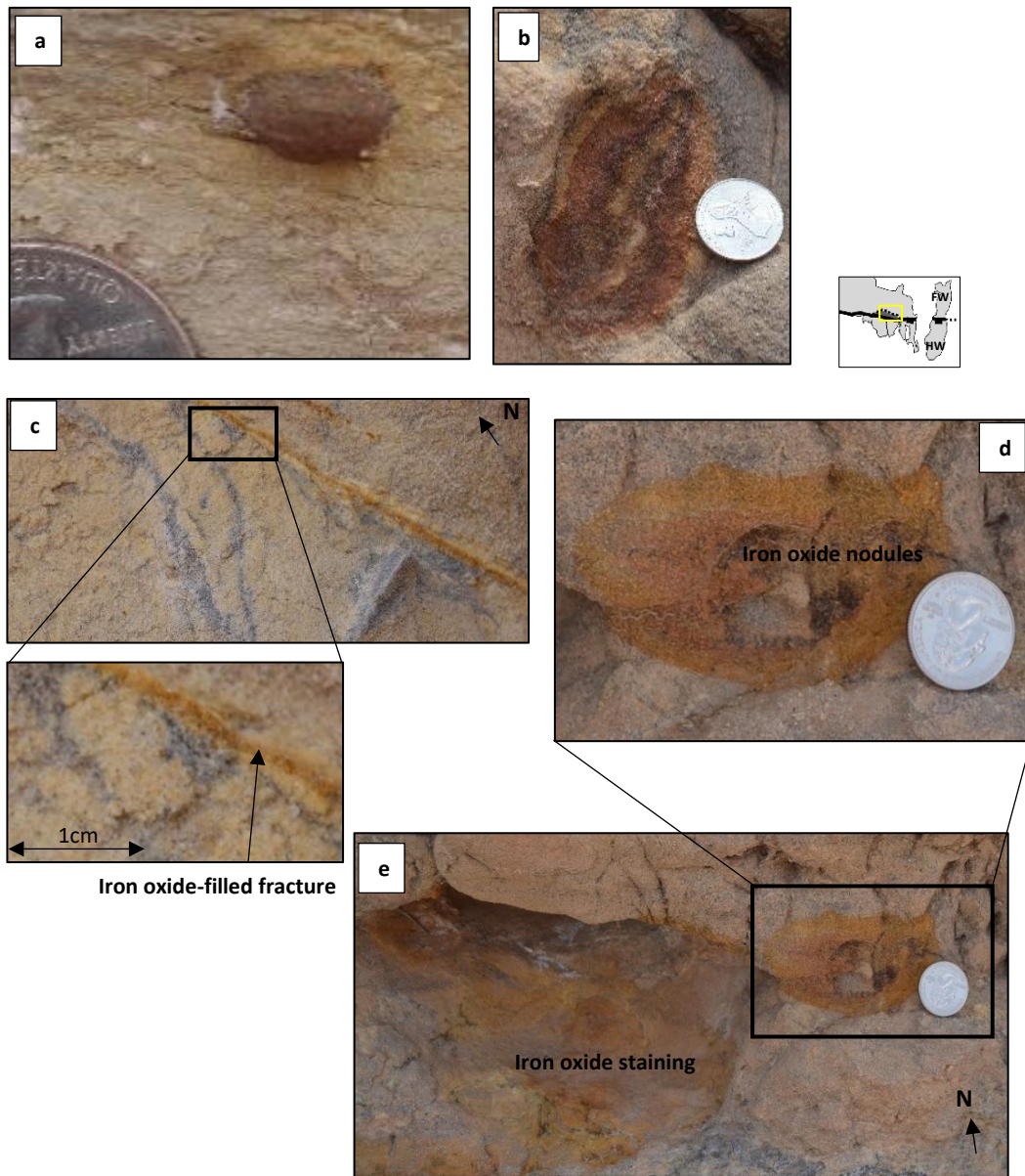
Figure 5.9 – Iron oxide is observed at the Crow's Nest Fault in three ways, as iron oxide nodules (a, b, d, e), as iron oxide staining (e) and as iron-rich fractures (c).

Iron oxide nodules and staining are exposed at all localities and lithologies at the Crow's Nest Fault. However, iron-rich fractures are only exposed in the Slick Rock Entrada at the Brush Valley lens site.

Iron nodules at the Crow's Nest Fault are observed in two forms; as hard, protruding concretions (figure 5.9a) and as iron oxide staining in a nodular shape which are flat to the surface (figures 5.9b and 5.9d). Both types of iron oxide nodules are tan, burnt amber or orange in colour. Some nodules exhibit rings of different shades of tan or brown colouration with each lighter or darker then the next towards the centre of the nodule (figure 5.9b), whereas others nodules are one colour (figure 5.9d). Both types of iron oxide nodules range in size from 0.5cm to 10cm in diameter. When the top layer of the host rock is chipped off, iron oxide does continue below the surface of the rock.

Where iron oxide nodules are flat to the surface, iron staining is usually surrounding these nodules. However, iron oxide nodules which are hard concretions tend to be exposed independently and are not associated with iron oxide staining. Iron oxide staining is observed at the Crow's Nest Fault as areas of the host rock which have been stained orange, burnt amber or light brown (figure 5.9e). Iron oxide staining occurs on a range of scales from isolated patches of up to 2cm to areas spanning 5-6 metres of consistent iron oxide staining. Samples of the Slick Rock Entrada were taken from the Brush Valley locality and analysed under thin section (figure 5.10). Iron oxide is observed coating quartz grains and infilling pore spaces.
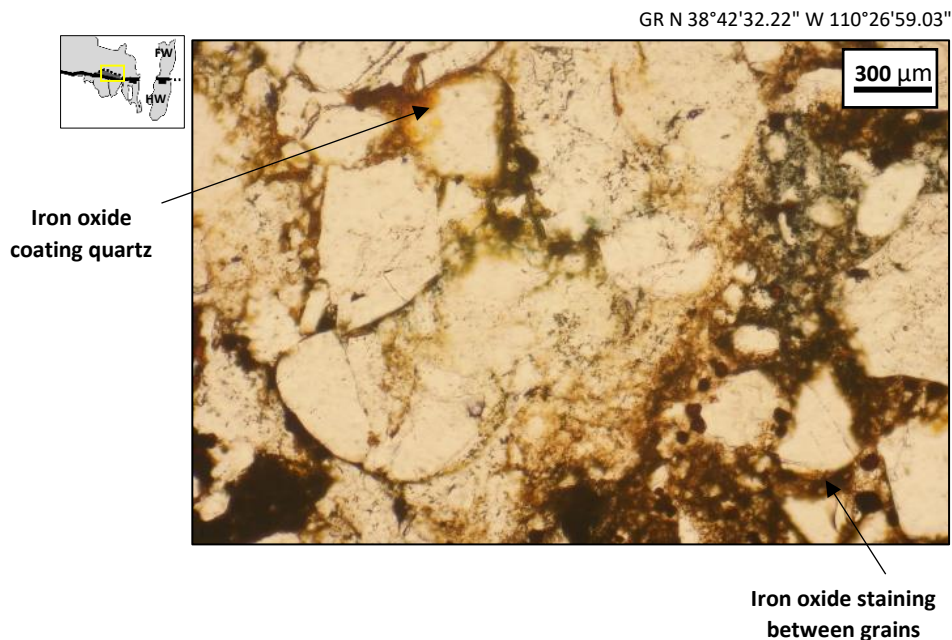
Figure 5.10 – Photomicrograph of a sample of the Slick Rock Entrada host rock which shows evidence of iron oxide infilling pore space and coating quartz.

Navajo Formation from the footwall at the Crow's Nest Spring locality show iron oxide

coating the quartz grains and infilling the pore spaces between grains (figure 5.11).

GR N 38°42'8.61" W 110°26'23.48"

200 µm

Iron oxide staining between grains
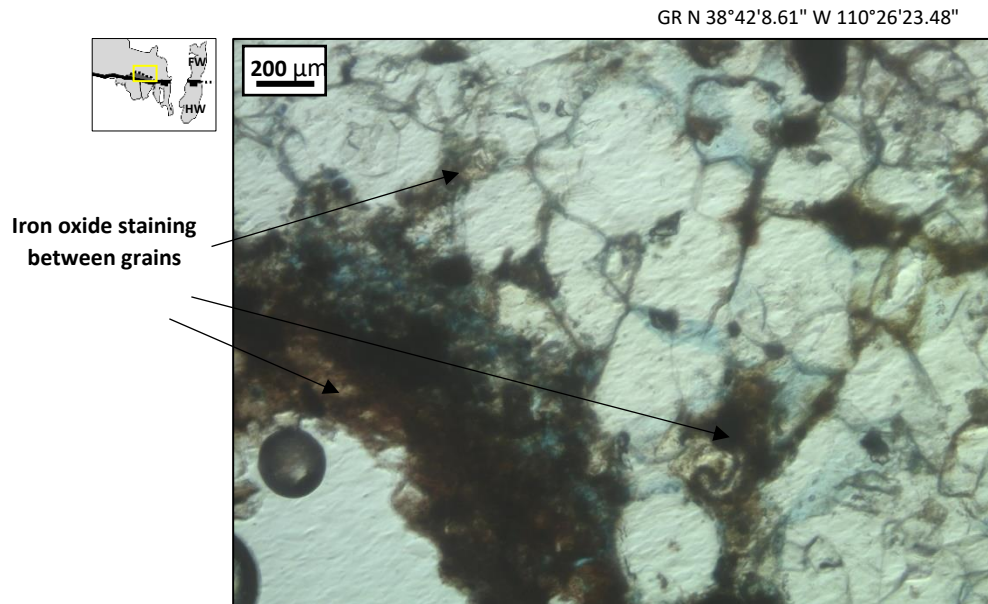
Figure 5.11 – Photomicrograph of a sample of the Navajo Formation host rock which shows evidence of iron oxide staining infilling pore space.

Elsewhere in Utah, the Slick Rock Entrada is characteristically orange and brown due to the

presence of iron oxide staining. For example and as shown in figure 5.12, in the Green River

area, the Entrada shows evidence of iron oxide coating grains which is the same as that

observed at the Crow's Nest Fault.

The presence of iron oxide within the Slick Rock Entrada is influenced by the amount of

detrital iron-bearing minerals present. It is thought that the presence of iron oxide staining

is due to the laterally extensive reduction of iron oxide as a result of hydrocarbon migration

(Garden et al., 2001). The origins and chemistry of iron oxide is discussed in more detail in

section 5.4.2.
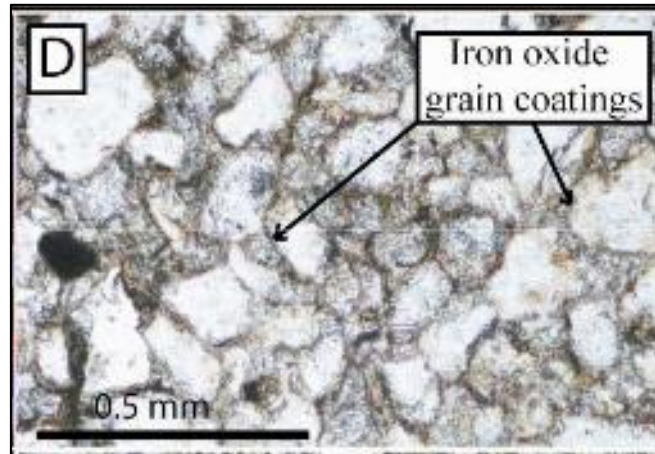
Figure 5.12 – Photomicrograph of the Entrada Formation showing evidence of iron oxide coating grains in the Green River Area (Wigley et al., 2012).

Fractures which are filled or partially filled with iron oxide appear tan or burnt orange in colour (figure 5.13b). Iron oxide infilling is observed only in north-south orientated fractures in the Slick Rock Entrada at the Brush Valley lens (section 5.3).

Under thin section, where iron oxide infills fractures there is a sharp boundary between the fracture and the surrounding host rock. Within the surrounding host rock there is evidence of iron oxide infilling vacant pore space and coating quartz grains (figure 5.13a). However, there does not appear to be an increase in iron oxide infilling the surrounding host rock here than elsewhere within the same locality.
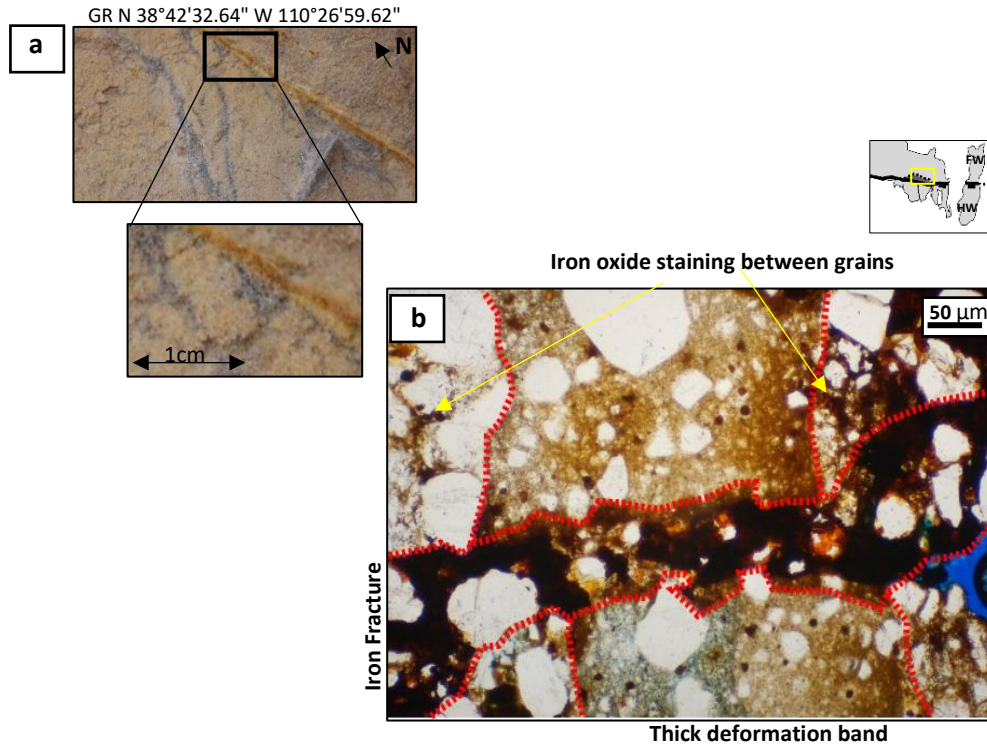
Figure 5.13 – (a) Fractures filled with iron oxide in outcrop and (b) thin section of 5.10a which shows fractures filled with iron oxide. This photomicrograph shows an iron oxide filled fracture cross cutting a thick deformation band.

Within the literature there is a lack of evidence to suggest iron-rich fractures are common within the Slick Rock Entrada across Utah.

5.2.3 Bleaching and dissolution of calcite cement

In most of the Paradox Basin, rocks which are described as 'bleached' were thought to be previously red until chemically altered by fluids, resulting in rock which has a pale cream, pink or grey hue (Chan et al., 2005). The red pigment in the rock results from the thin coating of grains with hematite. The hematite is usually a result of iron which has broken down from detrital ferromagnesian minerals during early diagenesis (Walker, 1979; Beitler et al., 2003). However, for iron to become mobile in sediments, it must be reduced from Fe to Fe^{2+} (Beitler et al., 2003). The mixing of iron rich reducing fluids with groundwater which has been oxidised often results in the precipitation of iron concretions (Chan et al., 2005; Busigny and Dauphas, 2007).

Bleaching at the Crow's Nest Fault is defined by a colour change within the host rock. Characteristically red rocks of the Earthy Entrada within the hanging wall and salmon pink rocks of the Slick Rock Entrada within the lens have been bleached cream and white (figure 5.14).

Bleaching is observed in three main ways; as bleached fractures, bleached bedding planes and as bleached host rock. Fractures and bedding that are bleached are seen in the Earthy Entrada within the hanging wall at the Brush Valley locality and are surrounded by cream or white halos ranging from 1cm to 1m in size (figure 5.14c).
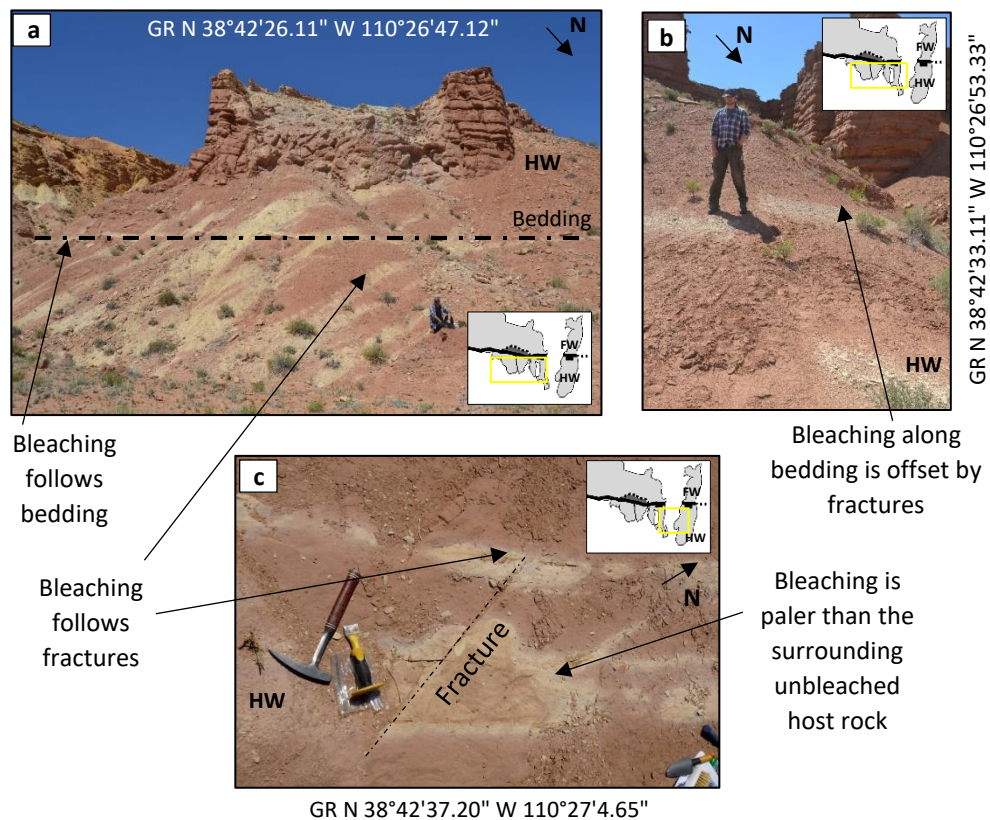
Figure 5.14 – (a) Bleached rock following bedding shows a sharp transition between bleached and un-bleached host rock. (b) Bleached bedding is offset. (c) Bleaching follows fractures – there is a clear transition between bleached and unbleached host rock. All photographs are taken in Earthy Entrada in the hanging wall at Crow's Nest Fault.

Within the Slick Rock Entrada, exposed at the Brush Valley lens site, host rock is bleached entirely as shown by a colour change from salmon pink and brown to cream and white (figure 5.15).
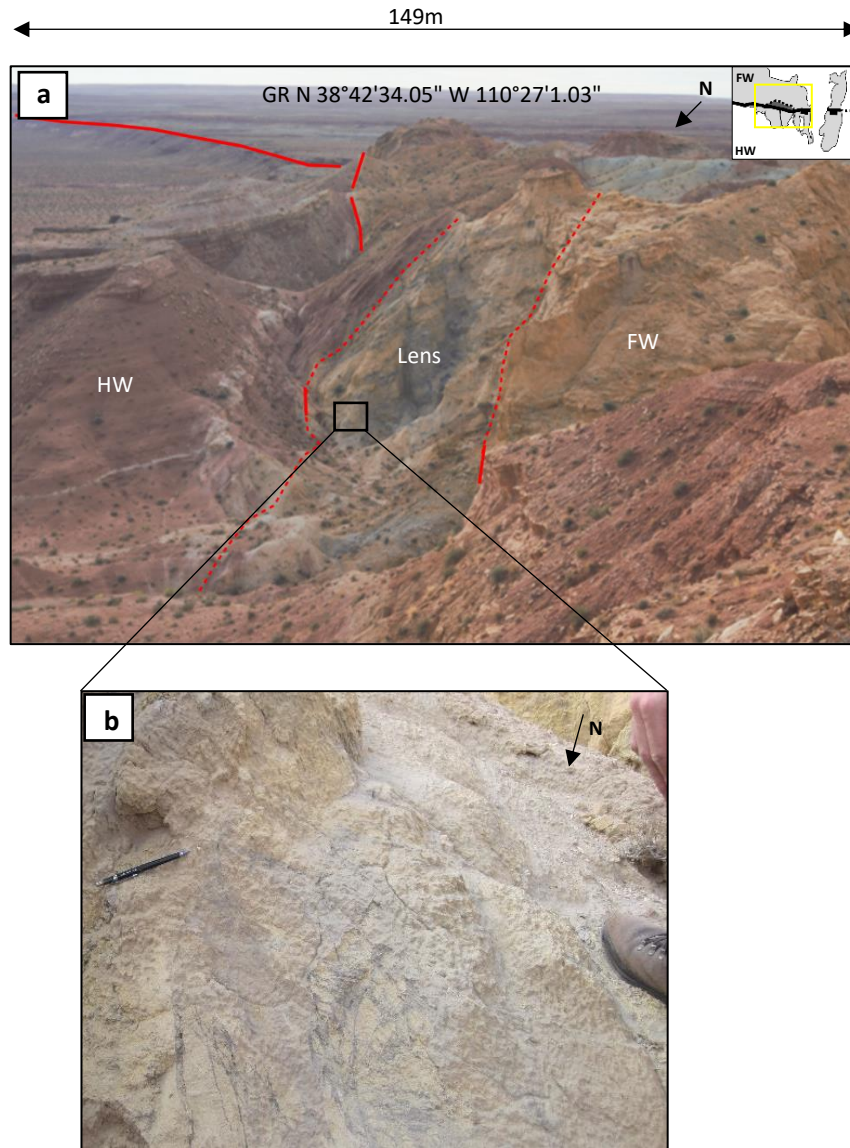
Bleached host rock (Slick Rock Entrada) in the lens at the Brush Valley site

Figure 5.15 – (a) The Slick Rock Entrada is bleached entirely in the lens shown in (b) where the host rock is characteristically white compared to a characteristically salmon pink to grey and light brown colouration.

Bleached rock is more fragile and crumbly than unbleached rock. Due to the fragility of bleached host rock, no samples were successfully prepared for microanalysis from the Earthy Entrada in the hanging wall.

Blue epoxy resin was impregnated into thin section samples within the Brush Valley lens. Thin sections from the Slick Rock Entrada at the Brush Valley lens site show evidence of a lack of calcite cement between grains compared to unbleached Slick Rock Entrada (figures

5.16), indicative of dissolution. As outlined in section 4.9, there is an average of 2% calcite cement within samples of the Slick Rock Entrada within the Brush Valley lens locality. Elsewhere in Utah, unbleached Slick Rock Entrada has a variable cement content of between 1% and 25% and is typically calcite and iron oxide rich (Johansen et al., 2005).

GR N 38°42'32.91" W 110°27'0.48"

Vacant pore space/lack of calcite cement between grains in the bleached host rock

0.5mm
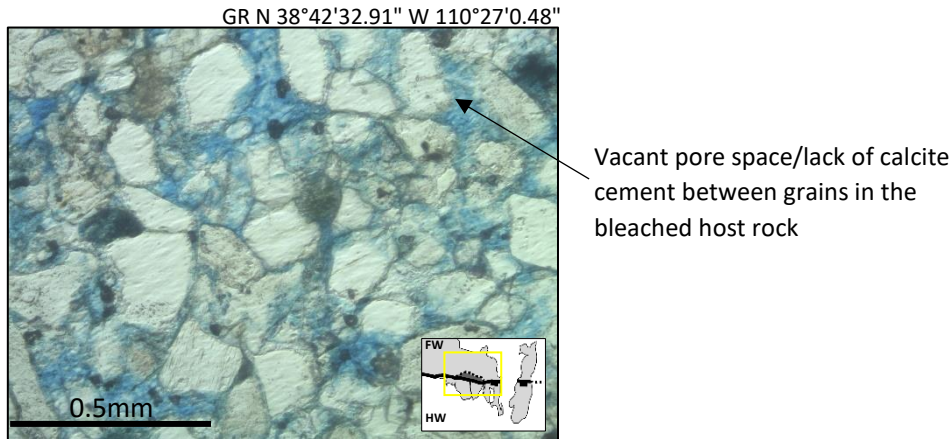
Figure 5.16 – Photomicrograph of the Slick Rock Entrada in the lens at the Brush Valley site. The sample comes from host rock which has been bleached.

Thin sections of the Slick Rock Entrada from the Brush Valley lens site were analysed under SEM. SEM analysis shows evidence of altered k-feldspar, dolomite and clays. In addition, carbonate cement is present between grains and has been identified through EDS (figure 5.17).

a

GR N 38°42'32.91" W 110°27'0.48"

Dolomite

Calcite cement

Dolomite

Kaolinite (clays)

| 10 µm | 20.00 kV | AsB | 843 X | 25 Nov 2014 | ZEISS |
| | WD = 9.5 mm | File Name = BV33_01.tif | | 10:00:40 | |
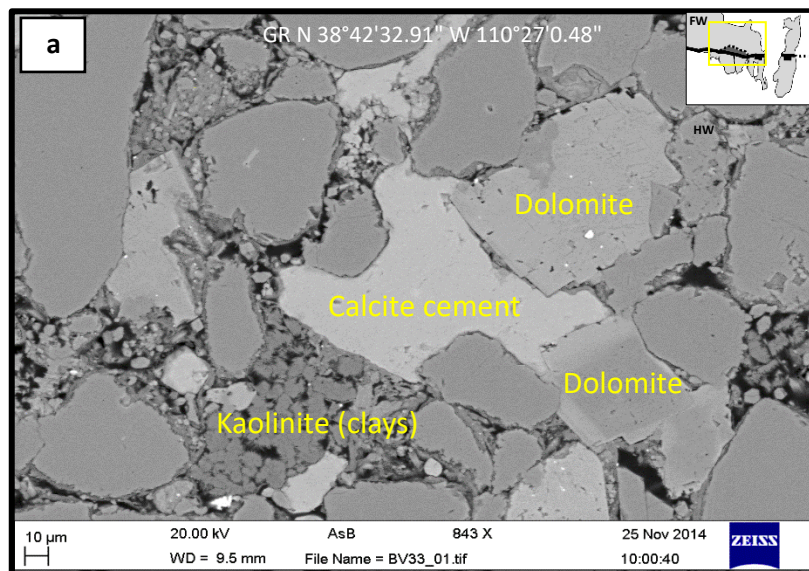
Figure 5.17 – (a) SEM image of bleached Slick Rock Entrada within the sandstone lens at Brush Valley locality. Most calcite cement has been dissolved and dolomite and kaolinite clays have been precipitated.

Under the SEM, k-feldspar is up to 100µm in size and appears altered (figure 5.16). The k-feldspar appears to have a crack-seal texture containing fluid inclusions. Such texture has been observed in fractures and cements in Wyoming (Laubach et al., 2010). To constrain the fluid within the inclusions, crush-leaching analysis could be undertaken.

Dolomite is up to 50µm in size and is older than the surrounding calcite. Calcite cement has infilled space between the quartz grains and ranges from <10µm to 160µm in size. Kaolinite clays as recognised through EDS, are observed infilling spaces between the quartz grain and surrounding host rock and are up to 15µm in size (figure 5.18).

During regional burial diagenesis, the Entrada Formation developed partial dissolution of k-feldspar and minor kaolinite within the matrix (Wigley et al., 2012). It is thought that calcite cement and dolomite are fault-related cements (Eichhubl et al., (2009). Isotopic analysis by Chan et al., (2000) suggested that cements at the Moab Fault were a product of reprecipitation when upward-migrating reduced brines mixed with water of meteoric origin at the fault.

Studies of unbleached Entrada Formation at the Courthouse Branch Point of the Moab Fault show evidence of calcite cement and dolomite (Foxford et al., 1996; Johansen et al., 2005). Calcite cement is sporadic and dolomite shows evidence of overgrowing the surrounding cement, similar to that seen at the Crow's Nest Fault. However, there is no evidence of kaolinite present within the matrix of the host rock. Elsewhere in Utah, there is little evidence of clays present within unbleached Entrada. At the Yellow Cat Graben, the Slick Rock Entrada shows evidence of a sporadic and patchy calcite cement that lacks any clay content (Bright, 2006).

The lack of clays in unbleached Slick Rock Entrada compared to bleached rock suggests that bleaching has had an effect on clay content. It is thought that all host rock within Utah were originally red in colour due to initial iron oxides and clays that coated grains during deposition (Walker et al., 1975). However, reducing fluids that flow through fractures and faults within the host rock removes iron by mobilising the iron (Chan et al., 2000; Beitler et al., 2003; Parry et al., 2004; Kampman et al., 2009). In mobilising the iron, reducing fluid is able to release metals from iron oxides and clays and redeposit them, for example, as clays

within the Slick Rock Entrada. This suggests that diagenesis through bleaching has likely increased the clay content for the Slick Rock Entrada exposed at the Brush Valley lens site.
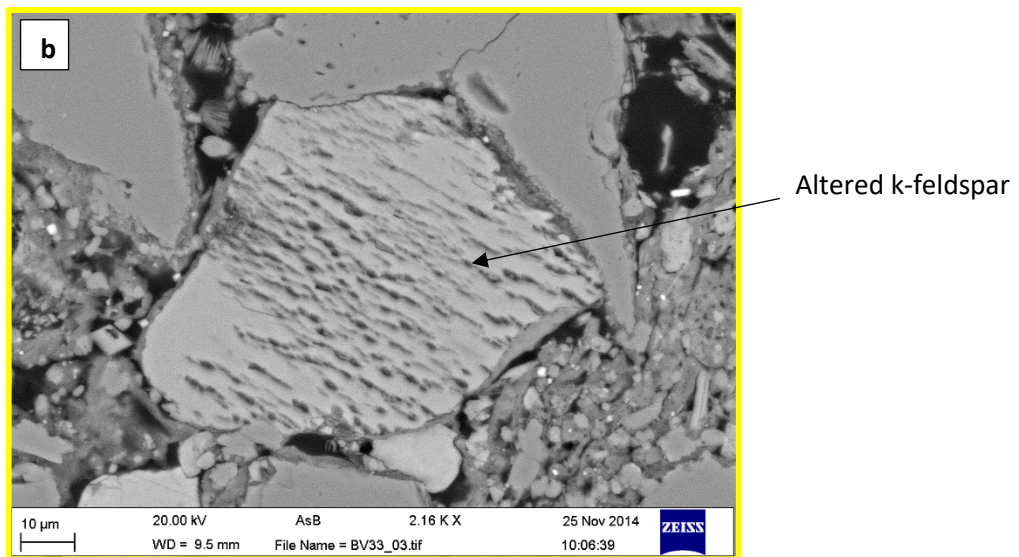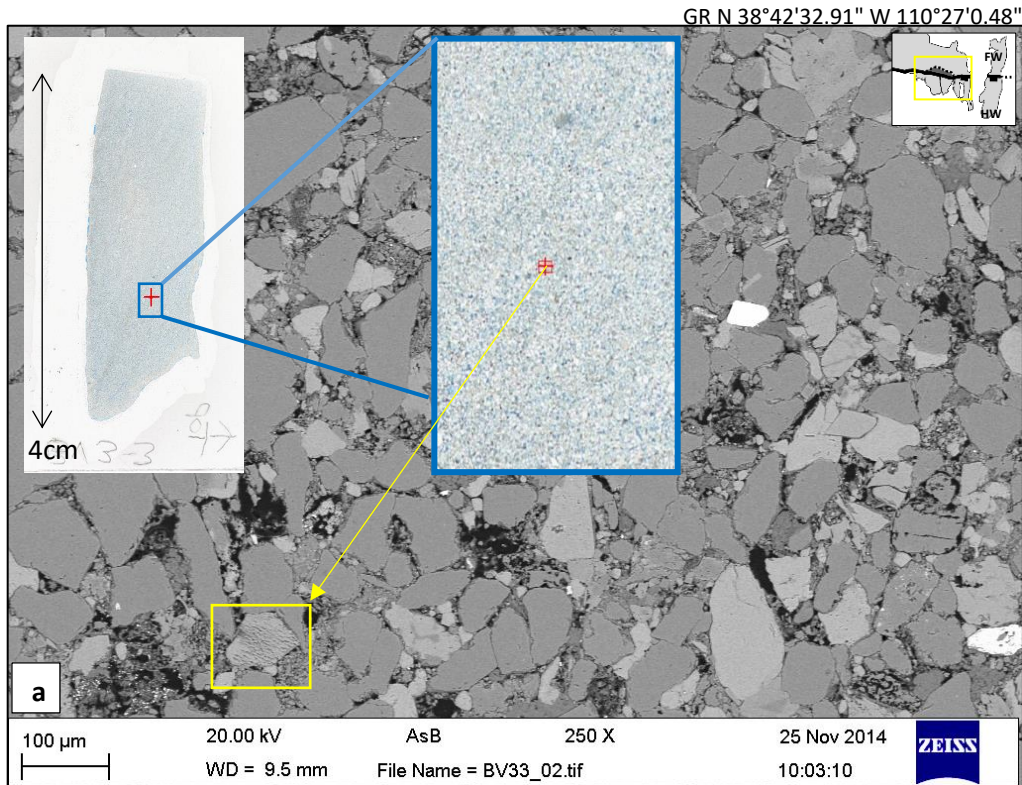
Figure 5.18 – (a) SEM analysis of a thin section sample of host rock (Slick Rock Entrada) within the sandstone lens. (b) Altered k-feldspar

5.2.4 Modern day and ancient fluid evidence

A modern day spring is observed at the Crow's Nest Fault lens which is composed of the Carmel Formation (figure 5.19). The modern day spring at Crow's Nest Fault is 13m in length x 5m in width. The spring has not been sampled and the chemistry of the fluid is unknown.

A spring is recorded on the topographic map at the Cottonwood Wash site but was not seen during field work due to dense vegetation.
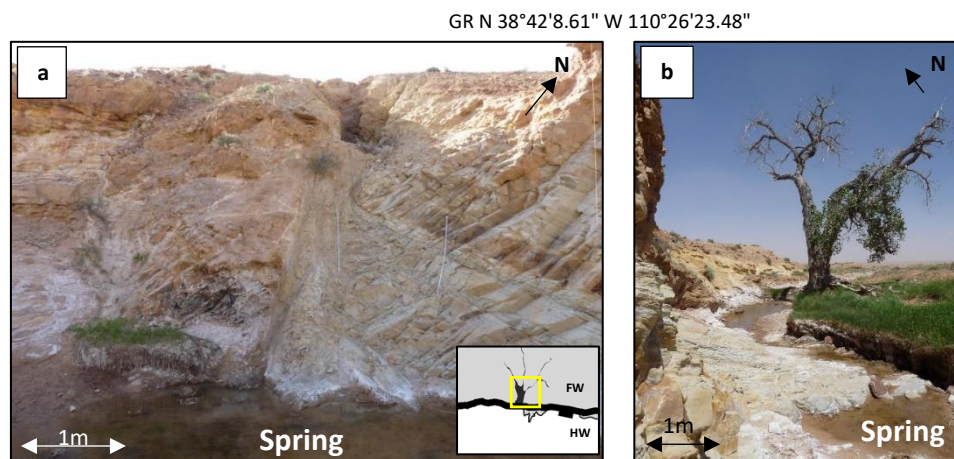
Figure 5.19 – A modern spring located in the lens at the Crow's Nest Spring site (a) looking NNW and (b) looking NNE.

Elsewhere at the Cottonwood Wash locality, there is evidence of possible ancient water flow in the form of travertine within the Earthy Entrada hanging wall (figure 5.20).
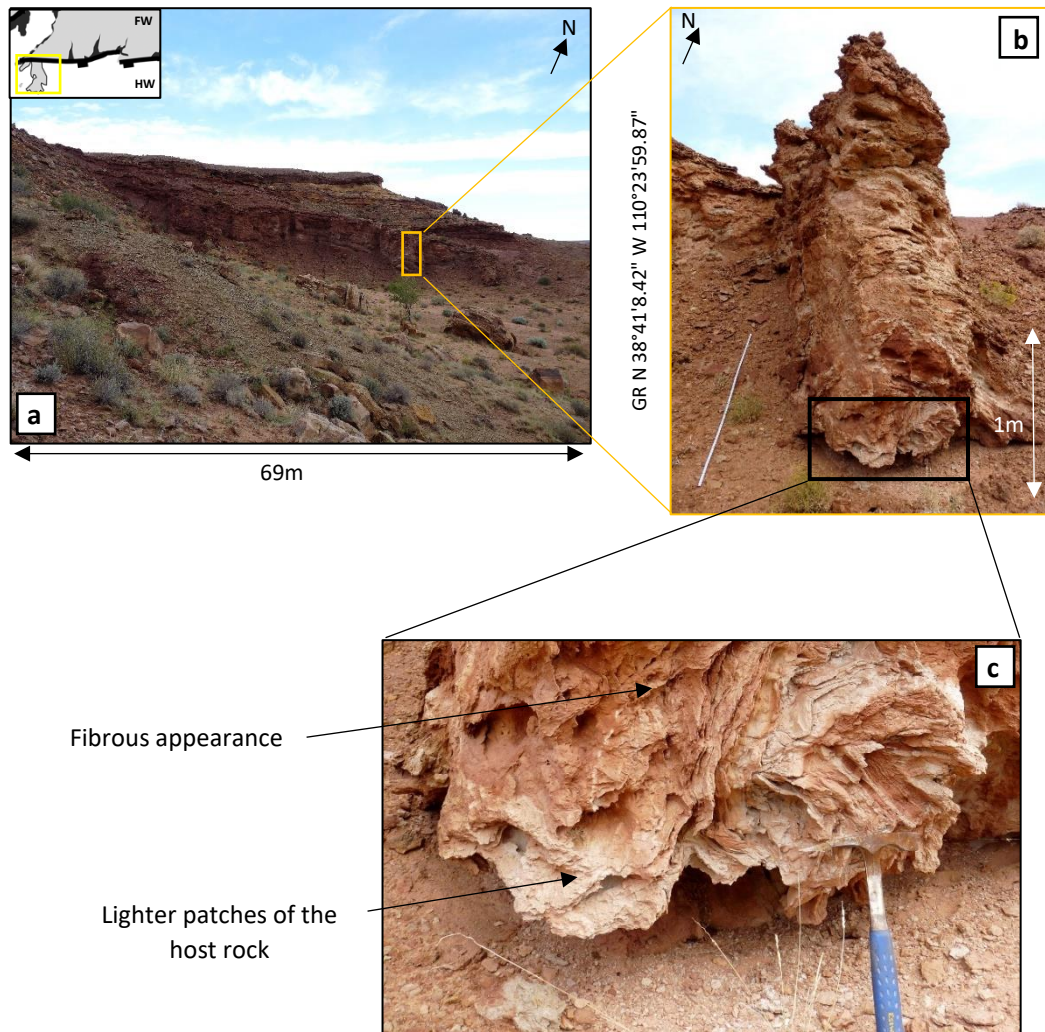
Figure 5.20 – (a) Evidence for possible ancient water flow at the Cottonwood Wash site. The host rock (Earthy Entrada) appears fibrous and lighter in patches (b) and (c).

This fibrous appearance is characteristic of travertine, (Melezhik and Fallick, 2003) a $CaCO_3$ deposit which is precipitated from mineral and hot springs (Greer et al., 2015). Travertine is formed when CO_2 is lost from the following reaction: H2O + CO2 + CaCO3 $\leftrightarrow$ Ca (HCO3)2 (Brogi and Capezzuoli, 2009). A number of factors can induce the degassing of carbonate rich fluid from thermal springs, including; a drop in fluid pressure, fluid flow turbulence and biological activity such as bacteria and algae which extract CO_2 from the fluid (Chafetz and Folk 1984; Ford and Pedley, 1996).

For a sample to be confirmed as travertine, both aragonite and calcite need to be present (Pentecost, 2005). However, there is limited discussion within the literature on what

percentages of aragonite and calcite need to be present in order to truly identify and characterise a sample as travertine.

XRD analysis allows for the identification between the two polymorphs of $CaCO_3$; aragonite has its greatest peak at [111] and has several peaks which are much lower (figure 5.20). Calcite peaks at [104] and has several lower peaks (Railsback, 2006). The identification of aragonite and calcite within a pure sample is easy, however most samples which are analysed are impure. For samples which are mixed, either the aragonite [221] peak is identified or the aragonite [221] and calcite [113] peaks are compared (figure 5.21).
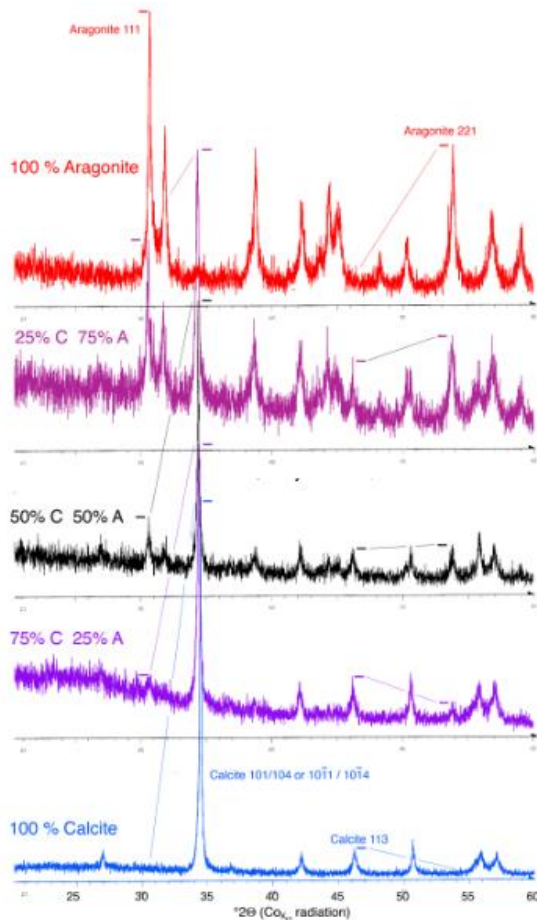
Figure 5.21 – XRD analysis showing an example of how to distinguish between calcite and aragonite. Aragonite and calcite have their highest intensity peaks at two different positions; aragonite has its greatest peak at [111] and has several peaks which are much lower (Photo from Railsback, 2006).

A sample of the Earthy Entrada from the hanging wall at the Cottonwood Wash locality was analysed for the percentages of aragonite and calcite using XRD. The results show that there is a high concentration of calcite but almost zero aragonite present within the sample (figure 5.22).
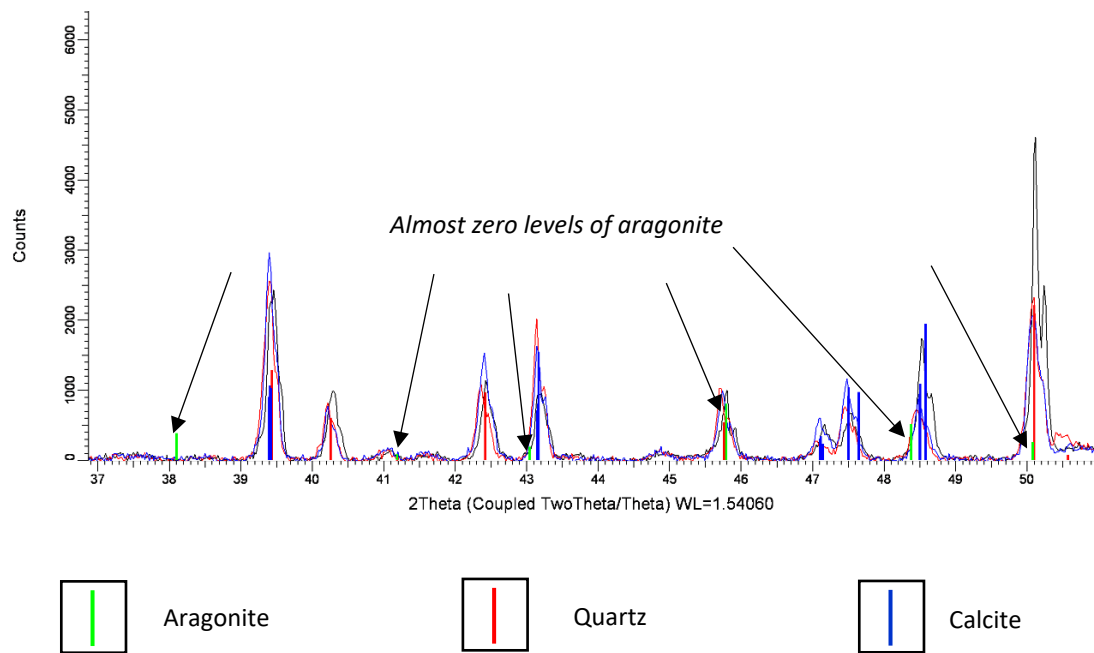
Figure 5.22 – XRD analysis of a sample of the Navajo Formation at the Crow's Nest Fault that shows a high concentration of calcite but very low levels of aragonite

To more accurately test whether the host rock has been altered by mineral springs, more samples would need to be sampled and analysed.

Typically, evidence for water is expressed as mounds and bubbling CO_2. For example, the Little Ground Wash Fault in Utah has carbonate springs and actively forming travertine deposits which are localised at and along the fault zone (Shipton et al., 2004) (section 5.4.4). However, at the Crow's Nest Fault there is a distinct lack of any carbonate springs or accumulations of travertine deposits.

This lack of evidence for spring mounds or any obvious CO_2 bubbling at the Crow's Nest Fault coupled with a lack of travertine present suggests very little evidence for any leakage of CO_2 rich groundwater.

Alternatively, this area of fibrous and distorted Earthy Entrada in the hanging wall may be crenulated bedding which is not uncommon within the Entrada Formation throughout Utah. Dane, (1935) suggested a wavy crenulation of a group of beds in the Entrada is likely due to movement in either unconsolidated or partially consolidated sediment during or post deposition.

5.3 Location of fluid flow evidence at the Crow's Nest Fault

This section will describe in detail the evidence for fluid flow at each studied locality at the Crow's Nest Fault. From south-east to north-west, a section for each locality will outline evidence for paleo fluid flow, where the evidence for fluid flow is in relation to the fault zone and in which lithologies it is exposed.

5.3.1 Cottonwood Wash

In the hanging wall, iron oxide staining covers the Earthy Entrada where exposed up to 5m from the fault and in patches between 2-3cm and for up to 50cm (figure 5.23c) Iron nodules are exposed as tan and brown rings of staining which are flat to the surface. Iron oxide nodules range from 2cm to 6.5cm in size (figure 5.23d).
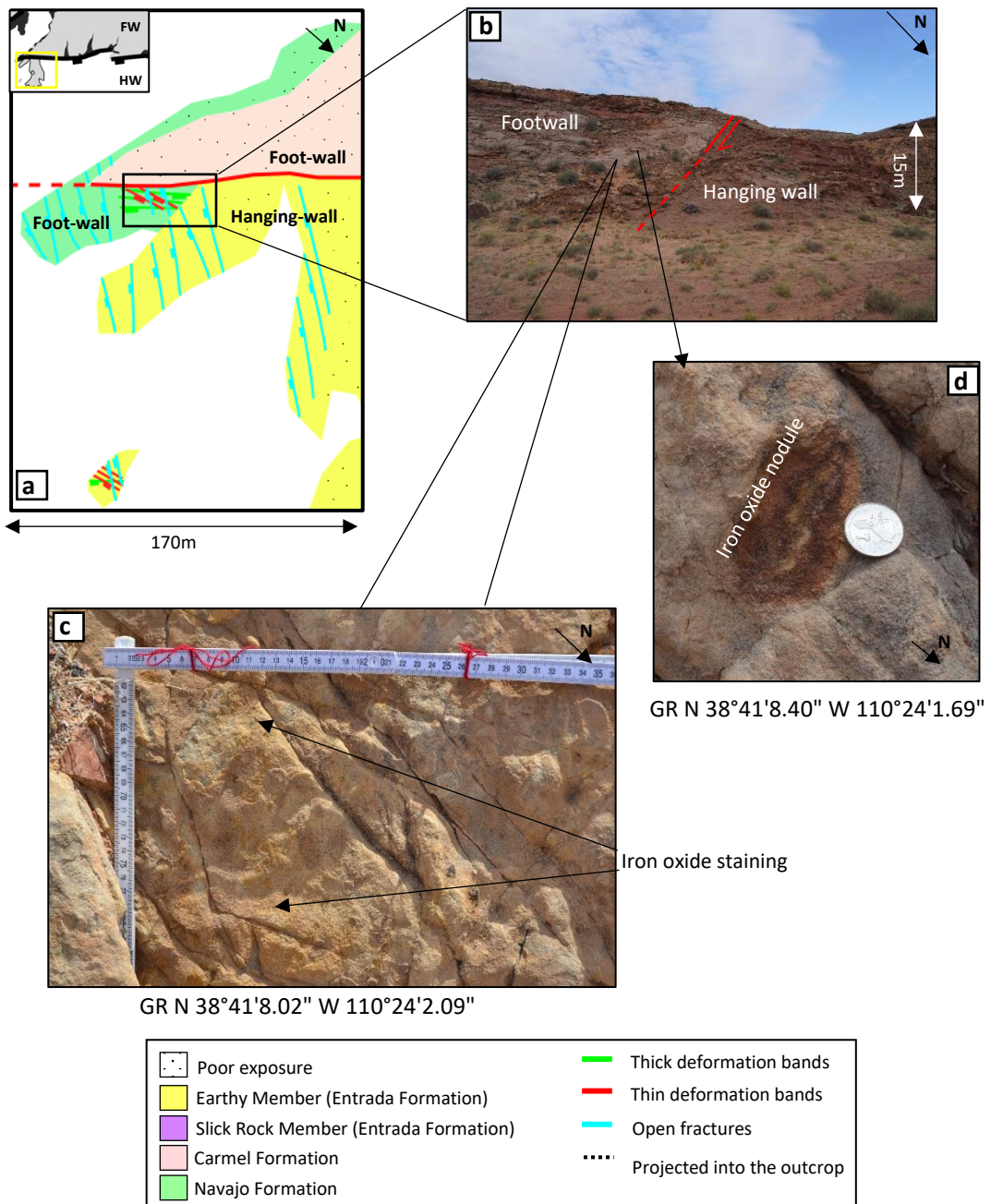
Figure 5.23 – The Cottonwood Wash site (a, b) shows evidence for iron oxide staining (c) and iron oxide nodules (d) in the Navajo Formation.

Although the footwall damage zone is exposed in the Navajo Formation in an area measuring 30m x 21m, only a 15cm x 6cm patch of the exposed host rock is stained by iron oxide. Iron oxide staining is light brown and tan, appearing slightly raised to the surface (figure 5.24b). In thin section, brown Fe-stained clays infill pore space between quartz grains (figure 5.24c).

GR N 38°41'7.41" W 110°24'0.39"

Small specs of iron oxide staining in quartz grains indicating overgrowth of less pure quartz

Iron oxide staining in pore spaces
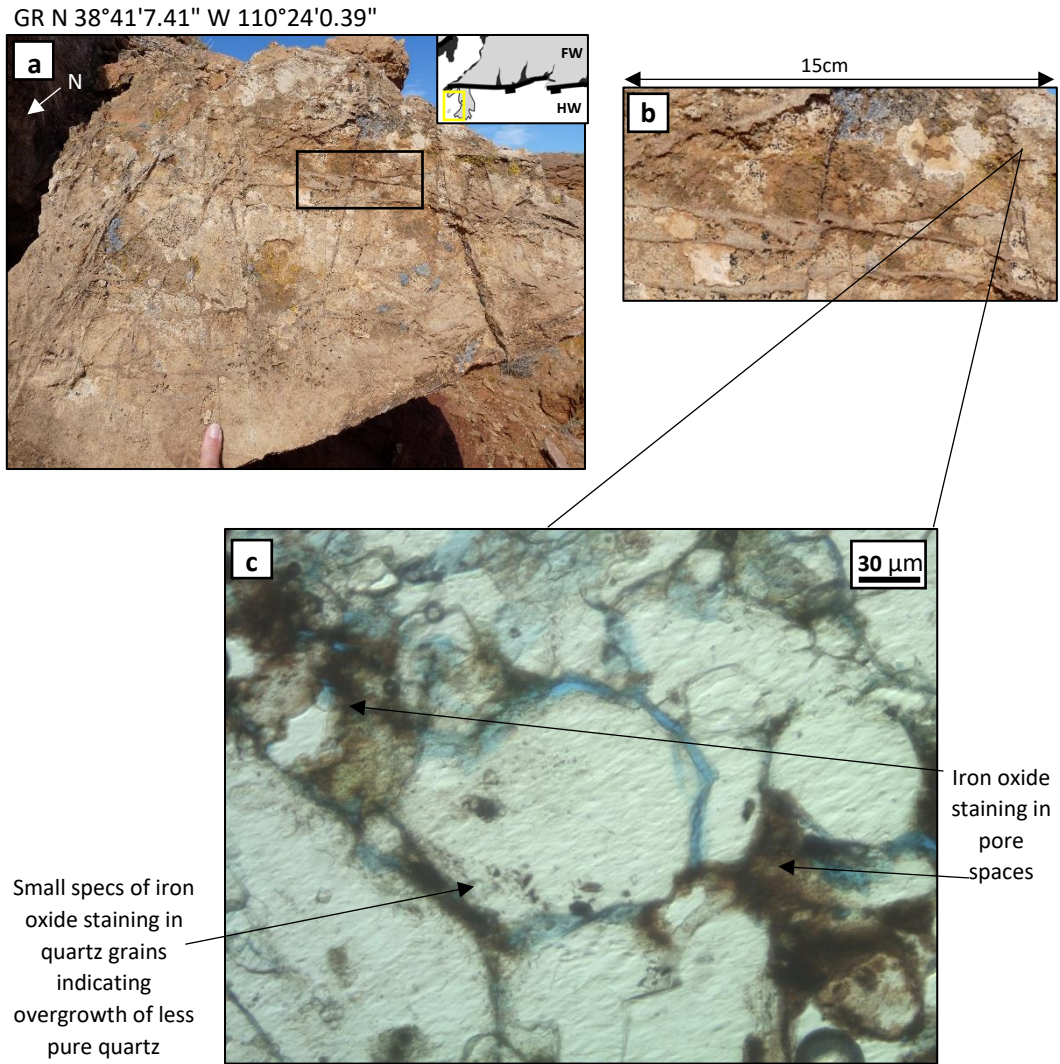
Figure 5.24 – The Cottonwood Wash site (a) shows evidence for iron oxide staining in outcrop (b) and in thin section, iron oxide stains vacant pore space (c).

The bleaching of beds in the hanging wall only occurs in the prominent, more resistant beds of the Earthy Entrada as shown in figure 5.25a. Bleached bedding appears as white or as very pale colouration (figure 5.25c). The bleached beds range from 0.5cm to 6cm in

thickness. There is evidence of soft sediment deformation where bleaching has occurred in a small 3m x 3m area of the hanging wall and this can be seen in figure 5.25c.
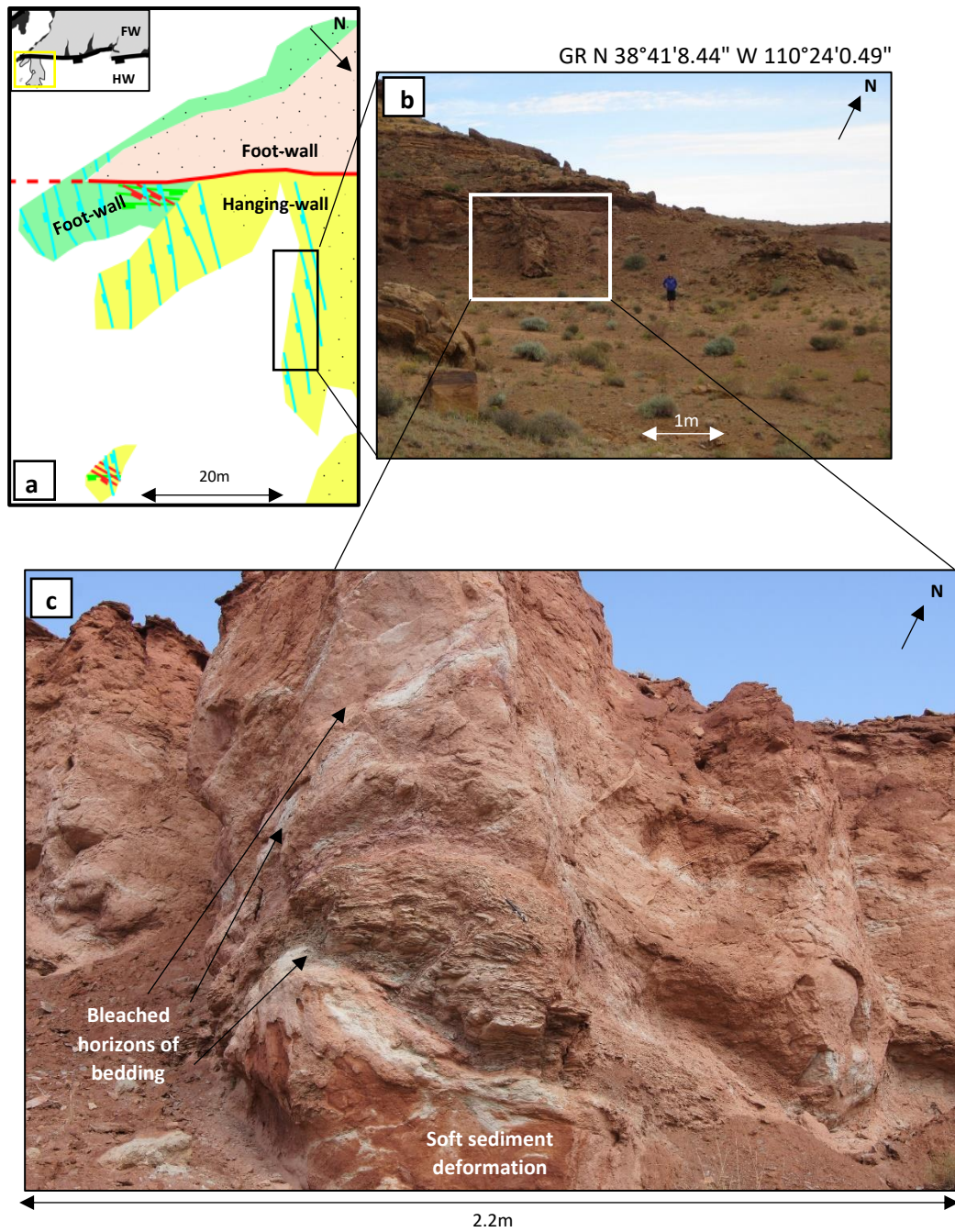
Figure 5.25 – The Cottonwood Wash site (a) shows evidence for bleached Earthy Entrada (b) and this is expressed by bleached bedding which is picking out soft sediment deformation (c).

5.3.2 Crow's Nest Spring

Hydrocarbon seepage is exposed in the Navajo Formation in the footwall and the Carmel Formation in the Crow's Nest Spring lens. In the Crow's Nest Spring lens, hydrocarbon seepage is exposed as black and dark brown viscous fluid which escapes from fracture junctions in the Carmel Formation (figures 5.26). Where two or more fractures join, hydrocarbons seep from the junctions but there is no seepage observed along single fractures. Of the visible fracture junctions at the Crow's Nest Spring lens, approximately 80% show evidence of hydrocarbon seepage when estimated by eye in the field site.

In the Carmel Formation, hydrocarbon seepage is exposed as dark, non-shiny liquid. In comparison, hydrocarbons which seep from the Navajo Formation in the footwall appear more viscous and shiny. In the Navajo Formation, surrounding the hydrocarbon seeps, hydrocarbons appear to have stained the host rock (figure 5.26). This difference could be due to a function of flow rate between the two areas.
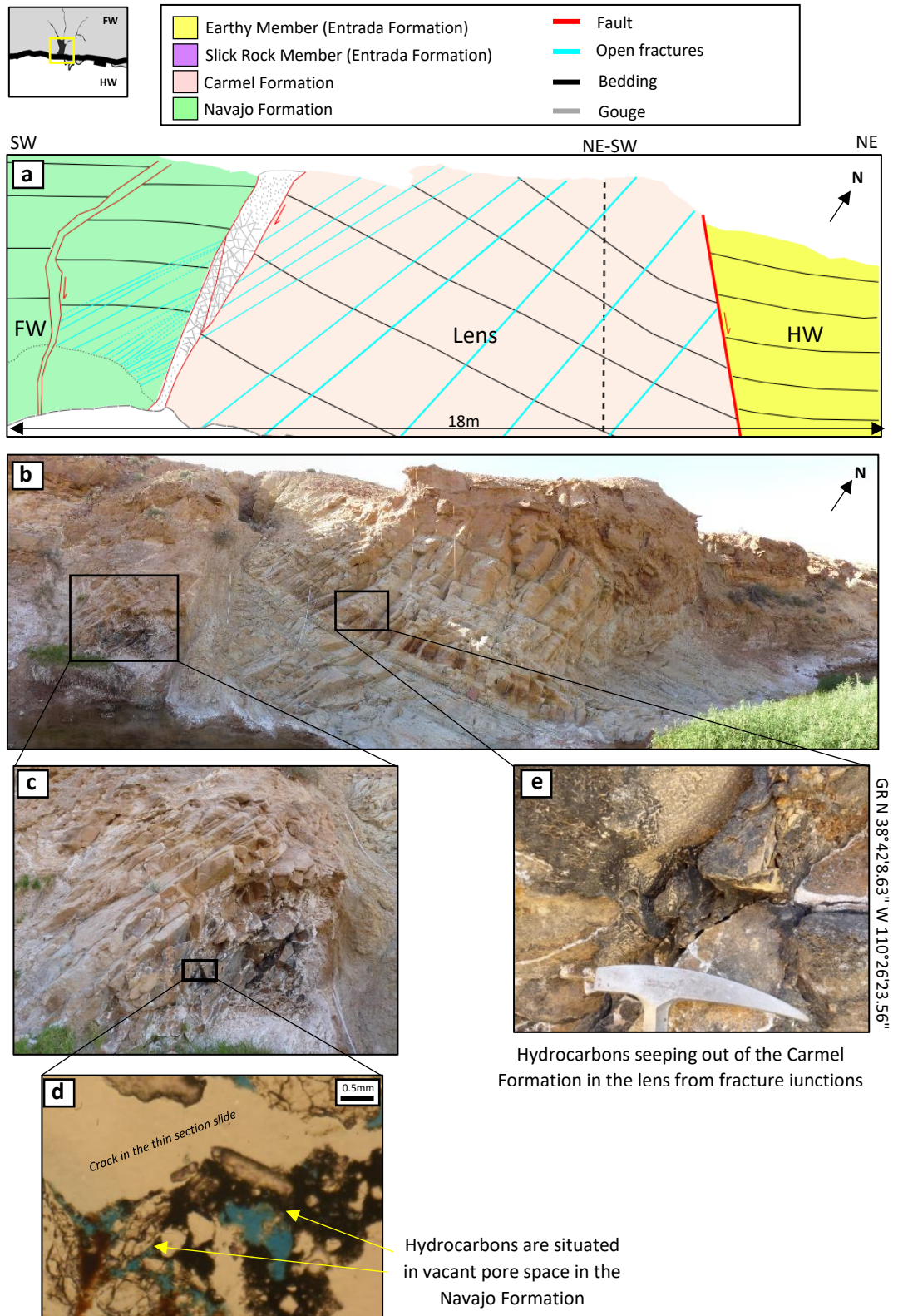
Figure 5.26 – Hydrocarbon seepage exposed at the Crow's Nest Spring site (a, b) is expressed by hydrocarbons seeping from fracture junctions in the Navajo Formation (c), (d) and in the Carmel Formation (e).

Four samples of the Navajo Formation host rock from the footwall were prepared for microanalysis and five photomicrographs of each sample were analysed. Hydrocarbons identified through EDS analysis appear as black material infilling pore space (figure 5.26d). Twenty photomicrographs of the Navajo Formation were point counted. Samples were taken randomly from areas of the Navajo Formation which were stained with hydrocarbons. From the twenty photomicrographs, it was estimated that 35-40% of the exposed Navajo Formation at the Crow's Nest Spring site is stained with hydrocarbons.

Iron oxide staining is exposed in the Navajo Formation in the footwall and the Carmel Formation in the Crow's Nest Spring lens. Iron oxide staining is tan and brown discolouration of the host rock exposed either flat to the surface or raised 2-5mm above the surface (figure 5.27).

Iron oxide staining in the Carmel Formation is exposed approximately 82m south-west of the fault gouge at GR N 38°42'8.57" W 110°26'23.84. Once 10m away from the fault, iron oxide staining becomes more common. The main canyon (figure 5.27b) then cuts through the lithology to expose the Navajo Formation in the footwall at GR N 38°42'7.13" W 110°26'25.53". There is no evidence of iron oxide staining in the Navajo Formation until the main canyon opens out and exposes the fault zone. Iron oxide staining in the Navajo Formation is exposed in the fault zone as shown in figure 5.27.

GR N 38°42'8.57" W 110°26'23.84

Iron oxide staining in a linear pattern

GR N 38°42'8.56" W 110°26'23.51"

Legend:
- Earthy Member (Entrada Formation)
- Slick Rock Member (Entrada Formation)
- Carmel Formation
- Navajo Formation
- Fault
- Open fractures
- Bedding
- Gouge
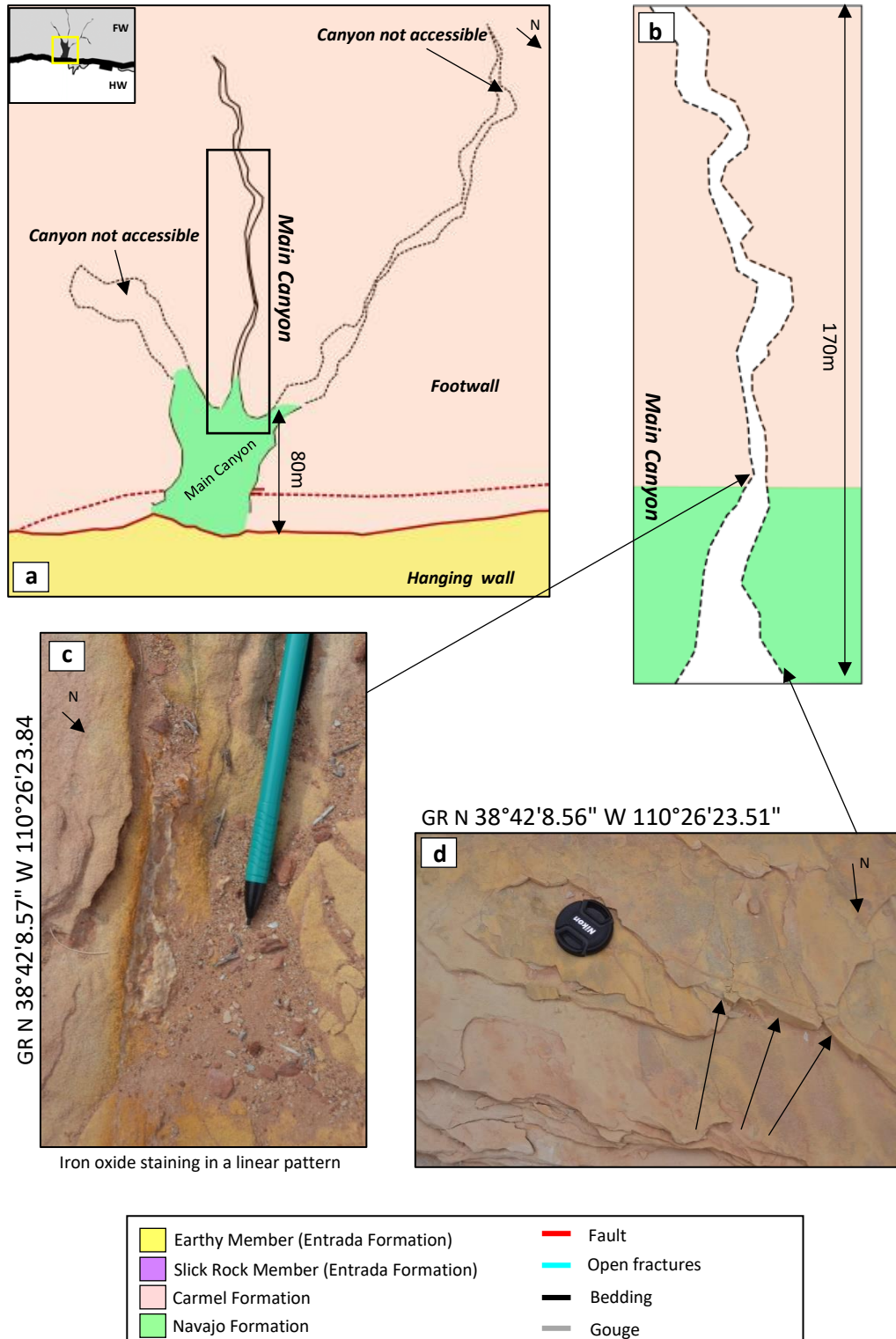
Figure 5.27 - The Crow's Nest Spring site (a) shows evidence for iron oxide staining in the Carmel (c) and Navajo Formations (b).

5.3.3 Old Mine

Hydrocarbon seepage is exposed in the Navajo Formation of the footwall at the Old Mine Site. At the Old Mine site, hydrocarbons appear as black, hardened pieces with a high shine but are not sticky to the touch (figure 5.28). Although the Old Mine site exposes a canyon measuring 47 in height x 17m in width, hydrocarbon filled fractures are only exposed within an area measuring 14m by 15m right next to the fault.
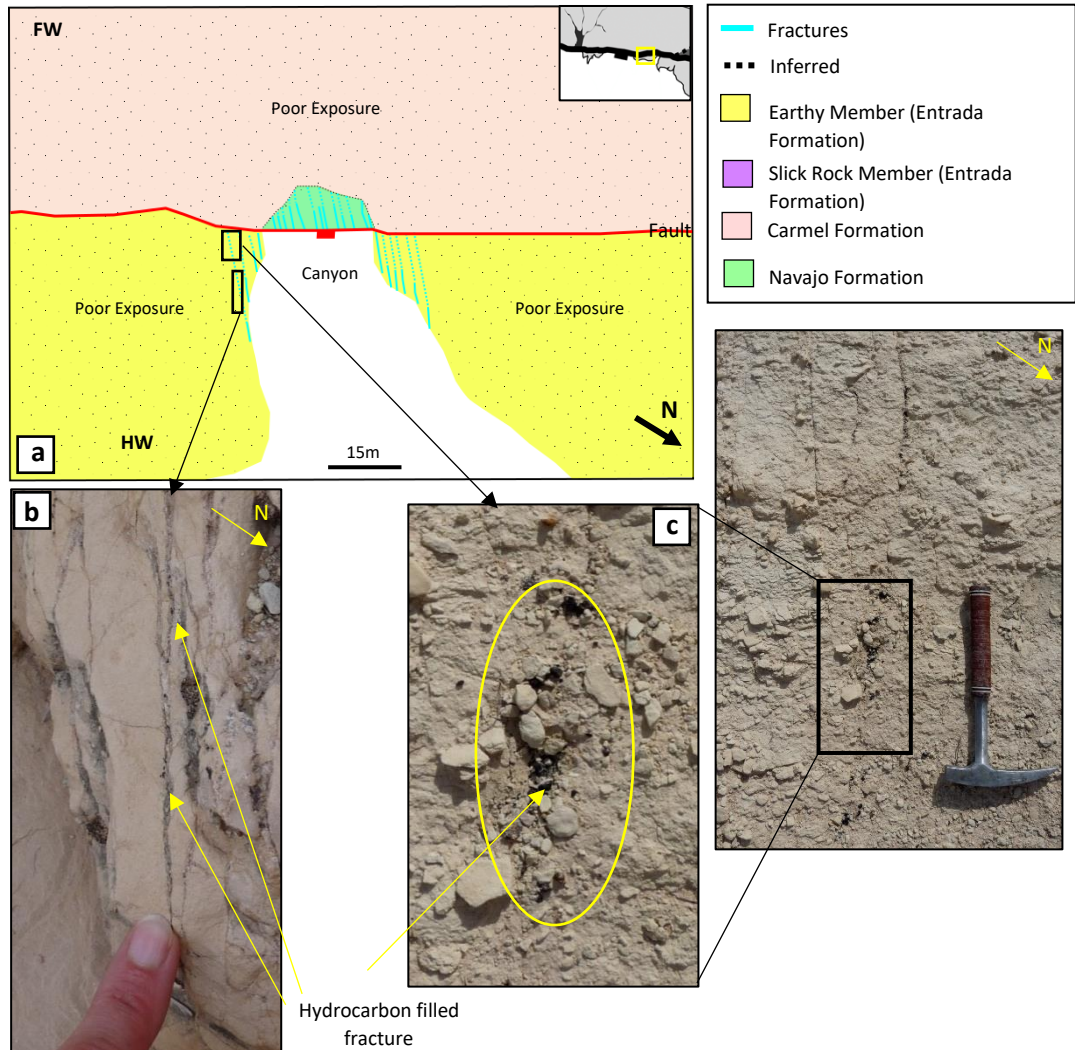
Figure 5.28 - The Old Mine site (a) shows evidence for hydrocarbon filled fractures in the Navajo Formation footwall (b, c).

5.3.4 Zippy Canyon

Hydrocarbon staining is exposed in the (Brush Valley) lens at Zippy Canyon as dark brown and black colouration to the surrounding pale host rock (figure 5.29). Although Zippy Canyon exposes a 58m long section of the Slick Rock Entrada, hydrocarbon staining is only exposed in an area measuring 72cm by 24cm right next to the main fault trace (figure 5.29).

Exposed hydrocarbon staining in the lens
GR N 38°42'30.69" W 110°26'55.65"

Hydrocarbon staining in areas of the host rock which are visibly coarser/more porous
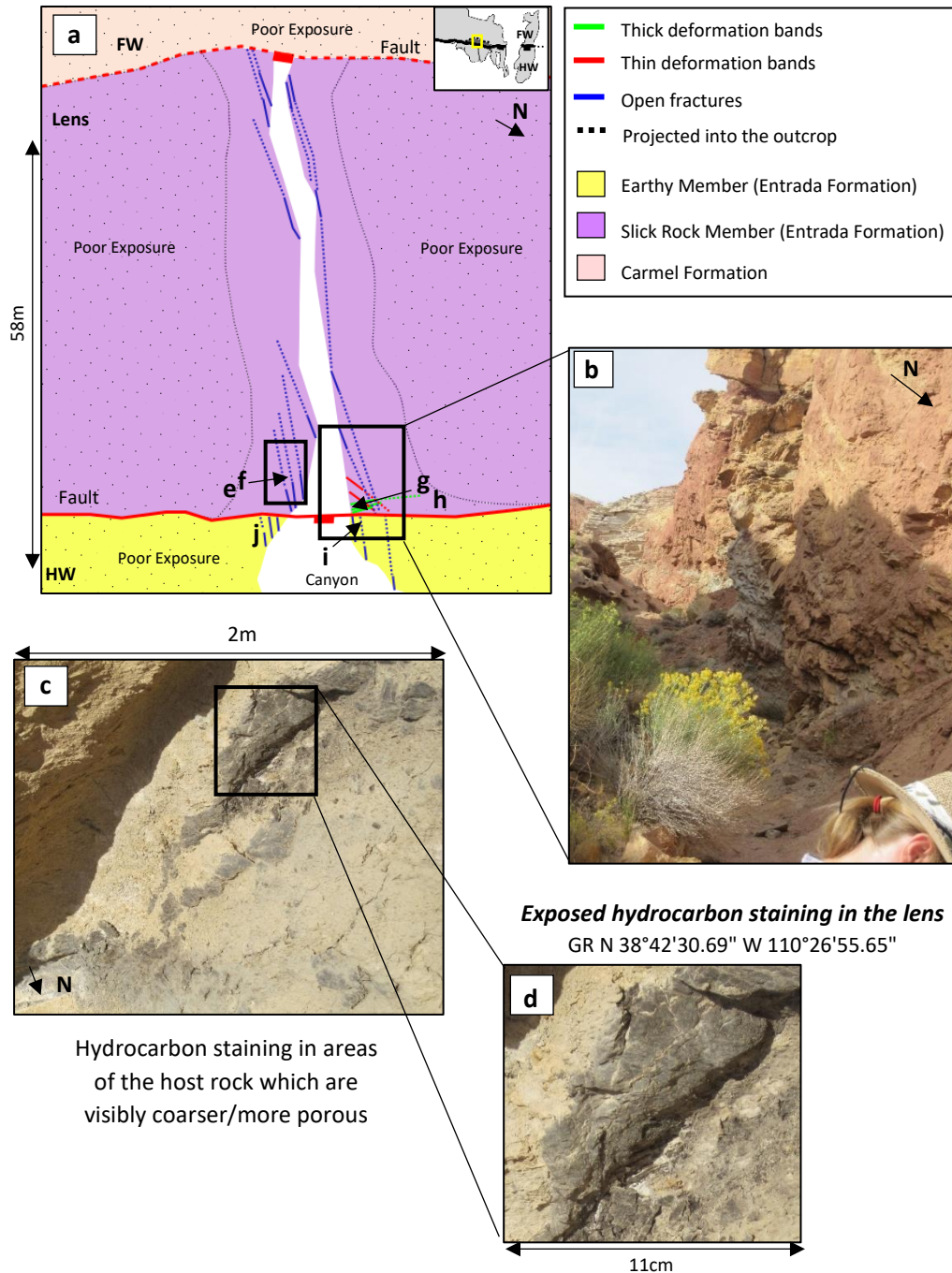
Figure 5.29 – Hydrocarbon staining is exposed at the opening of the Zippy Canyon (a, b). Hydrocarbon staining appears black and dark grey staining the host rock.

Iron oxide staining is exposed in the (Brush Valley) lens at Zippy Canyon as orange and burnt amber colouration to the host rock (figure 5.30). The staining appears up to 0.5cm raised from the surface but can also be seen when the top layer of the host rock has been chipped off. The iron oxide staining is only exposed in one 82cm x 44cm patch of the Slick Rock Entrada on the south-east side of the exposed canyon. Elsewhere in the Zippy Canyon, iron oxide staining is not visible.

Exposed iron oxide staining in the lens
GR N 38°42'30.69" W 110°26'55.65"

1.7m
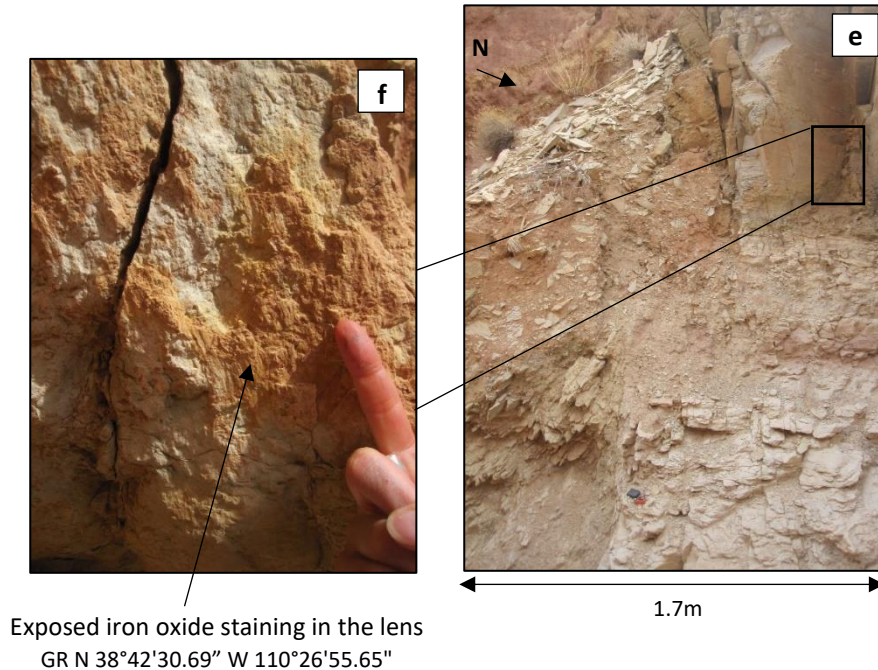
Figure 5.30-   Iron oxide staining is exposed at the Zippy Canyon site (e). Iron oxide staining appears orange to burnt amber in colour (f).

Evidence of bleaching is observed within the lens at Zippy Canyon. Where the lens is exposed, the Slick Rock Entrada appears crumbly, fragile and pale (figure 5.31).

There is evidence of bleached bedding and bleached fractures in the Earthy Entrada hanging wall at the Zippy Canyon site (figure 5.32). Bleached bedding appears as white or very pale colouration and haloes to some beds of the Earthy Entrada (figure 5.32). The bleaching of beds in the hanging wall only occurs where there are multiple weaknesses in the rock, for example, where multiple fractures are exposed and are bleached as shown in figure 5.32.

There is a higher frequency of bleached beds closer to the main fault trace. In the exposed hanging wall there are three bleached beds per metre horizontally from the fault which lie

parallel to the main fault trace. Bleached beds die out away from the fault into the hanging wall to one bleached bed per metre at approximately 4m away from the main fault trace.

Bleached fractures are exposed in the Earthy Entrada in the hanging wall (figure 5.32). Fractures are surrounded by a halo of discolouration to the host rock measuring between 1cm and 6cm surrounding the fracture. All of the observed fractures at the Zippy Canyon site are bleached.

Looking south-west into the canyon standing in the hanging-wall, looking into the lens
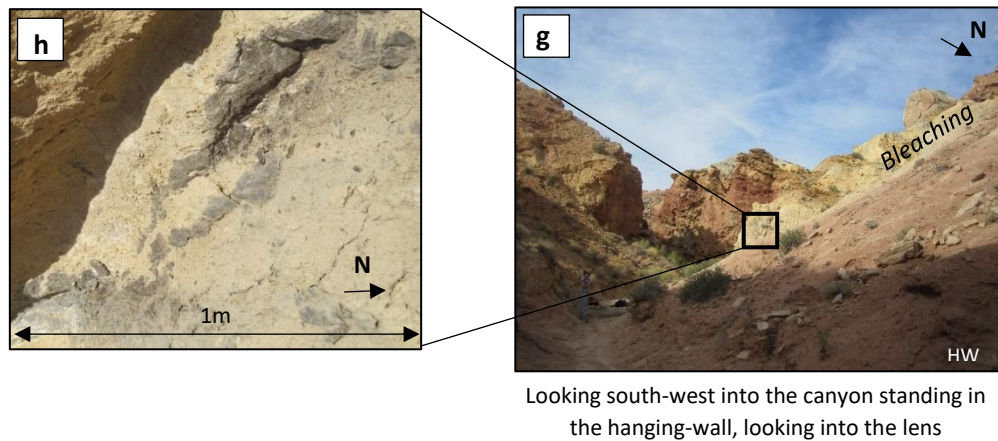
Figure 5.31 – The Slick Rock Entrada appears much more fragile and crumbly within the lens than elsewhere at the field locality (g, h).
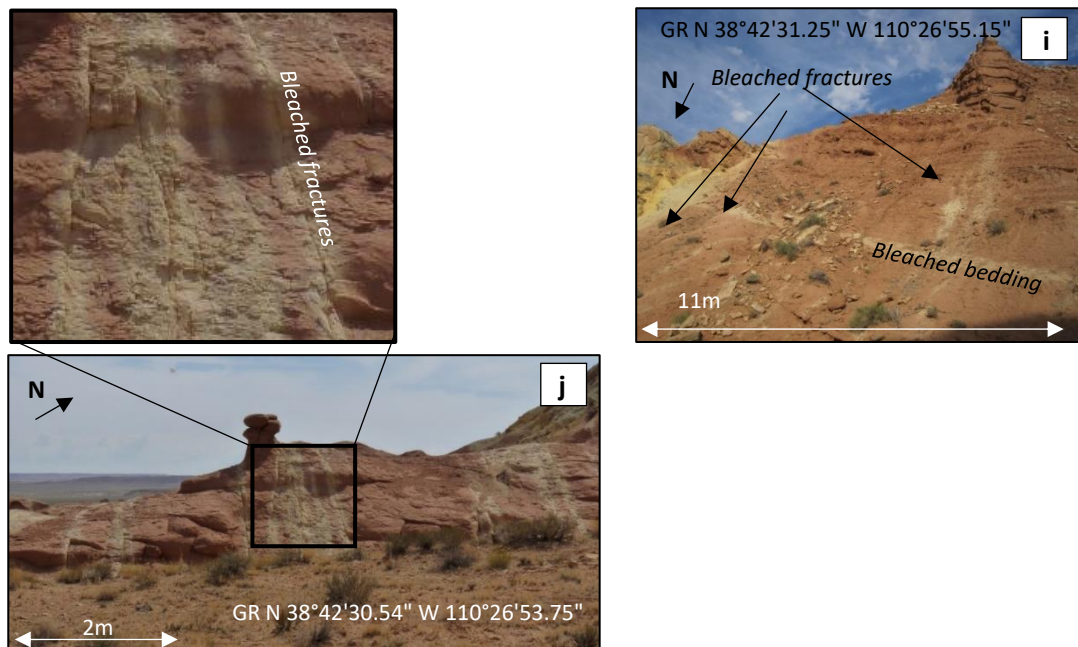
Figure 5.32 -   The Zippy Canyon shows evidence of bleached fractures (j) and bedding (i) in the Earthy Entrada hanging wall.

5.3.5 Brush Valley

In the Brush Valley lens hydrocarbon staining appears as dark brown and black colouration to the surrounding Slick Rock Entrada pale host rock (figure 5.33). From estimating in the field, approximately 20-30% of the Slick Rock Entrada at the Brush Valley lens is stained with hydrocarbons. Where the rock face has been incised, there is typically a higher percentage of hydrocarbon staining present (~30%) compared to low lying, flat areas of the host rock which have less hydrocarbon staining present (~>10%).
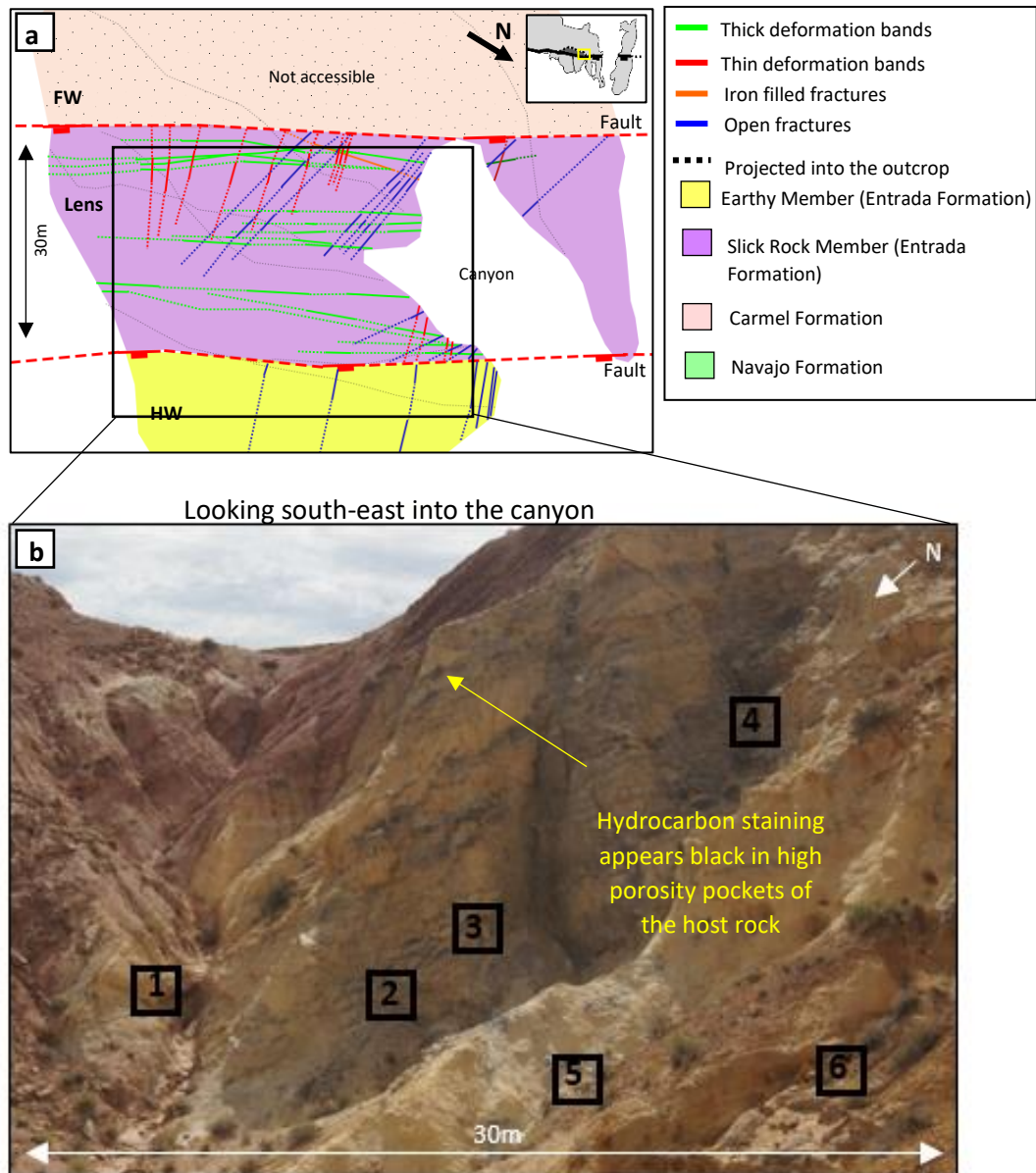
Figure 5.33 – The Brush Valley site has evidence for hydrocarbon staining (a). Six samples were taken from the Brush Valley site as indicated in b.

Where there is hydrocarbon staining, the rock is fragile and crumbly (figure 5.34). Hydrocarbon staining occurs in isolated or continuous patches measuring between 1-2cm and up to 8-9m. Hydrocarbons stain in pockets of more visibly porous and coarser grained rock (figure 5.34).

Square 1 - 40cm x 40cm at GR N 38°42'32.44" W 110°26'58.48"
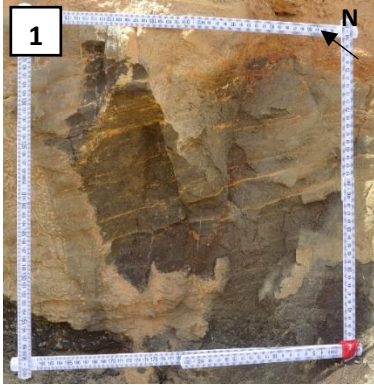
Square 2 - 1m x 1m at GR N 38°42'32.24" W 110°26'58.89"

Square 3 - 1m x 1m at GR N 38°42'32.11" W 110°26'58.96"

Square 4 - 1m x 1m at GR N 38°42'32.24" W 110°26'58.89"
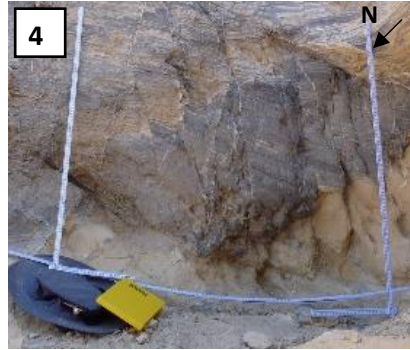
Square 5 – 20cm x 20cm at GR N 38°42'32.10" W 110°26'59.27"
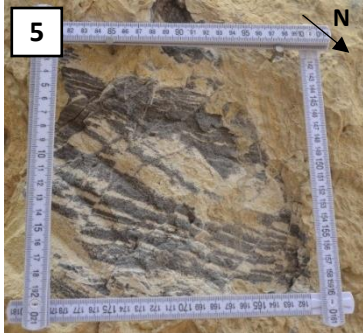
Square 6 – 20cm x 20cm at GR N 38°42'32.28" W 110°26'59.62"
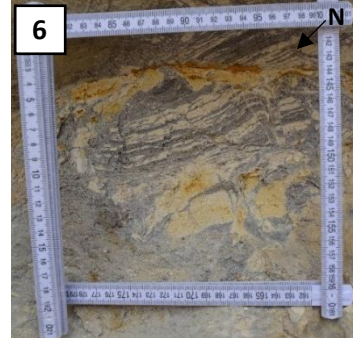
Figure 5.34 – 1-6 show the six samples taken from the Brush Valley lens site.

Six samples have been collected from the Brush Valley site and the locations of these are show in figures 5.33 and 5.34. These six samples were chosen on the basis of good exposure and where samples could be collected accessibly. However, only four samples were successfully prepared for thin section, the remaining two samples were too fragile. From the four samples prepared, five photomicrographs of each sample have been analysed.

As shown by photomicrographs shown in figure 5.35, where there is no calcite cement, hydrocarbon stains the host rock by infilling pore space and coating quartz.

Evidence of iron oxide staining and nodules is observed in the Slick Rock Entrada at the Brush Valley lens (figure 5.36). Iron oxide staining in the lens appears as tan and orange colouration to the host rock which is flat to the surface (figure 5.36). Iron oxide staining is concentrated in areas of the host rock which are not filled or stained by hydrocarbons. Iron oxide staining is exposed as small 2-3cm isolated patches and as staining to areas which are 4-6 metres in size. Field observations estimate approximately up to 30% of the Slick Rock Entrada in the Brush Valley lens is stained with iron oxide.

In thin section, iron oxide staining is observed as brown coating around quartz grains, infilling pore space and associated with deformation bands (figure 5.36). Four samples of the Slick Rock Entrada were analysed from the Brush Valley lens and from an average of five photomicrographs analysed under thin section, it is estimated that iron oxide stains approximately 30-35% of the Slick Rock Entrada exposed at this locality. From analysing twenty photomicrographs, a mean of 28 and standard deviation of 67 was calculated from these estimations. Under thin section, iron oxide staining is mostly observed associated with deformation bands and less is observed infilling pore space. The relative timing of faulting with respect to fluid flow will be discussed in detail in chapter 6.
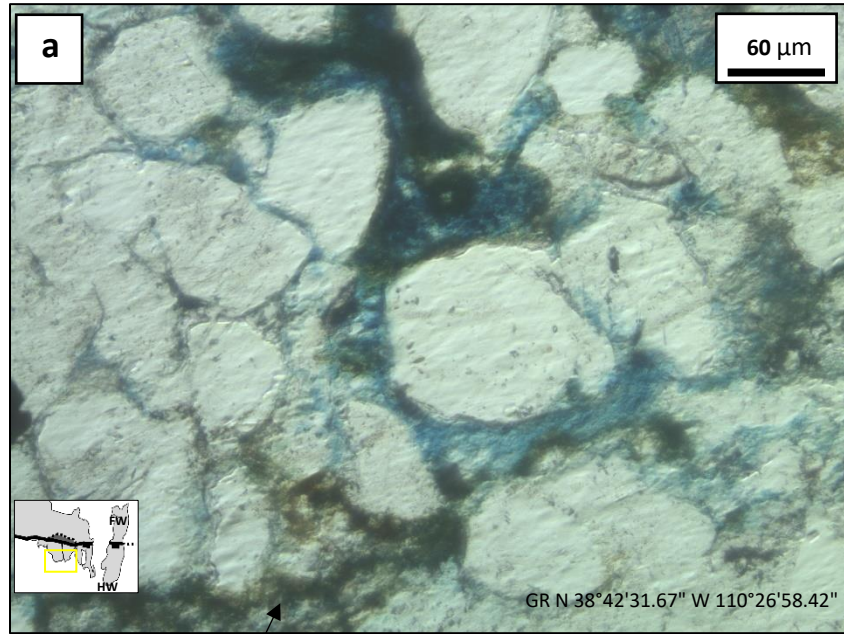
Coating of hydrocarbons surrounding the quartz
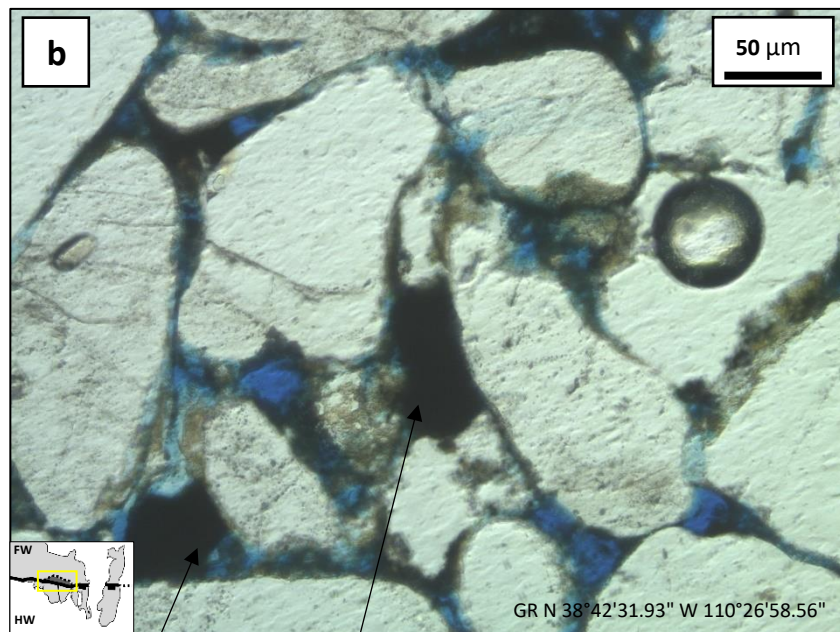
Hydrocarbon infilling pore space

Figure 5.35 – Hydrocarbon staining coats quartz (a) and infills vacant pore space (b) at the Brush Valley site.
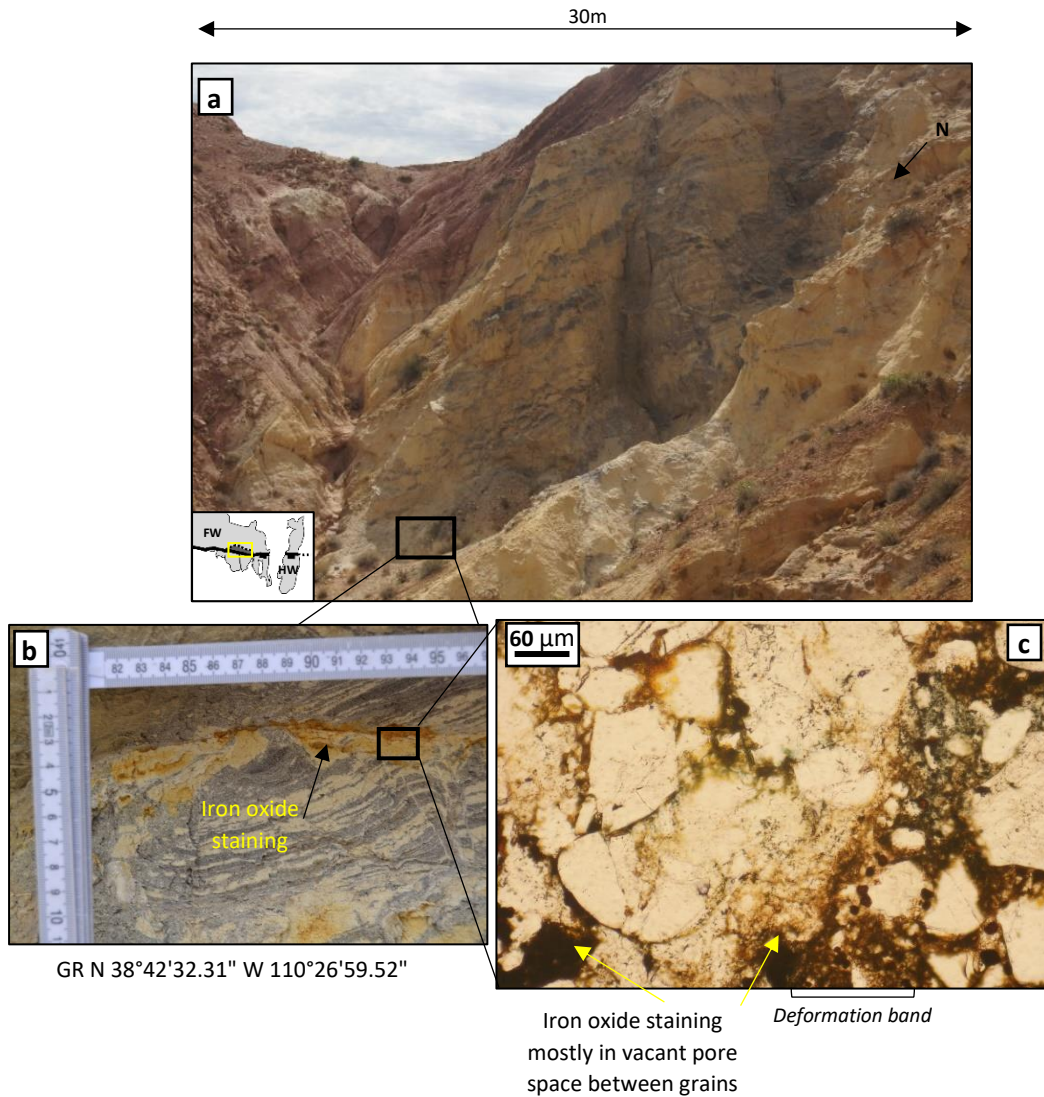
Figure 5.36 – Iron oxide staining at the Brush Valley site (a) is exposed as orange to tan colouration to the host rock (b).

Iron oxide nodules are exposed within the Slick Rock Entrada at the Brush Valley lens. Nodules appear as orange or light brown concretions (figure 5.37). Iron oxide nodules appear as either hard, protruding concentrations (figure 5.37b) or as nodular shaped concretions which lay flat to the surface (figure 5.37c). Nodular shaped concretions are defined differently than iron oxide nodules as both have the same shape but are different in their appearance.

Flat lying nodules are associated with iron oxide staining, however iron nodules which protrude from the surface are mostly isolated. Iron nodules which protrude out of the

surface are uniform in colour. Iron nodules which protrude from the surface are surrounded by hydrocarbon staining.
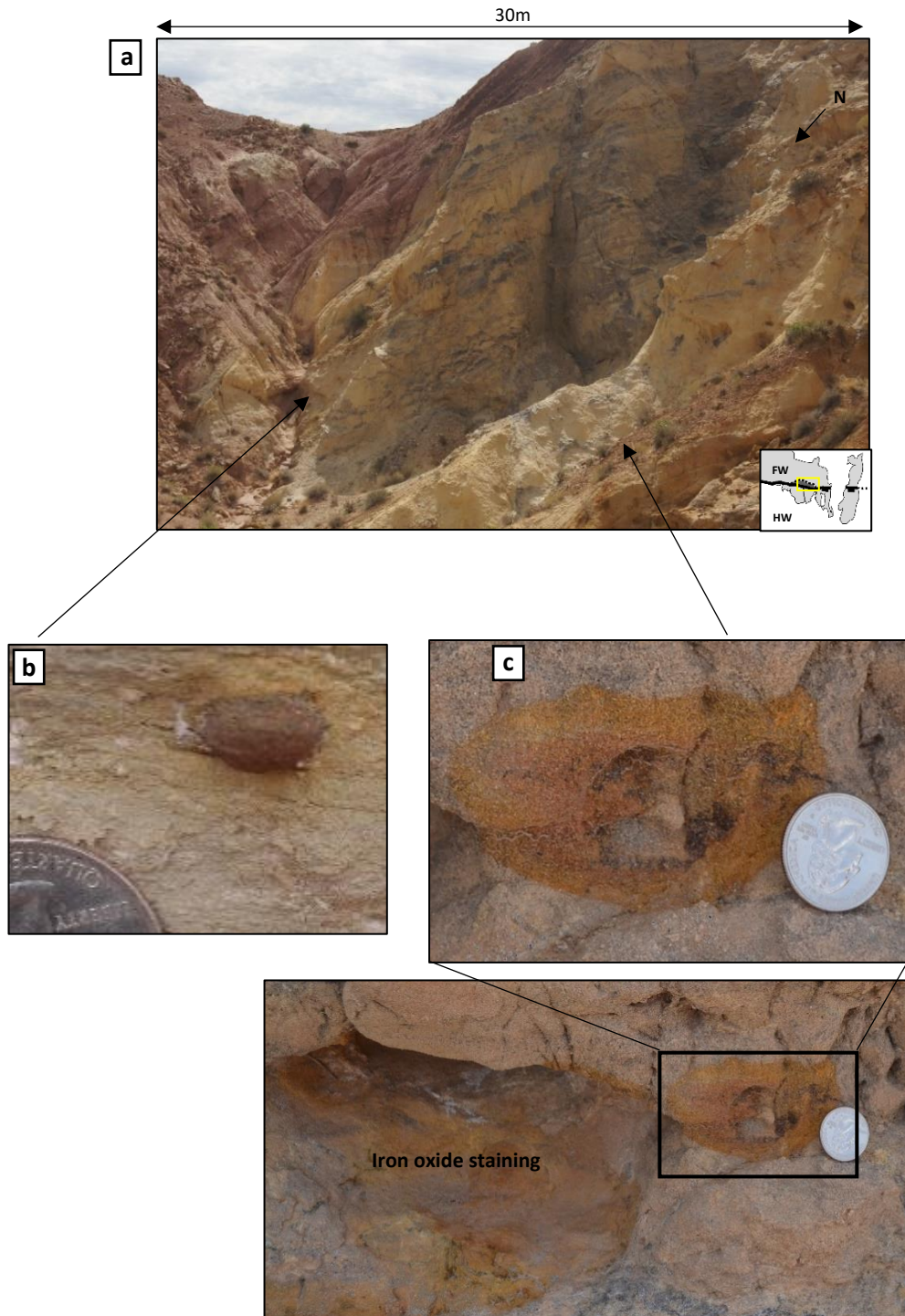
Figure 5.37 – Iron oxide nodules at the Brush Valley site (a) are either expressed as hard protruding nodules (b) or as nodules which are flat to the surface (c) and which usually are associated with iron oxide staining.

Iron-rich fractures are exposed in the Slick Rock Entrada of the Brush Valley lens site (figure 5.38). The Brush Valley lens is exposed as two sections measuring 29m in width x 52m in height in the south-west of the canyon and 13m width x 19m height in the north-east section of the canyon. However, iron-rich fractures are very limited in their distribution and are only observed within a 20cm x 30cm section of the host rock which is shown in figure 5.38.

In outcrop, iron-rich fractures are exposed as tan and brown stained fractures orientated north-south (figure 5.39c). In thin section, fractures which have been stained with iron oxide are continuously filled with iron oxide throughout the fracture (5.39d).

In thin section, iron-rich fractures appear tan or dark brown. As outlined in section 5.2.2, there are some large (up to 60μm) quartz grains within the fractures. Iron oxide staining appears to be mostly isolated within the fractures at this particular outcrop apart from some staining to the host rock as shown by figure 5.38d.   In thin section iron oxide staining is associated with the fractures as haloes and this is observed through iron oxide staining infilling pore space (figure 5.38d).

The entire exposed Slick Rock Entrada at the Brush Valley lens shows evidence of dissolution through various changes in the host rock. Firstly, the host rock appears crumbly, fragile and much paler than the Entrada Formation exposed throughout much of the rest of the field area (figure 5.39).

Elsewhere, the Slick Rock Entrada is comprised of resistant sandstone with minor siltstones, but in the Brush Valley lens it appears fragile and highly porous. In thin section, the host rock is highly porous with an average of 16.5% vacant pore space and 13.7% filled porosity consisting of hydrocarbon and iron oxide staining (figure 5.40). The porosity of the Slick Rock Entrada is analysed further in section 4.9.

As the Slick Rock Entrada exposed within the Brush Valley lens is very fragile and lacks cement, this may have led to later infilling of iron oxide staining to fractures in a north-south orientation.
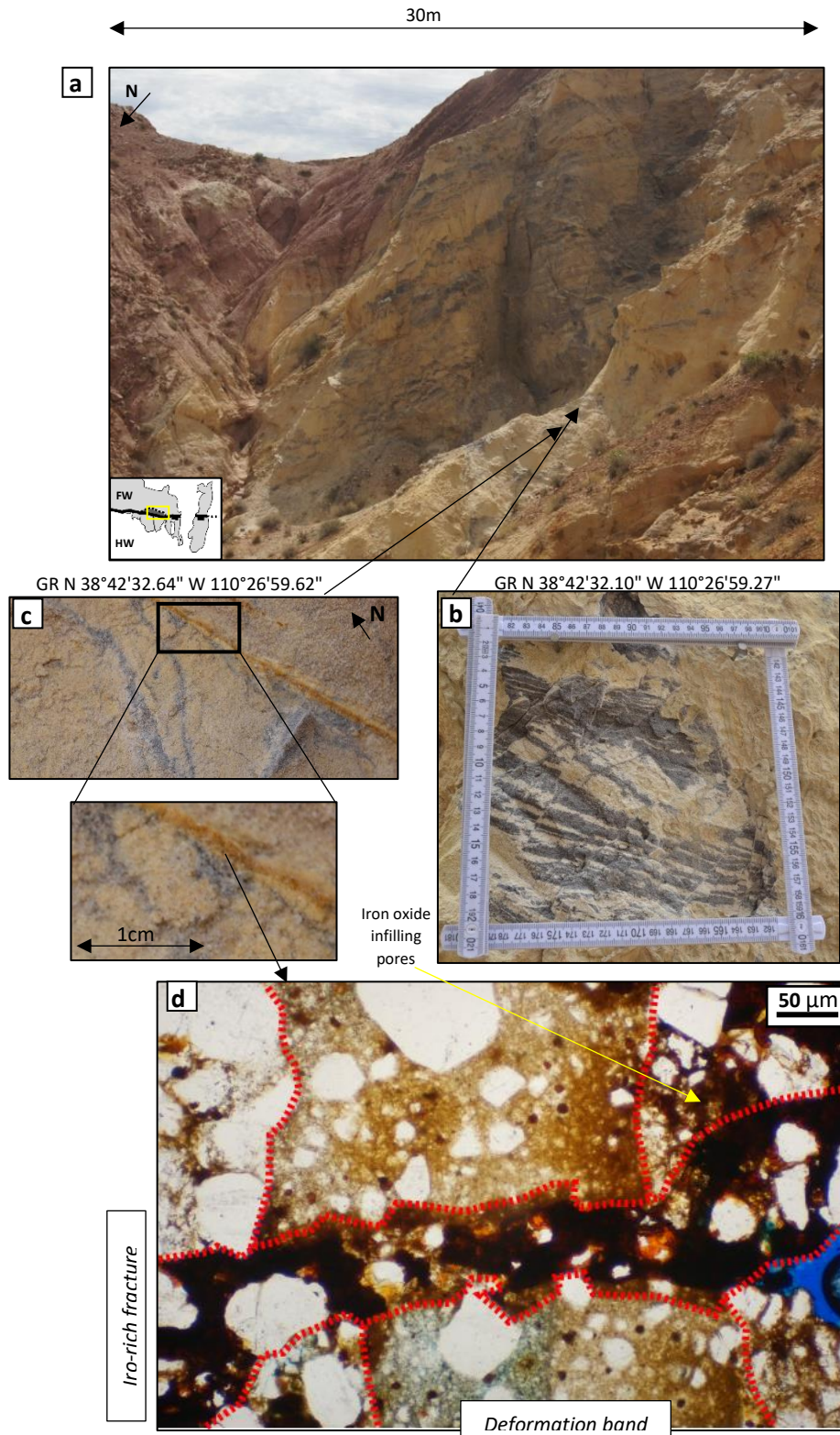
Figure 5.38 – Iron-rich fractures are exposed in the Brush Valley site (a) but only appear in a small 20cm x 30cm section (b). In outcrop fractures appear stained orange (c) and in thin section appear dark brown (d).
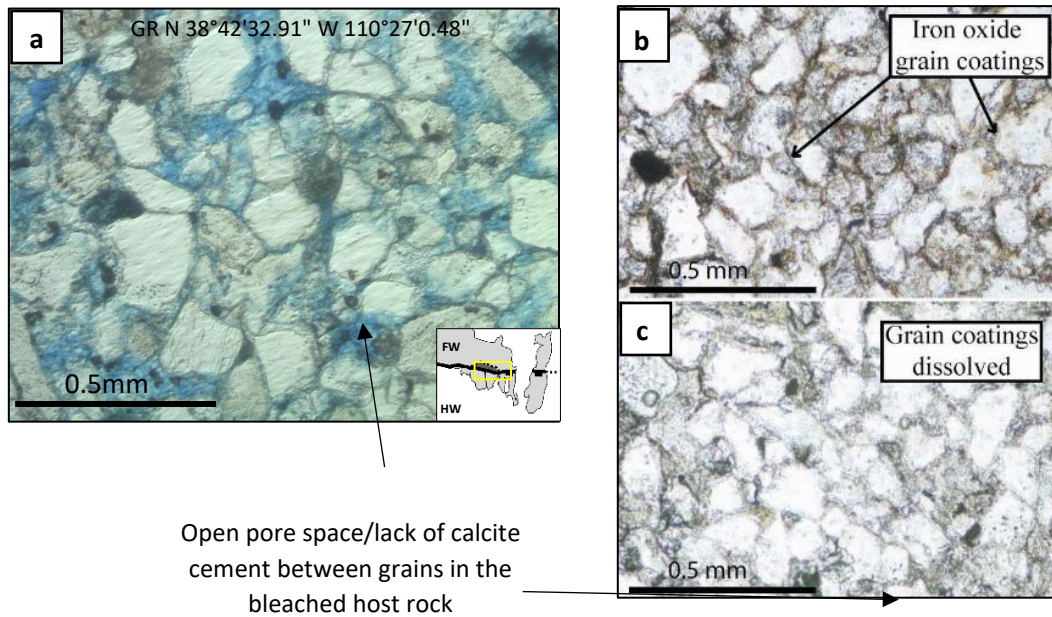
Figure 5.39 – (a) Photomicrograph of the bleached Slick Rock Entrada in the lens at the Brush Valley site. Iron oxide coatings are absent and the porosity is higher. (b) Photomicrograph of a sample of the Entrada Formation from the Green River area which is unbleached shows evidence of calcite cement between grains and grains coated in iron oxide compared to (c) where the Entrada Formation has been bleached and both calcite cement and grain coatings have been dissolved (Wigley et al., 2012).

In the hanging wall of the Brush Valley site, there is evidence of bleached bedding and fractures within the Earthy Entrada (figure 5.41). Bleached bedding is exposed as cream and white halos of between 1-2cm and 40cm aligned with some hardier, more resistant bedding (figure 5.40b).

The bleached fractures are exposed by bleached pale halos which surround the fracture between a few centimetres and up to 25cm (figure 5.40). Both bleached bedding and bleached fractures are exposed adjacent to the fault trace and fracturing decreases in frequency from 5-6 fractures per metre to less than 1-2 fractures per metre approximately 6 metres away from the fault trace. Scanlines were taken to measure fractures and the results, methods and analysis of this is outlined in section 4.6.3.
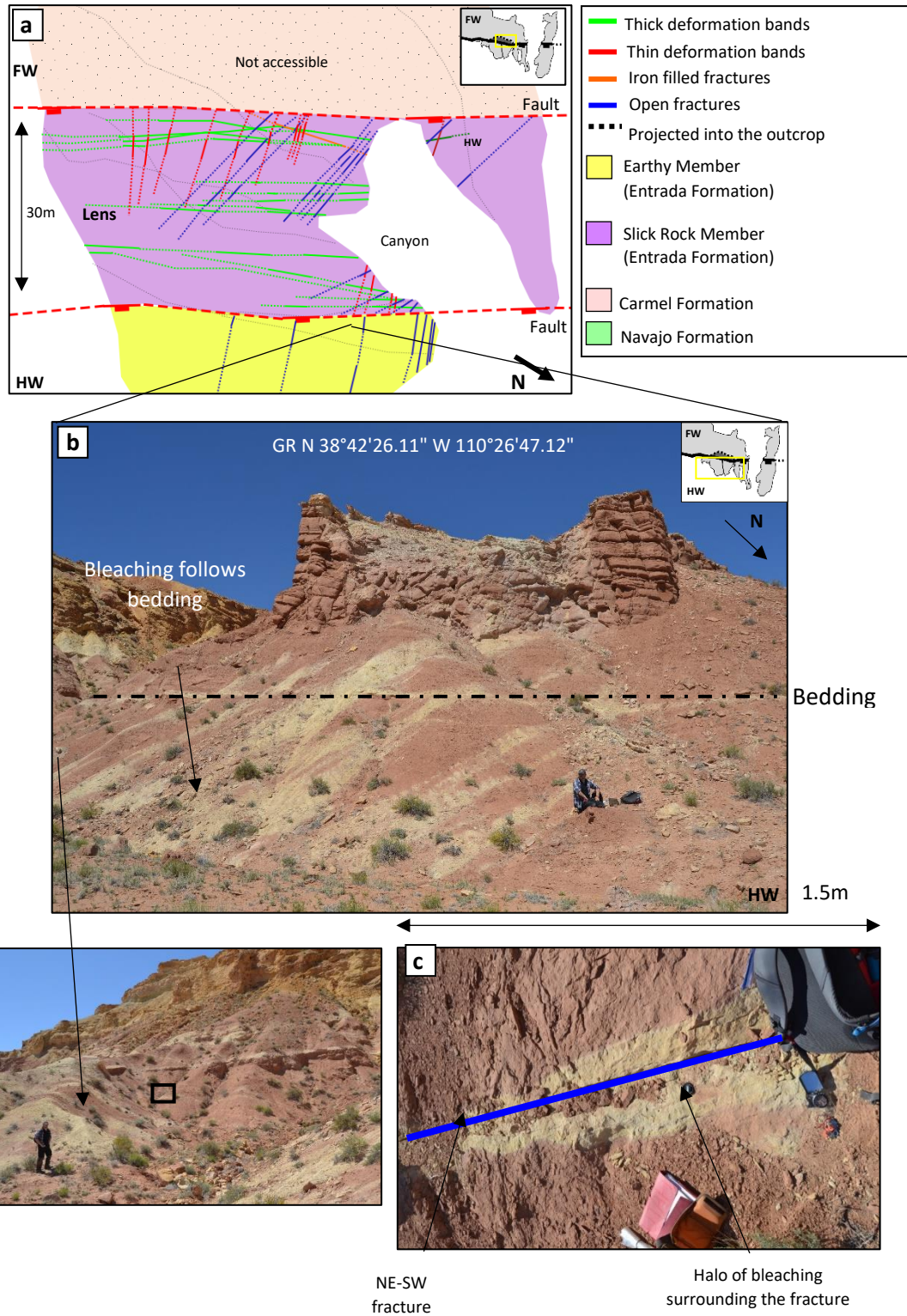
Figure 5.40 – Bleached bedding is exposed in the hanging-wall at the Brush Valley site (a). Bleaching of bedding is exposed as white or cream haloes (b). Haloes of bleaching surround NE-SW trending fractures.

At the Crow's Nest Fault, hydrocarbons are only observed staining the rock within the Slick Rock Entrada which is exposed within the Brush Valley lens at the Brush Valley and Zippy Canyon localities. Throughout Utah, the Entrada Formation has been documented as a carrier-system for hydrocarbons which has facilitated hydrocarbon migration from depth (Garden et al., 2001). The Brush Valley lens shows evidence for multiple episodes of paleo fluid flow (dissolution, iron oxide staining, bleaching) which suggests the Brush Valley lens is stained because of its position within the fault structure as opposed to lithology being the only control on hydrocarbon staining.

5.3.6 Spider Canyon

Iron oxide staining is exposed in the footwall at the Spider Canyon site as tan and light brown discolouration to the host rock which is flat to the surface (figure 5.41). The Spider Canyon site is exposed as a 35m wide by 71m long high section into the footwall, however there is very little iron oxide staining present in the exposed Carmel Formation in the footwall. Iron oxide staining is confined to six patches of staining which are exposed between 15cm and 1.1m in size. Patches of exposed iron oxide staining are spaced randomly throughout the Carmel Formation host rock and show no indication of an increase towards the main fault trace.
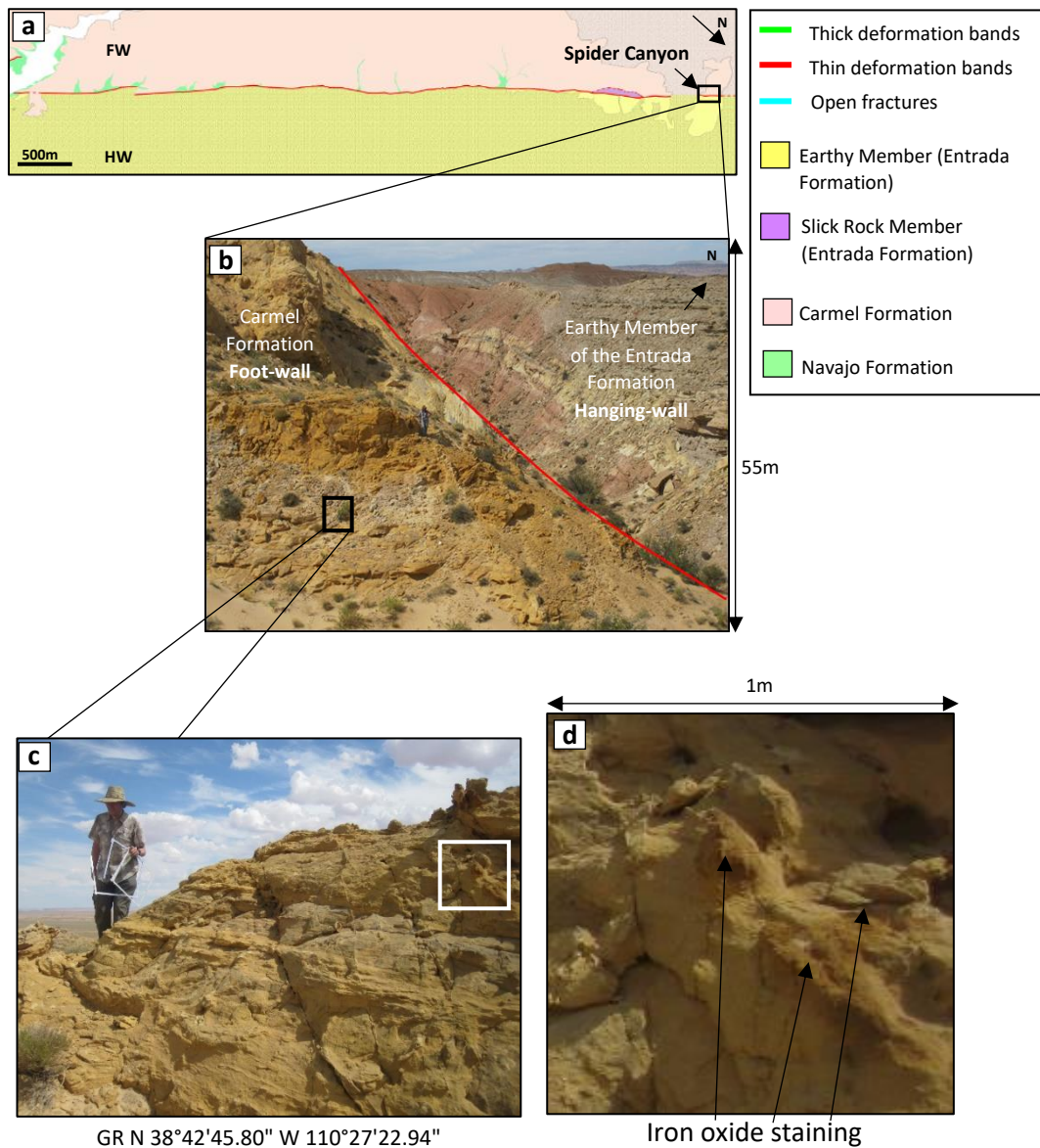
Figure 5.41 – The Spider Canyon (a) exposes the Carmel Formation in the foot-wall (b). Within the Carmel Formation there is evidence of iron oxide staining (c, d).

Bleached bedding is expressed in the Earthy Entrada of the hanging wall as halos of cream and white colouration to the host rock of exposed bedding (figure 5.42). Where beds are bleached, the host rock appears crumbly and fragile. Bleached halos range from 4cm to 10m in thickness.

There is a higher frequency of bleached beds closer to the main fault trace. In the exposed hanging wall there are five bleached beds per metre horizontally from the fault which lie parallel to the main fault trace. Bleached beds die out away from the fault into the hanging wall to one bleached bed per metre at approximately 12m away from the main fault trace.
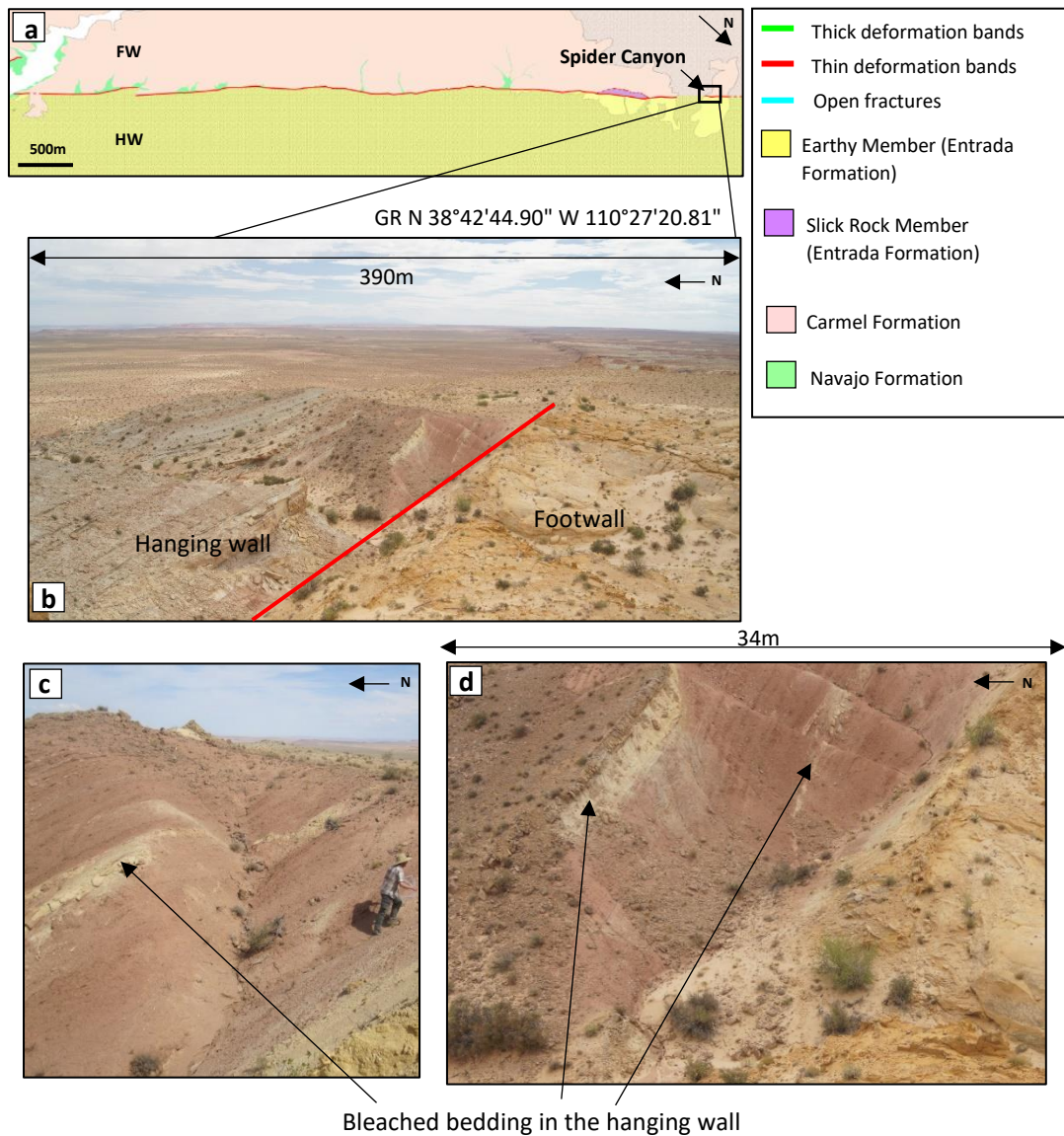
Figure 5.42 – Bleached bedding is exposed in the hanging wall at the Spider Canyon site (a, b). Within the hanging wall, bleached bedding is exposed as white and cream discoloration to the host rock (c, d).

5.3.7 Ballooning Relay Ramp

Between the Brush Valley site and the Spider Canyon site is the Ballooning Relay Ramp exposing the Earthy Entrada (figure 5.43b). The relay ramp shows evidence of both bleached bedding and bleached fractures (figure 5.43c). Bleached bedding is discontinuous and is exposed as white haloes between 5cm and 1m wide surrounding some prominent, more resistant beds (figure 5.43). Bleached fractures are surrounded by cream and pale

yellow haloes which are between 4cm and 80cm wide (figure 5.43d). There is no indication of an increase in bleached fractures or bedding towards the main fault trace.
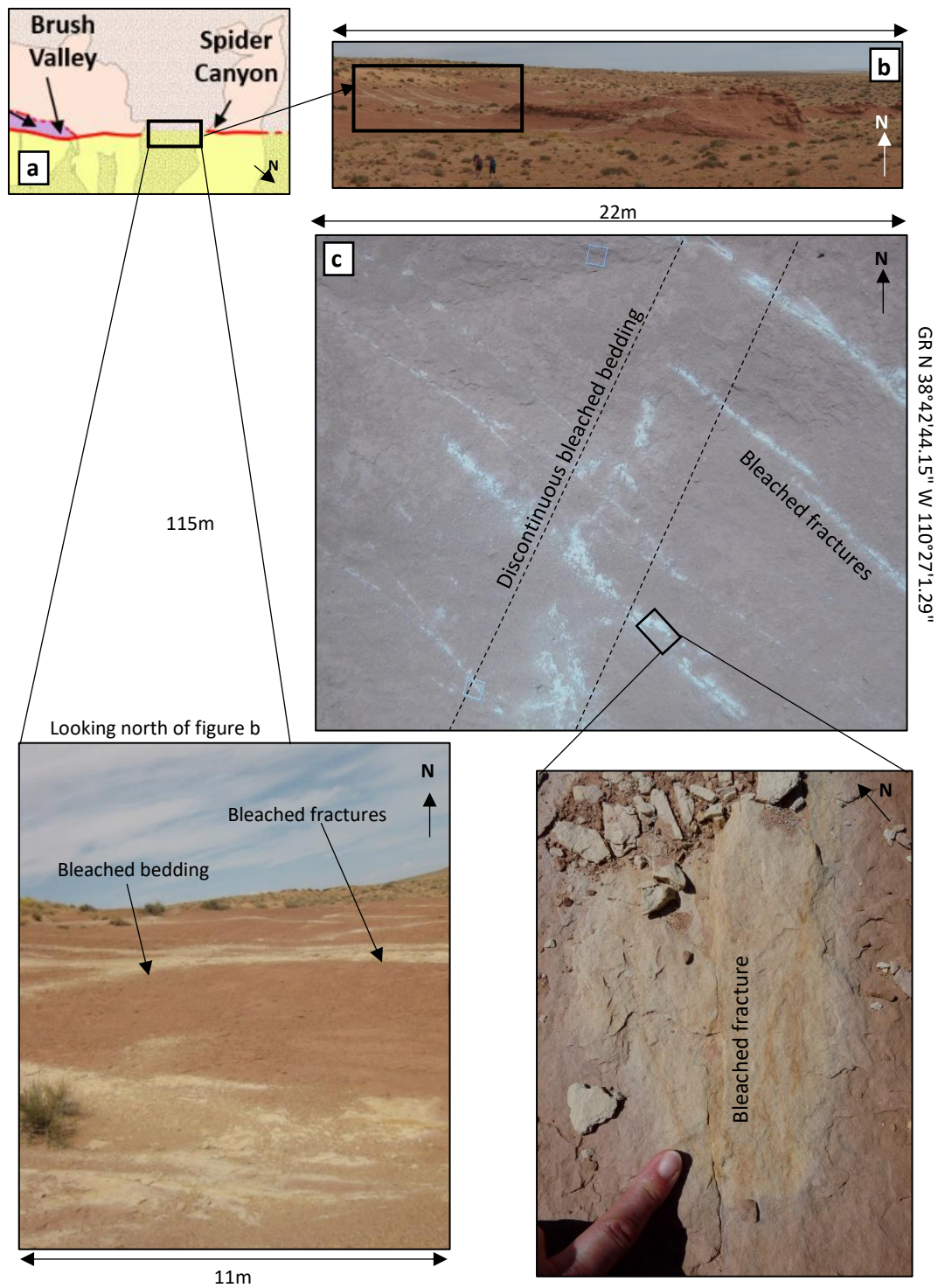
Figure 5.43– The relay ramp between the Brush Valley site and the Spider Canyon site (a-c) is exposed as the Earthy Entrada and bleached bedding and fractures are observed.

5.4 Fluids in the basin – origins and chemistry

5.4.1 Modern hydrocarbons

Hydrocarbon staining is observed at the Crow's Nest Fault within high porosity/low cement areas of the host rock, as hydrocarbons seeping from fracture junctions and infilling fractures.

Elsewhere in Utah, hydrocarbons have been observed in the form of hydrocarbon staining within joints and as bitumen veins (Chan et al., 2000; Eichhubl et al., 2009). Along the Moab Fault, spherical calcite deposits accumulate where hydrocarbons stain joints. Calcite deposits are typically up to 5cm in diameter and form cemented layers (Chan et al., 2000). Under thin section, calcite fills pore space surrounding hydrocarbons, suggesting later, secondary deposition. Chan et al., (2000) suggested that the fluids responsible for the precipitation of calcite at the Moab Fault were reducing and this was likely due to interaction with hydrocarbons.

It is thought that bleaching and the accumulation of calcite surrounding hydrocarbon deposits was likely arbitrated through the microbial oxidation of hydrocarbons from basinal fluids that have ascended from the underlying organic rich Pennsylvanian source rocks (Nuccio and Condon, 1996). During the microbial breakdown of hydrocarbons, ^{13}C depleted carbon dioxide is released into pore waters and calcite is deposited (Roberts and Aharon, 1994).

Oil and gas in Utah was likely generated in the Paradox Basin during the Cretaceous from Mid- Pennsylvanian source rocks; the Islay Creek Cycle and the Cane Creek Cycle (Nuccio and Condon, 1996) (figure 5.44).
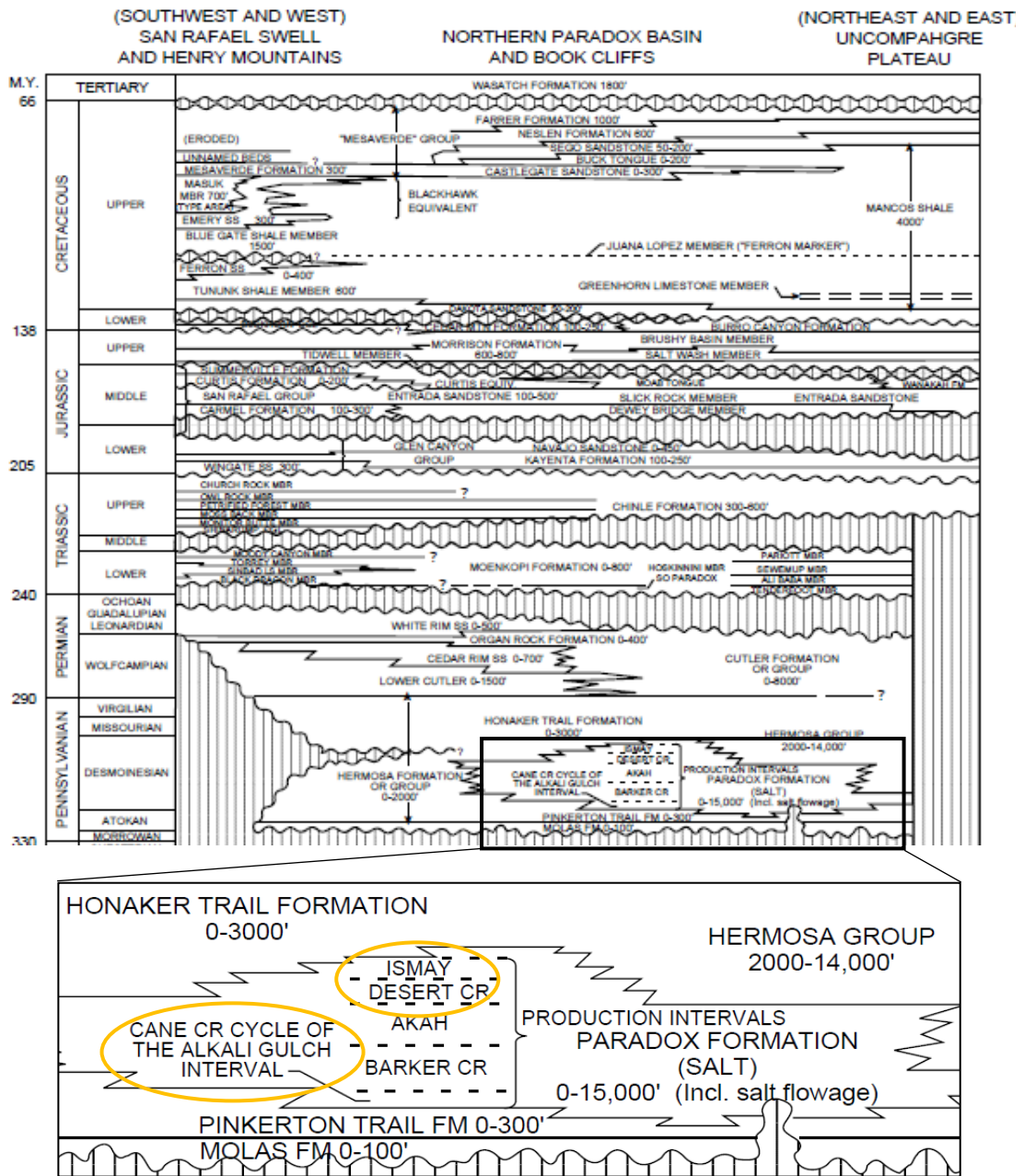
Figure 5.44 – Correlation chart for the lithology of the Paradox Basin and surrounding vicinity. Original figure from Molenaar, (1987) has been modified by Nuccio and Condon, (1996). The figure presents the Cane Creek Cycle and Islay Creek Cycle as potential hydrocarbon source rocks in the Paradox Basin.

Approximately 10km north-west of the Crow's Nest Fault lies the largest accumulation of heavy oil or 'tar' in the U.S.A spanning over 600km^2 (Demaison, 1977; Sanford, 2000) (figure 5.45). Tar is predominantly found within the Lower Permian White Rim Sandstone of the Cutler Group (Campbell and Ritzma, 1979). There is estimated to be 12.5-16 billion barrels

of tar in this area (Campbell and Ritzma, 1979). Formed by a classic stratigraphic trap, tar formed as the White Rim Sandstone juxtaposed against Monument Uplift (Baars and Seager, 1970). The source of the petroleum in this area is thought to be from the Late Proterozoic Chuar Group found in west central Utah. Kerogen was produced prior to maximum burial in the Late Jurassic or Early Cretaceous according to Nuccio and Condon, (1996) and (Sanford, 2000).

The search for petroleum first began in 1847 in Utah with the first oil production in 1907 (Stowe, 1972). Since 1970 when the oil fields were closed there have been 391,335,318 barrels of oil produced (Stowe, 1972). As shown by figure 5.45a, the Moab and Green River areas have been actively explored for petroleum such as kerogen and bitumen.
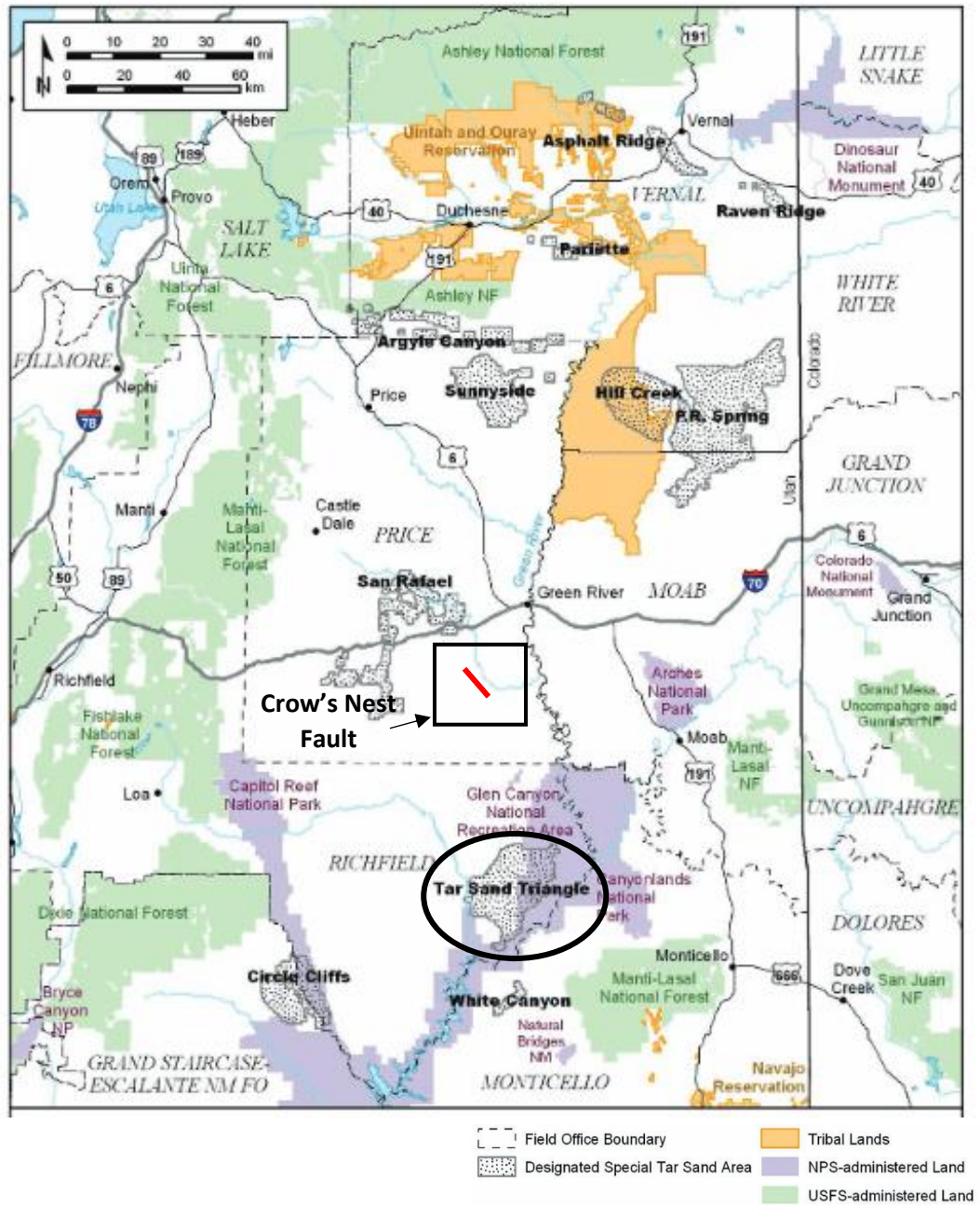
Figure 5.45 – Map detailing the Tar Sand Triangle with respect to the Crow's Nest Fault. Figure modified from Shale, (2008).

5.4.2 Iron oxide staining and nodules

Iron nodules provide useful information of diagenesis and of the interaction between fluids and sediments (Bowen et al., 2008). By constraining the conditions in which iron nodules form, better interpretations can be made for the diagenetic histories of iron nodule hosted lithologies.

Iron nodules have been extensively studied in the Jurassic Navajo Formation in southern central Utah (Chan et al., 2000; Garden et al., 2001; Chan et al., 2004; Beitler et al., 2005; Chan et al., 2005, 2006, 2007).

In the Escalante area of Utah, small percentages of pyrite have been detected in iron nodules which suggests that Fe was likely mobilised and transported as Fe^{2+} (Beitler et al., 2003; Chan et al., 2005; Busigny and Dauphas, 2007). The mixing of Fe-rich reducing fluids with oxidising groundwater results in the precipitation of Fe as hydrous ferric oxide (HFO). Over time, HFO dehydrates to goethite (FeOOH) and finally to hematite (Fe_2O_3) (Busigny and Dauphas, 2007). Fe-isotopes also revealed that precipitation of iron concretions was not associated with any kinematic isotope fractionation (Busigny and Dauphas, 2007).

Concretions formed in Utah are thought to be late-stage diagenetic products formed through the bleaching of red, hematite rich beds by reducing fluids (Bowen et al., 2008). The mixing of Fe-rich reducing fluids with oxidising groundwater results in the formation of iron concretions and iron staining.

Elsewhere, examples of iron nodules have been extensively studied on Mars and at Lake Brown, Western Australia. These examples serve as an analogue for Crow's Nest Fault. Similar to iron nodules formed in Utah, nodules on Mars are thought to be precipitated initially as goethite and then dehydrated to hematite (Chan et al., 2005; Tosca et al., 2005). However, nodules on Mars are interpreted only by comparison to nodules on Earth so cannot be used as an analogue. Iron nodules observed at Lake Brown, a saline lake in southern Western Australia are actively precipitating in-situ (Bowen et al, 2008). For nodules to form, there must be an iron source, mobilisation and mass transfer of iron and a geochemical influx which drives precipitation of nodules (Bowen et al., 2008).

Lake Brown is underlain by Archean metamorphic and igneous rocks. It is thought that the iron source at this location comes from widespread weathering of the underlying bedrock as evident by extensive zones of bleaching (Bowen et al., 2008). Iron was likely transported as Fe^{2+} by reducing groundwater. Iron nodules at Lake Brown are commonly found in permeable beds bound by impermeable clay rich beds. Nodule bearing beds typically represent an area of mixing between oxidising surface waters and saline groundwater which leads to hematite precipitation (Bowen et al., 2008).

At Lake Brown, iron nodules are typically 2-5mm in diameter and are filled with halite, gypsum and quartz (Bowen et al., 2008). In comparison, iron nodules imaged on Mars are observed less than 0.5cm in diameter and consist of up to 50% hematite with the remainder consisting of basinal muds and evaporites (Bowen et al., 2008). Due to the spherical shape and colour of the nodules, they have been termed 'martian blueberries' (Squyeres et al., 2004).

Iron nodules in Utah are typically spherical and contain a solid hematite (Bowen et al., 2008) or quartz rich cement (Busigny and Dauphas, 2007). The Fe isotopic signatures of iron concretions at the Gran Escalante National Monument, Utah have been analysed through the use of anion exchange chromatography using multiple-collector inductively coupled plasma mass spectrometry (MC-ICP-MS) (Busigny and Dauphas, 2007). Results of the analysis show that concretions are comprised mostly of quartz with FeO making up as little as 30% of the composition (Busigny and Dauphas, 2007).

Throughout Utah, nodules range in size, appearance, texture and chemistry. For example, at the Capitol Reef National Park and Gran Escalante National Monument, iron concretions are approximately 1-6cm in diameter and are found protruding from the surface or lying flat to the surface (Busigny and Dauphas, 2007). However nodules have been recorded up to 30cm in diameter in the Moab area and are observed both flat lying and protruding from the surface (Loope et al., 2010).

As seen at the Crow's Nest Fault, evidence for iron nodule precipitation is usually associated alongside other paleo fluid flow evidence such as hydrocarbon staining, modern day springs and dissolution of cement. Chan et al., (2000) suggested that the distribution of iron oxide staining and nodules can be used to determine the movement of reducing saline fluids within the Entrada Formation along the Moab Fault, suggesting a likely relationship between basinal fluids and iron oxide precipitation. Evidence of flow at the Crow's Nest Fault suggests it is likely that iron nodules at the Crow's Nest Fault formed through mixing of Fe-rich reducing fluids with oxidising groundwater. Evidence includes the presence of bleached haloes surrounding fractures and dissolution of calcite cement. The presence of hematite and goethite in iron nodules indicate iron mobility in groundwater flow (Chan et al., 2007).

5.4.3 Bleaching and dissolution of calcite cement

Bleaching provides useful information for controls on fault zone deformation and fluid flow migration. Examples of bleaching have been observed in the hematite Pennsylvanian sandstones of Wyoming (Shebl and Surdam, 1996). Characteristically red sandstone samples were subject to laboratory pyrolysis of water-rock-oil mixtures. As water went through the system it became more reducing with increasing temperature. Samples with the highest % of calcite cement present were subject to the most bleaching and turned grey due to hematic reduction.

In the Paradox Basin, Utah, the Navajo and Entrada formations have been extensively studied for their characteristic bleaching (Chan et al., 2000; Beitler et al., 2003; Busigny and Dauphas, 2007; Parry et al., 2007; Loope et al., 2010; Wigley et al., 2012). At the Moab Fault bleaching within the Navajo Formation appears white adjacent to the fault, however, just east of Moab, the Navajo Formation appears orange suggesting a likely bleaching event at the Moab Fault.

Studies of bleaching in the Navajo Formation at Capitol Reef National Park and Grand Staircase Escalante National Monument, southern Utah have shown extended zones of bleaching (Busigny and Dauphas, 2007). The Navajo Sandstone of the Escalante anticline, south-central Utah appears bleached, however, towards the south-east it is un-bleached (Busigny and Dauphas, 2007). This colour change is explained by Beitler et al., 2003 by the migration of buoyant reducing fluids through the Navajo Formation resulting in a hydrocarbon reservoir within the Escalante anticline. Beitler et al., (2003) suggested that faults of Laramide origin act as conduits for reducing fluids, causing bleaching in the Navajo Formation and result in the secondary migration of hydrocarbons.

The Escalante anticline (figure 5.46) is Permian in age and is a large source of gas holding approximately 1.5-4 trillion cubic feet of gas, whereas most of the petroleum source in the Paradox Basin is trapped in rocks of Triassic age and older (Allison, 1997). Faulting could likely have initiated the transportation of petroleum.
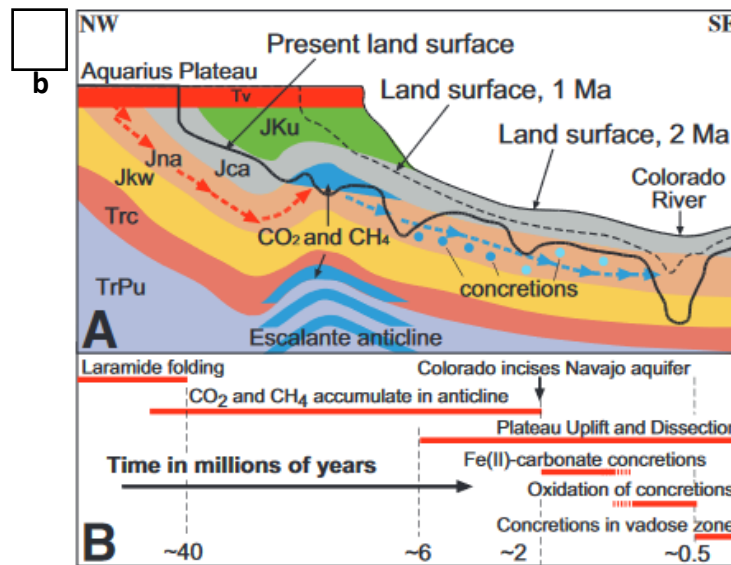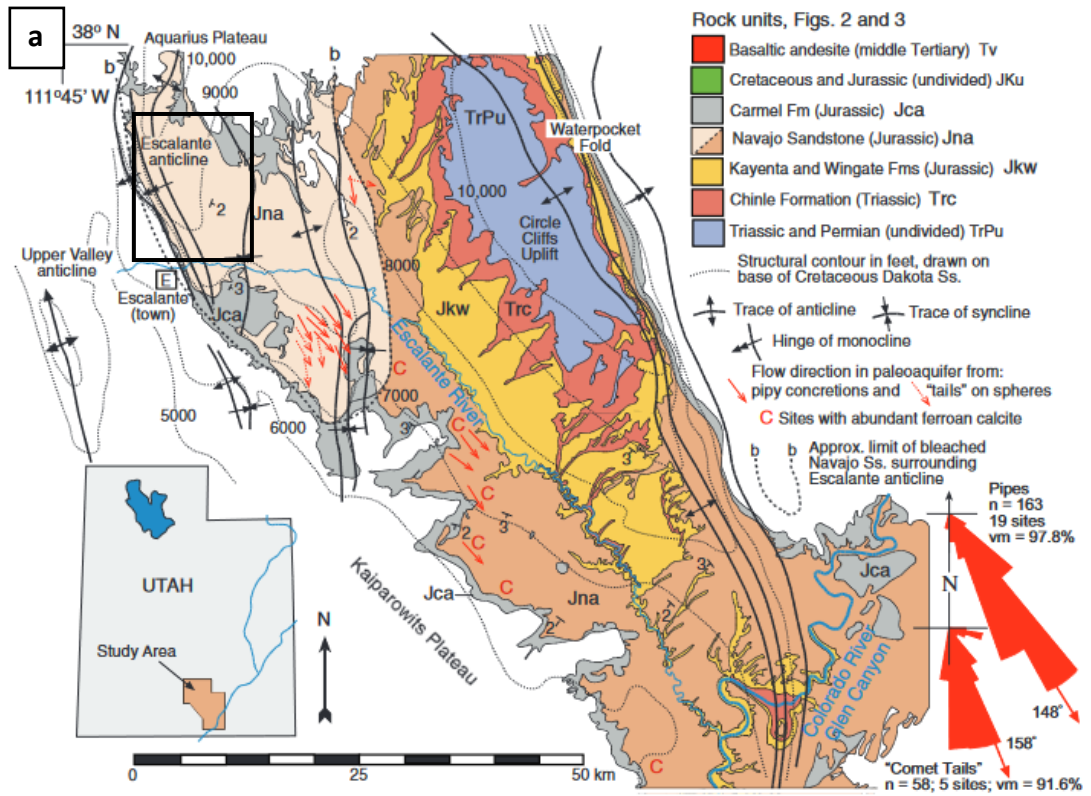
Figure 5.46 – Map showing the Escalante anticline (modified from Loope et al., 2010) and (b) a cross section of the Escalante anticline (Loope et al., 2010).

Regional bleaching suggests that reducing buoyant fluids are likely to have migrated up faults of Laramide age and become trapped within anticlinal folds associated with the Paradox Basin (Beitler et al., 2003; Busigny and Dauphas, 2007).

Alternatively, where bleaching occurs over several kilometres, it is thought that Fe has been transported regionally for a prolonged distance prior to precipitation. Iron was transported for a great distance because it was transported by groundwater that flowed through a CO_2- and methane charged reservoir within the Escalante anticline (Loope et al., 2010).

Fluids are widely debated to be either hydrocarbon rich (Beitler et al., 2003; Busigny and Dauphas, 2007; Loope et al., 2010) or from sources of CO_2 (Haszeldine et al., 2005; Parry et al., 2007; Wigley et al., 2012). Although the origin of reducing fluids has not been completely agreed upon, further evidence such as the presence of tar sands in bleached Navajo sandstone (Beitler et al., 2003) and the presence of bleached bitumen veins along the Moab Fault (Chan et al., 2000) strongly support a hypothesis for the presence of hydrocarbon rich fluids.

At the Crow's Nest Fault, bleaching is observed in both the Slick Rock Entrada and the Earthy Entrada. The Earthy Entrada is characteristically red in its unaltered state. However, fractures and bedding of the Earthy Entrada are bleached white or cream.

At the Brush Valley site, the Slick Rock Entrada is entirely bleached. Typically, the Slick Rock Entrada appears grey, light brown and salmon pink when unaltered. At the Brush Valley lens site, the host rock appears crumbly, fragile and pale in colour.

Elsewhere in Utah there is evidence for bleaching of both the Navajo Formation and the Entrada Formation (Chan et al., 2000; Beitler et al., 2003; Shipton et al., 2004; Haszeldine et al., 2005; Busigny and Dauphas, 2007; Loope et al., 2010; Wigley et al., 2012). There is no evidence of bleaching in the Navajo Formation at the Crow's Nest Fault, however, studies by Beitler et al., (2003) suggest that the base of the Navajo Formation is red when unaltered. The Navajo Formation at the Crow's Nest Fault appears grey and light brown suggesting that is could possibly have been bleached, however in thin section, there is a lack of evidence supporting any removal of cement which would indicate bleaching. However, the base of the Navajo Formation is not exposed in this field area.

It is likely that reducing fluids at the Crow's Nest Fault were hydrocarbon in origin. This is evident by the deposition of secondary hydrocarbons at the Brush Valley and Crow's Nest Spring lenses. Additionally, the redepositing of hematite as iron oxide is observed throughout the Crow's Nest Fault in the form of iron oxide staining, iron-rich fractures and nodules.

5.4.4 Modern water flow

Observations of vertical fluid flow is limited at faults. However, modern day water flow observed at springs allows insight into vertical flow associated with fault zones. Springs are commonly associated with fault zones because vertical groundwater flow is typically enhanced (Caine et al., 1996; Evans at al., 1997; Rowland et al., 2008). Springs offer valuable data of fluid flow potential, flow rates, pressure and the geochemistry and origin of fluids.

Fault related water flow has been observed at the Little Grand Wash Fault, Utah (Shipton et al., 2005; Burnside, 2010). Where the faults have been juxtaposed against the Green River Anticline, waters charged with CO_2 have been vertically channelled up the faults. Rather than springs, large volumes of CO_2 have leaked into the atmosphere in the form of fossilised travertine deposits. At the Little Grand Wash Fault, travertine mounds are restricted to the fault trace and are associated with the Salt Wash Graben (figure 5.47).
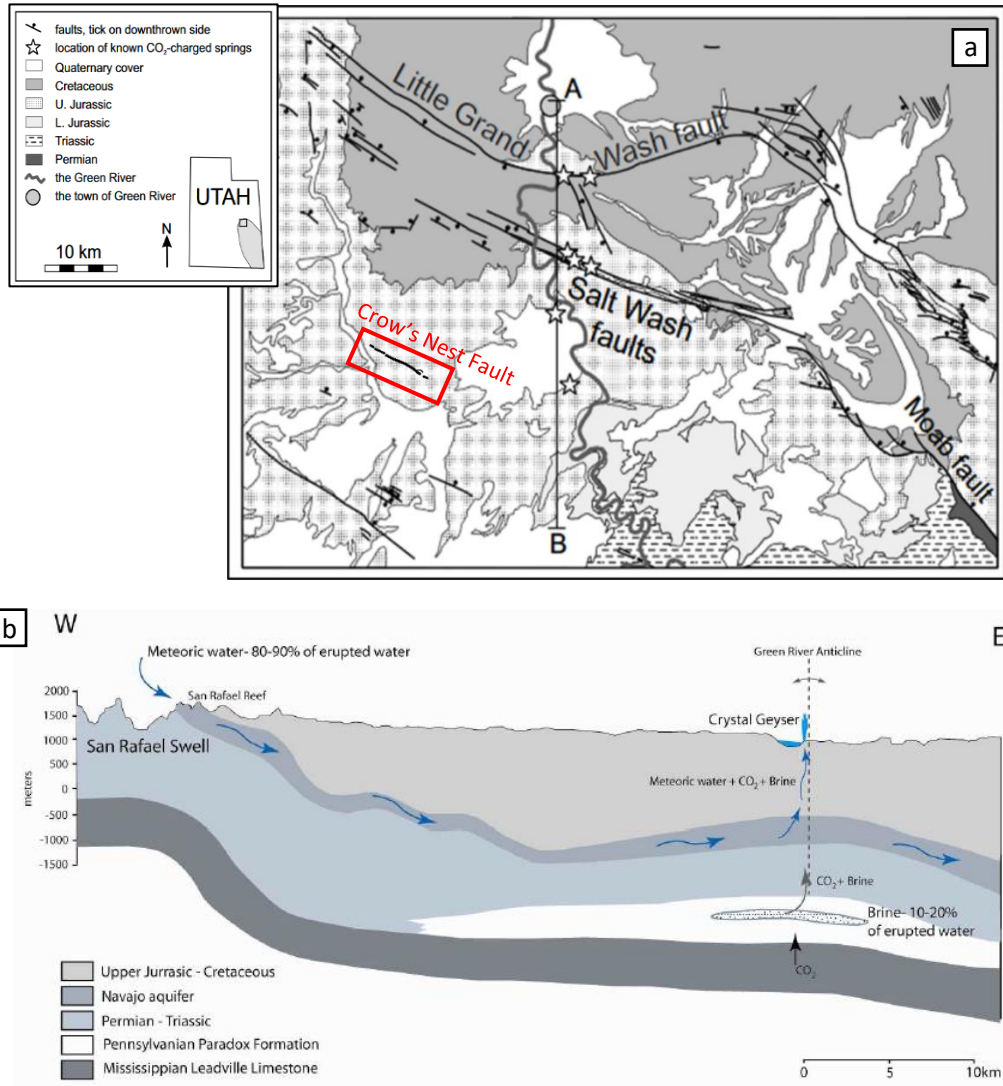
Figure 5.47 – (a) Map showing the location of the Crystal Geyser with relation to the Crow's Nest Fault. Adapted from Shipton et al., (2004). (b) Cross section through the plane of the Little Grand Wash Fault indicating groundwater sources for spring waters/deposits. Figure taken from Burnside, (2010) and after Kampman et al., (2009).

5.5 Summary

Evidence for paleo fluid flow at the Crow's Nest Fault includes; modern hydrocarbons, iron oxide staining, nodules and iron-rich fractures, bleaching and dissolution of calcite cement and modern water flow. From analysing the evidence for paleo fluid flow in the field and under thin section, the spatial evidence for paleo fluid flow has been constrained.

Hydrocarbons are only exposed within the two fault lenses and at the Old Mine site. Hydrocarbons seep from fracture junctions at the Crow's Nest Spring lens whereas hydrocarbons stain the host rock within the Brush Valley lens. At the Old Mine site, hydrocarbons infill fractures. It is likely hydrocarbons have ascended the fault from depth and migrated up the fault and become trapped within the lenses. Hydrocarbons were likely generated in the Paradox Basin during the Cretaceous from Mid- Pennsylvanian source rocks; the Islay Creek Cycle and the Cane Creek Cycle (Nuccio and Condon, 1996).

Iron oxide staining and nodules are observed everywhere in the footwall and Brush Valley lens at the Crow's Nest Fault. However, there is more iron oxide staining and nodules exposed within both the Brush Valley site lens and Crow's Nest Spring site lens then elsewhere along the Crow's Nest Fault. There is little evidence for any observed iron oxide staining in the hanging wall, however no samples were analysed under thin section to confirm this. Iron oxide staining likely formed through mixing of Fe-rich reducing fluids with oxidising groundwater.

Bleaching of bedding and fractures occurs in the hanging wall only at study sites which are close to fault tips and within the Ballooning Relay Ramp. There is no evidence for any bleaching in the footwall. Dissolution of calcite cement is observed at the Brush Valley lens and in the footwall at Cottonwood Wash which is located at the end of a fault tip.

A modern day spring at the Crow's Nest Spring site lens and there is no other evidence for present day springs at the Crow's Nest Fault.

A prospect pit, probably for uranium, is located above the Crow's Nest Spring site. It is likely that the source of water came from the Navajo aquifer and migrated vertically up the fault through fractured Carmel Formation (Burnside, 2010).

Evidence for paleo fluid flow is concentrated on the ends of fault strands/at fault tips, within lenses and at well exposed relay ramps. Where there is evidence for paleo fluid flow at fault tips and lenses, there is evidence for an increase in porosity compared to host rock exposed elsewhere in Utah by up to 20%.

There is a lack of calcite cement within the host rock at the Cottonwood Wash site, located at a fault tip and the Brush Valley site, located in a lens at the site of a fault tip. Both of these sites expose host rock which ranges between 20-30% porosity. However, at the lens at the Crow's Nest Spring site, there is not a lack of calcite cement and this lens is located in

the middle of a fault strand with a porosity of 15.9% on average which is formed of the Carmel Formation. Further studies could focus on evidence for cement dissolution, for example by imaging cement relics or etch textures under SEM.

In summary, evidence for paleo fluid flow is observed at fault tips, in lenses and at well exposed relay ramps. Fault tips and lenses that are situated at fault tips are evidence for calcite cement dissolution and are the most porous areas of the Crow's Nest Fault.

Chapter 6

Discussion

6.1 Introduction

This chapter compares the evolutionary stages of normal faults, including the growth and initiation of faults in sandstones and other lithologies to the Crow's Nest Fault. Normal faults from Utah and the rest of the world are compared to the results of this study throughout this chapter.

An evolutionary model outlining the timings and events for how the Crow's Nest Fault has evolved is presented in section 6.2 and comparisons are made to other evolutionary models. Section 6.3 outlines the controls on fault zone thickness and the relationship to fault displacement. In section 6.4, a possible burial history including likely depths of where fluid flow could have potentially come from which ascended the Crow's Nest Fault is outlined. Section 6.5 outlines the implications of fault architecture for industry, including a classification scheme for predicting fault rock and evaluating fault seal potential. This chapter is summarised in section 6.6.

6.2 Development of an evolutionary model of the Crow's Nest Fault

Observations described in Chapter 4 show that there are four types of deformation structures present at the Crow's Nest Fault; thick deformation bands, thin deformation bands, iron-rich fractures and open fractures. From analysing cross cutting relationships in the field and under thin section, the relative timing of these structures was constrained.

Thick deformation bands were shown, based on cross-cutting relationships to be the oldest deformation structure to form at the Crow's Nest Fault. Back rotation of the bedding within the Brush Valley lens was used to deduce that thick deformation bands formed before the tilting of the bedding within the lens. Hence, these structures are precursors to fault formation. Further, the axis of rotation of the bedding in the lens is horizontal, and no change in strike is observed for the thick deformation bands. This implies there is no 'twisting' of the bedding during lens formation (i.e. such as would occur due to lateral propagation and linkage of two normal faults). This could occur if two pre-existing overlapping normal fault segments propagated upwards from depth, for example, due to formation of a monocline.

From cross cutting relations, the next deformation structures to form were thin deformation bands, followed by iron-rich fractures and then open fractures. Similar analysis of bedding rotation shows that these structures formed after lens formation.

Based on the known geological history of the basin and the observed relationships between faulting, deformation structures and fluid flow, a six stage evolutionary model has been constructed for the timing of fluids in relation to fault growth and evolution at the Crow's Nest Fault (figure 6.1).

Stage 1 – The host rock sediments were laid down at the Crow's Nest Fault between the Middle and Lower Jurassic. Between the Late Jurassic and Late Tertiary, the Crow's Nest Fault was initiated, possibly from the reactivation of a basement fault. Regionally, there is evidence that supports the reactivation of basement faults across the Paradox Basin, for example the Moab Fault. Evaporites of the Pennsylvanian Paradox Basin which have been deformed, have resulted in a series of NW-SE trending salt anticlines such as the Moab Fault (Baars and Stevenson, 1981; Chan et al., 2000). Salt anticlines are parallel to basement faults and it is thought that the influence of basement faults in addition to extension along the anticlines resulted in the formation of NW-SE trending faults such as the Moab Fault (Chan et al., 2000).

Between the Jurassic and Tertiary, thick deformation bands were formed as precursory structures to fault formation. Thick deformation bands are orientated parallel to the Crow's Nest Fault and cross cutting relationships in the field and in thin section confirm that thick deformation bands were the first structures to form. Additionally, thick deformation bands are typically observed in high porosity sediments (Johansen et al., 2005).

Stage 2 – Between the Jurassic and the Tertiary, the Crow's Nest Fault formed a through-going fault. Fault strands were already linked in the basement as evident by the formation of fault lenses and a breached relay ramp at a fault segment tip.

Between the Cretaceous and Tertiary, further sediments were laid down which buried the Jurassic sediments between 900m and 1.2km, as an approximate back-stripped thickness (Doelling, 1988).

Stage 3 – Oil and gas were generated during the Cretaceous from Mid-Pennsylvanian source rocks; the Islay Creek Cycle and the Cane Creek Cycle (Nuccio and Condon, 1996). Hydrocarbons/fluid reached the Cretaceous units from the Mid Pennsylvanian source rocks

by ascending the Crow's Nest Fault at the Crow's Nest Spring lens. This is evident by hydrocarbons present at the Crow's Nest Spring lens yet there still being calcite cement in the host rock.

Stage 4 – From the Cretaceous onwards, thin deformation bands formed. Thin deformation bands are thinner than thick deformation bands due to a decrease in the porosity of the host rock as a result of increased compaction from burial. This is evident from cross cutting relationships between thick and thin deformation bands observed in the field and under thin section. Although perpendicular to the fault and thick deformation bands, thick and thin deformation bands are always observed together.

Stage 5a – From the Late Tertiary-Holocene onwards, Cretaceous and Tertiary sediments were eroded away, exposing Jurassic sediments at the Crow's Nest Fault.

Post Late Tertiary/Holocene, open fractures formed and then filled with iron in an isolated patch of bands within the Brush Valley lens. Cross cutting relationships in the field and under thin section indicate that open fractures were the last deformation structures to form at the Crow's Nest Fault.

Stage 5b – Post Late Tertiary/Holocene, open fractures formed everywhere along the Crow's Nest Fault but remain unfilled. Fractures cut every lithology exposed at the Crow's Nest Fault including high porosity host rock. It is therefore more likely that fracturing is a result of uplift rather than burial and more closely follows the model by Davaztes and Aydin, (2003).

Stage 6 – Reducing fluid ascended the Crow's Nest Fault, likely at the relay ramps and bleached the host rock. Bleaching must have occurred after the open fractures formed because open fractures in the hanging wall are bleached surrounding the fault tips and relay ramps. The characteristic pale bleached areas represent the stripping of hematite. Redepositing of hematite as iron oxide is observed as iron oxide staining and iron nodules exposed throughout the Crow's Nest Fault.

The reducing fluid ascended the Brush Valley lens and removed the calcite cement. The bleaching fluid is likely to be hydrocarbon in origin and channelled within the high porosity layers where the calcite cement has been stripped out. Modern oil-staining in the lens at Brush Valley is only visible in the higher porosity layers.

Both the Brush Valley lens and the Crow's Nest Spring lens are bound by low permeability fault gouge which would have acted as a barrier to across fault flow, trapping the fluid within the lenses.

Stage 1 - Thick DFB formation and fault initiation
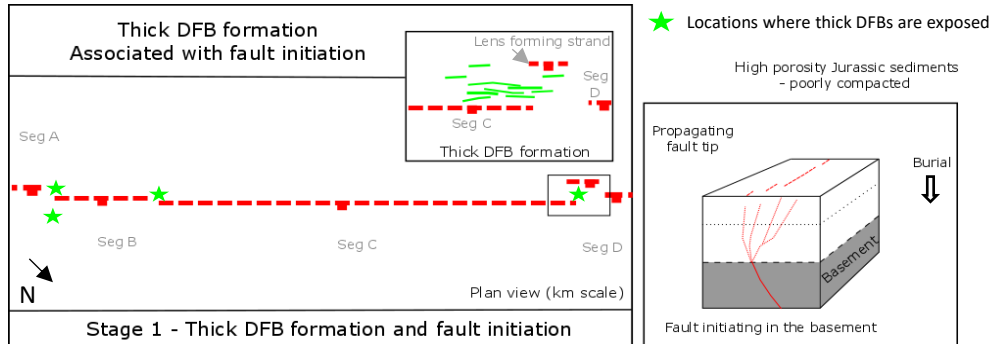
Stage 1:

Time	Event	Evidence
Mid – Lower Jurassic	Jurassic sediments were laid down	Stratigraphic age of sediments
Late Jurassic – Late Tertiary	CNF was initiated possibly from reactivation of a basement fault	- Regionally, evidence supports faulting in the basement across the Paradox Basin (e.g. seismic surveys of the SRS – Baars and Stevenson, 1981)
Jurassic - Tertiary	**Thick DFBs** formed as precursors to fault formation	- Thick DFBs in the same orientation as CNF. - Cross cutting relations show thick DFBs were the first defm structure to form. There are no known/published minimum depths for deformation band formation.

Stage 2 - Fault formation and linkage & burial
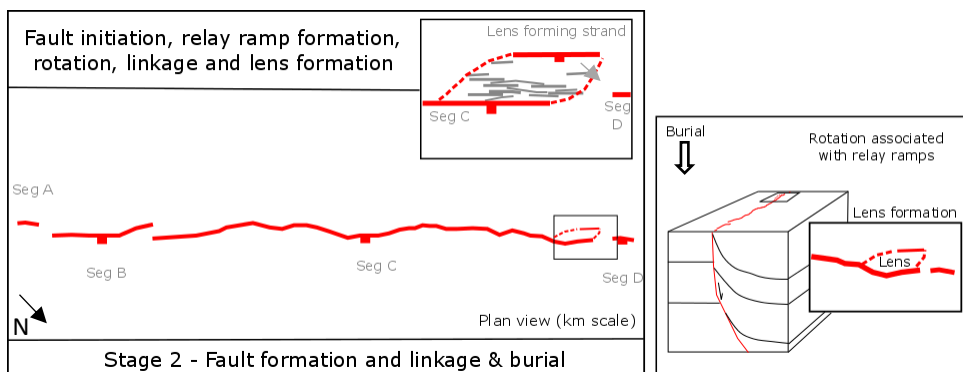
Stage 2:

Time	Event	Evidence
Jurassic - Tertiary	- CNF formed into a through-going fault within Jurassic sediments (already linked up in the basement) - Breaching of relay ramp to form the lens	- Breached relay at fault segment tip - Presence of fault lenses - Thick DFBs are typically found in high porosity sediments (Johansen et al., 2005)
Cretaceous - Tertiary	- Cretaceous and Tertiary sediments were laid down which buried the Jurassic sediments between 900m and 1.2km	- Thickness of stratigraphic units (Doelling, 1988)
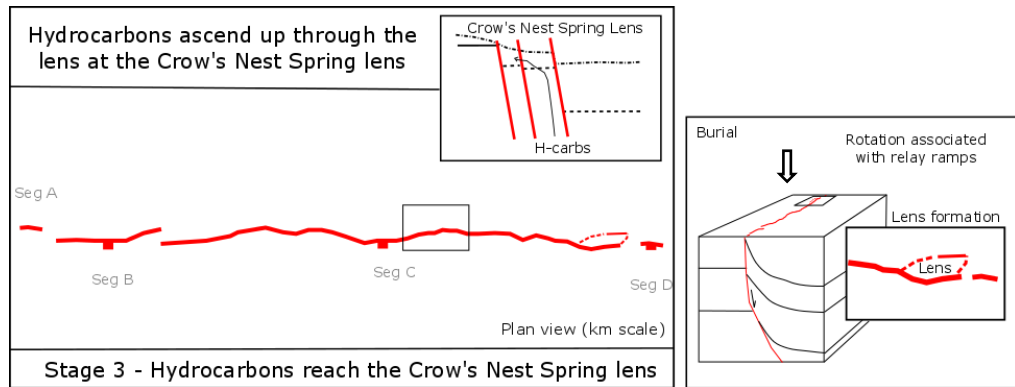
Stage 3:

Time	Event	Evidence
Cretaceous	- Mid-Pennsylvanian oil and gas was generated during the Cretaceous from source rocks; the Islay Creek Cycle and the Cane Creek Cycle	- Well logs and basin modelling from Nuccio and Condon, (1996)
Cretaceous	- Hydrocarbons/fluid reached the Cretaceous units from the Mid Pennsylvanian source rocks through ascending the CNF at the Crow's Nest Spring lens	- The oil and gas needed a way to reach the Cretaceous units, and seems to be highly localised along the fault - Hydrocarbons present at the Crow's Nest Spring lens and calcite cement is still present within the host rock

Stage 4 - Thin DFB formation & erosion of sediments
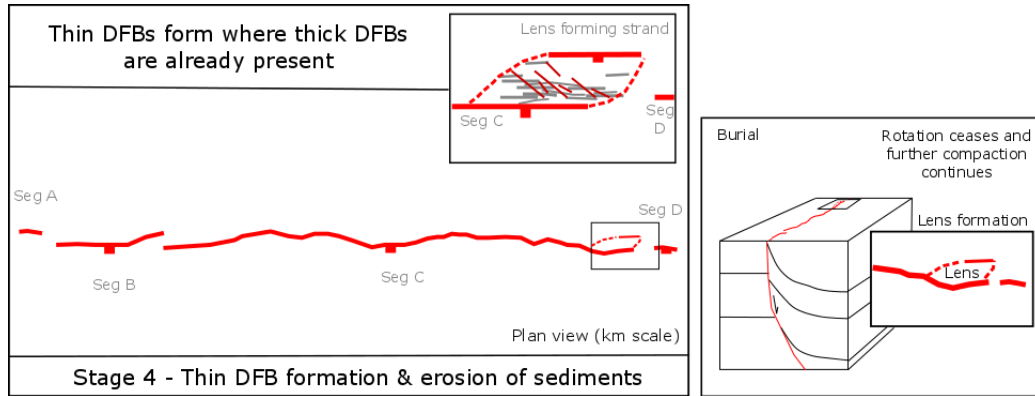
Stage 4:

Time	Event	Evidence
Cretaceous	- **Thin DFBs** formed due to a decrease in the porosity of the host rock during burial related compaction	- Cross cutting relationships in the field and under thin section

Stage 5a - Iron filled fracture formation
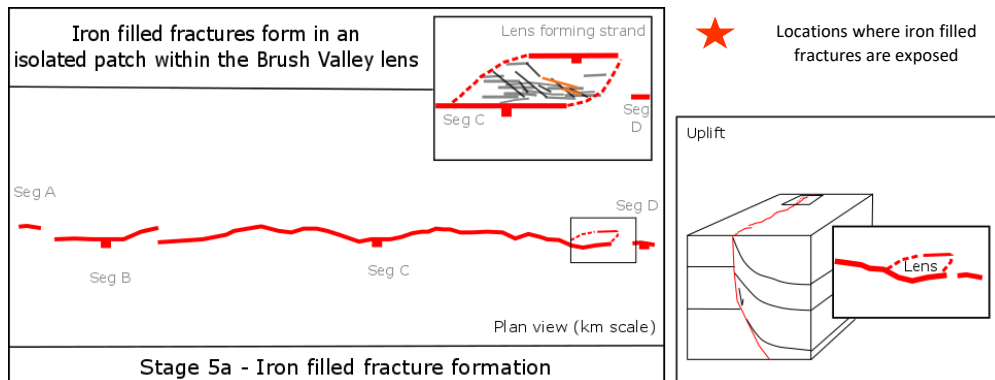
Stage 5a:

Time	Event	Evidence
Late Tertiary/Holocene	- Cretaceous and Tertiary sediments were eroded away - Jurassic sediments at CNF were exposed due to the erosion of the overlying Cretaceous and Tertiary sediments	- Data from Nuccio and Condon, (1996)
Post Late Tertiary/Holocene	- **Open fractures** formed, then **filled with iron**	- Cross cutting relationships in the field and under thin section - Fractures cut high porosity rock so they cannot follow the model by Johansen et al., (2005) and instead are more like the model from

		Davaztes and Aydin, (2003) where jointing at the Moab Fault is thought to be related to uplift

Stage 5b:

Time	Event	Evidence
Post Late Tertiary/Holocene	**Open fractures** formed	- Cross cutting relationships in the field and under thin section - Fractures cut high porosity rock so they cannot follow the model by Johansen et al., (2005) and instead are more like the model from Davaztes and Aydin (2003) and post-erosion
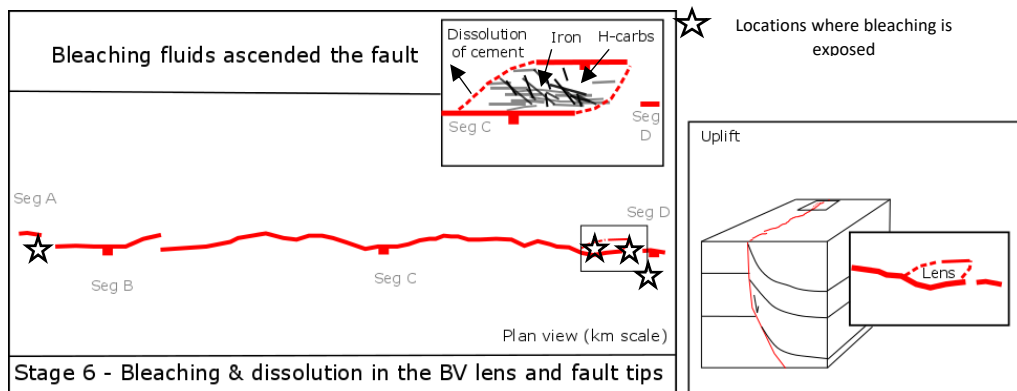
Stage 6:

Time	Event	Evidence
Post Late Tertiary/Holocene	- Fluid (reducing) ascended CNF at the relay ramps and **bleached** the	- Open fractures are bleached - Bleaching only at ends of fault

	rock, stripping it of hematite and redepositing **iron oxide** as staining and nodules - The bleaching fluid ascended the Brush Valley lens and **removed the calcite cement** - The bleaching fluid ascended the Crow's Nest Spring lens and resulted in a spring - The bleaching fluid is likely hydrocarbon in origin, **depositing hydrocarbons** in the high porosity parts of the Brush Valley lens	strands and HW - Hydrocarbons at the Brush Valley lens are only in high porosity parts of the host rock where calcite cement has been dissolved, so the cement must have been dissolved to make room for the hydrocarbons

Figure 6.1 – Six stage evolutionary model for the Crow's Nest Fault.

6.3 Fault thickness and displacement

Figure 6.2 shows a plot of fault zone thickness for faults in a range of sequences. Plotted on the figure are values for the fault zone width, calculated from the damage zone and fault core combined, for the Crow's Nest Fault; green values are based on the minimum measured throw and red values are based on the maximum measured throw.
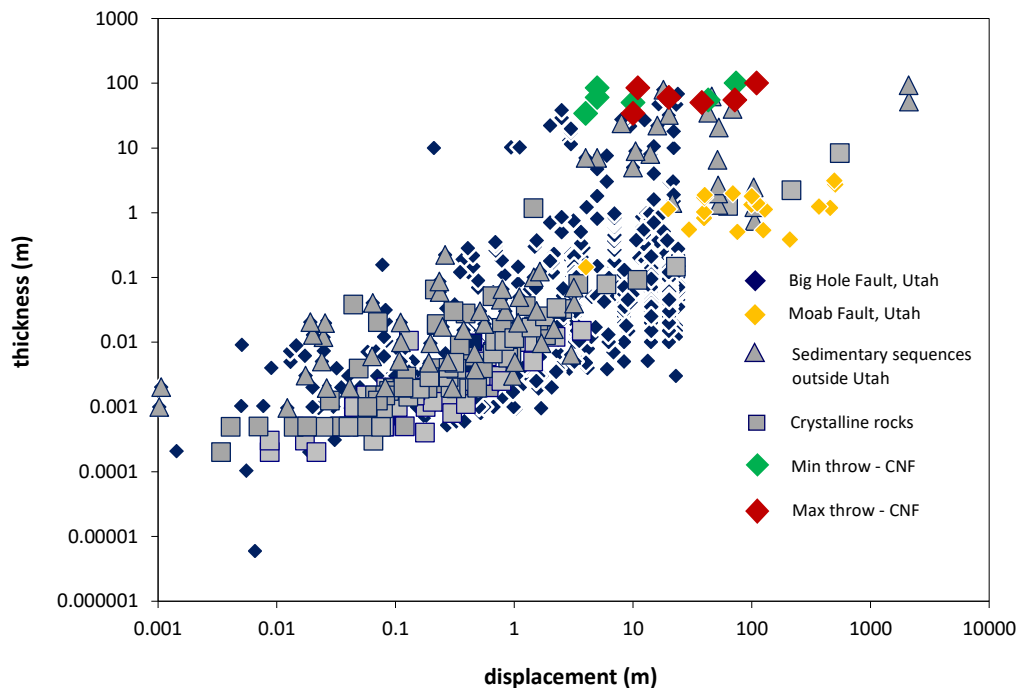
Figure 6.2 – Graph showing fault displacement data against fault thickness data from a number of different faults and lithologies (adapted from Shipton et al., 2006).

Figure 6.2 shows that, for the displacement at Crow's Nest Fault, the fault thickness is very high, when compared to the observations of other researchers. Although there may be some correlation between increasing fault thickness and increasing maximum throw at the Crow's Nest Fault, (Figure 6.2) it is extremely weak and no correlation is visible with the minimum throw estimate. There is little change along-strike in the fault thickness at the Crow's Nest Fault. The throw of the Crow's Nest Fault ranges from a minimum of 4m to a maximum of 110m, whereas the thickness of the fault ranges from 34m to 100m. The fault thickness has been calculated from the damage zone and fault core combined. The fault gouge exposed at fault lenses is thicker at 50cm compared to 20cm at the fault segment tip (Cottonwood Wash locality).

Some other studies have also found a similar lack of correlation between fault zone thickness and fault displacement, for example, studies of normal faults in porous sandstones within the North Sea by Fossen and Hesthammer (2000). At the Big Hole Fault, a small normal fault exposed in the Navajo Formation (for which the data are included in Figure 6.2) whilst a positive correlation was observed between damage zone thickness and displacement, there was no increase in fault core thickness with increasing displacement (Shipton and Cowie, 2001) for offsets greater than a few metres. Similarly, the Moab Fault shows some correlation between increasing fault thickness and fault throw (Foxford et a., 1998), but the relationship between the two is also weak.

Figure 6.2 shows that in relation to throw, the damage zone of the Crow's Nest Fault is very large. There are a number of potential reasons why the damage zone at the Crow's Nest Fault is much larger than expected and exhibits asymmetry across the fault. Firstly, the definition of what constitutes a damage zone is somewhat subjective. The definition of a damage zone is dependent on what deformation structures are included within the damage zone (Shipton et al., 2006).

The Crow's Nest Fault is proposed in Section 6.2 as having been formed by the reactivation of basement faults and there is evidence that inherited fault geometry has strongly influenced damage zone width: the damage zone at the Crow's Nest Fault appears to reflect a linked fault geometry (large scale precursory structure of four soft linked fault strands) rather than the throw profile. This will have affected fault damage zone development and width.

Studies by Schultz and Evans, (1998) suggest that the width of a damage zone can fluctuate by an order magnitude depending on what types of deformation structures are defined within the fault zone and this may be why the damage zone at Crow's Nest appears to exhibit asymmetry. At the Crow's Nest Fault there is evidence of folding in the hanging wall at the Brush Valley lens site at a breached relay. The asymmetry between the hanging wall and footwall damage zone widths could be as a result of the fault propagation fold.

Fault propagation folding has also been observed at Moab Fault and Little Grand Wash, where there is also evidence of folding in the hanging wall, as outlined in section 4.6.4. Studies of the Moab Fault by Lewis et al., (2002) suggested that damage zone asymmetry is also likely related to the development of the fault propagation fold, with a damage zone maximum thickness of 70m in the footwall, compared to a hanging wall thickness of 210m (Berg and Skar, 2005).

Asymmetrical strain distribution observed across damage zones can also be attributed to factors such as lithology, host rock thickness and displacement.

In Utah, studies of the Big Hole Fault show a broadly linear relationship between damage zone thickness and displacement (Shipton and Cowie, 2001). This has been attributed to deformation still being accommodated within the damage zone after a through going fault has developed. At the Big Hole Fault, the damage zone is controlled by localised strain around the through going fault rather than the regional strain field. There is a much less linear relationship between fault thickness and displacement at the Moab Fault, Utah. This has been attributed to an asymmetric stress field which developed during fault propagation and folding of the hanging wall (Berg and Skar, 2005).

The relationship between fault thickness and displacement from faults of the Gullfaks Field, North Sea (Fossen and Hesthammer, 2000) and some data of the Big Hole Fault, Utah (Shipton and Cowie, 2001) are the most similar to findings of the Crow's Nest Fault (figure

6.2). Although with a much smaller maximum displacement at 23m (Foxford et al., 1996) compared to 110m at the Crow's Nest Fault, the Moab Fault also shows a similar displacement-thickness relationship as the Crow's Nest Fault. All of these studies are situated in high porosity (up to 34%) Jurassic sandstones which are often highly deformed by deformation banding. Furthermore, it is likely that lithology and in particular porosity, are a strong influence on damage zone thickness.

6.4 Burial history and the timing and origins of fluids at the Crow's Nest Fault

Nuccio and Condon (1996) have extensively studied the burial, thermal and petroleum-generation history of the Paradox Basin through the use of well logs in various locations across the region (figure 6.3).
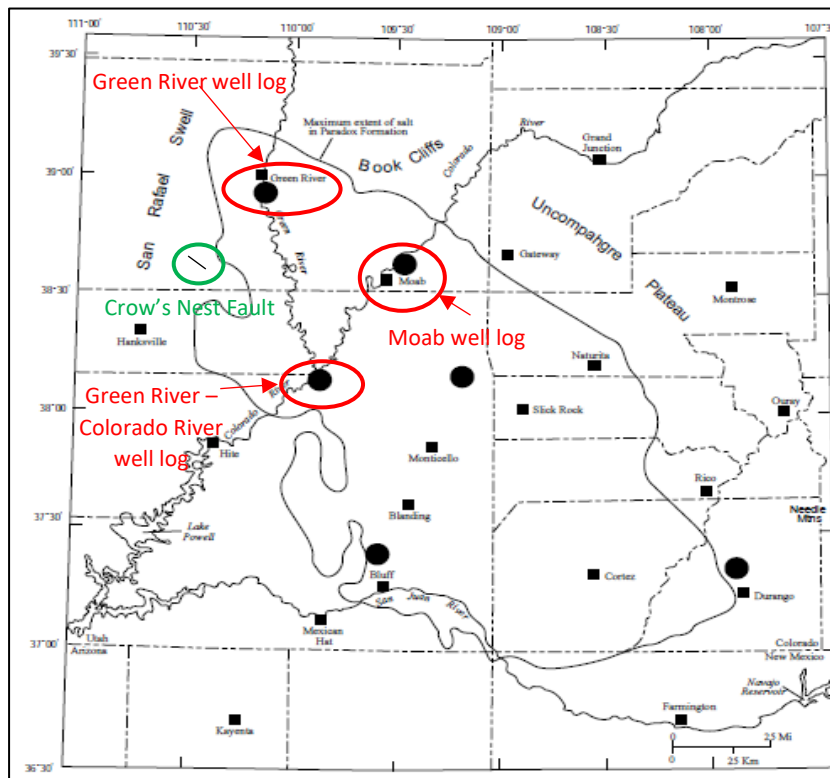
Figure 6.3 – Location map showing the extent of the Paradox Basin. Crow's Nest Fault sits on the flank of the Paradox Basin but is within close proximity to the Green River, Green River – Colorado River and Moab well logs as indicated on the map. Map is modified from Nuccio and Condon, (1996).

237

Various well logs have been taken by Nuccio and Condon, (1996) from locations nearby to the Crow's Nest Fault; the Green River log, the Green River-Colorado River confluence log and the Moab log (figure 6.3). Although the Crow's Nest Fault is on the flank of the Paradox Basin, the stratigraphy and regional geology are similar to the surrounding area. By studying these logs in the surrounding area, a better understanding of the burial history at Crow's Nest Fault can be gained and allows for the likely burial history of the field area to be obtained within this thesis.

The Green River well log is from approximately 30km south-west of the Crow's Nest Fault. One of the most thermally mature areas within the Paradox Basin, Jurassic rocks were buried to 730m (Nuccio and Condon, 1996; Figure 6.4). This supports a hypothesis of sustained burial and compaction post-faulting in the region.
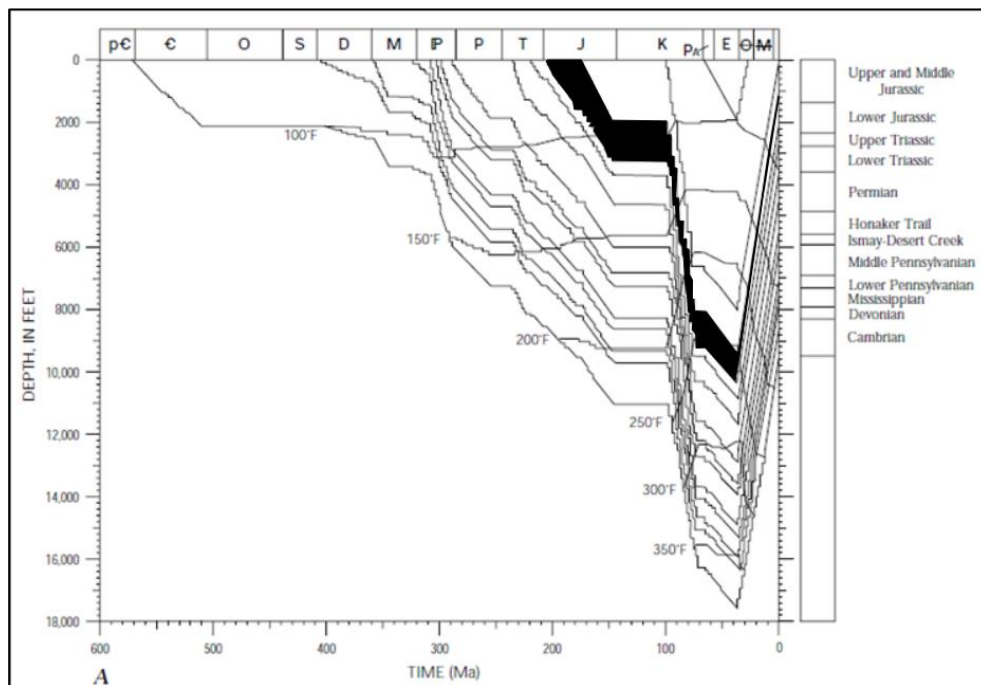
Figure 6.4 – Burial history curve for the Green River well log (Nuccio and Condon, 1996). The black layer represents host rocks exposed at the Crow's Nest Fault.

The Green River-Colorado River well log is from approximately 70km south-east of the Crow's Nest Fault. Erosion has removed Tertiary, Mesozoic and Permian sediments. Jurassic rocks were buried to 2.8km (Nuccio and Condon, 1996).

The Moab well log (figure 6.5) is from approximately 76km east of the Crow's Nest Fault. This area experienced rapid subsidence during the Palaeozoic which resulted in the deposition of thick Pennsylvanian and Permian sedimentary layers and approximately 970m of Jurassic and Triassic sediments (Nuccio and Condon, 1996). Following this it is estimated that 1.8km of Cretaceous and 610m of Palaeocene and Eocene rocks were deposited. Since 37Ma there has been continuous uplift and erosion and 3.5km of strata has been eroded away (Nuccio and Condon, 1996). Jurassic rocks were buried to a maximum of 3.5km which is much deeper than the surrounding areas of Green River and the Green River-Colorado River well logs.
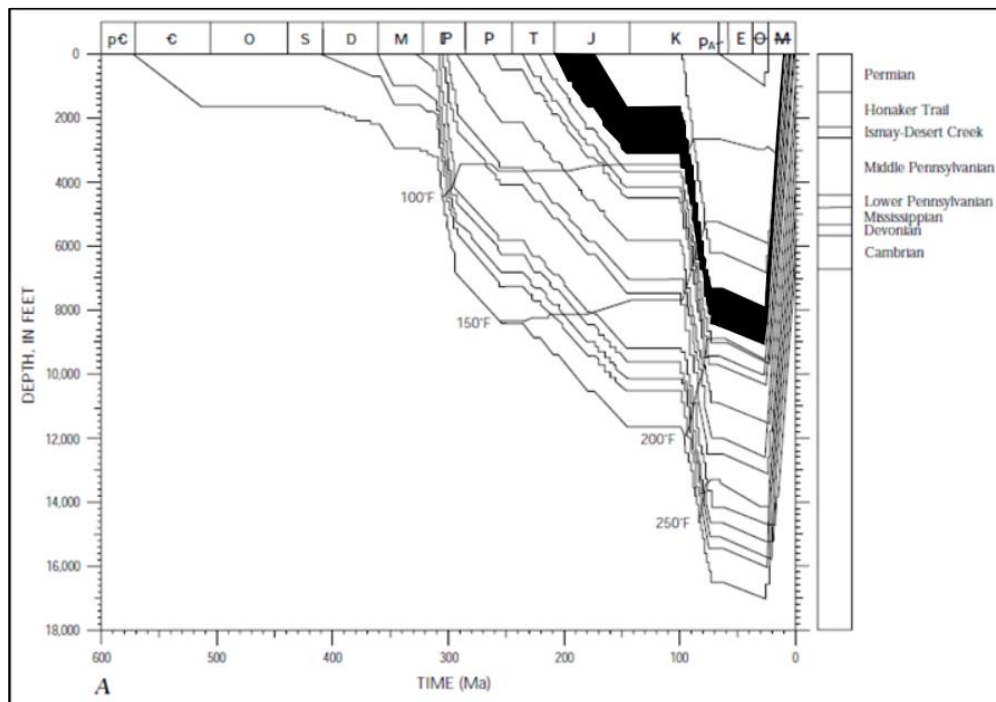
Figure 6.5 – Burial history cure for the Green River – Colorado River well log (Nuccio and Condon, 1996). The black layer represents host rocks exposed at the Crow's Nest Fault.

The Moab well log (figure 6.6) is from approximately 76km east of the Crow's Nest Fault. This area experienced rapid subsidence during the Palaeozoic which resulted in the deposition of thick Pennsylvanian and Permian sedimentary layers and approximately 970m of Jurassic and Triassic sediments (Nuccio and Condon, 1996). Following this it is estimated that 1.8km of Cretaceous and 610m of Palaeocene and Eocene rocks were deposited. Since 37Ma there has been continuous uplift and erosion and 3.5km of strata has been eroded away (Nuccio and Condon, 1996). Jurassic rocks were buried to a maximum of 3.5km which is much deeper than the surrounding areas of Green River and the Green River-Colorado River well logs.
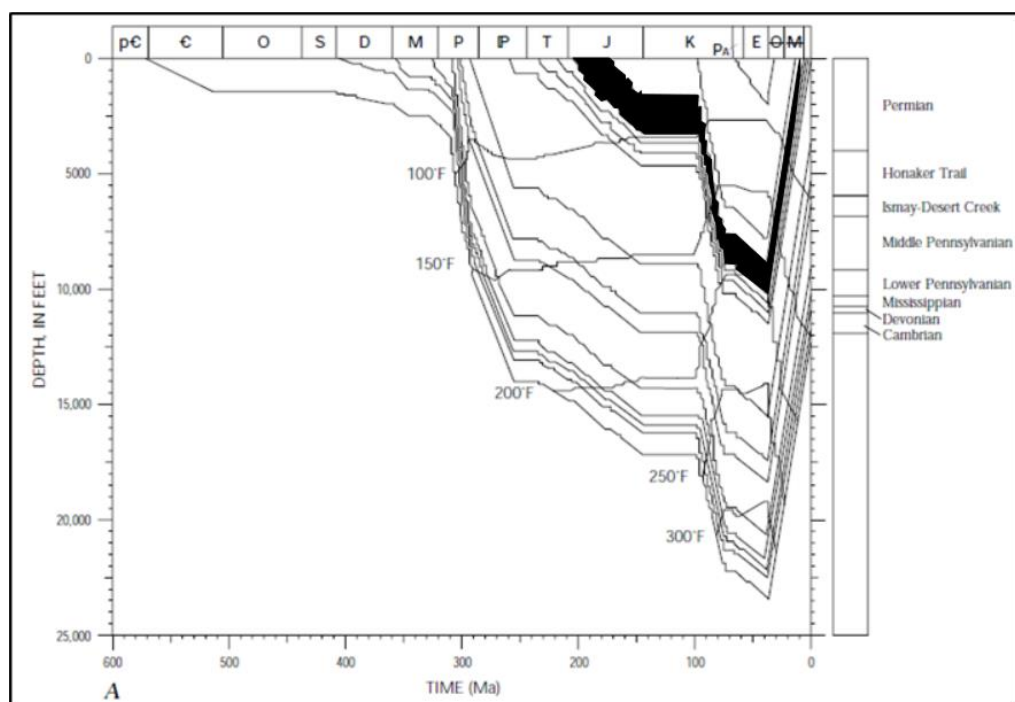
Figure 6.6 – Burial history curve for the Moab well log (Nuccio and Condon, 1996). The black layer represents host rocks exposed at the Crow's Nest Fault.

Based on these burial history data, the maximum burial depth of Jurassic rocks at the Crow's Nest Fault is likely to range from 2.5km to 3km. Fluids which ascended from the Mid-Pennsylvanian source rocks travelling up to the Jurassic rocks exposed at the Crow's Nest Fault would have to go through a series of low permeability rocks. If the pathway for those fluids was the Crow's Nest Fault, it would have to extend down to at least 780m to conduct hydrocarbons from the source rocks in the Mid-Pennsylvanian. The Crow's Nest Fault likely formed from reactivation of a basement fault structure. Seismic surveys of the San Rafael Swell and Paradox Basin by Baars and Stevenson, (1981) show evidence of basement structures and suggest that modern surface structures actively developed during the deposition of salt and predate Laramide orogeny. It is therefore possible that the Crow's Nest Fault may be part of a much larger fault system or that fluids migrated up a set of faults, of which the Crow's Nest Fault is part of.

Over recent years the area influenced by the Paradox Basin has been investigated for hydrocarbons and fluids rich in CO_2 (Shipton et al., 2004; Shipton et al., 2006; Lewicki et al., 2007). Less than 10km north of Crow's Nest Fault is the Green River anticline which is cut by faults such as the Little Grand Wash Fault which results in CO_2 rich fluids ascending from springs and geysers (Dockrill and Shipton, 2010). 'Carrier' beds of CO_2 rich fluids in this region include the Navajo Formation and Entrada Formation (Heath et al., 2009). Both the Navajo and Entrada Formations show evidence of possible interaction with CO_2 rich fluid. For example, there is evidence of distorted bedding which has been tested for evidence of travertine deposits at the Cottonwood Wash site at the Crow's Nest Fault. Although not able to confirm whether the deposits are travertine in origin the presence of a modern day spring and proximity to the Little Grand Wash suggests that the Crow's Nest Fault could potentially have been influenced by fluids rich in CO_2.

The Little Grand Wash and Salt Wash Graben have been estimated to offset rocks of Pennsylvanian age (286-320Ma) and the Crow's Nest Fault is estimated to do the same. It is likely that the fluid originates from as deep as the Paradox Formation but that cap rocks have inhibited the migration of fluid vertically, except in the presence of faults. The Carmel Formation is likely to act as a cap rock above the Navajo Formation (Trimble and Doelling, 1978; Dockrill and Shipton, 2010).

It is well documented that areas of fault interaction often provide high permeability pathways for fluid flow (Gartrell et al., 2003; Ligtenberg, 2005; Wibberley et al., 2008; Burnside, 2010). However, high shear strain at fault planes typically results in a high production of fault gouge. Low permeability fault gouge has been identified as a potential barrier to fluid flow (Caine et al., 1996; Freeman et al., 1998; Shipton et al., 2004; Bense and Person, 2006).

At the Crow's Nest Fault there is fault gouge exposed in three locations; at the Cottonwood Wash site located at the tip of fault strand B, at the Crow's Nest Spring lens site and at the Brush Valley lens site, located at a breached relay at the tip of fault strand C (figure 6.7).
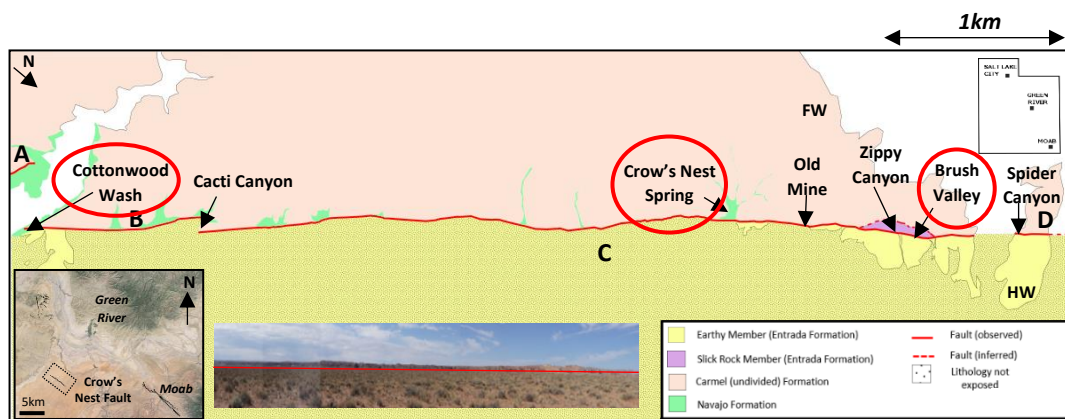
Figure 6.7– Plan view map of the Crow's Nest Fault indicating the three exposures of fault gouge; the Cottonwood Wash site, the Crow's Nest Spring site and the Brush Valley site. Modified from Doelling (2002).

Fault gouge from all three exposed sites at the Crow's Nest Fault has been analysed using an SEM and has identified as clay rich, low permeability gouge with high concentrations of illite in each sample, as seen in chapter 4. At the Cottonwood Wash site a single strand of fault gouge is present. Whereas at both the Crow's Nest Spring lens site and the Brush Valley lens site there is fault gouge exposed on both strands of the fault that bind the lens. High permeability lenses, bounded by fault gouge, have been noted by other authors as being able to behave as conduits and, hence, channel flow through the fault zone (Faulkner et al., 2003). At the Crow's Nest Fault, hydrocarbons are only observed within the Crow's Nest Spring lens and the Brush Valley lens. Hence, it is likely that low permeability fault gouge has focussed hydrocarbon flow within the lens, inhibiting its escape into the surrounding host rocks (figure 6.8).
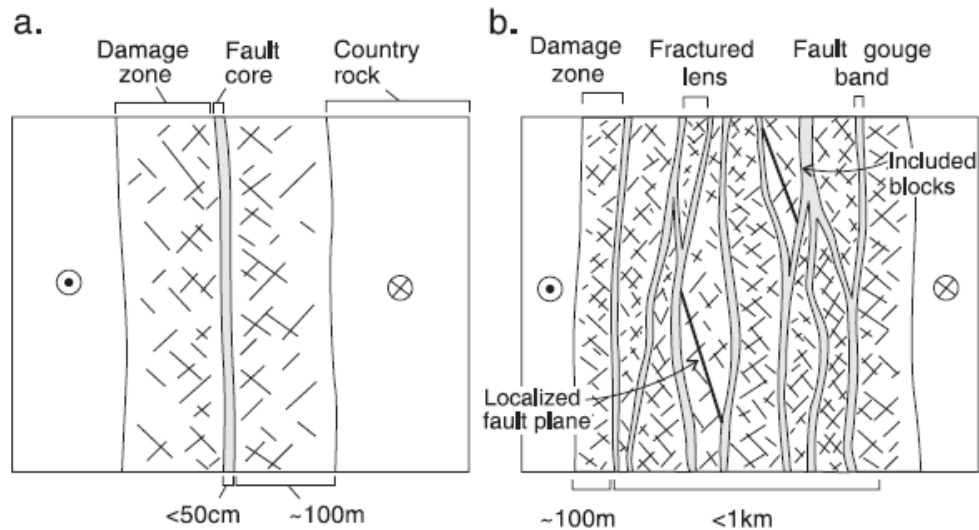
Figure 6.8 – (a) Conceptual model of a typical fault zone using the fault zone model of Caine et al., (1996) which contains a fault core, damage zone and country (host) rock. (b) A conceptual model which presents a fault zone with multiple strands of fault gouge amid a damage zone. Where there are two or more strands of fault gouge, a lens forms and this is where fluid can get trapped. Figure by Faulkner et al., (2003).

The Crow's Nest Spring lens is exposed in the middle of a fault strand, whereas the Brush Valley lens is exposed at a breached relay ramp. As outlined in section 5.2.1, hydrocarbons are expressed as hydrocarbon seepage from fracture junctions at the Crow's Nest Spring lens site. Whereas, within the Brush Valley lens, hydrocarbons are expressed as hydrocarbon staining of the high porosity layers of the host rock. The host rock observed at the Brush Valley lens is fragile, crumbly and appears to have been altered by a fluid which has removed the calcite cement (as outlined in section 5.2.3). By contrast, there is no evidence of calcite dissolution at the Crow's Nest Spring lens site, although hydrocarbons are present. This is likely because the original host rock was less porous and so the original deformation mechanism at this location would have been fracturing as opposed to deformation bands. Once fractured, fluid was then focussed into the fractures, expressed at fracture junctions rather than the host rock. This may be why the host rock has not been stripped of calcite cement.

At the Crow's Nest Spring lens site, hydrocarbons likely ascended up the fault and into the lens by travelling through the Navajo Formation as it is the most permeable formation (figure 6.9). The Navajo Formation, exposed at the Crow's Nest Spring lens site, is a highly porous sandstone which is well documented as a good reservoir rock/aquifer (Moulton, 1975; Parry et al., 2007; Loope et al., 2010).

The Crow's Nest Spring Lens Site
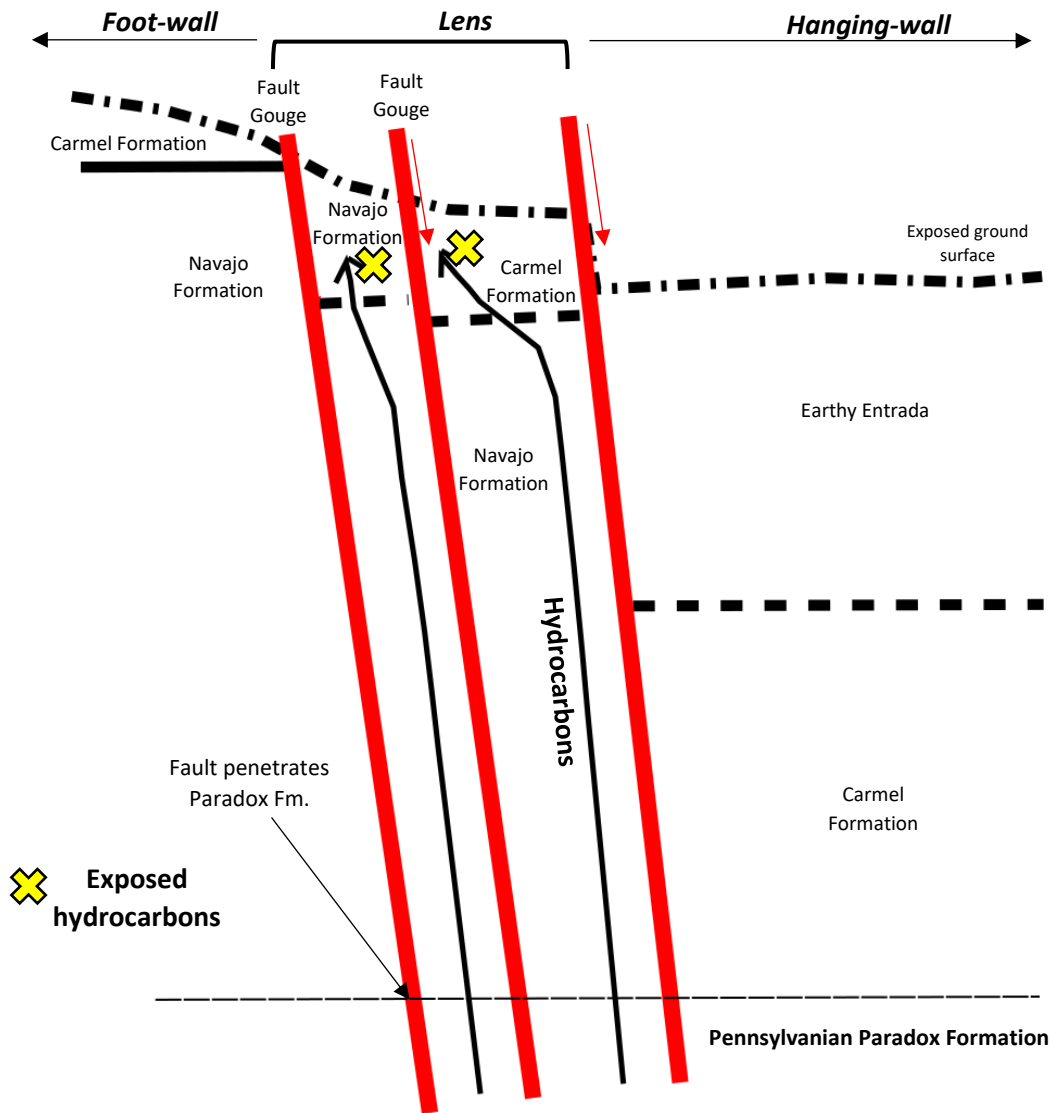
Figure 6.9 – Cartoon of the Crow's Nest Spring lens site which shows hydrocarbons ascending the fault through the Navajo Formation and Carmel Formation in the lens.

The Brush Valley Lens Site
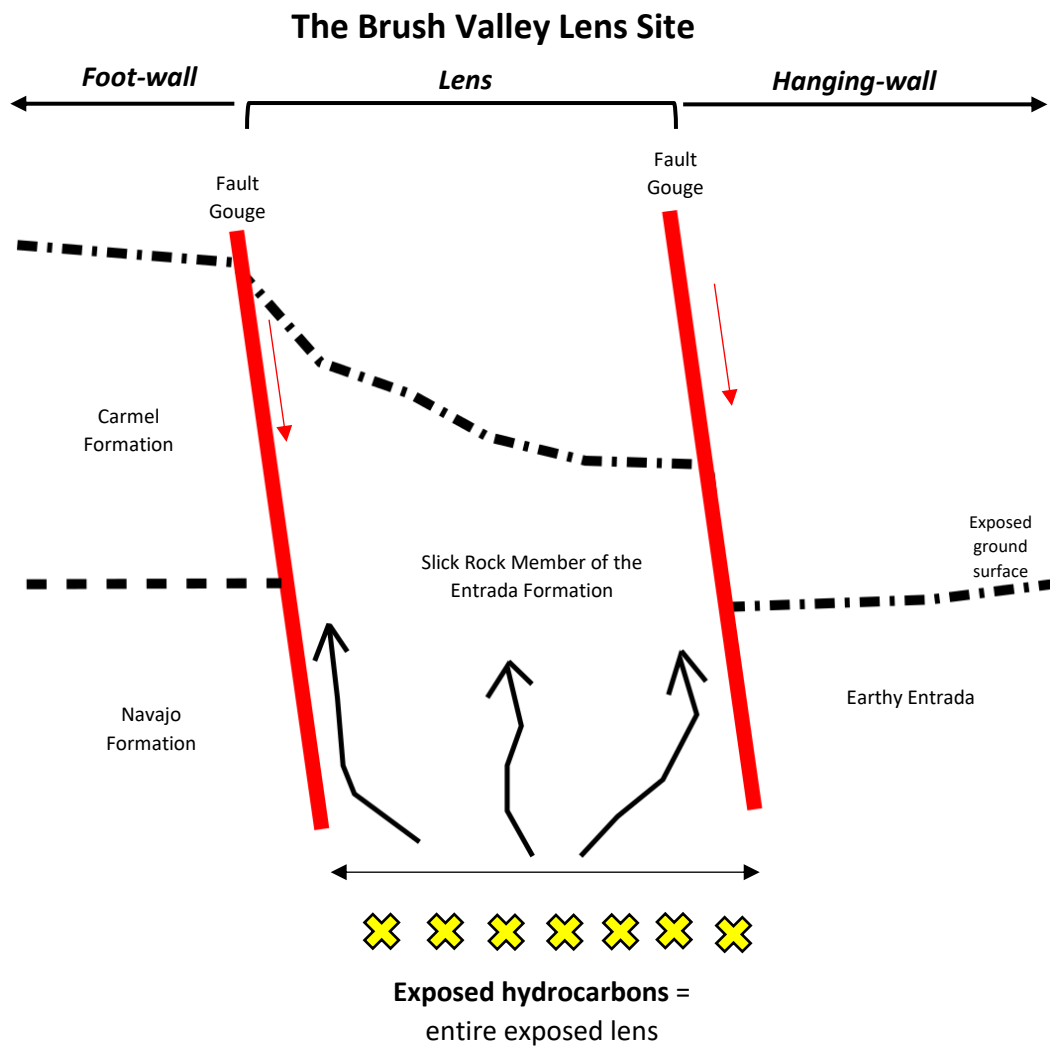
Figure 6.10 – Cartoon of the Brush Valley lens site showing hydrocarbons ascending the lens through the Slick Rock Member of the Entrada Formation in the lens.

At the Brush Valley lens site, hydrocarbons likely ascended the fault and travelled into the lens through the Slick Rock Entrada (figure 6.10). The Slick Rock Entrada, exposed at the Brush Valley lens site is a sandstone interbedded with siltstone which, prior to having calcite cement dissolved, would not have acted as a good a reservoir host rock as the Navajo Formation at the Crow's Nest Spring lens site. Throughout Utah, deformation bands are widely observed in the Entrada Formation (Aydin, 1978; Antonellini et al., 1994; Fossen, 2010). It is likely that the porosity of the Entrada Formation at the Brush Valley lens locality was high enough to deform by banding rather than fracturing. Then, once fluid was in the host rock, it stripped out the cement making it yet more porous.

The Brush Valley lens contains very widespread oil staining which is unusual in a host rock that is characterised by relatively low porosity. Observations of porosity in thin sections shows that there is a lack of calcite cement compared to the Slick Rock Entrada elsewhere in Utah, and that there is a resulting higher porosity. Therefore, whatever fluid was responsible for stripping the calcite cement has enhanced porosity, enabling the hydrocarbons to flow within the Slick Rock Entrada and this has been documented in chapter 5.

Hydrocarbons are also observed infilling fractures at the Old Mine site within the footwall. The Old Mine site is situated between the two lenses which could suggest that the two lenses are in fact one, that the Old Mine is part of one of those two lenses or that the Old Mine is an entirely separate lens itself. There is little exposure at the Old Mine site both in the field and via aerial imagery to definitively say for certain. However, the footwall consists of the Carmel Formation and hydrocarbons are infilling or leaking from fractures which is also observed at the Crow's Nest Spring lens. This suggests that the Carmel exposed at this locality could in fact be part of the Crow's Nest Spring lens rather than the footwall.

6.5 Predicting fault rock and fault seal properties

One of the major factors influencing fault zone hydraulic properties is lithology. When certain lithologies are juxtaposed against each other, different fault rocks are formed. Faults exposed in high permeability sandstones which juxtapose high permeability sandstones typically deform by deformation banding. With increasing displacement they may become dominated by cataclasites, impeding fault parallel and fault perpendicular flow.

Faults exposed in high permeability sandstones which are juxtaposed against low permeability lithologies rich in clays, shales and silts tend to be dominated by low permeability clay rich gouge with fractured adjacent units. Clay rich gouge acts as a barrier to across fault flow but fracturing enhances along fault flow. As a fault gets more displaced, clay gouge can smear resulting in beds of clay-rich material to develop and lower fault permeability.

Cerveny et al., (2004) present a model for fault rock classification relating to clay content,

lithification and fragmentation. This model is adapted here for fault rocks at the Crow's Nest Fault (figure 6.11). Lithologies are separated into three categories which are dependent on clay content, these are; clean sandstones and silts, impure sandstones and silts and claystones and shales (figure 6.11). Each category is then used to make predictions on the type of fault rock that might form as a result of faulting. Fault rock types fall into the three following categories; quartz rich lithologies (deformation band) fault rock series, phyllosilicate framework fault rock series and clay smear series. Fault rocks are then sub-defined depending on the percentage of lithification and fragmentation relating to displacement.

Following the model by Cerveny et al., (2004), faults which displace high permeability sandstones with a clay content of less than 15% are likely to develop low permeability fault seals. Fault rock formed in this scenario would likely be quartz rich and have experienced a reduction in porosity due to grain crushing and often deformation banding. However, deformation bands do not always behave as true barriers to fluid flow. Studies of deformation band cores in Jurassic rocks at the Yellow Cat Graben, Utah by Bright, (2006) indicate that deformation band cores have the potential to act as conduits or baffles to fluid flow at different points along strike and under different conditions of stress and fluid pressure.

Phyllosilicate framework fault rocks are typically formed when faults cut impure sandstones and silts (15-40% clays). The resultant fault rocks formed are lower in porosity and permeability due to increased compaction and the mixing of clays and quartz.
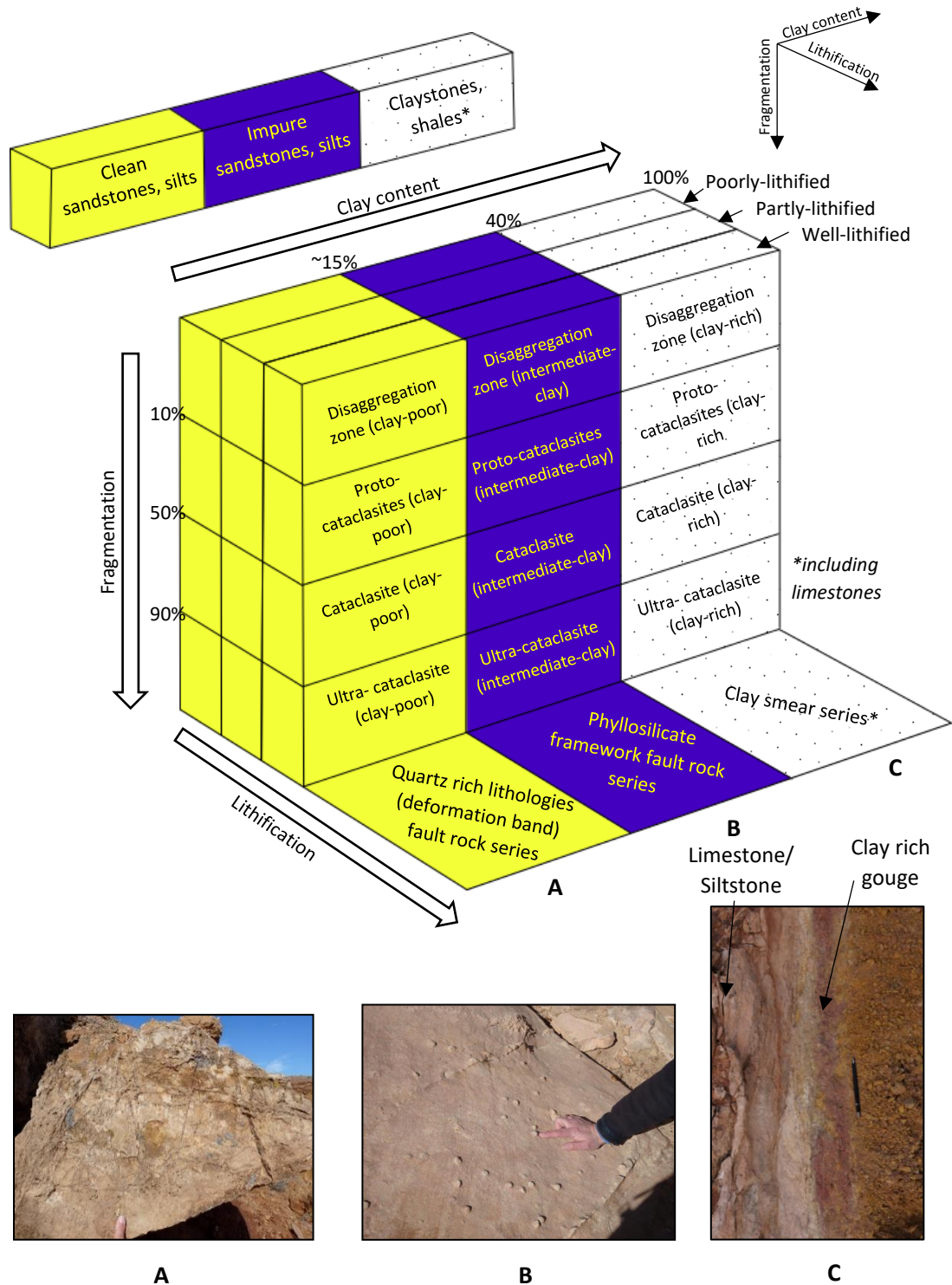
Figure 6.11 – Fault rock classification system adapted from Cerveny et al., (2004) indicating three main categories for defining fault rocks; (a) clean sandstones, silts, (b) impure sandstones, silts and (c) claystones, shales (incl. limestones).

Faults which cut through clay rich lithologies (>40% clays), deform by clay smear. Clays and shales are dragged and smeared along the fault plane and form a low permeability (gouge) barrier for across fault flow (Fisher and Knipe, 1998). These fault rocks are defined as the clay smear series. The model by Cerveny et al., (2004) requires further consideration for fault rock prediction at the Crow's Nest Fault. For instance, it is well documented in the literature that host rocks rich in limestone can form cap rocks to reservoir rocks; the Carmel Formation is a known cap rock overlying the Navajo Formation reservoir unit (Trimble and Doelling, 1978). The Carmel Formation is a complex sequence of sandstones, siltstones, mudstones and limestones which presents a problem to the fault rock classification model because it does not entirely fit into one classification. Furthermore, it has been classified into the 'clay smear series' category of the model by Cerveny et al., (2004) but for the purpose of this study, has been reclassified as the 'limestones' category.

To apply the model of Cerveny et al., (2004) to the Crow's Nest Fault, it is first necessary to determine a history of fault juxtaposition at the site. This can be achieved through the use of Allan diagrams. Allan diagrams are maps which view the hanging wall and footwall of a fault superimposed onto a modelled fault surface (Cerveny et al., 2004). These maps assess possible pathways for fluid flow, areas of leakage and sealing potential by using well log data to interpret any stratigraphic changes and seismic data to evaluate the offset of horizons. However, Allan diagrams require a large amount of data which is not always possible to obtain. Juxtaposition and triangle diagrams offer a more simplified model that evaluates the juxtaposition of different lithologies with increasing throw (figure 6.12). These juxtaposition diagrams can be used to predict fault rocks rich in sandstone and clay/shale. In doing so, predictions for fault permeability within hydrocarbon reservoirs can be estimated, i.e. where there are likely seals and conduits along a fault.
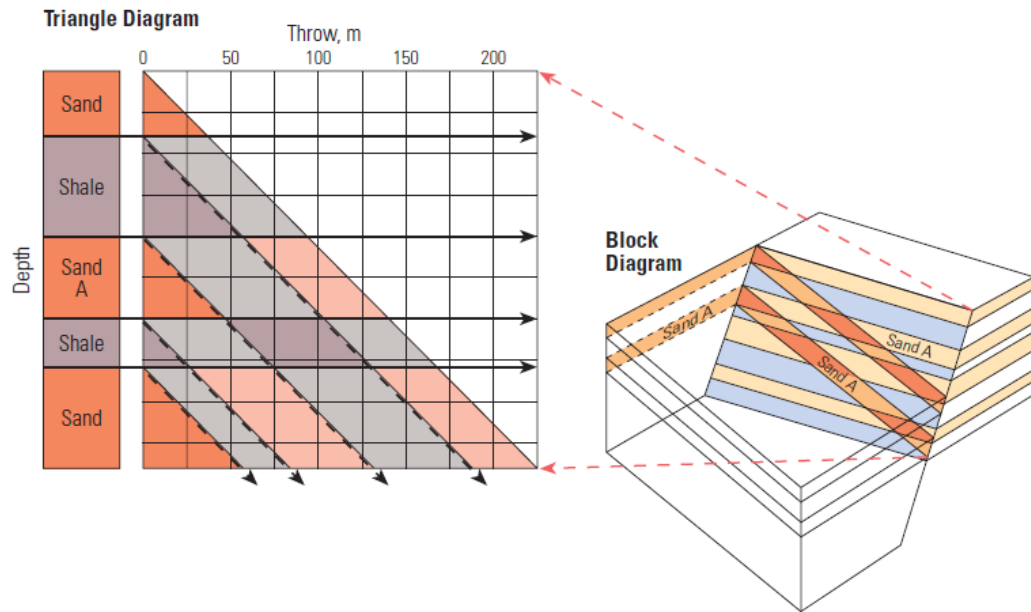
Figure 6.12 – Triangle diagram (left) which is taken from a block diagram (right) where the juxtaposition of different lithologies with increasing throw can be estimated. Cerveny et al., (2004).

Juxtaposition and fault rock diagrams have been produced to predict fault rock types at the Crow's Nest Fault (figure 6.13). In figure 6.14, at low displacements (<10m), all units self-juxtapose. For high porosity quartz rich sandstones this results in fracture dominated fault rocks which may lead to fluid leakage (figure 6.14a). For clay rich rocks and limestone rich rocks, this can potentially lead to sealing and inhibiting flow across the fault.

With increasing displacement, self-juxtaposed quartz rich, high permeability 'clean' sandstones will form cataclastic fault rocks and potentially form deformation bands (figure 6.14b). These fault rocks have the potential to leak fluid flow across fault or trap it, depending on the degree of grain crushing. Clean sandstones juxtaposed against clay rich lithology may act as a conduit or baffle during low displacements, however, with increasing displacement and increasing clay smear, the permeability reduces and a seal forms, sealing off across-fault fluid migration (figure 6.19d), and similarly the same happens with limestone juxtaposition (figure 6.19f). At approximately 50m displacement, up-fault fluid migration is estimated to seal off.
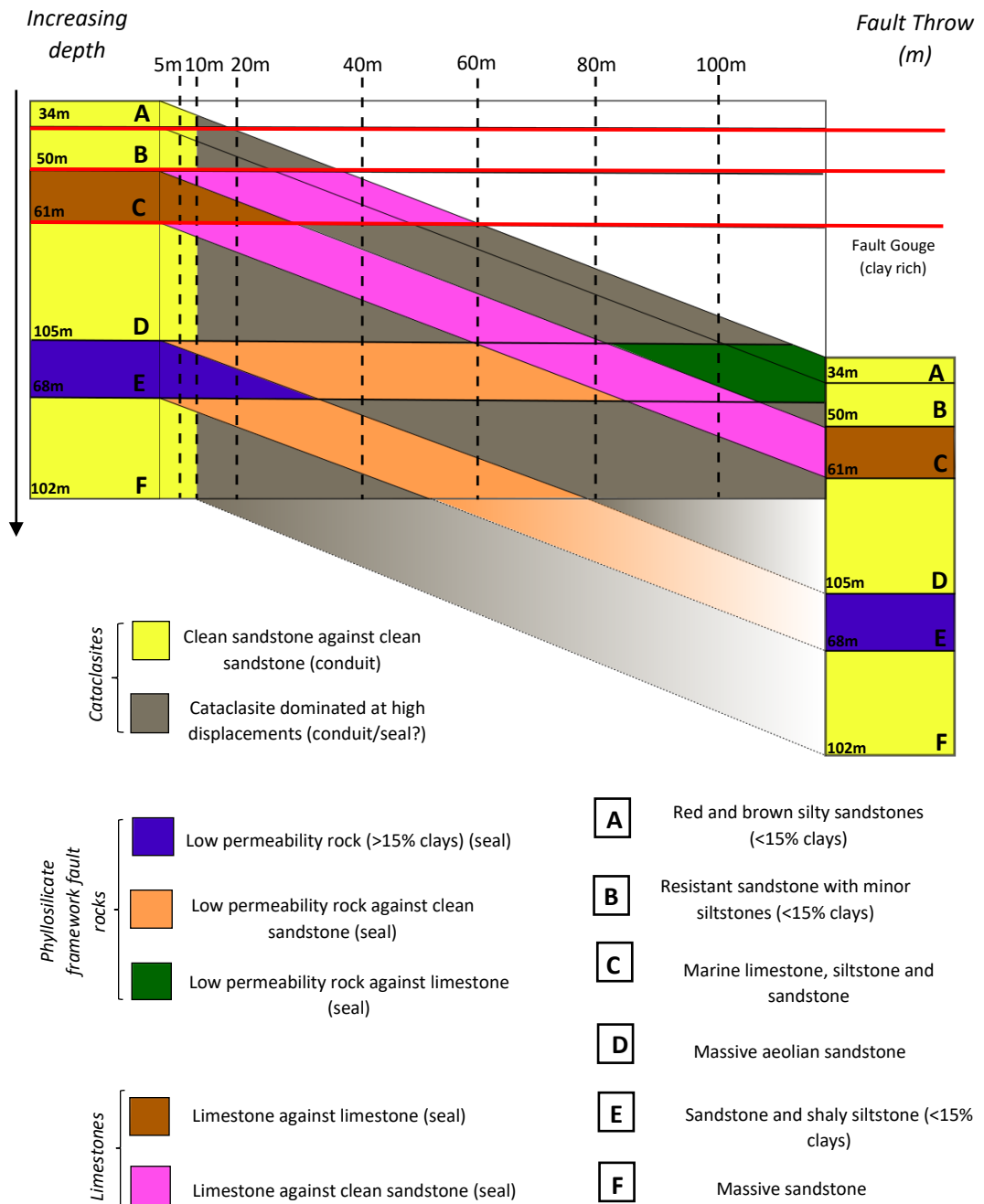
Figure 6.13 – Juxtaposition diagram for the Crow's Nest Fault.
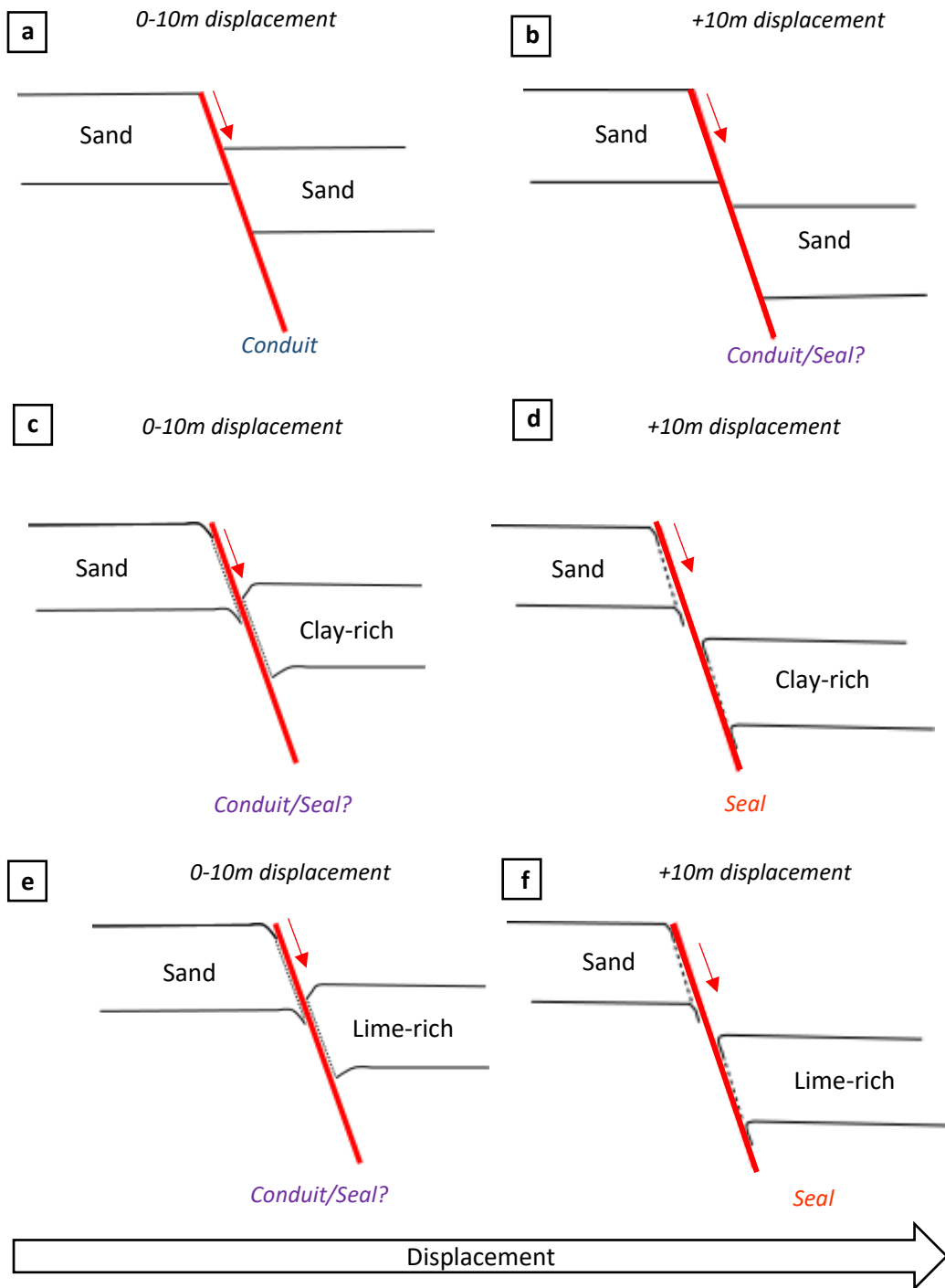
Figure 6.14 – Cartoons to show the juxtaposition of sandstones, clay rich lithologies and limestone rich lithologies at the Crow's Nest Fault.

To better visualise fault seal behaviour at the Crow's Nest Fault, a triangle diagram has been constructed, showing likely conduits and seals in figure 6.15.
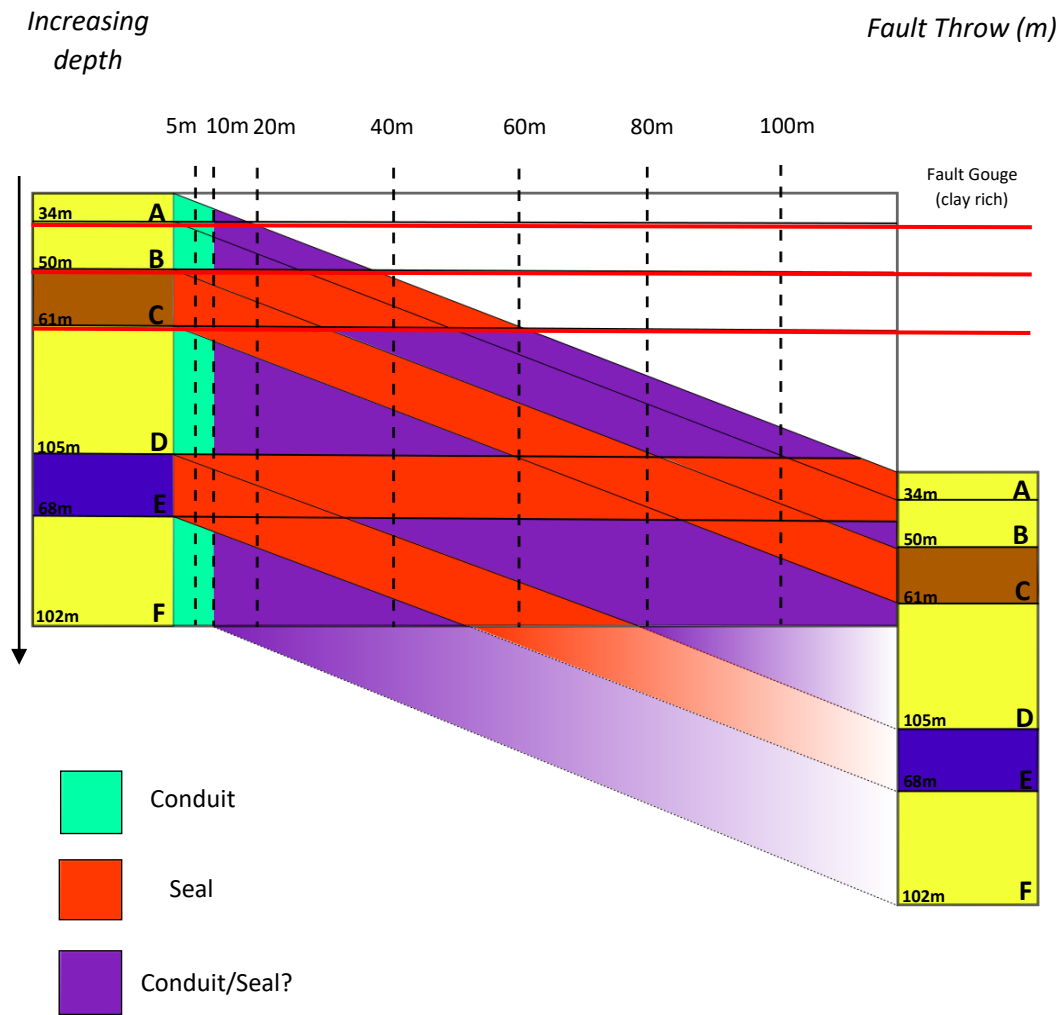
Figure 6.15 – Triangle diagram using the same lithologies from figure 6.18 estimating the fault seal potential for lithologies at the Crow's Nest Fault.

The Brush Valley lens site is composed of a sandstone and siltstone lens (Slick Rock Entrada) bound by two slip surfaces. The Brush Valley lens is juxtaposed against the Carmel Formation in the footwall and the Earthy Entrada in the hanging wall with throw ranging from 5m to 20m. At throws of up to 10m, the Cerveny et al., (2004) juxtaposition diagram identifies an area of leakage where the Earthy Entrada in the hanging wall is juxtaposed against the Slick Rock Entrada in the lens. However, with increasing throw there is the potential for the area of leakage to seal. The Slick Rock Entrada in the Brush Valley lens juxtaposed against the Carmel Formation in the lens is predicted to seal and remain sealed with increasing fault displacement based on the juxtaposition diagram.

In the field, there is evidence that the Slick Rock Entrada has deformed by clay smearing because there is low permeability fault gouge exposed where the unit juxtaposes between the underlying (Earthy Entrada) and overlying lithological units (Carmel Formation). Although predicted correctly for the juxtaposition of the Carmel Formation in the footwall against the Slick Rock Entrada in the lens, the juxtaposition diagram does not correctly identify an area of sealing between the Earthy Entrada hanging wall and the Slick Rock Entrada lens.

Current industry practice does not take into account fault lenses or breached relay ramps. As observed at the Crow's Nest Fault, sandstone lenses have the potential to be good conduits for fluid flow, but are not analysed as such. Although an interbedded sandstone and siltstone, the Slick Rock Entrada lens has been found to contain less than 15% clay content and so has been classified as a 'clean' sandstone and siltstone for the purposes of the Cerveny et al., (2004) juxtaposition model.

Elsewhere at the Crow's Nest Fault there is a further fault lens (Crow's Nest Spring lens) juxtaposing the Carmel Formation (limestone) against the Navajo Formation (aeolian sandstone). Using the juxtaposition diagram, this area would be considered a conduit to fluid flow. However, in the field area there is evidence of multiple strands of low permeability, clay rich fault gouge suggesting that this area has inhibited fluid flow.

Both of these fault lenses would not be taken into account when assessing fault seal potential, yet these are the only locations at the Crow's Nest Fault where hydrocarbons are exposed and are areas where there is abundant evidence of paleo fluid flow. This reiterates the importance of deformation and lithological controls on bulk permeability in normal faults.

Current industry techniques such as the fault rock classification system by Cerveny et al., (2004) do not take into account host rock rich in limestone even though it is well documented that rocks rich in limestone can act as cap rocks to reservoirs (Trimble and Doelling, 1978) and can deform by smearing. Studies of faults in limestone rich lithologies have been undertaken by Soliva and Benedicto, (2004; 2005); results have shown that fault linkage at fault tips is highly influenced by localised changes in relay ramp shear strength which is controlled by the host rock lithology.

Elsewhere along the fault, low permeability fault gouge is observed at the Cottonwood Wash locality where Carmel Formation and Navajo Formation in the footwall juxtapose Earthy Entrada in the hanging wall. Using the juxtaposition diagram, this area lies on a boundary between behaving as a conduit or barrier to fluid flow (figure 6.20). In the field, there is low permeability fault gouge exposed between the Navajo Formation and the Earthy Entrada, however it would be very difficult to determine the behaviour at this locality without visiting the field area.

It is clear from a comparison of the field observations at the Crow's Nest Fault, with the fault seal predictions in Figure 6.15, that the fault rock classification system by Cerveny et al., (2004) does not predict the hydraulic behaviour of the Crow's Nest Fault. Key to this lack of predictability are fault lens formation and the presence of limestone within the host rocks. These are therefore highlighted as areas requiring further model development, which may be achieved through theoretical studies and the use of multiple field observations.

6.6 Summary

Between the Late Jurassic and Late Tertiary, the Crow's Nest Fault was initiated from the reactivation of a basement structure. Thick deformation bands formed as precursors to fault formation and thin deformation bands formed after Jurassic sediments were buried up to 1.2km. The Crow's Nest Fault experienced a change in deformation mechanism from deformation banding to fracturing which occurred during a period of uplift. Porosity is the biggest influence on deformation style.

The Crow's Nest Fault exhibits an asymmetrical damage zone dominated by deformation bands and fractures. With a combined maximum width of 100m, the damage zone is much

larger than expected for a fault of this size and displacement. The types of deformation structures present, variations in porosity and asymmetry due to a propagation fold are all factors which have influenced the fault architecture. The damage zone reflects the linked geometry of the four soft linked fault strands, rather than the throw profile. With increasing displacement, there is very little change in fault thickness (damage zone and fault core combined).

Low permeability fault gouge is exposed at three locations at the Crow's Nest Fault with thicknesses ranging from 20cm to 50cm at areas of fault linkage. Where fault gouge is present at the fault lenses, evidence for hydrocarbons is observed. The fault tapped into the Paradox Formation and hydrocarbons ascended up the fault and into the Crow's Nest Spring lens becoming trapped within by clay rich gouge. Fluid ascended up the fault and into the Brush Valley lens, stripping calcite cement, enhancing porosity and enabling hydrocarbons to enter and become trapped by clay rich gouge.

By comparing field observations at the Crow's Nest Fault with fault seal prediction and fault rock classification of the Cerveny et al., (2004) model, it is clear that the hydraulic behaviour of the fault is not predicted. This is largely due to complex fault geometry such as the presence of fault lenses and limestone within the host rock. Further model development including theoretical studies and further field work are needed to aid better prediction. When it comes to evaluating fault seal behaviour and fault rock classification, other studies of faults in similar lithologies, sizes and displacements will complement the results from the Crow's Nest Fault field study (Foxford et al., 1998; Shipton and Cowie, 2001; 2003, Solum et al., 2005; Dockrill and Shipton, 2010; Eichhubl et al., 2010).

Chapter 7

Conclusions and Future Work

7.1 Conclusions and Recommendations

The aims of this thesis were to improve the understanding of how fault heterogeneity can influence fluid flow and how fluid flow can influence fault architecture in order to make better predictions of faulting at depth.

These aims were met through detailed field mapping and extensive microanalysis of samples in thin sections.

7.1.1 Fault zone architecture - field based conclusions

- ***Field mapping of the Crow's Nest Fault has allowed for a detailed description of the fault zone architecture.*** The Crow's Nest Fault consists of four soft linked fault strands which vary in length from 302m to 4.5km. There are three relay ramps which separate the four fault strands. The Crow's Nest Fault has a minimum measured throw of 4m and a maximum measured throw of 110m with juxtapositions of sandstones and limestones against clay and silt rich lithologies. Host rock exposed in the field area includes the Navajo Formation, the Carmel Formation and the Slick Rock and Earthy Members of the Entrada Formation. The host rock lithology ranges in age from the Lower to Middle Jurassic.

- ***The fault architecture of the Crow's Nest Fault consists of deformation structures, fault lenses, and fault gouge.*** Deformation structures consist of thick deformation bands, thin deformation bands, iron-rich fractures and unfilled fractures, all of which decrease in density away from the fault. There are two fault lenses present; the Brush Valley lens (exposed as 35m x 110m) and the Crow's Nest Spring lens (exposed as 11m x 5m). Fault gouge is exposed in three locations; Cottonwood Wash, Crow's Nest Spring and Brush Valley and is between 20cm and 50cm thick.

- ***Deformation bands are typically the earliest deformation structures to form.*** Cross cutting evidence from the field suggests that thick deformation bands are the earliest structures to form, followed by thin deformation bands. Iron-rich fractures form after thin deformation bands and the youngest deformation structures exposed are unfilled fractures.

- ***Damage zone width reflects linked fault geometry rather than throw profile.***
  There is some correlation between fault thickness and displacement. However,
  with increasing maximum throw there is an extremely weak correlation. There is no
  correlation with the minimum throw estimate. Instead, the damage zone is wider at
  fault linkage zones and fault segment tips, reflecting the geometry of the four soft
  linked fault strands as opposed to where maximum displacement is accommodated
  in the middle of the fault.

- ***Porosity strongly influences damage zone width.*** Porosity controls the way in
  which a rock will deform. For example, high porosity rocks typically will deform by
  deformation banding and low porosity rocks will typically deform by fracturing. At
  the Crow's Nest Fault, deformation bands are associated with the fault segment
  tips. At the fault segment tips, porosity is typically 6.7-14.1% higher than elsewhere
  along the fault and there is 8.3-8.5% less calcite cement present. Away from the
  fault segment tips the host rock is less porous (15.9%), well cemented and there are
  no deformation bands exposed.

- **Between the Late Jurassic and Early Tertiary, the Crow's Nest Fault was likely
  initiated from the reactivation of a basement fault.** Thick deformation bands acted
  as precursory structures to fault formation, as determined by cross cutting relations
  in the field and under thin section. This likely occurred between the Jurassic and
  Tertiary, based on published burial history curves and the relative timing of the
  observed structures.

- ***Fractures are likely related to uplift in the Late Tertiary – Holocene.*** Field
  observations show that fractures cut high porosity rock so they cannot follow the
  model by Johansen et al., (2005) which suggests that fractures formed due to a
  decrease in porosity resulting from the precipitation and mineralisation of calcite
  cement. However, at the Crow's Nest Fault there is evidence for the dissolution of
  calcite cement. The cross cutting relations are more like the model from Davaztes
  and Aydin, (2003) where jointing at the Moab Fault is thought to be related to
  uplift.

- ***High porosity fault lenses channel fluid flow up the fault but impede across fault
  flow due to low permeability, clay rich fault gouge.*** Fault gouge is exposed in three
  locations at the Crow's Nest Fault (Cottonwood Wash, Crow's Nest Spring and
  Brush Valley) and varies in thickness from 20cm to 50cm. Fault gouge at the Crow's

Nest Fault appears very similar mineralogically everywhere along the fault. Samples collected of the fault gouge at each of the three locations show evidence illite which can precipitate into the pores of sandstones, impeding flow. Evidence of hydrocarbons are exposed within fault lenses which are bound by low permeability clay rich gouge which likely restricted across fault flow.

7.1.2 Fault architecture – industry based conclusions

- ***Current industry algorithms fail to consider lithologies other than sandstone or shale/clay when assessing fluid flow potential.*** Algorithms which are used in industry to estimate the percentage of shale gouge (SGR), shale smear (SSF) and clay smear (CSP) fail to incorporate diagenesis and mixing of sediments. These algorithms only estimate sands and shales/clays. Juxtaposition diagrams for the Crow's Nest Fault indicate that lithologies rich in limestone have the potential to act as a barrier or baffles to fluid flow, however limestones or any lithology bar sands and shales/clays are not taken into consideration in conventional fault seal analysis. Therefore, these algorithms need to consider how lithologies other than sands and shales/clays can potentially affect the hydraulic properties of faults.

- ***Fault lenses have the potential to act as high permeability pathways for fluid flow but are rarely seismically resolvable or identified using industry data.*** The Crow's Nest Fault has two fault lenses which have acted as pathways to fluid flow. Both lenses at the Crow's Nest Fault are exposed in lithologies which are either low porosity (Slick Rock Entrada – siltstone rich) or lithology not identified when using juxtaposition methods (Carmel Formation – limestone rich). More field and lab work should be undertaken focussing on how porosity influences fault architecture and the effect deformation mechanisms have on fault permeability. Studies could look into the controls on fault architecture for permeability, especially the influence limestone-rich lithologies have on permeability at higher displacements. It is not possible to predict every potential fault lens from seismic imaging however, further research could be undertaken to understand how host rock rich in limestone deforms and what types of fault rocks are formed in limestone hosted faults.

- ***Understanding that two sandstones juxtaposed will likely result in deformation banding and impede flow, and the juxtaposition of sands against low***

permeability rocks will likely result in fracturing and enhance flow is an important step in improving predictions for the oil and gas, radioactive waste and CO$_2$ storage industries. As a result, the Crow's Nest Fault may not be a suitable area for storing radioactive waste or CO$_2$, however it may be prosperous area for oil and gas. Knowing what lithology a fault is likely cutting, and the regional setting of a fault is crucial to better estimate the types of fault rocks produced and how the fault rocks might deform. Making better estimations of how a rock might deform leads to better estimations for the hydraulic properties of the fault zone. Studies could place emphasis on the level of risk or uncertainty presented by juxtapositions. For example, when studying two lithologies juxtaposed together, a level of certainty could be place on whether there might be a fault lens or segmented fault present. A percentage would represent the level of certainty or uncertainty there is for there being a fault lens/segmented fault present. The percentage would be deduced from looking into factors such as burial depth, burial history, temperature, lithology and porosity data gained from studied faults in the same region. A classification system could then be devised when studying faults; for example, a fault could be classified as 'high risk' for having a fault lens which would not be seismically resolvable.

7.1.3 Fluid flow

- ***The Crow's Nest Fault shows evidence for paleo fluid flow.*** This includes modern hydrocarbons, iron oxide staining, nodules and iron-rich fractures, bleaching and the dissolution of calcite cement and water flow.

- ***Fluid rich in hydrocarbons was the earliest fluid to ascend the Crow's Nest Fault but only at the Crow's Nest Spring lens.*** Hydrocarbons are present in well-cemented host rock at the Crow's Nest Spring locality, indicating no prior dissolution of cement by reducing fluids.

- ***Hydrocarbons are only exposed at the fault lenses.*** At the Crow's Nest Spring lens site, the fault has likely tapped into the Paradox Formation and hydrocarbons ascended up the fault and into the lens travelling through the Navajo Formation. At the Brush Valley lens site, hydrocarbons likely ascended the fault and travelled into the lens through the Slick Rock Entrada. The Slick Rock Entrada is a sandstone

interbedded with siltstone and which, prior to having calcite cement dissolved, would not have acted as a good a reservoir host rock as the Navajo Formation at the Crow's Nest Spring lens site. For hydrocarbons to have stained the host rock at the Brush Valley lens site, the ccalcite cement would have had to be stripped out in order to increase the porosity of the lens host rock enough to host fluid flow.

- ***Iron oxide was present at the Crow's Nest Fault prior to the formation of open fractures.*** Only fractures orientated north-south are filled with iron oxide.

- ***Bleaching fluids post-date all other fluids which ascended the Crow's Nest Fault.*** Bleaching fluids are the last fluids to have ascended the Crow's Nest Fault. Fluid (reducing) ascended the Crow's Nest Fault at the relay ramps and bleached the rock, stripping it of hematite and redepositing iron oxide as staining and nodules. Only open fractures are bleached and cross cutting relations suggest that these were the last deformation structures to form.

- ***Bleaching fluids ascended the Brush Valley lens, removed the calcite cement and deposited hydrocarbons in high porosity areas of the host rock.*** Hydrocarbons at the Brush Valley lens are only observed in high porosity parts of the host rock where calcite cement has been dissolved so the calcite cement must have been dissolved to make room for the hydrocarbons.

- ***Bleaching fluid likely ascended up the relay ramps and fault segment tips of the Crow's Nest Fault.*** Bleaching is only observed at the fault segment tips and relay ramps.

- ***For low porosity host rock to act as a conduit or baffle to fluid flow, carbonate cement needs to be removed.*** The Slick Rock Entrada is a sandstone interbedded with low porosity siltstones. At the Brush Valley lens, the host rock has been stripped of calcite cement and this has increased the porosity and allowed for hydrocarbons to be channelled into the lens.

- ***Porosity of the Navajo Formation is variable across Utah, but porosity of the Navajo Formation is much higher at up to 22.6% at the Crow's Nest Fault.*** The porosity of the Navajo Formation is higher at the fault segment tips (up to 22.6%) compared to the middle of the fault strand (15.9%).

- ***Deformation bands control vertical fluid flow but low permeability clay rich gouge controls horizontal, across fault flow.*** Deformation bands typically control flow up

a fault and are barriers at the Crow's Nest Fault. Low permeability clay rich gouge has behaved as a barrier to flow across the Crow's Nest Fault.

- ***Low permeability fault gouge which is continuous along strike can trap fluids inside a fault lens.*** Where the Crow's Nest Fault is well exposed along strike, fault gouge is exposed. Assuming that fault gouge is continuous along strike, fluids have ascended the fault through the lenses and hydrocarbons have been trapped by strands of low permeability fault gouge.

7.2 Future Work

The aims of this thesis have been addressed to gain a better understanding on the controls of fault architecture and fluid flow migration in normal faults. A number of questions still remain unanswered leaving room for further work, which are outlined in this section.

1. ***How can algorithms used by industry be improved to better predict the permeability of normal faults in the sub-surface?***

Current industry recognised algorithms such as Shale Gouge Ratio, Clay Smear Potential and Shale Smear Factor do not take into account how much material from the host rock is integrated into the fault zone, assumes homogenous mixing and constant host rock porosity.

Fluids which have ascended the Crow's Nest Fault have altered and weakened the host rock. Where fluids have ascended the fault at the fault segment tips and lenses, the porosity has been increased.

Current industry algorithms fail to take into account diagenesis and assumes uniform thickness of the fault zone. At the Crow's Nest Fault, there are many small scale heterogeneities such as changes in porosity and fault zone thickness that industry algorithms do not account for in their calculations.

It is unrealistic and impossible to study all faults independently, but estimations could be improved by incorporating variables such as porosity, detailed stratigraphy, burial depth, temperature, stress and strain histories and geochemistry of fluid flow into industry

workflows. However, many more detailed studies of fault zone architecture will be needed to achieve this.

2. ***How can the size, orientation, distribution and frequency of high permeability sandstone lenses be predicted/estimated in the future?***

As shown by the Crow's Nest Fault, sandstone lenses have the potential to be high permeability conduits which channel fluid flow both up the fault and into the fault zone.

To try and improve estimations for fault lenses, it is important to consider the lithology lenses are formed in as lithology is a key control on fault architecture. By studying fault lenses in different lithologies and then simulating the conditions of each lithology in a laboratory, the conditions of how lenses form can be better constrained. Within a laboratory setting, a fault lens could be represented by a sand block in the shape of a lens. Fluid could be pumped through the lenses shape whilst changing the variables to mimic different lithologies. For example, the fault lens could have pressure applied to mimic a well cemented and compacted host rock and the clay content could be increased to mimic how clay content affects fluid flow through fault lenses.

3. ***How can juxtaposition of host rock lithology be applied to faulted lithology at depth?***

Juxtaposition diagrams are a useful tool for estimating fault rock type and the effects on fault architecture and permeability. However, juxtaposition diagrams should be used with caution. One of the biggest limitations in industry modelling is the lack of understanding and examples of the types of fault rocks produced from high displacement faults compared to low displacement faults.

The Crow's Nest Fault has a maximum displacement of 110m and juxtaposes silty sandstones against limestones, high porosity 'clean' sandstones and interbedded sands and silts. Although initiated by precursory deformation bands, the fault is dominated by fractures.

However, faults with lower displacements will typically produce different fault rocks then faults with higher displacements. Further work should focus on studying smaller faults in the field to determine the effect that host rock porosity has on deformation mechanisms. The influx of fluid flow may alter the fault zone and weaken it, or increased mineralisation may strengthen the fault rock. Other factors to take into consideration include diagenesis and mixing of sediments through clay and shale smear which can alter fault architecture.

4. *What is the geochemistry of fluids at the Crow's Nest Fault?*

The origin of the reducing fluid which bleached the host rock at the Crow's Nest Fault is likely from a source rich in hydrocarbons or CO_2. However, without testing the evidence for paleo fluid flow at the Crow's Nest Fault, the geochemistry of the fluid is unknown.

At the Crow's Nest Fault there is evidence for calcite cement and dolomite present within the host rock. However, it is not known whether these originate from the host rock or are a secondary mineralisation related to fluids. By analysing the geochemistry of the calcite cement, the fluid controls on fault rock composition can be better understood.

To deduce the geochemistry of the fluids present at the Crow's Nest Fault, a number of tests need to be made on the evidence of paleo fluid flow. Firstly, further samples need to be taken from the field area. Carbon and oxygen isotopes of cements in the host rock could be compared against the carbon and oxygen isotopes of hydrocarbons across the rest of the Paradox Basin to determine fluid origin. To determine fluid geochemistry, analysis such as gas chromatography and hydrocarbon fingerprinting could be undertaken. Cathodoluminescence (CL) could be used to determine precipitations of fluids in the fault gouge.

References

Abrams, M.A., (1996). Distribution of subsurface hydrocarbon seepage in near-surface marine sediments. In: Schumacher, D., and Abrams, M.A. (eds.) Hydrocarbon migration and its near-surface expression. American Association of Petroleum Geologists, Memoir, **66**, 1-14

Allan, U.S., (1989). Model for hydrocarbon migration and entrapment within faulted structures. *AAPG bulletin*, **73**, (7), 803-811

Allison, M.L., (1997). A Preliminary Assessment of Energy and Mineral Resources within the Grand Staircase-Escalante National Monument (C-93)

Antonellini, M. and Aydin, A., (1994). Effect of faulting on fluid flow in porous sandstones: petrophysical properties. *AAPG bulletin*, **78**, (3), 355-377

Antonellini, M. and Aydin, A., (1995). Effect of faulting on fluid flow in porous sandstones: geometry and spatial distribution. *AAPG bulletin*, **79**, (5), 642-670

Aydin, A. and Eyal, Y., (2002). Anatomy of a normal fault with shale smear: Implications for fault seal. *AAPG bulletin*, **86**, (8)

Aydin, A. and Johnson, A.M., (1978). Development of faults as zones of deformation bands and as slip surfaces in sandstone. In *Rock Friction and Earthquake Prediction* (pp. 931-942). Birkhäuser Basel.

Aydin, A., (1978). Small faults formed as deformation bands in sandstone. *Pure and Applied Geophysics*, **116**, (4-5), 913-930

Aydin, A., (2000). Fractures, faults, and hydrocarbon entrapment, migration and flow. *Marine and petroleum geology*, **17**, (7), 797-814

Baars, D.L. and Doelling, H.H., (1987). Moab salt-intruded anticline, east-central Utah. *Geological Society of America Centennial Field Guided Rocky Mountain Section*, 275-280

Baars, D.L. and Seager, W.R., (1970). Stratigraphic control of petroleum in White Rim sandstone (Permian) in and near Canyonlands National Park, Utah. *AAPG Bulletin*, **54**, (5), 709-718

Baars, D.L. and Stevenson, G.M., (1981). Tectonic evolution of the Paradox basin, Utah and Colorado.

Beitler, B., Chan, M.A. and Parry, W.T., (2003). Bleaching of Jurassic Navajo sandstone on Colorado Plateau Laramide highs: Evidence of exhumed hydrocarbon supergiants? *Geology*, **31**, (12), 1041-1044

Beitler, B., Parry, W.T. and Chan, M.A., (2005). Fingerprints of fluid flow: chemical diagenetic history of the Jurassic Navajo Sandstone, southern Utah, USA. *Journal of Sedimentary Research*, **75**, (4), 547-561

Bense, V.F., and Person, M.A., (2006), Faults as conduit-barrier systems to fluid flow in siliciclastic sedimentary aquifers: *Water Resources Research*, **42**, p. doi: 10.1029/2005WR004480.

Berg, S.S. and Skar, T., (2005). Controls on damage zone asymmetry of a normal fault zone: outcrop analyses of a segment of the Moab fault, SE Utah. *Journal of Structural Geology*, **27**, (10), 1803-1822

Bouvier, J.D., Kaars-Sijpesteijn, C.H., Kluesner, D.F., Onyejekwe, C.C. and Van der Pal, R.C., (1989). Three-dimensional seismic interpretation and fault sealing investigations, Nun River Field, Nigeria. *AAPG Bulletin*, **73**, (11), 1397-1414

Bowen, B.B., Benison, K.C., Oboh-Ikuenobe, F.E., Story, S. and Mormile, M.R., (2008). Active hematite concretion formation in modern acid saline lake sediments, Lake Brown, Western Australia. *Earth and Planetary Science Letters*, **268**, (1), 52-63

Bright, A.M. (2006). 'Characterising the Structure and Petrophysical Properties of Deformation Band Fault Cores in Reservoir Sandstone'. PhD, Trinity College, Dublin

Brogi, A. and Capezzuoli, E., (2009). Travertine deposition and faulting: the fault-related travertine fissure-ridge at Terme S. Giovanni, Rapolano Terme (Italy). *International Journal of Earth Sciences*, **98**, (4), 931-947

Burnside, N.M., (2010). *U-Th dating of travertines on the Colorado Plateau: implications for the leakage of geologically stored CO2* (Doctoral dissertation, University of Glasgow).

Busigny, V. and Dauphas, N., (2007). Tracing paleofluid circulations using iron isotopes: A study of hematite and goethite concretions from the Navajo Sandstone (Utah, USA). *Earth and Planetary Science Letters*, **254**, (3), 272-287

Caine, J.S. and Forster, C.B., (1999). Fault zone architecture and fluid flow: Insights from field data and numerical modelling. *Faults and Subsurface Fluid Flow in the Shallow Crust*, 101-127

Caine, J.S., Evans, J.P. and Forster, C.B., (1996). Fault zone architecture and permeability structure. *Geology*, **24**, (11), 1025-1028

Campbell, J.A. and Ritzma, H.R., (1979). Geology and petroleum resources of the major oil-impregnated sandstone deposits of Utah

Cartwright, J., Huuse, M. and Aplin, A., (2007). Seal bypass systems. *AAPG bulletin*, **91**, (8), 1141-1166

Cartwright, J.A. and Mansfield, C.S., (1998). Lateral displacement variation and lateral tip geometry of normal faults in the Canyonlands National Park, Utah. *Journal of Structural Geology*, **20**, (1), 3-19

Cartwright, J.A., Trudgill, B.D. and Mansfield, C.S., (1995). Fault growth by segment linkage: an explanation for scatter in maximum displacement and trace length data from the Canyonlands Grabens of SE Utah. *Journal of Structural Geology*, **17**, (9), 1319-1326

Cerveny, K., Davies, R., Dudley, G., Kaufman, P., Knipe, R.J. and Krantz, B., (2004). Reducing uncertainty with fault-seal analysis. *Oilfield Review*, **16**, (4), 2005

Chafetz, H.S. and Folk, R.L., (1984). Travertines: depositional morphology and the bacterially constructed constituents. *Journal of Sedimentary Research*, **54**, (1)

Chan, M.A., Beitler, B., Parry, W.T., Ormö, J. and Komatsu, G., (2004). A possible terrestrial analogue for haematite concretions on Mars. *Nature*, **429**, (6993), 731-734

Chan, M.A., Bowen, B.B., Parry, W.T. and Ormö, J., (2005). Red rock and red planet diagenesis. *GSA today*, p.5

Chan, M.A., Johnson, C.M., Beard, B.L., Bowman, J.R. and Parry, W.T., (2006). Iron isotopes constrain the pathways and formation mechanisms of terrestrial oxide concretions: A tool for tracing iron cycling on Mars? *Geosphere*, **2**, (7), 324-332

Chan, M.A., Ormö, J., Park, A.J., Stich, M., Souza-Egipsy, V. and Komatsu, G., (2007). Models of iron oxide concretion formation: field, numerical, and laboratory comparisons. *Geofluids*, **7**, (3), 356-368

Chan, M.A., Parry, W.T. and Bowman, J.R., (2000). Diagenetic hematite and manganese oxides and fault-related fluid flow in Jurassic sandstones, southeastern Utah. *AAPG bulletin*, **84**, (9), 1281-1310

Chester, F.M. and Logan, J.M., (1986). Implications for mechanical properties of brittle faults from observations of the Punchbowl fault zone, California. *Pure and Applied Geophysics*, **124**, (1-2), 79-106

Childs, C., Manzocchi, T., Walsh, J.J., Bonson, C.G., Nicol, A. and Schöpfer, M.P., (2009). A geometric model of fault zone and fault rock thickness variations. *Journal of Structural Geology*, **31**, (2), 117-127

Childs, C., Nicol, A., Walsh, J.J. and Watterson, J., (1996). Growth of vertically segmented normal faults. *Journal of Structural Geology*, **18**, (12), 1389-1397

Childs, C., Nicol, A., Walsh, J.J. and Watterson, J., (2003). The growth and propagation of synsedimentary faults. Journal of Structural Geology, **25**, (4), 633-648

Clark, R.M. and Cox, S.J.D., (1996). A modern regression approach to determining fault displacement-length scaling relationships. *Journal of Structural Geology*, **18**, (2), 147-152

Clausen, J.A. and Gabrielsen, R.H., (2002). Parameters that control the development of clay smear at low stress states: an experimental study using ring-shear apparatus. *Journal of Structural Geology*, **24**, (10), 1569-1586

Condon, S.M., (1997). *Geology of the Pennsylvanian and Permian cutler group and Permian Kaibab limestone in the Paradox Basin, southeastern Utah and southwestern Colorado* (No. 2000). US Government Printing Office.

Cooley, M.E., Harshbarger, J.W., Akers, J.P. and Hardt, W.F., (1969). *Regional hydrogeology of the Navajo and Hopi Indian Reservations, Arizona, New Mexico, and Utah* (pp. 1-61). US Government Printing Office.

Cowie, P.A. and Scholz, C.H., (1992). Physical explanation for the displacement-length relationship of faults using a post-yield fracture mechanics model. *Journal of Structural Geology*, **14***, (10), 1133-1148

Cowie, P.A. and Shipton, Z.K., (1998). Fault tip displacement gradients and process zone dimensions. *Journal of Structural Geology*, 20, (8), 983-997

Crawford, B.R., Faulkner, D.R. and Rutter, E.H., (2008). Strength, porosity, and permeability development during hydrostatic and shear loading of synthetic quartz-clay fault gouge. *Journal of Geophysical Research: Solid Earth*, **113**

Crider, J.G. and Peacock, D.C., (2004). Initiation of brittle faults in the upper crust: a review of field observations. *Journal of Structural Geology*, **26***, (4), 691-707

Dane, C.H., (1935). *Geology of the Salt Valley anticline and adjacent areas, Grand County, Utah* (No. 863). US Govt. Print. Off.,.

Darcy, H., (1856). Les fontaines publique de la ville de Dijon. *Dalmont, Paris*, *647*

Dauphas, N., Cates, N.L., Mojzsis, S.J. and Busigny, V., (2007). Identification of chemical sedimentary protoliths using iron isotopes in the> 3750 Ma Nuvvuagittuq supracrustal belt, Canada. *Earth and Planetary Science Letters*, **254**, (3), 358-376

Davatzes, N.C. and Aydin, A., (2003). Overprinting faulting mechanisms in high porosity sandstones of SE Utah. *Journal of Structural Geology*, **25**, (11), 1795-1813

Davatzes, N.C., Aydin, A. and Eichhubl, P., (2003). Overprinting faulting mechanisms during the development of multiple fault sets in sandstone, Chimney Rock fault array, Utah, USA. *Tectonophysics*, **363**, (1), 1-18

Davatzes, N.C., Aydin, A., (2005). Distribution and nature of fault architecture in a layered sandstone and shale sequence: an example from the Moab fault, Utah. In: Sorkhabi, R., Tsuji, Y. (Eds.), Faults, Fluid Flow, and Petroleum Traps. *American Association of Petroleum Geologists Memoir*, **85**, 153-180

Davis, G.H., (1999). *Structural geology of the Colorado Plateau region of southern Utah, with special emphasis on deformation bands* (Vol. 342). Geological Society of America.

Dawers, N.H. and Anders, M.H., (1995). Displacement-length scaling and fault linkage. *Journal of Structural Geology*, **17***, (5), 607-614

Dawers, N.H., Anders, M.H. and Scholz, C.H., (1993). Growth of normal faults: Displacement-length scaling. *Geology*, **21***, (12), 1107-1110

Demaison, G.J., (1977). Tar sands and supergiant oil fields. *AAPG Bulletin*, **61**, (11), 1950-1961

Di Toro, G., Pennacchioni, G. and Teza, G., (2005). Can pseudotachylytes be used to infer earthquake source parameters? An example of limitations in the study of exhumed faults. *Tectonophysics*, **402**, (1), 3-20

Dockrill, B. and Shipton, Z.K., (2010). Structural controls on leakage from a natural CO 2 geologic storage site: Central Utah, USA. *Journal of Structural Geology*, **32**, (11), 1768-1782

Doelling, H.H., (1988). Geology of Salt Valley Anticline and Arches National Park, Grand County, Utah. In: Doelling, H.H., Oviatt, C.G., Huntoon, P.W. (Eds.), Salt Deformation in the Paradox Region, Utah Utah Geological and Mineral Survey Bulletin, vol. 122, pp. 1–60.

Doelling, H.H., (2002). Geologic map of the Moab and eastern part of the San Rafael Desert 30'x 60'quadrangles, Grand and Emery Counties, Utah, and Mesa County, Colorado. Utah Geological Survey

Doelling, H.H., Blackett, R.E., Hamblin, A.H., Powell, J.D. and Pollock, G.L., (2000). Geology of Grand Staircase-Escalante National Monument, Utah. *Geology of Utah's parks and monuments: Utah Geological Association Publication*, **28**, 189-231

Doelling, H.H., Oviatt, C.G. and Huntoon, P.W., (1988). *Salt deformation in the Paradox region* (Vol. 122). Utah Geological Survey.

Doughty, P.T., (2003). Clay smear seals and fault sealing potential of an exhumed growth fault, Rio Grande rift, New Mexico. *AAPG bulletin*, **87**, (3), 427-444

Downey, M.W., (1984). Evaluating seals for hydrocarbon accumulations. *AAPG bulletin*, **68,** (11), 1752-1763

Dunn, D.E., LaFountain, L.J. and Jackson, R.E., (1973). Porosity dependence and mechanism of brittle fracture in sandstones. *Journal of Geophysical Research*, **78**, (14), 2403-2417

Egholm, D.L., Clausen, O.R., Sandiford, M., Kristensen, M.B. and Korstgård, J.A., (2008). The mechanics of clay smearing along faults. *Geology*, **36**, (10), 787-790

Eichhubl, P., Davatzes, N.C. and Becker, S.P., (2009). Structural and diagenetic control of fluid migration and cementation along the Moab fault, Utah. *AAPG bulletin*, **93**, (5), 653-681

Eichhubl, P., Hooker, J.N. and Laubach, S.E., (2010). Pure and shear-enhanced compaction bands in Aztec Sandstone. Journal of Structural Geology, **32**, (12), 1873-1886

Engelder, J.T., (1974). Cataclasis and the generation of fault gouge. *Geological Society of America Bulletin*, **85**, (10), 1515-1522

Evans, J. P., C. B. Forster, and J. V. Goddard (1997), Permeability of fault related rocks, and implications for hydraulic structure of fault zones, *Journal of Structural Geology*, **19**, (11), 1393-1404

Færseth, R.B., (2006). Shale smear along large faults: continuity of smear and the fault seal capacity. Journal of the Geological Society, **163**, (5), 741-751

Fairley, J. P., and J. J. Hinds (2004), Permeability distribution in an active Great Basin fault zone, *Geology*, **32**, 825-828

Fairley, J., Heffner, J. and Hinds, J., (2003). Geostatistical evaluation of permeability in an active fault zone. *Geophysical Research Letters*, **30**, (18)

Faulkner, D.R. and Rutter, E.H., (2001). Can the maintenance of overpressured fluids in large strike-slip fault zones explain their apparent weakness? *Geology*, **29**, (6), 503-506

Faulkner, D.R., Jackson, C.A.L., Lunn, R.J., Schlische, R.W., Shipton, Z.K., Wibberley, C.A.J. and Withjack, M.O., (2010). A review of recent developments concerning the structure, mechanics and fluid flow properties of fault zones. *Journal of Structural Geology*, **32**, (11), 1557-1575

Faulkner, D.R., Lewis, A.C. and Rutter, E.H., (2003). On the internal structure and mechanics of large strike-slip fault zones: field observations of the Carboneras fault in southeastern Spain. *Tectonophysics*, **367**, (3), 235-251

Fay, N.P. and Humphreys, E.D., (2005). Fault slip rates, effects of elastic heterogeneity on geodetic data, and the strength of the lower crust in the Salton Trough region, southern California. *Journal of Geophysical Research: Solid Earth*, **110**

Ferrill, D.A. and Morris, A.P., (2003). Dilational normal faults. *Journal of Structural Geology*, **25**, (2), 183-196

Ferrill, D.A., Stamatakos, J.A. and Sims, D., (1999). Normal fault corrugation: Implications for growth and seismicity of active normal faults. *Journal of Structural Geology*, **21**, (8), 1027-1038

Fetter C. W. (1993) *Containment hydrogeology 2nd Addition*. Pretence-Hall International (UK)

Fisher, Q.J. and Knipe, R., (1998). Fault sealing processes in siliciclastic sediments. *Geological Society, London, Special Publications*, **147**, (1), 117-134

Fisher, Q.J. and Knipe, R.J., (2001). The permeability of faults within siliciclastic petroleum reservoirs of the North Sea and Norwegian Continental Shelf. *Marine and Petroleum Geology*, **18**, (10), 1063-1081

Fisher, Q.J., Harris, S.D., McAllister, E., Knipe, R.J. and Bolton, A.J., (2001). Hydrocarbon flow across faults by capillary leakage revisited. *Marine and Petroleum Geology*, **18**, (2), 251-257

Folk, R.L., (1959). Practical petrographic classification of limestones. *AAPG Bulletin*, **43**, (1), 1-38

Foos, A., (1999). Geology of the Colorado Plateau. *Geology Field Trip Guides by Anabelle Foos, University of Akron. Available online at: http://www2.nature.nps. gov/geology/education*.

Ford, T.D. and Pedley, H.M., (1996). A review of tufa and travertine deposits of the world. *Earth-Science Reviews*, **41**, (3), 117-175

Fossen, H. and Hesthammer, J., (1997). Geometric analysis and scaling relations of deformation bands in porous sandstone. *Journal of Structural Geology*, **19**, (12), 1479-1493

Fossen, H. and Hesthammer, J., (2000). Possible absence of small faults in the Gullfaks Field, northern North Sea: implications for downscaling of faults in some porous sandstones. *Journal of Structural Geology*, **22**, (7), 851-863

Fossen, H., (2010). Deformation bands formed during soft-sediment deformation: Observations from SE Utah. *Marine and Petroleum Geology*, **27**, (1), 215-222

Fossen, H., (2010). Deformation bands formed during soft-sediment deformation: Observations from SE Utah. Marine and Petroleum Geology, 27, (1), 215-222

Fossen, H., Schultz, R.A. and Torabi, A., (2011). Conditions and implications for compaction band formation in the Navajo Sandstone, Utah. *Journal of Structural Geology*, **33**, (10), 1477-1490

Fossen, H., Schultz, R.A., Shipton, Z.K. and Mair, K., (2007). Deformation bands in sandstone: a review. *Journal of the Geological Society*, **164**, (4), 755-769

Foxford, K.A., Garden, I.R., Guscott, S.C., Burley, S.D., Lewis, J.J.M., Walsh, J.J. and Watterson, J., (1996). The field geology of the Moab fault. 265-284

Foxford, K.A., Walsh, J.J., Watterson, J., Garden, I.R., Guscott, S.C. and Burley, S.D., (1998). Structure and content of the Moab fault zone, Utah, USA, and its implications for fault seal prediction. *Geological Society, London, Special Publications*, **147**, (1), 87-103

Freeman, B., Yielding, G., Needham, D.T. and Badley, M.E., (1998). Fault seal prediction: the gouge ratio method. *Geological Society, London, Special Publications*, **127**, (1), 19-25

Fristad, T., Groth, A., Yielding, G. and Freeman, B., (1997). Quantitative fault seal prediction: a case study from Oseberg Syd. *Norwegian Petroleum Society Special Publications*, **7**, 107-124

Fulljames, J.R., Zijerveld, L.J.J. and Franssen, R.C.M.W., (1997). Fault seal processes: systematic analysis of fault seals over geological and production time scales. *Norwegian Petroleum Society Special Publications*, **7**, 51-59

Garden, I.R., Guscott, S.C., Burley, S.D., Foxford, K.A., Walsh, J.J. and Marshall, J., (2001). An exhumed palaeo-hydrocarbon migration fairway in a faulted carrier system, Entrada Sandstone of SE Utah, USA. *Geofluids*, **1**, (3), 195-213

Gardner, K.L., (1980). Impregnation technique using colored epoxy to define porosity in petrographic thin sections. *Canadian Journal of Earth Sciences*, **17**, (8), 1104-1107

Gartrell, A., Zhang, Y., Lisk, M. and Dewhurst, D., 2003. Enhanced hydrocarbon leakage at fault intersections: an example from the Timor Sea, Northwest Shelf, Australia. *Journal of Geochemical Exploration*, *78*, pp.361-365.

Géraud, Y., Diraison, M. and Orellana, N., (2006). Fault zone geometry of a mature active normal fault: a potential high permeability channel (Pirgaki fault, Corinth rift, Greece). *Tectonophysics*, **426**, (1), 61-76

Gibson, R.G., (1994). Fault-zone seals in siliciclastic strata of the Columbus Basin, offshore Trinidad. *AAPG bulletin*, **78**, (9), 1372-1385

Greer, H.F., Zhou, W. and Guo, L., (2015). Phase transformation of Mg-calcite to aragonite in active-forming hot spring travertines. *Mineralogy and Petrology*, **109**, (4), 453-462

Gupta, A. and Scholz, C.H., (2000). A model of normal fault interaction based on observations and theory. *Journal of Structural Geology*, **22**, (7), 865-879

Haszeldine, R.S., Quinn, O., England, G., Wilkinson, M., Shipton, Z.K., Evans, J.P., Heath, J., Crossey, L., Ballentine, C.J. and Graham, C.M., (2005). Natural geochemical analogues for carbon dioxide storage in deep geological porous reservoirs, a United Kingdom perspective. Oil & gas science and technology, *60,* (1), 33-49

Heath, J.E., Lachmar, T.E., Evans, J.P., Kolesar, P.T. and Williams, A.P., (2009). Hydrogeochemical Characterization of Leaking, Carbon Dioxide-Charged Fault Zones in East-Central Utah, With Implications for Geologic Carbon Storage. Carbon Sequestration and Its Role in the Global Carbon Cycle, 147-158

Hesthammer, J. and Fossen, H., (2000). Uncertainties associated with fault sealing analysis. *Petroleum Geoscience*, **6**, (1), 37-45

Hintze, L. F. (1988). Geologic history of Utah. Brigham Young University Geology Studies, Special Publication, 7.

Hood, J.W. and Patterson, D.J., (1984). Bedrock aquifers in the northern San Rafael Swell area, Utah, with special emphasis on the Navajo Sandstone (No. 78). Utah Department of Natural Resources, Division of Water Rights

Huggins, P., Watterson, J., Walsh, J.J. and Childs, C., (1995). Relay zone geometry and displacement transfer between normal faults recorded in coal-mine plans. *Journal of Structural Geology*, **17**, (12), 1741-1755

Hull, J., (1988). Thickness-displacement relationships for deformation zones. *Journal of Structural Geology*, **10**, (4), 431-435

Johansen, T.E.S., Fossen, H. and Kluge, R., (2005). The impact of syn-faulting porosity reduction on damage zone architecture in porous sandstone: an outcrop example from the Moab Fault, Utah. *Journal of Structural Geology*, **27**, (8), 1469-1485

Jones, R.M. and Hillis, R.R., (2003). An integrated, quantitative approach to assessing fault-seal risk. *AAPG bulletin*, **87**, (3), 507-524

Kampman, N., Bickle, M., Becker, J., Assayag, N. and Chapman, H., (2009). Feldspar dissolution kinetics and Gibbs free energy dependence in a CO 2-enriched groundwater system, Green River, Utah. Earth and Planetary Science Letters, **284**, (3), 473-488

Knipe, R.J., (1997). Juxtaposition and seal diagrams to help analyse fault seals in hydrocarbon reservoirs. *AAPG bulletin*, **81**, (2), 187-195

Knipe, R.J., Jones, G. and Fisher, Q.J., (1998). Faulting, fault sealing and fluid flow in hydrocarbon reservoirs: an introduction. *Geological Society, London, Special Publications*, **147**, (1), 7-21.

Knott, S.D., (1994). Structure, kinematics and metamorphism in the Liguride Complex, southern Apennines, Italy. *Journal of Structural Geology*, **16**, (8), 1107-1120

Knott, S.D., Beach, A., Brockbank, P.J., Brown, J.L., McCallum, J.E. and Welbon, A.I., (1996). Spatial and mechanical controls on normal fault populations. *Journal of Structural Geology*, **18**, (2-3), 359-372

Koledoye, A.B., Aydin, A. and May, E., (2000). Three-dimensional visualization of normal fault segmentation and its implication for fault growth. *The Leading Edge*, **19**, (7), 692-701

Krantz, R.W., 1988. Multiple fault sets and three-dimensional strain: theory and application. *Journal of Structural Geology*, **10**, (3), 225-237

Kremer, Y. (2014) *Deriving field-based statistical relationships to characterize the geometry, heterogeneity and permeability of faults in mixed sand-shale sequences: a new tool for upscaling flow properties.* Unpublished PhD thesis. University of Strathclyde

Kuiper, Y.D., Lin, S. and Jiang, D., (2011). Deformation partitioning in transpressional shear zones with an along-strike stretch component: An example from the Superior Boundary Zone, Manitoba, Canada. *Journal of Structural Geology*, **33**, (3), 192-202

Laubach, S.E., Eichhubl, P., Hilgers, C. and Lander, R.H., (2010). Structural diagenesis. *Journal of Structural Geology*, **32**, (12), 1866-1872

Lewicki, J.L., Birkholzer, J. and Tsang, C.F., (2007). Natural and industrial analogues for leakage of CO2 from storage reservoirs: identification of features, events, and processes and lessons learned. *Environmental Geology*, **52**, (3), 457

Lewis, G., Knipe, R. and Li, A., (2002). Fault seal analysis in unconsolidated sediments: a field study from Kentucky, USA. In: A.G. Koestler and R. Hunsdale (Editors), Hydrocarbon Seal Quantification. Norwegian Petroleum Society (NPF), Special Publication 11. Elsevier, Amsterdam

Ligtenberg, J.H., (2005). Detection of fluid migration pathways in seismic data: implications for fault seal analysis. *Basin Research*, **17**, (1), 141-153

Lindsay, N.G., Murphy, F.C., Walsh, J.J. and Watterson, J., (1993). Outcrop studies of shale smears on fault surfaces. *The geological modelling of hydrocarbon reservoirs and outcrop analogues*, 113-123

Little, T.A., (1995). Brittle deformation adjacent to the Awatere strike-slip fault in New Zealand: faulting patterns, scaling relationships, and displacement partitioning. *Bulletin of the Geological Society of America,* **107**, (11), 1255-1271

Lohr, T., Krawczyk, C.M., Oncken, O. and Tanner, D.C., (2008). Evolution of a fault surface from 3D attribute analysis and displacement measurements. *Journal of Structural Geology*, **30**, (6), 690-700

Loope, D.B., Kettler, R.M. and Weber, K.A., (2010). Follow the water: Connecting a CO2 reservoir and bleached sandstone to iron-rich concretions in the Navajo Sandstone of south-central Utah, USA. *Geology*, **38**, (11), 999-1002

MacLeod, C.J., Escartin, J., Banerji, D., Banks, G.J., Gleeson, M., Irving, D.H.B., Lilly, R.M., McCaig, A.M., Niu, Y., Allerton, S. and Smith, D.K., (2002). Direct geological evidence for oceanic detachment faulting: The Mid-Atlantic Ridge, 15 45' N. *Geology*, **30***,* (10), 879-882

Maerten, L., Gillespie, P. and Daniel, J.M., (2006). Three-dimensional geomechanical modelling for constraint of subseismic fault simulation. *AAPG bulletin*, **90***,* (9), 1337-1358

Mair, K., Elphick, S. and Main, I., (2002). Influence of confining pressure on the mechanical and structural evolution of laboratory deformation bands. *Geophysical Research Letters*, *29*(10).

Mair, K., Main, I. and Elphick, S., (2000). Sequential growth of deformation bands in the laboratory. *Journal of Structural Geology*, **22**, (1), 25-42

Manzocchi, T., Heath, A.E., Palananthakumar, B., Childs, C. and Walsh, J.J., (2008). Faults in conventional flow simulation models: a consideration of representational assumptions and geological uncertainties. *Petroleum Geoscience*, **14**, (1), 91-110

Manzocchi, T., Walsh, J.J., Nell, P. and Yielding, G., (1999). Fault transmissibility multipliers for flow simulation models. *Petroleum Geoscience*, **5**, (1), 53-63

Marone, C. and Scholz, C.H., (1989). Particle-size distribution and microstructures within simulated fault gouge. *Journal of Structural Geology*, **11**, (7), 799-814

Marrett, R. and Allmendinger, R.W., (1990). Kinematic analysis of fault-slip data. *Journal of structural geology*, **12**, (8), 973-986

Marrett, R. and Allmendinger, R.W., (1991). Estimates of strain due to brittle faulting: sampling of fault populations. *Journal of Structural Geology*, **13**, (6), 735-738

Marrett, R. and Allmendinger, R.W., (1992). Amount of extension on" small" faults: An example from the Viking graben. *Geology*, **20**, (1), 47-50

Mauldon, M., Dunne, W.M. and Rohrbaugh, M.B., (2001). Circular scanlines and circular windows: new tools for characterizing the geometry of fracture traces. *Journal of Structural Geology*, **23**, (2), 247-258

McLeod, A.E. and Underhill, J.R., (2000). The propagation and linkage of normal faults: insights from the Strathspey–Brent–Statfjord fault array, northern North Sea. *Basin Research*, **12**, (3-4), 263-284

Meinzer, O.E., (1923). *The occurrence of ground water in the United States with a discussion of principles* (Vol. 484). Govt. Print. Off.

Melezhik, V.A. and Fallick, A.E., (2003). δ 13 C and δ 18 O variations in primary and secondary carbonate phases: several contrasting examples from Palaeoproterozoic 13 C-rich metamorphosed dolostones. *Chemical geology*, **201**, (3), 213-228

Molenaar, C.M., (1987) Nomenclature chart of the Canyonlands and adjacent areas, *in* Fassett, J.E., ed. Canyonlands Country: Four Corners Geological Society Field Conference, 8th. P.142

Moriya, S., Childs, C., Manzocchi, T. and Walsh, J.J., (2005). Analysis of the relationships between strain, polarity and population slope for normal fault systems. *Journal of structural geology*, **27**, (6), 1113-1127

Moulton, F.C., (1975). Lower Mesozoic and upper Paleozoic petroleum potential of the Hingeline area, central Utah.

Nakatani, M. and Scholz, C.H., (2004). Frictional healing of quartz gouge under hydrothermal conditions: 1. Experimental evidence for solution transfer healing mechanism. *Journal of Geophysical Research: Solid Earth*, **109**

Nuccio, V.F. and Condon, S.M., (1996). Burial and thermal history of the Paradox Basin, Utah and Colorado, and petroleum potential of the Middle Pennsylvanian Paradox Formation.

O'Sullivan, R.B., (1981). Stratigraphic sections of Middle Jurassic Entrada Sandstone and related rocks from Salt Valley to Dewey Bridge in east-central Utah. US Geological Survey Oil and Gas Investigations Chart OC-113

Olig, S.S., Fenton, C.H., McCleary, J. and Wong, I.G., (1996). The earthquake potential of the Moab Fault and its relation to salt tectonics in the Paradox Basin, Utah.

Parry, W.T. and Blamey, N.J., (2010). Fault fluid composition from fluid inclusion measurements, Laramide age Uinta thrust fault, Utah. *Chemical Geology*, **278**, (1), 105-119

Parry, W.T., Chan, M.A. and Beitler, B., (2004). Chemical bleaching indicates episodes of fluid flow in deformation bands in sandstone. *AAPG bulletin*, **88**, (2), 175-191

Parry, W.T., Forster, C.B., Evans, J.P., Bowen, B.B. and Chan, M.A., (2007). Geochemistry of CO2 sequestration in the Jurassic Navajo Sandstone, Colorado Plateau, Utah. *Environmental Geosciences*, **14**, (2), 91-109

Payne, W.G., (2011). Controls on Porosity and Permeability in the Carmel Formation: Implications for Carbon Sequestration at Gordon Creek, Utah (Doctoral dissertation, New Mexico Institute of Mining and Technology)

Peacock, D.C.P. and Sanderson, D.J., (1994). Geometry and development of relay ramps in normal fault systems. *AAPG bulletin*, **78**, (2), 147-165

Pei, Y., Paton, D.A., Knipe, R.J. and Wu, K., (2015). A review of fault sealing behaviour and its evaluation in siliciclastic rocks. *Earth-Science Reviews*, **150**, 121-138

Pentecost, A., Jones, B. and Renaut, R.W., (2003). What is a hot spring? *Canadian Journal of Earth Sciences*, **40**, (11), 1443-1446

Pilcher, R. and Argent, J., (2007). Mega-pockmarks and linear pockmark trains on the West African continental margin. *Marine Geology*, **244**, (1), 15-32

Pollard, D.D. and Fletcher, R.C., (2005). *Fundamentals of structural geology*. Cambridge University Press.

Ponce, C., Druguet, E. and Carreras, J., (2013). Development of shear zone-related lozenges in foliated rocks. *Journal of Structural Geology*, **50**, 176-186

Pruess, K., (2008). On CO2 fluid flow and heat transfer behaviour in the subsurface, following leakage from a geologic storage reservoir. *Environmental Geology*, **54**, (8), 1677-1686

Railsback, L.B., (2006). Some fundamentals of mineralogy and geochemistry. *Department of Geology, University of Georgia, Athens, Georgia*, 30602-2501

Rawling, G.C. and Goodwin, L.B., (2006). Structural record of the mechanical evolution of mixed zones in faulted poorly lithified sediments, Rio Grande rift, New Mexico, USA. *Journal of Structural Geology*, **28**, (9), 1623-1639

Rice, J.R., (1992). Fault stress states, pore pressure distributions, and the weakness of the San Andreas fault. *International Geophysics*, **51**, 475-503

Roberts, H., Aharon, P. (1994). Hydrocarbon-derived carbonate buildups of the northern Gulf of Mexico continental slope: A review of submersible investigations. *Geo-Marine Letters*. **14**, 135-148

Rowland, J.C., Manga, M. and Rose, T.P., (2008). The influence of poorly interconnected fault zone flow paths on spring geochemistry. *Geofluids*, **8**, (2), 93-101

Rutqvist, J., (2012). The geomechanics of CO2 storage in deep sedimentary formations. *Geotechnical and Geological Engineering*, **30**, (3), 525-551

Sanford, W., (2002). Recharge and groundwater models: an overview. Hydrogeology journal, **10**, (1), 110-120

Schlomer, S., Kross, B.M., (1997). Experimental characterisation of the hydrocarbon sealing efficiency of cap rocks. Marine and Petroleum Geology, **14**, 565-580

Schmatz, J., Vrolijk, P.J. and Urai, J.L., (2010). Clay smear in normal fault zones–The effect of multilayers and clay cementation in water-saturated model experiments. *Journal of Structural Geology*, **32**, (11), 1834-1849

Schultz, R.A. and Fossen, H., (2002). Displacement–length scaling in three dimensions: the importance of aspect ratio and application to deformation bands. *Journal of Structural Geology*, **24**, (9), 1389-1411

Schulz, S.E. and Evans, J.P., (1998). Spatial variability in microscopic deformation and composition of the Punchbowl fault, southern California: implications for mechanisms, fluid–rock interaction, and fault morphology. *Tectonophysics*, **295**, (1), 223-244

Segall, P. and Pollard, D.D., (1983). Joint formation in granitic rock of the Sierra Nevada. *Geological Society of America Bulletin*, **94**, (5), 563-575

Segall, P. and Simpson, C., (1986). Nucleation of ductile shear zones on dilatant fractures. *Geology*, **14**, (1), 56-59

Shebl, M.A. and Surdam, R.C., (1996). Redox reactions in hydrocarbon clastic reservoirs: Experimental validation of this mechanism for porosity enhancement. *Chemical Geology*, **132**, (1-4), 103-117

Shipton, Z.K. and Cowie, P.A., (2001). Damage zone and slip-surface evolution over μm to km scales in high-porosity Navajo sandstone, Utah. *Journal of Structural Geology*, **23**, (12), 1825-1844

Shipton, Z.K. and Cowie, P.A., (2003). A conceptual model for the origin of fault damage zone structures in high-porosity sandstone. *Journal of Structural Geology*, **25**, (3), 333-344

Shipton, Z.K., Evans, J.P. and Thompson, L.B., (2005). The geometry and thickness of deformation-band fault core and its influence on sealing characteristics of deformation-band fault zones.

Shipton, Z.K., Evans, J.P., Kirschner, D., Kolesar, P.T., Williams, A.P. and Heath, J., (2004). Analysis of CO2 leakage through 'low-permeability'faults from natural reservoirs in the Colorado Plateau, east-central Utah. *Geological Society, London, Special Publications*, **233**, (1), 43-58

Shipton, Z.K., Evans, J.P., Robeson, K.R., Forster, C.B. and Snelgrove, S., (2002). Structural heterogeneity and permeability in faulted eolian sandstone: Implications for subsurface modelling of faults. *AAPG bulletin*, *86*(5), pp.863-883.

Shipton, Z.K., Soden, A.M., Kirkpatrick, J.D., Bright, A.M. and Lunn, R.J., (2006). How thick is a fault? Fault displacement-thickness scaling revisited. *Earthquakes: Radiated energy and the physics of faulting*, 193-198

Sibson, R.H., (1975). Generation of pseudotachylyte by ancient seismic faulting. *Geophysical Journal International*, **43**, (3), 775-794

Smith, R.B. and Bruhn, R.L., (1984). Intraplate extensional tectonics of the eastern Basin-Range: Inferences on structural style from seismic reflection data, regional tectonics, and thermal-mechanical models of brittle-ductile deformation. *Journal of Geophysical Research: Solid Earth*, **89**, 5733-5762

Soliva, R. and Benedicto, A., (2004). A linkage criterion for segmented normal faults. *Journal of Structural Geology*, **26**, (12), 2251-2267

Soliva, R. and Benedicto, A., (2005). Geometry, scaling relations and spacing of vertically restricted normal faults. *Journal of Structural Geology*, **27**, (2), 317-325

Solum, J.G., Davatzes, N.C. and Lockner, D.A., (2010). Fault-related clay authigenesis along the Moab Fault: Implications for calculations of fault rock composition and mechanical and hydrologic fault zone properties. *Journal of Structural Geology*, **32,** (12), 1899-1911

Solum, J.G., van der Pluijm, B.A. and Peacor, D.R., (2005). Neocrystallization, fabrics and age of clay minerals from an exposure of the Moab Fault, Utah. *Journal of Structural Geology*, **27**, (9), 1563-1576

Squyres, S.W., Grotzinger, J.P., Arvidson, R.E., Bell, J.F., Calvin, W., Christensen, P.R., Clark, B.C., Crisp, J.A., Farrand, W.H., Herkenhoff, K.E. and Johnson, J.R., (2004). In situ evidence for an ancient aqueous environment at Meridiani Planum, Mars. *science*, **306**, (5702), 1709-1714

Stewart, I.S. and Hancock, P.L., (1991). Scales of structural heterogeneity within neotectonic normal fault zones in the Aegean region. *Journal of Structural Geology*, **13**, (2), 191-204

Stowe, C., (1972). *Oil and gas production in Utah to 1970*. Utah Geological and Mineralogical Survey.

Torabi, A. and Fossen, H., (2009). Spatial variation of microstructure and petrophysical properties along deformation bands in reservoir sandstones. *AAPG bulletin*, **93**, (7), 919-938

Tosca, N.J., McLennan, S.M., Clark, B.C., Grotzinger, J.P., Hurowitz, J.A., Knoll, A.H., Schröder, C. and Squyres, S.W., (2005). Geochemical modeling of evaporation processes on Mars: Insight from the sedimentary record at Meridiani Planum. *Earth and Planetary Science Letters*, **240**, (1), 122-148

Trimble, L.M. and Doelling, H.H., (1978). Geology and uranium-vanadium deposits of the San Rafael River mining area, Emery County, Utah (Vol. 113). Utah Geological Survey

Trudgill, B. and Cartwright, J., (1994). Relay-ramp forms and normal-fault linkages, Canyonlands National Park, Utah. *Geological Society of America Bulletin*, **106**, (9), 1143-1157

Trudgill, B.D., (2011). Evolution of salt structures in the northern Paradox Basin: Controls on evaporite deposition, salt wall growth and supra-salt stratigraphic architecture. *Basin Research*, **23**, (2), 208-238

Turner, D.L., Triplehorn, D.M., Naeser, C.W. and Wolfe, J.A., (1980). Radiometric dating of ash partings in Alaskan coal beds and upper Tertiary paleobotanical stages. *Geology*, **8**, (2), 92-96

van der Zee, W. and Urai, J.L., (2005). Processes of normal fault evolution in a siliciclastic sequence: a case study from Miri, Sarawak, Malaysia. *Journal of Structural Geology*, **27**, (12), 2281-2300

van der Zee, W., Urai, J.L. and Richard, P.D., (2003). Lateral clay injection into normal faults, **8**, *Geoarabia-Manama*, 501-522

Vrolijk, P., Myers, R., Sweet, M.L., Shipton, Z.K., Dockrill, B., Evans, J.P., Heath, J. and Williams, A.P., (2005). Anatomy of reservoir-scale normal faults in central Utah: Stratigraphic controls and implications for fault zone evolution and fluid flow. *Field Guides*, **6**, 261-282

Walker, R.G. ed., (1979). Facies models. Geological Association of Canada.

Walker, R.R., Matulich, A., Amos, A.C., Watkins, J.J. and Mannard, G.W., (1975). The geology of the Kidd Creek mine. *Econ. Geol*, **70**, (1), 80-89

Walker, T. R., B. Waugh, and A. J. Crone, (1978), Diagenesis in first cycle desert alluvium of Cenozoic age, south-western United States and north-western Mexico: *Geological Society of America Bulletin*, **89**, 19-32

Walker, T. R., E. E. Larson, and R. P. Hoblitt, (1981), Nature and origin of hematite in the Moenkopi Formation (Triassic), Colorado Plateau: A contribution to the origin of magnetism in red beds: *Journal of Geophysical Research*, **86**, 317-333

Walker, T.T., (1975). Red beds in the western interior of the United States. US Geological Survey Professional Paper **853**, 49-56

Walsh, J.J. and Watterson, J., (1988). Analysis of the relationship between displacements and dimensions of faults. *Journal of Structural Geology*, **10**, (3), 239-247

Walsh, J.J. and Watterson, J., (1991). Geometric and kinematic coherence and scale effects in normal fault systems. *Geological Society, London, Special Publications*, **56***, (1), 193-203

Walsh, J.J., Nicol, A., Childs., (2002). An alternative model for the growth of faults. *Journal of Structural Geology,* **24**, 1669-1675

Wang, J., Su, R., Chen, W., Guo, Y., Jin, Y., Wen, Z. and Liu, Y., 2006. Deep geological disposal of high level radioactive wastes in China. *Chinese Journal of Rock Mechanics and Engineering*, **4**

Watterson, J., (1986). Fault dimensions, displacements and growth. *Pure and Applied Geophysics*, **124***, (1-2), 365-373

Watts, N.L., (1987). Theoretical aspects of cap-rock and fault seals for single-and two-phase hydrocarbon columns. *Marine and Petroleum Geology*, **4***, (4), 274-307

Wibberley, C.A., Yielding, G. and Di Toro, G., (2008). Recent advances in the understanding of fault zone internal structure: a review. Geological Society, London, Special Publications, 299, (1), 5-33

Wigley, M., Kampman, N., Dubacq, B. and Bickle, M., (2012). Fluid-mineral reactions and trace metal mobilization in an exhumed natural CO2 reservoir, Green River, Utah. Geology, **40**, (6), 555-558

Winograd, I.J., (1981). Radioactive waste disposal in thick unsaturated zones. *Science (Washington, DC)*, **212**, 1457-64

Wong, T.F., David, C. and Zhu, W., (1997). The transition from brittle faulting to cataclastic flow in porous sandstones: Mechanical deformation. *Journal of Geophysical Research: Solid Earth*, **102**, 3009-3025

Woodcock, N.H. and Fischer, M., (1986). Strike-slip duplexes. *Journal of structural geology*, **8***, (7), 725-735

Yielding, G., Freeman, B. and Needham, D.T., (1997). Quantitative fault seal prediction. *AAPG bulletin*, **81**, (6), 897-917

Zhu, M.Y., Babcock, L.E. and Peng, S.C., (2006). Advances in Cambrian stratigraphy and paleontology: integrating correlation techniques, paleobiology, taphonomy and paleoenvironmental reconstruction. *Palaeoworld*, **15**, (3), 217-222